Thèse

Pour l'obtention du titre de :

DOCTEUR de L'UNIVERSITÉ DE LORRAINE

Spécialité : *Physique*

Présenté par :

Mohammed Salah EL HADRI

Magnetization reversal mechanism leading to all-optical helicity-dependent switching

---

Thèse soutenue publiquement le 19 septembre 2016 à Nancy devant le jury composé de :

M. André Thiaville	Directeur de recherche, Laboratoire de Physique des Solides	Rapporteur
Mme Julie Grollier	Directrice de recherche, Unité Mixte de Physique CNRS/Thales	Rapportrice
M. Eric Fullerton	Professeur, University of California, San Diego	Examinateur
M. Jeffrey Bokor	Professeur, University of California, Berkeley	Examinateur
M. Alexey Kimel	Directeur de recherche, Radboud University Nijmegen	Examinateur
M. Stéphane Mangin	Professeur, Université de Lorraine	Directeur de thèse
M. Grégory Malinowski	Chargé de recherche, Institut Jean Lamour	Co-directeur de thèse

Institut Jean Lamour
UMR CNRS 7198 – Université de Lorraine, Nancy
Département de Physique de la Matière et des Matériaux
Équipe de Nanomagnétisme et Électronique de Spin

Remerciements

Je tiens tout d'abord à remercier sincèrement les membres du jury **André Thiaville**, **Julie Grollier**, **Eric Fullerton**, **Jeffrey Bokor** et **Alexey Kimel** pour avoir accepté d'examiner mon travail et pour leurs remarques sur le manuscrit.

Je voudrais remercier les membres de l'équipe de nanomagnétisme et électronique de spin pour avoir fait de mes trois années de thèse une magnifique expérience. J'aimerais remercier en premier lieu **Stéphane Mangin** et **Grégory Malinowski** pour leur encadrement et leur soutien permanent tout au long de ma thèse. Merci à **Stéphane Mangin** pour m'avoir accordé sa confiance, et pour sa disponibilité et son enthousiasme indéfectibles. Je le remercie pour tout ce qu'il m'a appris tant sur le plan humain que scientifique. Merci également à **Grégory Malinowski** pour son investissement profond dans ma thèse, et pour sa rigueur et sa perspicacité qui m'ont beaucoup apporté tout au long de ma thèse. Je tiens également à remercier vivement **Michel Hehn** pour son encadrement, sa disponibilité et les centaines d'échantillons faits avec sa pulvé. Ce fut pour moi un très grand plaisir de travailler avec lui. Aussi, je remercie grandement **Philipp Pirro** pour l'effort qu'il a fait pour m'encadrer. Je serai toujours reconnaissant pour tout ce qu'il m'a appris, vielen Dank !

Mes remerciements vont ensuite à toutes les personnes avec qui j'ai collaboré pendant ma thèse. Je remercie **Sébastien Petit-Watelot** et **François Montaigne** pour avoir contribué très précieusement à la réussite de cette thèse. Merci à **Sébastien Petit-Watelot** pour sa contribution sur les mesures électriques résolues en temps, et à **François Montaigne** pour les nombreuses lithographies faites dans le cadre de ma thèse et pour son aide précieuse avec les manips. Je tiens également à remercier **Nicolas Bergeard** pour ses conseils avisés et son soutien permanent. Merci à **Charles-Henri Lambert** pour sa contribution à ce travail de thèse et son amitié indéfectible. Un grand merci à mon successeur **Yassine Quessab** pour sa contribution et pour les bons moments passés ensemble, et aussi à **Pierre Vallobra** et **Patricia Riego** pour les moments sympas et pour leur aide avec les manips du retournement optique. Je leur souhaite à tous une bonne continuation !

Je voudrais remercier **Thomas Hauet**, responsable du CC magnétisme, pour sa disponibilité et sa bonne humeur. Merci à **Stéphane Suire** et à **Crosby Chang** pour la préparation de plusieurs dizaines de bidons d'hélium et d'azote et pour leurs interventions efficaces. Je remercie également **Gwladys Lengaigne** et **Laurent Bouvot** pour la formation en salle blanche et leur disponibilité tout au long de ma thèse. Merci à **Laurent Badie** pour ses conseils et pour la préparation des échantillons pour les TP. Je remercie également **Jean-Georges Mussot** et **Emmanuel Vatoux** pour les coups de main en atelier et leur bonne humeur.

Je tiens également à remercier **Isabelle Fournelle** et **Philippe Lambert** pour leur gentillesse et leur disponibilité pour régler les quelques petits problèmes administratifs. Je remercie **Daniel Lacour** pour sa bonne humeur et le beau colloque Louis Néel qu'il a organisé. Merci également à **Hélène Fischer** pour sa gentillesse et son soutien tout au long de ma thèse. Un grand merci à tous les membres permanents de l'équipe de nanomagnétisme et électronique de spin que j'ai croisés durant ma thèse mais que je n'ai pas cités !

J'ai aussi eu le plaisir de collaborer avec un grand nombre de personnes hors IJL. Je tiens à remercier vivement **Eric Fullerton** pour m'avoir accueilli au sein de son groupe à UCSD et **Vitaliy Lomakin** pour les discussions fructueuses. Je remercie également **Robert Tolley** et à

Raj Medapalli pour leur aide avec les manips. Un grand merci à **Majd Kuteifan**, **Sidi Fu** et **Iana Volvach** pour les moments sympas passés à San Diego. Je remercie également **Dafiné Ravelosona** de l'IEF pour sa collaboration et sa bonne humeur, et **Cyrille Beigné** de Spintec pour avoir effectué l'irradiation ionique sur les échantillons de Co/Pt. Finalement, je remercie grandement **Abdelilah Benyoussef**, **Ali Guedira** et **Omar Mounkachi** pour m'avoir accueilli au sein de MAScIR et pour la collaboration que nous avons pu monter ensemble. Un grand merci à **Mohamed Tadout** et **Khadija El Maalam** pour les bons moments passés à Nancy. Je leur souhaite une bonne continuation !

Je tiens ensuite à remercier vivement tous les doctorants et post-doctorants passés ou actuels de l'IJL : **Christopher Vautrin**, **Vincent Polewczyk**, **Sarah Xing**, **Damien Louis**, **Fahad Al-njiman**, **Marion Lavanant**, **Abdlhak Djeffal**, **Yong Xu**, **Bingshan Tao**, **Shiheng Liang**, **Guillaume Sala**, **Ludovic Pasquier**, **Elmer Monteblanco**, **Abbass Hamadeh**, **Julien Granet**, **Arnaud Hillion**. Merci pour tous les moments sympas qui resteront gravés dans mon esprit. Je n'oublie pas les anciens doctorants : **Amina Neggache**, **Jennifer Weimmerskirch-Aubatin**, **Mathias Bersweiler** et **Hanna Riahi**. Merci beaucoup pour les conseils et le soutien tout au long de ma première année de thèse.

Un grand merci à **Florent Hild**, **Sébastien Geiskopf** et **Jennifer Weimmerskirch-Aubatin** pour m'avoir accueilli dans le fameux bureau des doctorants de l'équipe de nanomatériaux. Ce fut un plaisir pour moi de les côtoyer tous les jours, et de partager avec eux des moments inoubliables ainsi que des discussions passionnantes pendant les pauses. Merci également de m'avoir permis de savourer le fauteuil mythique de l'IJL ! Je tiens également à remercier les personnes qui sont devenues pour moi une seconde famille : **Ayoub Bourjilat**, **Florent Hild**, **Lucas Eichenberger**, **Mathilde Blaise**, **Thomas Drouot**, **Anaïs Gillet**, **Marine Perry**, **Matthias Meier** et **Thomas Moinel**. Merci pour tous les moments inoubliables pendant les repas du midi, tous les délires, les matches (amicaux) et les aventures dans les Vosges et à Saverne !

Enfin, merci à toutes les personnes qui m'ont encouragé, et à tous ceux que j'ai croisé durant ces trois ans de thèse et que je n'ai pas cités !

Je dédie ce manuscrit

à mes Parents

à mon Frère

à ma Famille

à mes Amis

à la mémoire de mon Grand-père

et de mon Oncle Abdelkrim

Contents

Introduction

The control of magnetism without applied magnetic fields is an emergent field of research allowing for the exploration of novel physical phenomena and the development of technological applications such as data storage devices. In 2007, the discovery of the all-optical switching by Stanciu *et al.* as an intriguing new possibility to switching the magnetization triggered a great interest from the scientific community. This all-optical switching consists in using ultrashort laser pulses without any other stimuli to achieve a complete and persistent reversal of the magnetization. Indeed, all-optical switching was first demonstrated in ferrimagnetic GdFeCo alloy films and was helicity-dependent, since the magnetization can be deterministically reversed using circularly polarized fs laser beam. Later, it was shown on the same material that all-optical switching is helicity-independent and achieved using a single linearly-polarized laser pulse. While the helicity-independent behavior was attributed to the distinct dynamics of Gd and FeCo sublattices, the underlying physics of the helicity-dependent behavior is heavily debated and was mainly attributed to the circular magnetic dichroism. Recent experimental investigations have shown that all-optical switching is a much more general phenomenon as it is not restricted to GdFeCo alloys. Indeed, all-optical switching was also demonstrated in a large variety of ferrimagnetic materials using fs laser beam. In contrast to GdFeCo films, the all-optical switching of these materials appears to be always helicity-dependent independently of the laser power. More recently, the pioneering experiments by Lambert *et al.* in 2014 showed that all-optical helicity-dependent switching is a rather general phenomenon and occurs for a wide range of ferromagnetic thin films and granular FePt films, where the theoretical models explaining the switching in GdFeCo films do not appear to apply. These findings question the uniqueness of the microscopic origin of all-optical switching.

These recent discoveries triggered an intensive debate about several aspects of the all-optical switching mechanism in ferri- and ferro-magnets. Indeed, several investigations elucidated the magnetic parameters ruling the observation of the all-optical switching, the role of heating in the switching process, and the symmetry breaking mechanism in both ferri- and ferromagnets. In this thesis, we investigated the optical response of ferrimagnetic alloys and ferromagnetic multilayers under the action of fs laser pulses and addressed mainly two key issues regarding the rich physics underlying the all-optical switching. The first issue we addressed in this thesis the magnetic parameter governing the observation of all-optical switching in both ferrimagnetic TbCo alloys and ferromagnetic Co/Ni and Co/Pt multilayers. The second key issue we addressed is the uniqueness of the all-optical switching mechanism in both ferri- and ferro-magnets.

This manuscript is divided into four chapters. The first chapter consists in a state of the art of both experimental and theoretical investigations of the all-optical switching. The second chapter presents the experimental tools used in this thesis to fabricate the studied samples and to perform the all-optical switching experiments. The third chapter focuses on the comprehensive investigation of the magnetic parameters ruling the observation of all-optical switching in both ferri- and ferro-magnets. In the fourth chapter, we investigate the all-optical switching in Hall cross devices via the anomalous Hall effect. We distinguished between two types of all-optical switching mechanisms: a single pulse switching for ferrimagnetic GdFeCo alloys as previously reported in literature, and a cumulative two regimes switching process for both ferrimagnetic TbCo alloys and ferromagnetic Co/Pt multilayers.

Chapter 1

All-optical magnetization switching

1.1 Introduction

The manipulation of magnetism without magnetic fields has triggered great interest as an emergent field of research, due to the prospect of exploring novel physical mechanisms and impacting many technological applications such as low-power electronics, magnetic recording and spintronic devices. Promising physical mechanism of magnetization consists in tuning of magnetic properties using an electric field as discovered in the last decade [1, 2, 3], and the spin transfer torque switching arising from several mechanisms namely the direct momentum transfer [4, 5, 6], the spin-orbit interaction [7, 8] or the spin-Seebeck effect [9, 10, 11]. Nevertheless, an intriguing new possibility to switch the magnetization was discovered in the last decade, and consists in using ultrashort laser pulses without any other stimuli. This so-called "all-optical magnetization switching" was initially demonstrated in GdFeCo alloy films [12], and later in a variety of ferrimagnets and ferromagnets. After almost 10 years of experiments and theoretical studies, the underlying physics of the all-optical switching is still under debate. Therefore, this first chapter consists in a state of the art of the experimental and theoretical investigations of the all-optical switching, leading to an ongoing heavy debate on its microscopic origin. First, we present in section 1.1 the first experiments and microscopic modeling for the laser-induced ultrafast magnetization dynamics. Second, we report in section 1.2 on the discovery of the ultrafast all-optical magnetization switching in GdFeCo alloys. Third, we present in section 1.3 the extensive material-dependent investigation of all-optical switching demonstrating that the latter is a more general phenomenon. Finally, we discuss in section 1.4 different studies reported in the literature discussing the symmetry breaking mechanism, and the role of the laser heating and the orientation conservation in the achievement of all-optical switching.

1.2 Phenomenology of laser-induced ultrafast magnetization dynamics

1.2.1 Observation of ultrafast laser-induced demagnetization

The investigation of physical phenomena in metals using ultrashort lasers became possible thanks to the emergence of ultrafast optics in the eighties. Indeed, metals are first excited using a picosecond (ps) or femtosecond (fs) "pump" laser pulse, and later a delayed "probe" laser pulse strikes the metal. By measuring the reflection of the probe pulse, the laser-induced change in the magnetization is quantified as a function of delay time. In the early nineties, this "pump-probe" measurement did not show any laser-induced magnetization dynamics [13] or was not resolved due to the limited temporal resolution of the experiment [14]. Nevertheless, Beaurepaire *et al.* [15] performed in 1996 the first measurement on the laser-induced magnetization dynamics with a sub-picosecond temporal resolution. Using pump-probe experiment,

the magnetization of a Ni film under the action of a 60 fs laser pulse is measured as a function of delay time. As shown in figure 1.1, the magnetization drops during the first ps and partially recovers within 15 ps. This behavior was qualitatively explained by a three-temperature model [15]. However, the microscopic origin of this ultrafast demagnetization was unknown and is still under debate.

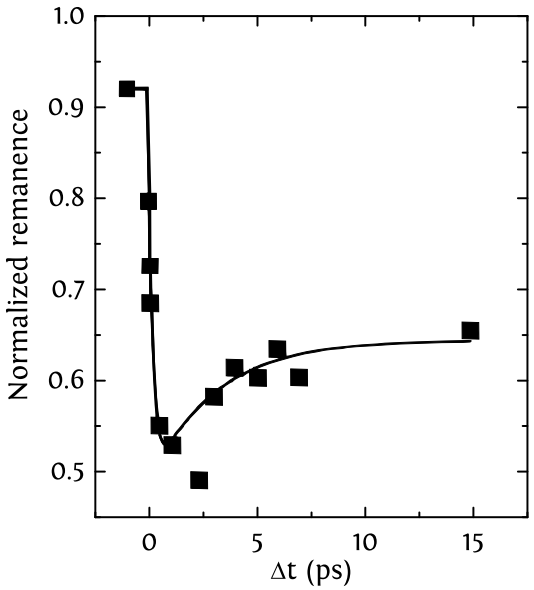

FIGURE 1.1: Normalized transient remanent MOKE signal of a Ni(20 nm)/MgF_2(100 nm) film for 7 mJ/cm^2 pump fluence. The line is a guide to the eye. Figure adapted from [15].

This pioneering measurement paved the way for the field of ultrafast magnetization dynamics, which triggered a great interest from the scientific community. It has also introduced further physical phenomena, namely the laser-induced generation of spin currents [16, 17, 18] and the laser-induced terahertz (THz) emission [19].

1.2.2 Modeling of the ultrafast magnetization dynamics

To explain the ultrafast magnetization dynamics, many theoretical models focus mainly on the thermalization of spins via the absorption of the laser pulse by the electronic system [20] and highlight the major role of laser heating in the demagnetization process [21, 22]. In the following we will discuss the different models proposed in the literature.

Phenomenological three-temperature model

The ultrafast demagnetization initially demonstrated in Ni films was first attributed to the energy transfer from the laser-excited electrons to the spin system [15]. To elucidate the demagnetization process, a simple model was proposed by Beaurepaire *et al.* [15] called the "three-temperature model" (3TM). This phenomenological model is based on the interactions between three different systems, namely the electrons, the lattice and the spins. Each system is a reservoir for energy. By taking into account the spin system, the 3TM is an extension of the two-temperature model (2TM) describing the energy transferred from the laser-excited electrons only to the lattice [23].

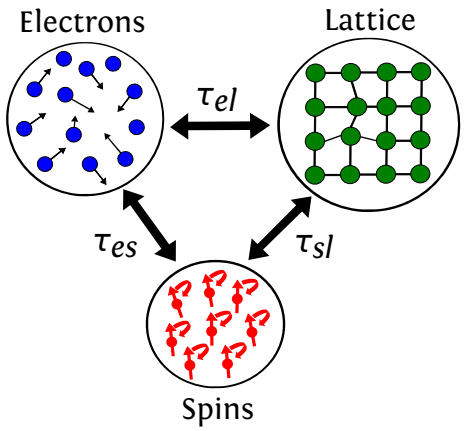

FIGURE 1.2: Interacting reservoirs (spin, electrons and lattice) in the 3TM model. The laser pulse is first absorbed by the electrons bath, then heat is transferred between the three-coupled reservoirs. τ_{ij} is the time constant associated with the interaction between reservoirs *i* and *j*. Figure adapted from [24].

As illustrated in figure 1.2, the absorption of a laser pulse by electrons leads to a heat transfer between three-coupled reservoirs. Each of these coupled reservoirs has then its own temperature and heat capacity. Taking into account the energy balance, the temporal evolution of the temperature in each reservoir can be expressed by the following coupled equations:

$$C_e(T_e)\frac{dT_e}{dt} = -G_{el}(T_e - T_l) - G_{es}(T_e - T_s) + P(t) \tag{1.1}$$

$$C_s(T_s)\frac{dT_s}{dt} = -G_{es}(T_s - T_e) - G_{sl}(T_s - T_l) \tag{1.2}$$

$$C_l(T_l)\frac{dT_l}{dt} = -G_{el}(T_l - T_e) - G_{sl}(T_l - T_s) \tag{1.3}$$

Where G_{ij} is the interaction constant between the reservoirs *i* and *j*. C_i and T_i are heat capacity and temperature of the reservoir *i*, respectively. $P(t)$ is the laser source term applying only to the electron term, since the initial laser-heating occurs only in the electrons reservoir.

The spin temperature is thus related to the magnetization through the measurement of M as function of temperature. The numerical solutions of the three-coupled equations are demonstrated in figure 1.3. The electron and spin temperature dynamics are in good agreement with the experimental data [15]. As shown in figure 1.3, T_e increases rapidly and separately within the first 500 fs. This rapid increase is attributed to the thermalization of electrons due to electron-electron interaction [25]. This thermalization is followed by an increase of T_s and T_l via electron-spin and electron-phonon interactions, respectively. T_s increases more rapidly than T_l since C_l is much larger than C_s. The increase of the spin temperature corresponds to the ultrafast demagnetization shown in figure 1.1. Since G_{el} is much larger than G_{ls}, the thermalized electrons relax their energy to the lattice due the electron-phonons interaction, while the spin reservoir remains hot. Once T_s becomes higher than T_e, the spin temperature decreases slowly, which corresponds to the remagnetization shown in figure 1.1.

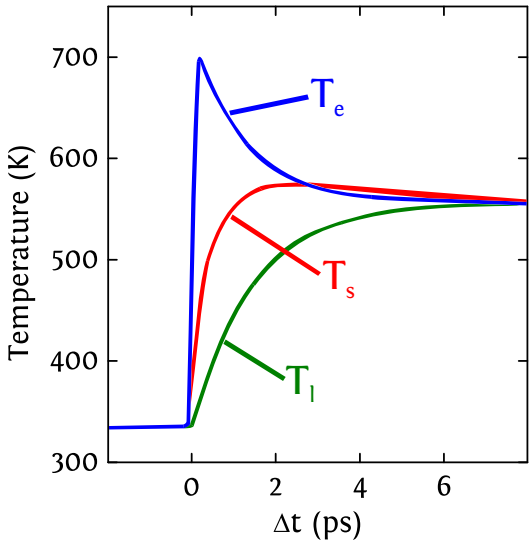

FIGURE 1.3: Evolution of spin T_s, electron T_e, and lattice T_l temperatures as a function of delay time, as calculated by Beaurepaire *et al.* [15].

The relaxation rates associated with the interaction between the reservoirs have also been measured. Indeed, the electron-lattice relaxation rate is of the order of few ps. The spin-lattice relaxation rate is of the order of 100 ps, whereas the spin-electron relaxation rate is shown to be of the order of 100 fs [26].

Atomistic spin dynamics

The magnetization dynamics is usually modeled using the macrospin approximation, which assumes that the magnetization in a ferromagnet is spatially uniform, meaning that all atomic spins point in the same direction. Using the macrospin approximation, the magnetization dynamics in a ferromagnet under an external applied field H_{app} is governed by the Landau-Lifshitz-Gilbert equation (LLG) [27, 28], which is expressed as follows:

$$\frac{d\vec{M}}{dt} = -\gamma\mu_o\vec{M} \times \vec{H}_{app} + \frac{\alpha}{M}\vec{M} \times \frac{d\vec{M}}{dt} \tag{1.4}$$

where γ is the gyromagnetic ratio, μ_o is the permeability constant, and α the Gilbert damping constant. The first term corresponds to the field torque leading to a processional motion of magnetization around the applied magnetic field. The second term is the phenomenological damping term, leading to the damped oscillations of magnetization until it gets aligned with the applied field. The period of the damped oscillations is of the order of 100 ps, whereas the relaxation rate is of the order of a few ns and is determined by the Gilbert damping constant. The LLG equation cannot be used to model the laser-induced magnetization dynamics, since it does not allow calculating the change in the amplitude of magnetization which is induced by an ultrashort laser pulse. To model the ultrafast magnetization dynamics in a metallic magnet, the LLG equation can be used to describe the spin dynamics of many atomistic spins instead of one single macrospin. As shown by Skubic *et al.* [29], this atomistic spin approach is based on a Born-Oppenheimer like approximation for the spin system, considering that atomistic spins are slow variables and the electrons as being very fast. Hence, the electronic dynamics will respond almost instantaneously to the pulse excitation.

A first difference from the LLG in equation (1.4) is that individual spins are coupled to their nearest neighbors via the exchange interaction. The contribution of the exchange interaction to the effective field experienced by the atomic spin "*i*" in a material is expressed as follows:

$$\vec{H}_{exi} = \sum_j J_{ij}\vec{m}_j \tag{1.5}$$

where *j* denotes to the atomic index of the nearest neighbors of the atomic spin *i* and m_j is the atomic moment of the atomic spin *j*. Moreover, another major difference from the LLG equation is a thermal stochastic field which is added to the effective field. This random field is a Gaussian stochastic process and is experienced by the individual atomic spins, leading to a random motion of the atomic moments $\vec{m}_i$. The amplitude of the thermal fields is calculated based on the so-called fluctuation-dissipation theorem [30]. By assuming that the spins are strongly coupled to the electrons than to the phonons bath, the amplitude of the thermal field H_{th} is given by:

$$H_{th} = \sqrt{\frac{k_B T_e}{\gamma m_s}\alpha} \tag{1.6}$$

where T_e is the electronic temperature, m_s the atomic magnetic moment and k_B Boltzmann's constant. The laser-induced rise of the electronic temperature T_e depicted in figure 1.3 leads to a large increase of the random fields' amplitude, thus creating a disordered spin system. The macroscopic magnetization measured by the pump-probe experiment is reduced. Furthermore, these atomistic spin calculations show that the demagnetization takes place within 100 fs for Ni [31] and 150 fs for Fe [29]. A further advantage of the atomistic spin approach is the fact that it can be applied to a large variety of magnetic systems such as ferrimagnetic alloys [32, 33]. However, the microscopic origin of the ultrafast demagnetization cannot be investigated with the atomistic spin calculations, since the conservation of the angular momentum is not taken into account in such approach.

Landau-Lifshitz-Bloch equation

Another approach derived from the atomistic spins stochastic dynamics is the Landau-Lifshitz-Bloch (LLB) equation, which combines the LLG equation at low temperatures and the Bloch equation at high temperatures. In the LLB equation, the exchange interaction is treated within the mean-field approximation (MFA) [34] leading to the following equation of motion for a macrospin *M*:

$$\frac{d\vec{M}}{dt} = \gamma_o\left[\vec{M}\times\vec{H}_{eff} + \frac{\alpha_{||}}{M}(\vec{M}.\vec{H}_{eff})\vec{M} - \frac{\alpha_\perp}{M}\vec{M}\times\vec{M}\times\vec{H}_{eff}\right] \tag{1.7}$$

where γ_o is the Larmor precession frequency, and H_{eff} is the effective field including the exchange interaction. $\alpha_{||}$ and $\alpha_\perp$ are the longitudinal and transverse damping parameters defined for temperatures *T* lower than the Curie temperature as follows:

$$\alpha_{||} = \alpha\frac{2T}{3T_c} \tag{1.8}$$

$$\alpha_\perp = \alpha\left[1 - \frac{T}{3T_c}\right] \tag{1.9}$$

For $T > T_c$, the longitudinal and transverse damping parameters are identical. The transverse damping $\alpha_\perp$ results from the transverse relaxation of the individual spins. Contrary to the LLG equation, the amplitude of *M* in the LLB equation is not conserved, and the results are in

good agreement with the experimental observations. The LLB equation has several advantages over the atomistic spin approach, such as the fast computational time and the calculation on micrometer size systems. However, LLB equation applies less to complex magnetic systems such as ferro- and ferri-magnetic alloys.

1.3 All-optical switching in GdFeCo thin films

1.3.1 Experimental demonstration of all-optical switching in GdFeCo alloy films

A fascinating outcome of the experimental investigations on the ultrafast magnetization dynamics in magnetic systems is the demonstration of the all-optical switching (AOS) of magnetization using femtosecond laser pulses. Indeed, Stanciu *et al.* showed in 2007 that the magnetization in a ferrimagnetic $Gd_{22}Fe_{74.6}Co_{3.4}$ alloy film could be deterministically reversed using circularly polarized laser pulses and without any external applied field [12]. The direction of magnetization is given by the right- or left-circular polarization of the pulses. Later, it was demonstrated by Radu *et al.* [32] that the magnetization in $Gd_{25}Fe_{65.6}Co_{9.4}$ alloy film could be also reversed using a single linearly polarized fs laser pulse. In this section we will introduce the pioneering experimental observations of the all-optical switching in GdFeCo alloy films.

Multiple-pulse and single-pulse helicity-dependent switching

In 2007, the first observation of AOS using circularly polarized light was demonstrated on a 30 nm-thick $Gd_{22}Fe_{74.6}Co_{3.4}$ alloy film with perpendicular magnetic anisotropy (PMA). The sample is first placed under the Faraday microscope. As shown in figure 1.4(a), the domains with magnetization "up" and "down" could be observed as white and black regions, respectively. The sample is then excited using a Ti: sapphire laser with a repetition rate of 1 kHz, a wavelength of 800 nm and a pulse duration of 40 fs. The Gaussian fs laser beam illuminates the sample perpendicularly to the film plane, and is swept at a high speed across the sample so that each pulse landed at a different spot. Figure 1.4(b) shows that $\sigma+$ (resp. $\sigma-$ pulses switch the magnetization in the black (resp. white) domain, without affecting the magnetization of the white (resp. black) domain. This reversal with circularly polarized light is called all-optical helicity-dependent switching (AO-HDS). The region exposed to linearly polarized light is turned into small domains randomly oriented up or down. Moreover, figure 1.4(b) shows that a demagnetized area is located to the right of the scanned region, at the point where the laser beam was turned off.

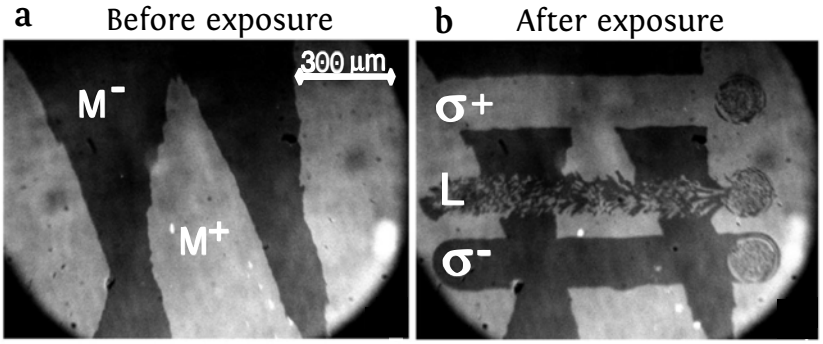

FIGURE 1.4: (a) Magneto-optical image of the initial magnetic state of the sample before laser exposure. White and black areas correspond to up (M^+) and down (M^-) magnetic domains, respectively. (b) Domain pattern obtained by sweeping at low speed 30 µm/s linear (L), right-handed (σ+), and left-handed (σ-) circularly polarized beams across the surface of the sample, with a laser fluence of about 11.4 mJ/cm^2. The central area of the remaining spots at the end of each scan line consists of small magnetic domains, where the ratio of up to down magnetic domains is close to 1. Figure is adapted from [12].

In order to investigate this behavior, the laser beam with the three different polarizations was focused onto a domain wall as depicted in figure 1.5. The gray area observed in the center of the laser beam has an intermediate contrast. This area consists of small domains randomly oriented up and down by each excitation, which are due to the strong heating above T_c in the central part of the Gaussian beam [12]. The effect of the helicity appears only on the perimeter of the gray area, as a white (resp. black) rim is observed with σ+ (resp. σ-) circularly polarized beam. However, a gray rim is observed with the linearly polarized beam indicating that only multiple domains are obtained, as shown in figure 1.5. By strongly decreasing the laser power, a complete helicity-dependent reversal of magnetization is obtained in the laser-excited area without causing overheating and demagnetization [12]. In the same study, Stanciu *et al.* were also able to achieve AO-HDS using a single 40 fs circularly polarized laser pulse.

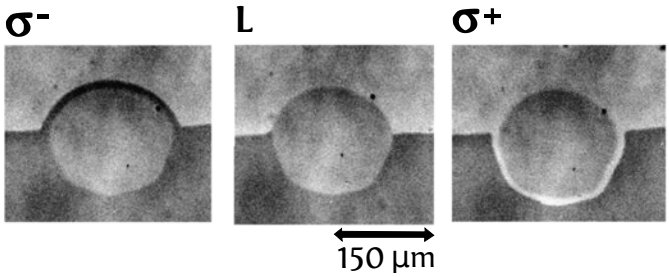

FIGURE 1.5: Images of the laser spot focused onto a domain wall during the 1 kHz pulsed laser excitation with three different helicity. The images were obtained for a pulse fluence of about 11.4 mJ/cm^2. In all three cases the central region of the optically excited area is demagnetized (gray color) due to extensive heating. For circularly polarized excitation (σ+ and σ-) opto-magnetic switching takes place on the perimeter of the excited area, where the temperature is just below T_c. Figure is adapted from [12].

Single-pulse helicity-independent switching

In 2011, Radu *et al.* revealed for the first time a striking feature of all-optical switching in GdFeCo alloy films [32]. Indeed, they demonstrated that the magnetization of a 30 nm-thick $Gd_{25}Fe_{65.6}Co_{9.4}$ alloy film can be reversed using a single linearly polarized pulse. This all-optical helicity-independent switching (AO-HIS) was achieved within 12 ps timescale and measured by probing the two sublattices (Gd and FeCo) of the investigated GdFeCo alloy using X-ray magnetic circular dichroism technique (XMCD) [35, 36]. Furthermore, such single-pulse and helicity-independent switching was also demonstrated on a 20 nm-thick $Gd_{24}Fe_{66.6}Co_{9.4}$ film with an out-of-plane (OOP) magnetization by Ostler *et al.* [33]. As shown in figure 1.6, the studied GdFeCo continuous film is illuminated with a sequence of 5 consecutive 100-fs laser pulses with linear polarization. Independently of the initial saturation, the magnetization in the laser-excited area switches completely with the first pulse, whereas the second pulse switches magnetization back to the initial state. Every pulse thereafter induces a complete reversal. Moreover, this single-shot AO-HIS was fully reproduced by the atomistic spin calculations introduced in section 1.2.2 [32, 33].

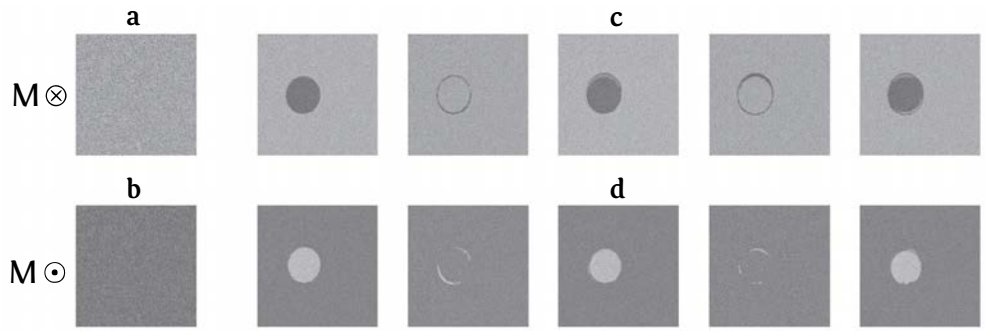

FIGURE 1.6: The magneto-optical images of a $Gd_{24}Fe_{66.5}Co_{9.5}$ continuous film obtained after the action of a sequence of N 100 fs laser pulses. (a) and (b) Initial homogeneously magnetized state of the film with magnetizations "up" and "down" as represented by the circled dot and cross respectively. The light grey region represents magnetization pointing "down" and the darker grey "up". (c) and (d) The film after an excitation with N (N = 1, 2...5) pulses with a fluence of 2.30 mJ/cm^2. Each laser pulse excites the same circular region of the film and reverses the magnetization within it. The scale bar on the right corresponds to 20 µm. Figure is adapted from [33].

The AO-HIS was also verified in patterned GdFeCo structures [33] in order to verify that such behavior is not driven by stray fields or domain walls motion as demonstrated in previous studies [37]. As shown in figure 1.7, the response of arrays of $Gd_{25}Fe_{65.6}Co_{9.4}$ disks to the action of consecutive pulses was investigated. The studied disks have a diameter of 2 µm and are therefore much smaller than the laser spot size (30 x 100 µm). The distance between the disks is as large as their diameter, leading to a negligible dipolar interaction between them. The magnetization reversal was measured with photoemission electron microscopy (PEEM) which employs the XMCD effect. Figure 1.7(a) shows that the magnetization of both disks is completely reversed due to the action of single linearly polarized pulse. Every pulse thereafter induces a complete magnetization reversal. The same behavior was obtained on GdFeCo patterned disks with in-plane (IP) anisotropy, as shown in figure 1.7(b). These findings undoubtedly show that the AO-HIS is deterministic and is not induced by stray fields [33].

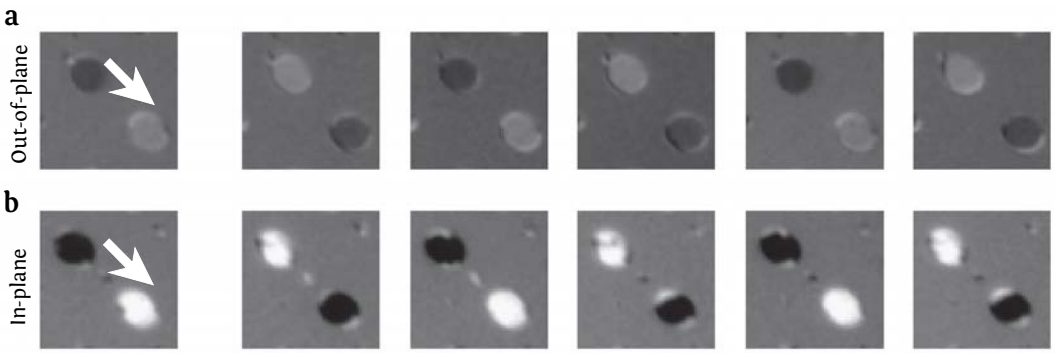

FIGURE 1.7: XMCD images at Fe L_3 edge of 2-μm wide $Gd_{25}Fe_{65.6}Co_{9.4}$ structures. (a) Images of microstructures with out-of-plane anisotropy, magnetized perpendicular to the sample plane. The first image in (a) shows the initial state of the microstructures where the magnetization of the darker structure points down while the magnetization of the brighter one points up. The next image is taken after excitation with a single linearly polarized laser pulse and shows that the magnetizations of both elements are reversed. This reversal occurs after every laser pulse, as can be seen in the subsequent images in (a). (b) Images of microstructures with in-plane anisotropy. The bright and dark areas correspond to magnetization directions in the plane of the sample pointing parallel or anti-parallel to the X-ray direction. Figure is adapted from [33].

1.3.2 Unification of helicity-dependent and heat-only switching

The observation of both AO-HDS and AO-HIS in GdFeCo films raised a number of questions about the underlying microscopic physics of these two aspects of all-optical switching. In this section, we will present the theoretical and experimental investigations reported in the literature on the microscopic origin of all-optical switching in ferrimagnetic GdFeCo alloys.

Transient ferromagnetic-like state

As mentioned in section 1.3.1, the first measurement of the magnetization switching in GdFeCo alloy films with single fs-pulses was performed using XMCD technique [32]. In the ferrimagnetic GdFeCo alloy, the net magnetizations of the transition metal (TM) "FeCo" and the rare-earth (RE) "Gd" sublattices are antiferromagnetically exchange coupled. Hence, the XMCD serves as an element-specific probe of spins in both sublattices. Figure 1.8 shows the evolution of the XMCD signals at Fe and Gd edges due to the action of a single linearly-polarized fs-pulse [32]. The net magnetizations of Gd and Fe sublattices vanish rapidly and rebuilt their magnetic moments at two different timescale. Indeed, the Fe component demagnetizes faster than the Gd one. Moreover, the Fe sublattice is found to switch within 300 fs, whereas the Gd reversal time is much slower and equals 1.5 ps. Due to the different spin dynamics of Fe and Gd, a transient ferromagnetic-like state characterized by a temporary alignment of the net Gd and Fe moments is observed despite their antiferromagnetic coupling.

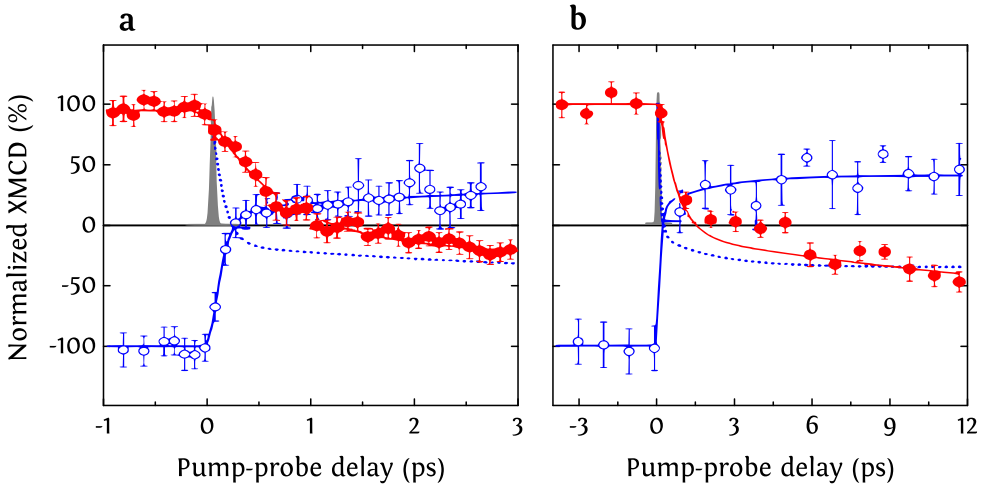

FIGURE 1.8: Element-resolved dynamics of the Fe and Gd magnetic moments measured by time-resolved XMCD with femtosecond time-resolution. (a) Transient dynamics of the Fe (open circles) and Gd (filled circles) magnetic, moments measured within the first 3 ps. (b) as (a) but on a 12 ps timescale. The measurements were performed at a sample temperature of 83 K for an incident laser fluence of 4.4 mJ/cm^2. Experimental time resolution of 100 fs is depicted by the solid Gaussian profile. Figure is adapted from [32].

Calculations based on the atomistic spin approach reproduced qualitatively the timescales for the demagnetization of each sublattice and the transient ferromagnetic-like state. More importantly, no transverse moment is observed during the reversal [32], thus indicating that the switching of the sublattice magnetizations occurs via the mechanism of linear reversal [38]. To conclude, AO-HIS in GdFeCo films is pure thermal and ultrafast. Moreover, its microscopic origin is attributed to distinct dynamics of Gd and FeCo sublattice, leading to the measured transient ferromagnetic-like state.

Role of magnetic circular dichroism

In regards to the AO-HDS in GdFeCo alloy films, it was demonstrated by Khorsand *et al.* [39] that the effect of the helicity using single fs laser pulses occurs only in a narrow window of fluence. As shown in figure 1.9, AO-HDS takes place only for laser fluence $F_{LC} < F < F_{RC}$, where F_{LC} and F_{RC} denote for the switching threshold for left-circularly and right-circularly polarized pulses, respectively. Moreover, AO-HIS occurs for fluences higher than F_{RC} [39]. The window of the AO-HDS is thus defined as:

$$\Delta = \frac{F_{RC} - F_{LC}}{\frac{1}{2}(F_{RC} + F_{LC})} \tag{1.10}$$

In order to determine the microscopic origin of such window, the relative absorption of σ+ and σ- was calculated:

$$MCD = \frac{A_{LC} - A_{RC}}{A_{LC}} \tag{1.11}$$

where A_{LC}, A_{RC} and A_{LP} denote the total absorption of light with σ-, σ+ and π polarization, respectively. Hence, it was shown that the window Δ corresponds to MCD for wavelengths ranging from 500 nm to 800 nm. More details on this experimental investigation are given in section 1.5.2. These findings show that magnetic circular dichroism (MCD) plays major role in the helicity-dependent reversal, indicating that laser-heating is behind the symmetry breaking

for both AO-HDS and AO-HIS in GdFeCo alloys. This thermal origin is in agreement with simulations describing the longitudinal relaxation of multisublattice magnets, and demonstrating that the exchange interaction between the two sublattices under nonequilibrium conditions favors the sublattices reversal [40].

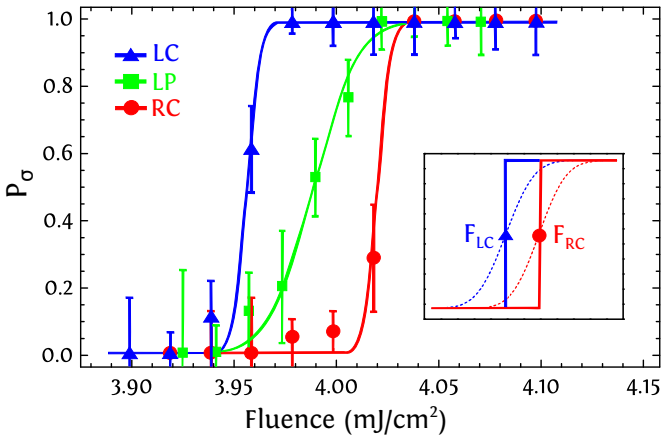

FIGURE 1.9: Switching probability P_σ as a function of the fluence at λ = 700 nm for three different polarizations. The measurements with RC and LC pulses were performed at a different time than the ones with LP pulses, and therefore the laser stability ϵ was different. Shown in the inset are the switching probabilities in case of zero (solid) and nonzero (dashed) laser fluctuations. F_{LC} and F_{RC} denote the switching threshold of GdFeCo for LC and RC excitation pulses, respectively. Figure is adapted from [39].

1.4 Novel materials for all-optical helicity-dependent switching

For a long time, all-optical switching has been extensively studied in GdFeCo alloy films. However, recent experimental investigations have shown that all-optical switching is a much more general phenomenon, since it is not restricted only to GdFeCo films. In this section, we will present the extensive material-dependent study reported in the literature showing that the all-optical switching can be observed in a variety of ferrimagnetic as well as ferromagnetic materials.

1.4.1 Ferrimagnetic materials

Recently it has been shown that all-optical switching is observed in a wide range of ferrimagnetic materials, namely RE-TM alloys with others RE [41, 42, 43, 44], RE/TM multilayers [43], RE-free synthetic ferrimagnets [43] and artificial zero moment magnets [45]. In order to investigate the optical response of these classes of ferrimagnets, the 100-fs laser beam with the three different polarizations is swept over the sample, thus the analog experiment performed on GdFeCo alloys by Stanciu *et al.* [12].

Ferrimagnetic alloys and multilayers

Mangin *et al.* [43] investigated a large range of RE-TM alloys, with RE = Gd, Tb, Dy and Ho and TM = Fe, Co or Fe-Co, in order to study the influence of the RE type and concentration on the observation of AO-HDS. The net magnetization of such RE-TM alloys (M) is given by the sum

of the magnetization of the RE (M_{RE}) and TM (M_{TM}) sublattices. Hence, the net magnetization at a given temperature can be equal to zero at given RE concentration x_{comp}. For larger (resp. lower) RE concentration, M is pointing along M_{RE} (resp. M_{TM}) and the net magnetization will be named "RE dominant" (resp. "TM dominant"). Moreover, RE-TM alloys show a magnetic compensation temperature (T_{comp}) at which the two collinear sublattice magnetizations M_{RE} and M_{TM} compensate. The studied ferrimagnetic alloys exhibit a wide range of magnetic parameters such as the exchange coupling, the spin-orbit interaction, the magnetization and the compensation temperature [46, 47]. For instance, the spin-orbit coupling of Gd-based alloys is supposed to be small due to the zero net orbital momentum of Gd, resulting in a low magneto-crystalline anisotropy. At the opposite of the zero net orbital momentum of Gd, the orbital momentum in Tb, Dy and Ho is large, thus leading to a stronger spin-orbit coupling and larger magnetic anisotropy. This difference in the spin-orbit coupling (SOC) between Gd and the other RE is reported to be at the origin of different ultrafast demagnetization processes induced by ultrashort laser pulses [48].

Four types of RE-TM alloys have been studied by Mangin *et al.* [43], namely 25 nm-thick Gd_xFeCo_{1-x}, Tb_xCo_{1-x} and Ho_xFeCo_{1-x}. All samples were grown on a Glass/Ta(4 nm) substrate, and were capped with a Ta(4 nm) layer to prevent sample oxidation. Most of the studied samples show strong PMA. Gd_xFeCo_{1-x} alloys showed in-plane remanent magnetization for x ‹ 22% and x › 28% due to the low magneto-crystalline anisotropy. The response for each of these samples to the action of circular polarized beam is probed with a Faraday microscope. Therefore, figure 1.10 shows the response to optical excitation of the studied RE-TM alloys as a function the RE concentration x [43]. As shown in figure 1.10, AO-HDS is observed for all of the studied ferrimagnetic alloys independently of the RE element, but only for a narrow window of RE concentrations around 25%. Such behavior has also been reported in other studies [41, 42], indicating that this is a general response for RE-TM alloys. More importantly, figure 1.10 shows clearly that AO-HDS is observed only when T_{comp} is near or above room temperature (RT), indicating that heating across T_{comp} favors the observation of AO-HDS in RE-TM alloys [41, 43].

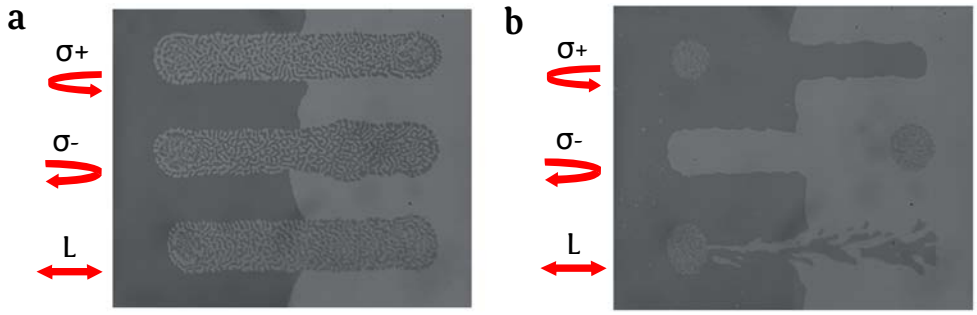

FIGURE 1.10: Examples of the two optical responses for two different samples, $[Co(0.8nm)/ Tb(0.4nm)]_{21}$ multilayers showing thermal demagnetization (a) and $[Co(0.5nm)/Tb(0.4nm)]_{28}$ multilayers showing AO-HDS (b). For each sample, three types of polarized laser beam were swept over the sample and the magnetization pattern was subsequently imaged: from top to bottom, right circularly polarized light (σ+), left circularly polarized light (σ-) and linear polarized light (L). In the image, dark contrast corresponds to one orientation of magnetization and light contrast the opposite. Figure adapted from [43].

Mangin *et al.* extended these studies to RE-TM multilayers, in order to investigate the role of the atomic ordering and thus the exchange coupling between the RE and TM sublattice on AO-HDS [43]. For instance, it was demonstrated that the ultrafast demagnetization can be quite

different in alloys compared with multilayers, as shown in a comparison between FeNi alloy [49] and Fe/Ni multilayers [50]. The systems studied by Mangin *et al.* [43] are $[RE(t_1)/TM(t_2)]_N$, where N is the number of repeats and were grown by DC sputtering on Glass/Ta(4 nm) substrate and capped with Ta(4 nm). The total thickness of the multilayers was kept constant at 25 nm to be comparable to the RE-TM alloy films.

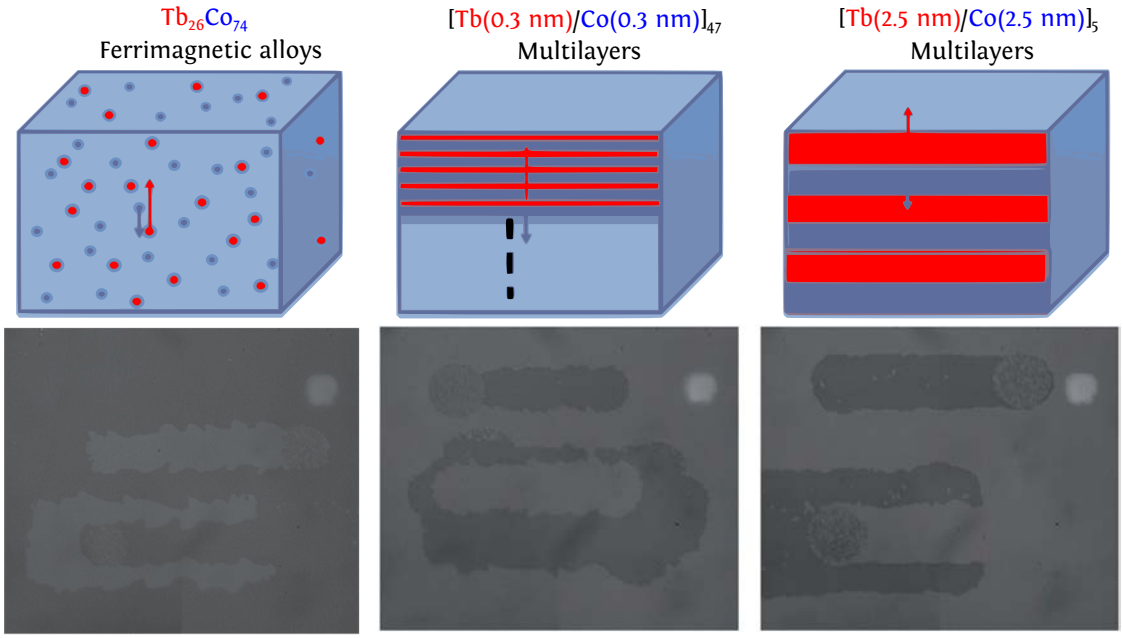

FIGURE 1.11: Circularly polarized beams (σ+ or σ-) have been swept over the samples. All-optical switching can be observed for three different samples: a $Tb_{26}Co_{74}$ alloy, a $[Tb(0.3nm)/\ Co(0.3nm)]_{42}$ multilayer and a $[Tb(2.5nm)/Co(2.5nm)]_5$ multilayer, which have the same average concentration of Tb and Co atoms. Figure adapted from [43].

The RE-TM ratio is kept constant while growing different structures starting from a homogeneous isotropic amorphous alloy to RE-TM multilayers [43]. To keep a constant thickness and RE-TM ratio, the sample heterogeneity in RE-TM multilayers is tuned by increasing the layer thicknesses and reducing the number of repetition. In RE-TM multilayers, the magnetization of the RE layers M_{RE} is antiferromagnetically coupled to the one of the TM layers M_{TM}. Moreover, a T_{comp} can also defined in RE-TM multilayers from the sign change of the Kerr signal and the divergence of the coercivity [43].

For the studied [Tb/Co] and [Ho/CoFe] multilayers, the PMA is strong even for 3 nm-thick RE layers, whereas for [Gd/Co] multilayers, the PMA becomes weak and the magnetization lies in-plane once t_{Gd} exceeds 1 nm. Figure 1.11 shows the response to optical excitation of three different samples with the same RE-TM ratio and total thickness, namely $Tb_{26}Co_{74}$ (25 nm) alloy, $[Tb(0.3\ nm)/Co(0.3\ nm)]_{42}$ and $[Tb(2.5\ nm)/Co(2.5nm)]_5$ multilayers. AO-HDS is observed on these three samples, indicating that AO-HDS is not limited to alloys. As shown in figure 1.10, AO-HDS is observed in RE-TM multilayers only for a narrow range of composition, which corresponds to T_{comp} near or above RT. For instance, figure 1.12 shows that $[Co(0.8\ nm)/Tb(0.4\ nm)_{21}$ sample with a T_{comp} below RT shows thermal demagnetization. To conclude, the investigation of the optical response for RE-TM systems highlights the role of the PMA and the antiferromagnetic coupling between non-equivalent sublattices in the observation of AO-HDS

[43]. These requirements have been proposed by Kimel as rules to achieve the all-optical magnetization switching [51].

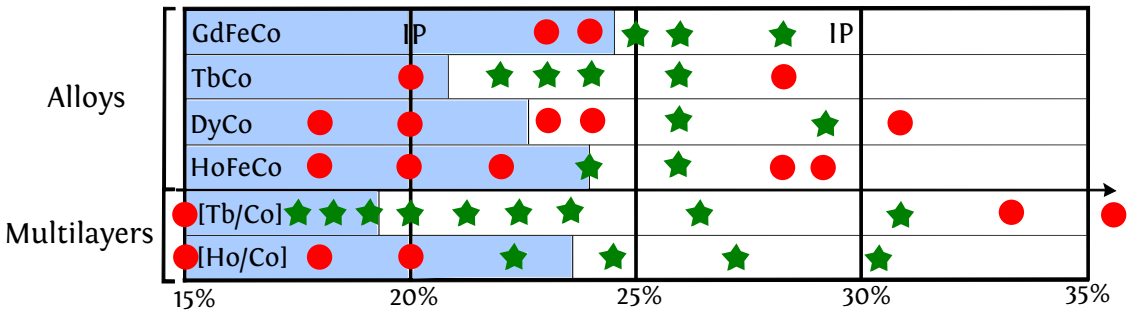

FIGURE 1.12: Response to optical excitation for RE-TM alloys (Gd_xFeCo_{1-x}, Tb_xCo_{1-x}, Dy_xCo_{1-x}, Ho_xFeCo_{1-x}) and two types of RE-TM multilayer ([Tb/Co] and [Ho/CoFe]) as a function of the RE concentration (x). Red dots indicate thermal demagnetization and green stars AO-HDS. All of these alloys show perpendicular anisotropy except the two GdFeCo alloys marked IP (for in-plane anisotropy). The regions shaded correspond to alloy compositions for which T_{Mcomp} is below RT. For the multilayers the RE layer thicknesses varied from 0.3 to 0.5 nm and the TM layers varied from 0.25 to 1.0 nm. Figure adapted from [43].

Rare earth-free synthetic ferrimagnetic heterostructures

Furthermore, Mangin *et al.* [43] investigated the occurrence of AO-HDS in RE-free synthetic ferrimagnetic heterostructures (SFI), since they exhibit magnetic characteristics similar to the ones of RE-TM alloys and multilayers. Indeed, SFI exhibit PMA and consist of two distinct and antiferromagnetically coupled magnetic sublattices. Moreover, the two sublattices have different temperature dependences and show a T_{comp} near or above RT, as depicted in figure 1.13 (a).

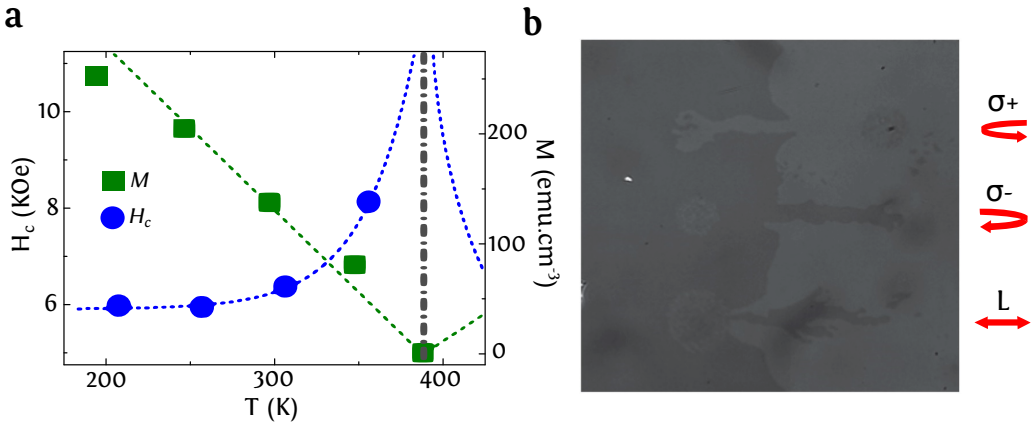

FIGURE 1.13: Magnetic measurements of a Ta(4 nm)/Pd(3 nm)/[Co(1 nm)/Ir/Co(0.4 nm)/Ni(0.6 nm)/Pt(0.3 nm)/Co(0.4 nm)/Ir]$_5$/Pd(3 nm) SFI structure. (a) Remanent magnetization M and coercive field H_c as a function of temperature allow us to define a compensation temperature at T_{Mcomp} = 380 K. (b) Images after scanning the laser with three types of polarized beam that were swept over the sample: from top to bottom, right circularly polarized light (σ+), left circularly polarized light (σ-) and linear polarized light (L). Figure adapted from [43].

In this context, Mangin *et al.* [43] synthesized Co/Ir multilayers based SFI, since Co/Ir multilayers possess PMA and a strong antiferromagnetic interlayer coupling [52]. In order to maximize the antiferromagnetic coupling between ferromagnetic layers, the Ir layer thickness was 0.4 nm. The optical response of $[Co(1\ nm)/Ir/Co(0.8\ nm)]_N$ antiferromagnetically coupled structures was first studied [43]. This structure does not exhibit AO-HDS. This was attributed to the fact that this structure does not exhibit T_{comp}, since the 1 nm-thick Co layer has both a higher moment and a higher Curie temperature T_c than the 0.8 nm-thick layer [43]. Hence, the 0.8 nm-thick Co layer is substituted by [Co(0.4 nm)/Ni(0.6 nm)/Pt(t)/Co(0.4 nm) magnetic layer, where t allows controlling the total magnetic moment and the exchange interaction, and thus the Curie temperature of the SFI. Therefore, the SFI structure engineered by Mangin *et al.* is Ta(4 nm)/Pd(3 nm)/$[Co(1\ nm)/Ir/Co(0.4\ nm)/Ni(0.6\ nm)/Pt(0.3\ nm)/Co(0.4\ nm)/Ir]_5$/Pd(3 nm). This structure exhibits PMA and a strong antiferromagnetic exchange coupling. As shown in figure 1.13, T_{comp} equals 380 K and AO-HDS is observed.

Artificial zero moment magnets

The AO-HDS ability was also investigated in another class of ferrimagnetic materials called "artificial zero moment magnet" by Schubert *et al.* [45]. Such artificial zero moment magnets consist of two ferrimagnetic alloy layers designed to yield a zero remanent net magnetization at RT via an antiparallel interfacial exchange coupling of the dominant moments. Indeed, the studied artificial zero moment magnet is made of $Tb_{36}Fe_{64}$ and $Tb_{19}Fe_{81}$ alloys layers. Moreover, single $Tb_{36}Fe_{64}$ and $Tb_{19}Fe_{81}$ layers are Tb and Fe dominated, respectively. Both of these single layers show thermal demagnetization under the action of fs circularly polarized beam, which is in agreement with other studies [42, 43]. Contrary to this, the studied $Tb_{36}Fe_{64}/Tb_{19}Fe_{81}$ bilayer exhibits AO-HDS as depicted in figure 1.14. This was attributed to the zero remanence of the bilayer, leading to vanishing demagnetizing fields. This finding provides evidence that the ability for AO-HDS is correlated to the remanent sample magnetization and thus to the difference in magnetic moment of RE and TM sublattices [45], indicating that the low remanence is a criterion for the observation of AO-HDS [44].

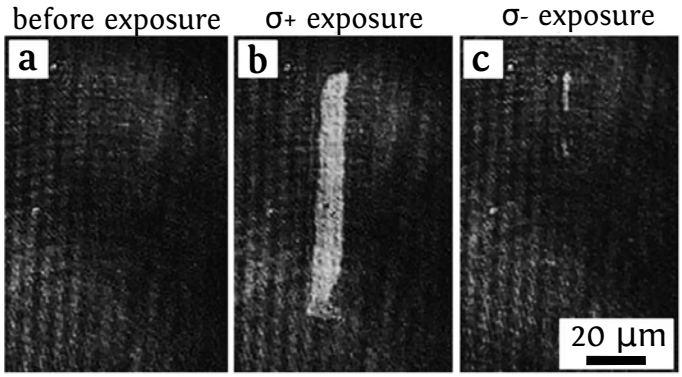

FIGURE 1.14: All-optical helicity dependent magnetic switching in a $Tb_{36}Fe_{64}/Tb_{19}Fe_{81}$ bilayer. (a) Faraday image of the homogeneously magnetized (in M^- direction) bilayer before laser irradiation. (b) Faraday image showing a written stripe domain after interaction with right-handed circularly polarized laser light (σ+) of (1.136 ± 0.08) mJ/cm^2. (c) Erased stripe with left-handed circularly polarized laser light (σ-) using the same fluence as in (b). Figure adapted from [45].

1.4.2 Ferromagnetic materials

Since the discovery of the all-optical magnetization switching in GdFeCo alloy films by Stanciu *et al.* in 2007 [12], efforts have been made to identify the microscopic origin of AOS in ferrimagnets [12, 32, 33, 41, 42, 43, 45, 51] without reaching a consensus. Another key issue regarding the material-dependence of all-optical switching is whether the AO-HDS is specific to ferrimagnets or is a general process and can also be observed in the ferromagnetic materials. In 2014 the pioneering experiments by Lambert *et al.* [53] show that AO-HDS is a rather general phenomenon and occurs for a wide range of ferromagnetic thin films as well as granular FePt films.

Ferromagnetic films

Lambert *et al.* investigated the AO-HDS ability in a large range of ferromagnetic thin films with PMA including Co/Pt, Co/Pd, $Co_{1-x}Ni_x$/Pd and Co/Ni multilayers [53]. For instance, figure 1.15 shows the optical response of $[Co(0.4\ nm)/Pt(0.7\ nm)]_N$ multilayers with N = 8, 5 and 3, to the action of 100-fs laser beam with three different polarizations. For figures 1.15(a)-1.15(c), the laser is scanned across a region of the films having both magnetization directions, whereas the laser beam is kept static in figure 1.15(d).

As depicted in figure 1.15(a), a thermal demagnetization (TD)is observed for N = 8. The scanned region by the laser is filled with small disordered stripe subdomains minimizing the dipolar energy [53, 54]. A rim is observed at the edge of the scanned area with a magnetic orientation opposite to the background. This rim is stabilized by dipolar fields from the surrounding film. For N = 5, a TD is also observed as depicted in figure 1.15(b). Moreover, the average size of the subdomains in the scanned region gets larger. This increase of the equilibrium domain size is attributed to the reduction of the film thickness [54]. While for N = 3, a pure AO-HDS is observed as depicted in figure 1.15(c). The multiple domains created with the linear polarization are much larger for N = 3, in accord with the small dipolar energy gain by domain formation [53]. Furthermore, AO-HDS is also observed for N = 3 with a laser spot kept at a fixed position, as shown in figure 1.15(d). The effect of the helicity appears only on a rim of a demagnetized area. By decreasing the laser power, the demagnetized area disappears and a complete AO-HDS of the laser-excited area is obtained.

The AO-HDS was also observed in a large variety of ferromagnetic materials classes including Co/Pd, $Co_{1-x}Ni_x$/Pd and Co/Ni multilayers [53]. In a similar manner to Co/Pt multilayers, the transition from AO-HDS to TD in these ferromagnetic materials takes place by increasing the number of repeats, which was attributed to the demagnetizing field increase. However, the pioneering experiments by Lambert *et al.* did not include the response to single fs laser pulses. Hence, the microscopic mechanism governing the all-optical switching in these ferromagnets is not yet understood.

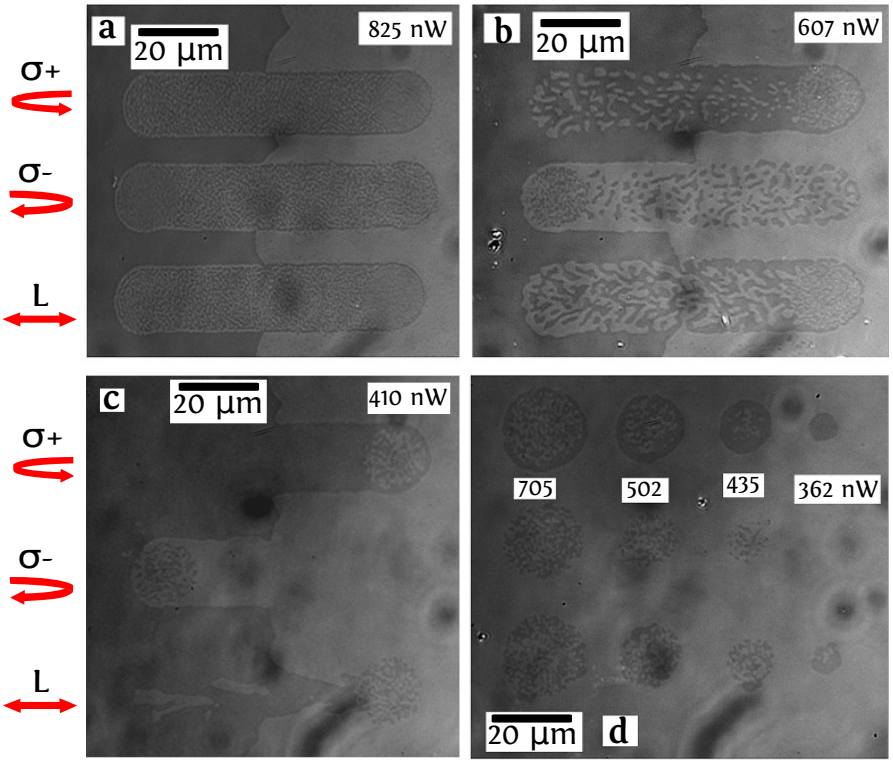

FIGURE 1.15: Magneto-optical response in zero applied magnetic field of $[Co(0.4nm)/Pt(0.7nm)]_N$ multilayer samples to various laser polarizations where $N = 8$ (a), $N = 5$ (b) and $N = 3$ (c and d). For each image the laser is circularly polarized ($\sigma+$ or $\sigma-$) or linear polarized (L). For (a)-(c) the laser beam was swept over a region of the sample with two perpendicularly oriented magnetic domains showing black/white contrast in the images, with a domain wall that runs vertically in the middle of each image. In (d) the laser was fixed at individual spots over a region of the sample with uniform magnetization (white contrast). The average laser intensity at different spots is indicated in the image. Figure adapted from [53].

Granular media

Furthermore, Lambert *et al.* explored the response of high anisotropy granular FePt films to the action of fs laser beam in combination with applied magnetic fields. These granular films are considered as a potential material for heat assisted magnetic recording (HAMR) media and are expected as the next generation of magnetic recording media [55, 56]. The media investigated by Lambert *et al.* are FePtAgC and FePtC granular films which form high anisotropy FePt grains separation by C grain boundaries. The room temperature magnetic anisotropy and coercive fields are 7 T and 3.5 T, respectively. The average grain size is 9.7 nm and 7.7 nm for the FePtAgC and FePtC, respectively.

Figure 1.16 shows the optical response of the FePtAgC granular film which is initially in a random magnetic state with equal up or down [53]. The randomly magnetized sample appears grey, since the grain size is smaller than the resolution of the Faraday microscope. As shown in figure 1.16(a), the fs laser beam is swept over the sample with the three different polarizations and without any applied fields. There is a clear net magnetization achieved that depends on the helicity of the circularly polarized light, while no change is observed with linear polarization. This clearly demonstrates that a percentage of the film is controlled by the polarization of the light, which is estimated to 80-90% by comparing the contrast to the saturated film [53]. The lack of saturation was attributed to at least two effects. The first effect

is that AO-HDS is only affecting a subset of grains, whereas the second effect is that the magnetic grains are highly thermally activated [53]. The AO-HDS is also observed with a laser kept at a fixed position as depicted in figure 1.16(b). In a similar manner to Co/Pt multilayers, the helicity-dependence occurs only in a rim of the optimum intensity. Furthermore, Lambert *et al.* quantified the role of the thermal activation on AO-HDS, by applying an external magnetic while the sample is illuminated by the polarized light. It was shown that a modest applied field of 70 mT is sufficient to suppress the effects of the helicity, indicating that the laser is heating the sample near T_c [53].

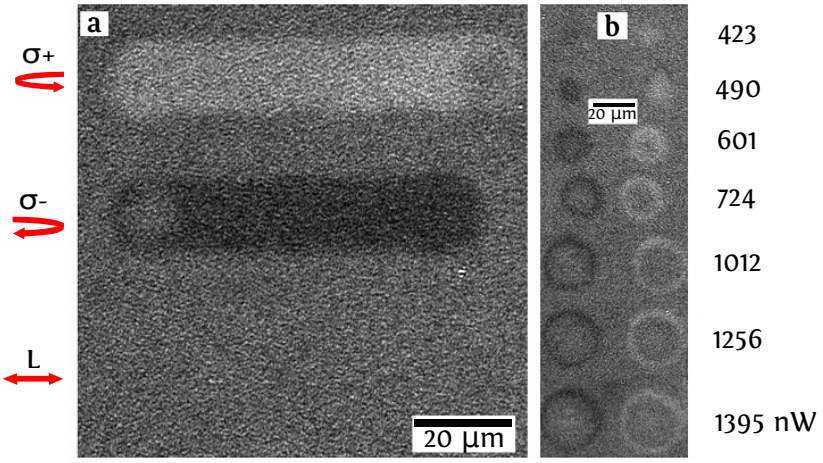

FIGURE 1.16: Magneto-optical response in zero applied magnetic field of a 15-nm FePtAgC granular film sample starting with an initially demagnetized sample. (a) Line scans for σ+, σ- and linear polarized light (L). The laser beam was swept over the sample and the magnetization pattern was subsequently imaged. (b) Images of magnetic domains written by keeping the laser spot at a fixed position on the sample. The laser was either σ+ polarized (left column) or σ- polarized (right column). The laser power is given next to the image. Figure adapted from [53].

1.5 Any general mechanism for all-optical switching ?

While AOS in ferrimagnetic GdFeCo alloys might be helicity-dependent and helicity-independent, the material study performed by Mangin *et al.* [43] showed that AOS in a large variety of ferrimagnetic systems is only helicity-dependent. Moreover, the experiments by Lambert *et al.* [53] demonstrate that AOS is not restricted to ferrimagnetic materials, and thus the antiferromagnetic coupling between two non-equivalent sublattices is not required. These observations triggered huge interest from the scientific community, and raised the questions whether there is a general mechanism for AOS in both ferri- and ferro-magnets and what are the parameters limiting the achievement of AOS in these material classes ? In this section, we will discuss the experimental and theoretical studies reported in the literature investigating the underlying physics of AOS in ferrimagnets. Hence, we will discuss the temperature influence on AOS in ferrimagnets, the possible origins of the symmetry breaking, and the material-related criteria for the observation of AOS.

1.5.1 Temperature influence on the AO-HDS of ferrimagnets

It was mentioned in section 1.2 that the fs-pulsed laser heating plays an important role in the demagnetization process [21, 22], which was qualitatively explained by the three-temperature

model [15]. Hence, the temperature of the interacting reservoirs is also expected to play a crucial role in the AOS process. Different approaches to investigate the temperature influence on AOS in ferrimagnets have been explored in previous studies [44, 57, 58].

Heat-induced reestablishment of all-optical switching

A first approach consists in heating the sample with a resistor or by tuning the pulse repetition rate to reestablish the AOS ability in ferrimagnetic films, as demonstrated by Hassdenteufel *et al.* [44]. Indeed, they investigated the optical response of a 16 nm-thick $Tb_{34}Fe_{66}$ alloy film to the action of 100 fs-laser beam. The temperature influence is studied either by increasing the repetition rate υ from 10 kHz to 250 kHz, or by externally increasing the sample temperature by a heatable sample holder via Joule heating. Indeed, a pure thermal demagnetization is observed for υ = 10 kHz at room temperature, as depicted in figures 1.17(d)-1.17(f). However, AO-HDS is reestablished by increasing the repetition rate from 10 kHz to 250 kHz at RT, as shown in figures 1.17(a)-1.17(c). Moreover, AO-HDS is also reestablished gradually for υ = 10 kHz by increasing the sample temperature up to 370 K. In both cases, the reestablishment of AOS was attributed to the heat-induced reduction of the remanence and the coercivity [44].

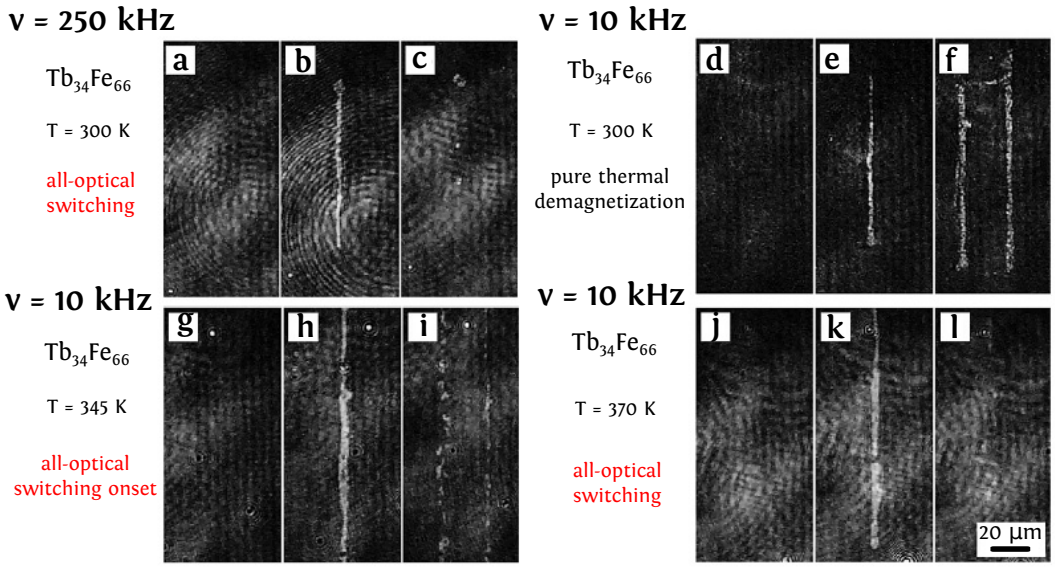

FIGURE 1.17: AO-HDS in $Tb_{34}Fe_{66}$ at a pulse repetition rate of 250 kHz or 10 kHz. The left column shows the initial homogeneously magnetized state, the middle column after exposure with right-handed circularly polarized (σ+) laser pulses, and the right column images the state after exposure with left-handed circularly polarized (σ-) laser pulses at the same fluence as used in the corresponding previous image. (a–c) 250 kHz pulse repetition rate and substrate temperature of T = 300 K. The threshold fluence for all-optical switching (AOS) is F = 1.0 $\pm$ 0.3 mJ/cm^2. (d–l) 10 kHz repetition rate and different substrate temperatures. (d–f) Pure thermal demagnetization (PTD) at a substrate temperature of T = 300 K and F = 1.46 $\pm$ 0.2 mJ/cm^2. (g–i) AOS onset at a substrate temperature of T = 345 K and F = 0.9 $\pm$ 0.1 mJ/cm^2. (j–l) AOS at a substrate temperature of T = 370 K and F = 0.5 $\pm$ 0.1 mJ/cm^2. Figure adapted from [44].

Heat-induced switching fluence threshold shift

A second approach consists in investigating the shift of the AO-HDS fluence threshold by direct laser pulse heating of the sample or by externally cooling the sample using a cryostat. Indeed, Hohlfeld *et al.* demonstrated that the AOS fluence threshold decreases by externally cooling

a $Gd_{22}Fe_{74.6}Co_{3.4}$ alloy sample below 250 K, thus indicating that AO-HDS in GdFeCo alloys is a non-thermal process [57].

In this context, Alebrand *et al.* performed an intriguing experiment on a $Gd_{24}Fe_{66.5}Co_{9.5}$ alloy film, which is called "σ-π experiment" [58]. In the σ-π experiment, the pulse inducing the AO-HDS is split in one circularly (σ) and one linearly (π) polarized pulse [58]. The σ pulse is used to transfer the helicity information, while the π pulse heats the sample. First, the switching fluence threshold with only σ pulse for a repetition rate υ = 5.2 kHz is determined F_{min} = 3.43 mJ/cm^2. In the σ-π experiment, the σ pulse is used with a fluence F_σ = 3.31 mJ/cm^2 < F_{min}, and is spatially and temporally overlapped with a heating π pulse with a fluence F_π = 1.93 mJ/cm^2. Hence, figure 1.18 shows the delay range where the two-pulse switching was obtained. Negative (resp. positive) delays indicate that the π (reps. σ) pulse arrives on the sample before the σ (resp. π) pulse. AOS is obtained with both delay signs. More importantly, the width of the delay window in which the switching occurs is shown to be dependent on the fluence of the π pulse [58]. The experiment by Alebrand *et al.* highlights the crucial role of heating in the observation of AO-HDS in GdFeCo alloys in agreement with other studies [39]. Moreover, it contradicts the classification of this process as a non-thermal effect by Hohlfeld *et al.* [57]. Furthermore, Cheng *et al.* showed that the switching fluence threshold in $Tb_{14}Fe_{68}Co_{18}$ alloy increases by cooling the sample temperature from RT down to 110 K [59]. The results are a hint that sample heating plays an important role in the achievement of AO-HDS, and are in agreement with the experiment by Alebrand *et al.*

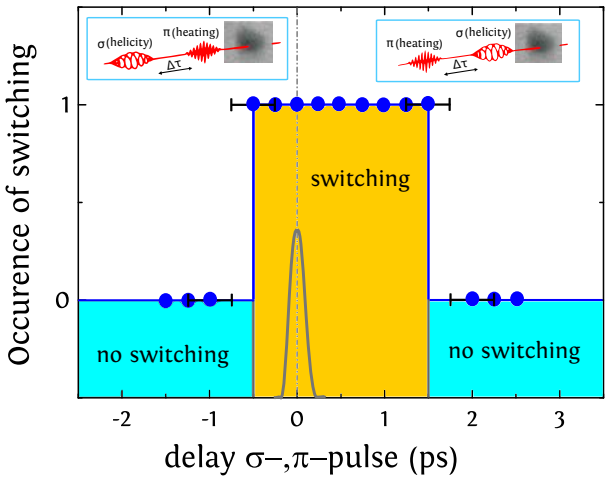

FIGURE 1.18: Results of the σ-π switching experiment, performed by varying the delay between the σ and the π pulse in both directions (measured at υ_r = 5.2 kHz). Negative delays indicate that the π pulse arrives before the σ pulse, and positive delays vice versa. Occurrence of switching 1(0) means yes(no). We used F_π = 1.93 mJ/cm^2 and F_σ = 3.31 mJ/cm^2, which is lower than the threshold fluence for one-pulse switching (F_{min} = 3.43 mJ/cm^2). The pulses had a FWHM of 100 fs, as sketched in the graph. Figure adapted from [58].

1.5.2 Possible origins of the symmetry breaking for AO-HDS

One of the most challenging issues in the topic of AO-HDS is the origin of the symmetry breaking. Several origins have been proposed in the literature during the past decade, and can be divided into two categories, i) pure thermal origins such as the magnetic circular dichroism [39] and the distinct sublattices dynamics [32], and ii) non-thermal origin such as the inverse Faraday effect [60] and the transfer of angular momentum of light [43]. In this section we

discuss the models reported in the literature which investigate the symmetry breaking mechanism in ferri- and ferro-magnets.

Inverse Faraday effect

Discovered by Michael Faraday in 1845, the Faraday effect consists in the rotation of the plane of polarization of an electromagnetic wave when interacting with a magnetized media. The Faraday effect results from the circular birefringence, which is the optical property of a material having different refractive indices for left- and right-circularly polarized light. Indeed, the two circular polarizations propagate at two different velocities, resulting in a phase shift called Faraday rotation. A reciprocal relationship was demonstrated between the Faraday rotation and the induction of a magnetization in a nonabsorbing material when illuminated by circularly polarized laser beam [61, 62, 63]. Hence, the circularly polarized pulses act on the magnetization as an effective magnetic field with a direction determined by the circular polarization. This effect is called the inverse Faraday effect (IFE).

The phenomenological expression of the effective field is expressed as follows:

$$H_{IFE}(t,r) = \epsilon_o \chi \left[E(t,r) \times E^*(t,r)\right] \tag{1.12}$$

where H_{IFE} is the effective opto-magnetic field, large ϵ_o is the vacuum permittivity and large χ is the magneto-optical susceptibility. E(t,r) and E^*(t,r) are the electric field of the light wave and its complex conjugate, respectively. In an isotropic media, H_{IFE} is directed along the wavevector of the light and reverses its orientation when the helicity of the light is reversed.

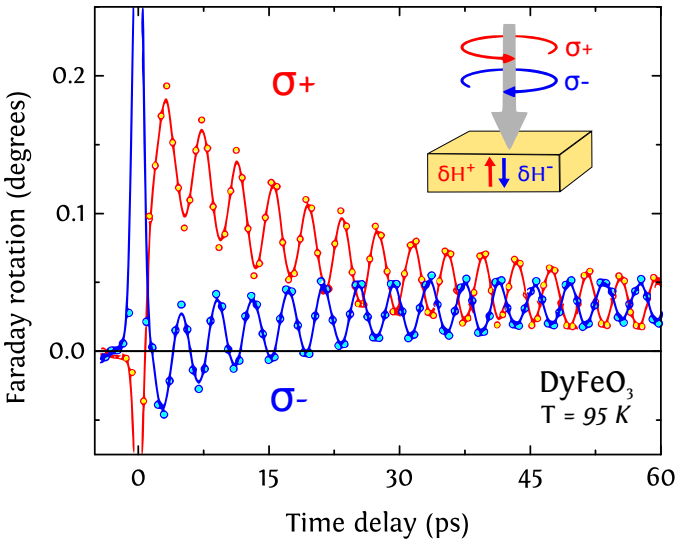

FIGURE 1.19: Magnetic excitations in $DyFeO_3$ probed by the magneto-optical Faraday effect. Two processes can be distinguished: (1) instantaneous changes of the Faraday effect due to the photoexcitation of Fe ions and relaxation back to the high spin ground state S = 5/2; (2) oscillations of the Fe spins around their equilibrium direction with an approximately 5 ps period. The circularly polarized pumps of opposite helicities excite oscillations of opposite phase. Inset shows the geometry of the experiment. Vectors δH+ and δH- represent the effective magnetic fields induced by right-handed σ+ and left-handed σ- circularly polarized pumps, respectively. Figure adapted from [64].

In 2005, a pioneering experiment by Kimel *et al.* demonstrated for the first time the ultrafast and non-thermal effect light in magnetic media [64]. Indeed, they showed that circularly

polarized fs laser pulses can be used to non-thermally excite and coherently control the spin dynamics in a $DyFeO_3$ sample by the way of the IFE [64]. Figure 1.19 shows that two different processes of the Faraday rotation start on the scale of 60 ps after excitation after excitation with a pump pulse. The helicity of the pump light controls the sign of the Faraday rotation, and thus the photo-induced magnetization. In the following years, the IFE has received much attention from the scientific community. Hence, theoretical work by Vahaplar *et al.* demonstrated that the IFE is a prominent candidate to explain the symmetry breaking in GdFeCo alloy films [60] (see figure 1.20).

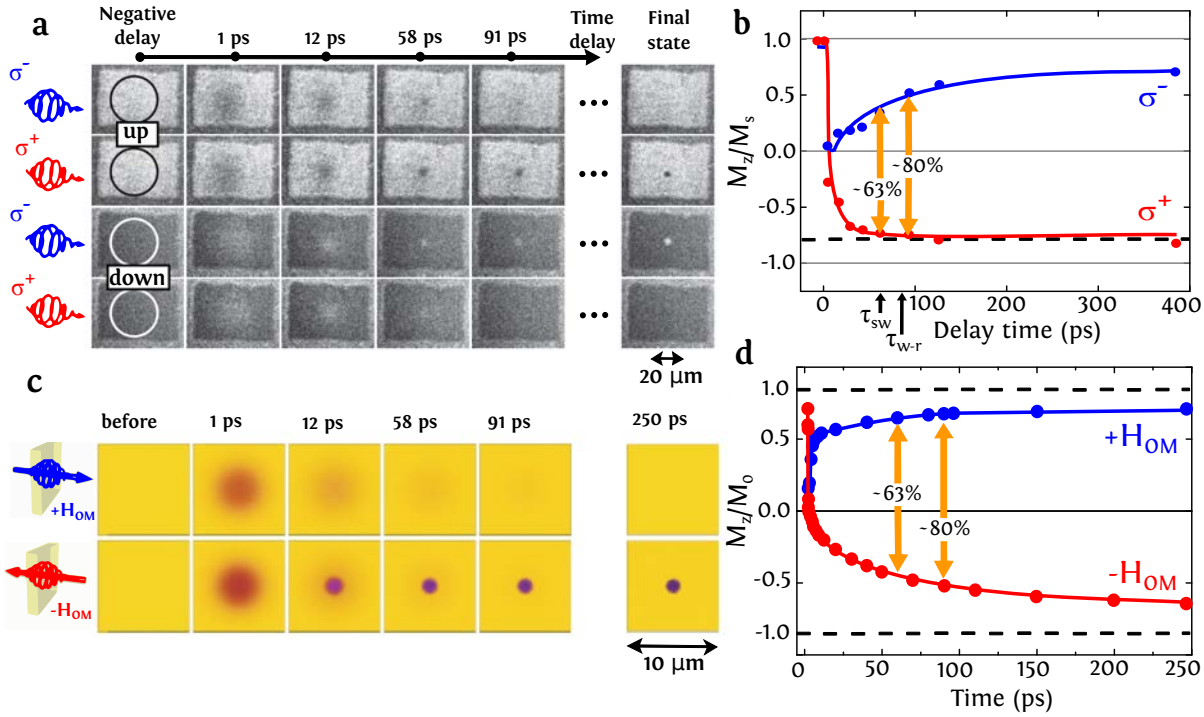

FIGURE 1.20: (a) The magnetization evolution in $Gd_{24}Fe_{66.5}Co_{9.5}$ after the excitation with σ+ and σ- circularly polarized pulses at room temperature. The domain is initially magnetized up (white domain) and down (black domain). The last column shows the final state of the domains after a few seconds. The circles show areas, where the effect of the laser pulse on the magnetic state is detected within the sensitivity of the setup. Note that the pump spot size is of 50-70 μm and larger than the images. (b) The averaged magnetization in the switched areas (5 μm) after σ+ and σ- laser pulses, as extracted from the single-shot images in (a) for the initial magnetization up. (c) Distributions of the z component of the magnetization across the 10 μm x 10 μm x 5 nm ferromagnetic film at different time delays after the combined action of a 100 fs long laser pulse and a 250 fs long optomagnetic field pulse as obtained from the multi-macrospin simulations. The peak electronic temperature is T_{el} = 1129 K. Yellow, red, and blue (in the black and white version: light gray, gray, and dark gray) regions correspond to positive, zero, and negative values of m_z, respectively. (d) The averaged magnetization in the switched areas (0.5 μm) vs time. Figure adapted from [60].

Vahaplar *et al.* solved the Landau-Lifschitz-Bloch (LLB) equation within the macrospin approximation by including the opto-magnetic field H_{IFE} [60]. By assuming the Gaussian profile of the intensity of the laser beam in space, H_{IFE} was introduced as:

$$\vec{H}_{IFE} = \sigma \frac{2\chi^F}{c\tau} f(t) e^{\left(\frac{-r^2}{2r_0^2}\right)} \vec{n} \tag{1.13}$$

where c is the speed of light, n is the unit vector in the direction of the wavevector of light

and r_0 characterizes the Gaussian spot size. The coefficient s gives the degree of circular polarization and is equal to $\pm$ 1 for a right- (σ+), left-handed (σ-) circularly polarized light and equal to 0 for a linearly polarized (π), respectively. F is the laser pulse fluence and τ is the pulse duration (FWHM). Hence, the amplitude of the electric field E_0 can be estimated as : $|E_0|^2 = \frac{c\epsilon_0\tau}{2F}$. The time-dependent function $f(t)$ and the space-dependent Gaussian function describe the temporal and spatial profiles of the effective field, respectively [60].

Experimental investigations by Vahaplar *et al.* shown in figures 1.20(a) and 1.20(b) demonstrate that the AO-HDS in $Gd_{24}Fe_{66.5}Co_{9.5}$ alloy films is a two-fold action, which consists of ultrafast laser-induced heating (1 ps) followed by a helicity-dependent relaxation to the equilibrium state (few tens of ps) [60]. In order to investigate the role of the IFE in this process, Vahaplar *et al.* performed the multimacrospin LLB calculations taking into account the opto-magnetic field H_{IFE}. Figure 1.20(c) shows the calculated distributions of the magnetization at various time delays for two opposite H_{IFE}, whereas figure 1.20(d) shows the calculated time evolution of the z component of the magnetization in the center of the magnetic element shown in figure 1.20(c). One can see that the calculations reproduce the experimentally observed two-fold AO-HDS. The circularly polarized laser pulse acts as an effective magnetic field of the amplitude up to 20 T. Therefore, the symmetry breaking in ferrimagnetic GdFeCo alloy films is attributed to the ultrafast IFE [60]. In a more recent theoretical work, Cornelissen *et al.* showed that the IFE can explain the AO-HDS also in ferromagnetic Co/Pt multilayers [65]. They demonstrated that due to the strong SOC in Co/Pt multilayers, the minimal lifetime of IFE needed to obtain switching is of the order of 0.1 ps. These calculations demonstrated a direct single-pulse AO-HDS in Co/Pt multilayers via the IFE, although it is unknown whether a single pulse switching of Co/Pt multilayers can be experimentally observed.

Magnetic circular dichroism

Even if the IFE represents a prominent model to describe the AO-HDS in ferrimagnetic GdFeCo alloys, the experimental study by Khorsand *et al.* showed that the magnetic circular dichroism (MCD) can quantitatively explain the AO-HDS [39]. As mentioned in section 1.3.2, it was shown the effect of the helicity using single fs laser pulses occurs only in a narrow window of fluence Δ. In order to understand the origin of this window, Khorsand *et al.* compared the spectral dependence of Δ, the effective opto-magnetic field B_{eff} and the relative absorption of σ+ and σ- MCD. Figure 1.21 (a) shows that the calculated B_{eff} has a strong wavelength dependence, while the measured switching window Δ and MCD are almost constant in this spectral range. Moreover, figure 1.22 (b) shows that AO-HDS depends on the amount of energy absorbed by the magnetic system independently of the wavelength. Indeed, the effective switching threshold $F^*_\sigma(\lambda) = F_\sigma(\lambda)A_\sigma(\lambda)$, i.e., the actual absorbed energy density in the GdFeCo layer at which switching occurs, is independent of the polarization σ and the wavelength λ (see section 1.3.2). These findings unambiguously demonstrate that the symmetry breaking in GdFeCo alloys originates from the MCD [39].

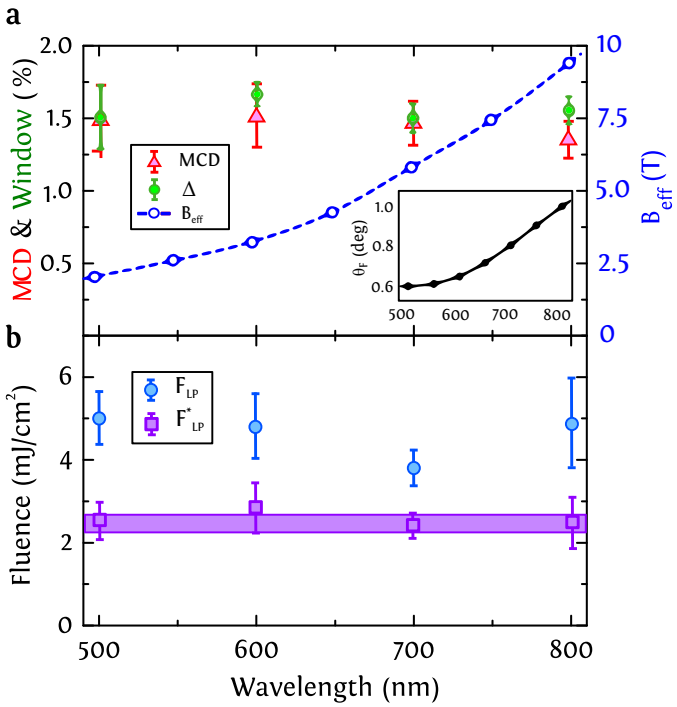

FIGURE 1.21: (a) The spectral dependence of the window Δ, IFE field B_{eff}, and MCD in GdFeCo. In the inset the spectral dependence of the Faraday rotation θ_F is shown. (b) The switching threshold fluence F_{LP} and the effective threshold fluence F^* plotted against λ. The solid line gives the intersection of the different values of F^*_{LP} and is equal to 2.6 $\pm$ 0.2 mJ/cm^2. Figure adapted from [39].

Angular momentum transfer

In addition to the IFE and the MCD, the direct transfer of angular momentum (AM) of light has been proposed in literature to be involved in the AO-HDS process [43]. Two types of AM of light can be distinguished, namely the spin angular momentum (SAM) and the orbital angular momentum (OAM) which are the components of AM of light associated with its polarization and wavefront, respectively. In the case of any Laguerre-Gaussian mode, the light has no helical wavefront thus leading to a zero OAM. Hence, the OAM of the Gaussian laser beam used in the AOS experiments is zero.

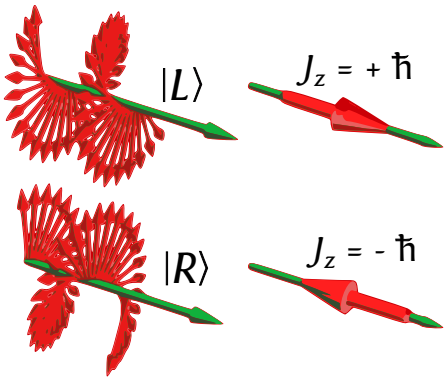

FIGURE 1.22: Left- and right-handed circular polarization, and their associated spin angular momentum.

The SAM of a single photon in the case of a Laguerre-Gaussian mode is very small. Indeed, Beth made the first observation of the SAM of light [67]. In his experiment, a half-wave plate was suspended by a fine quartz fiber. A beam light is circularly polarized by a fixed quarter-wave plate. The beam light passed then through the half-wave plate which transformed right-handed circularly polarized light into left-handed circularly polarized light and transferred $2\hbar$ of spin angular momentum for each photon to the birefringent plate. This measured torque is an agreement in sign and magnitude with that predicted by both wave and quantum theories of light. Therefore, the ratio of the angular momentum of N photons in the beam is $J = \pm N\hbar$, as depicted in figure 1.22 for a single photon.

1.5.3 Orientation conservation

Other key issues regarding the topic of AO-HDS are the material-dependent parameters ruling the observation of the switching for both ferri- and ferro-magnetic materials. Concerning ferrimagnetic materials, experimental investigations on ferrimagnets with a magnetic thickness $t \geqslant 20$ nm suggested that a T_{comp} near or above RT is a necessary condition to observe AO-HDS [41, 42, 43]. Kimel proposed the PMA and the antiferromagnetic coupling between non-equivalent sublattices as rules for the observation of AO-HDS [51]. Furthermore, Hassdenteufel *et al.* demonstrated that the low remanence ($M_R < 220$ kA/m) of 16 nm-thick ferrimagnets is a criterion for the observation of AO-HDS [44], as depicted in figure 1.23.

In a more recent study, Hebler *et al.* showed that this low remanence criterion applies to ferrimagnetic TbFe alloys with a magnetic thickness ranging from 5 nm to 85 nm [68]. Nevertheless, this low remanence criterion cannot apply to ferromagnets. As mentioned in section 1.4.2, Co/Pt multilayers with a high remanence ($M_R > 1400$ kA/m) exhibit AO-HDS if their thickness is strongly scaled down to 2.4 nm which was attributed to the reduction of stray fields [53]. Therefore, the existence of a material-dependent parameter ruling the observation of AO-HDS and being common for both ferro- and ferri-magnets is still unclear.

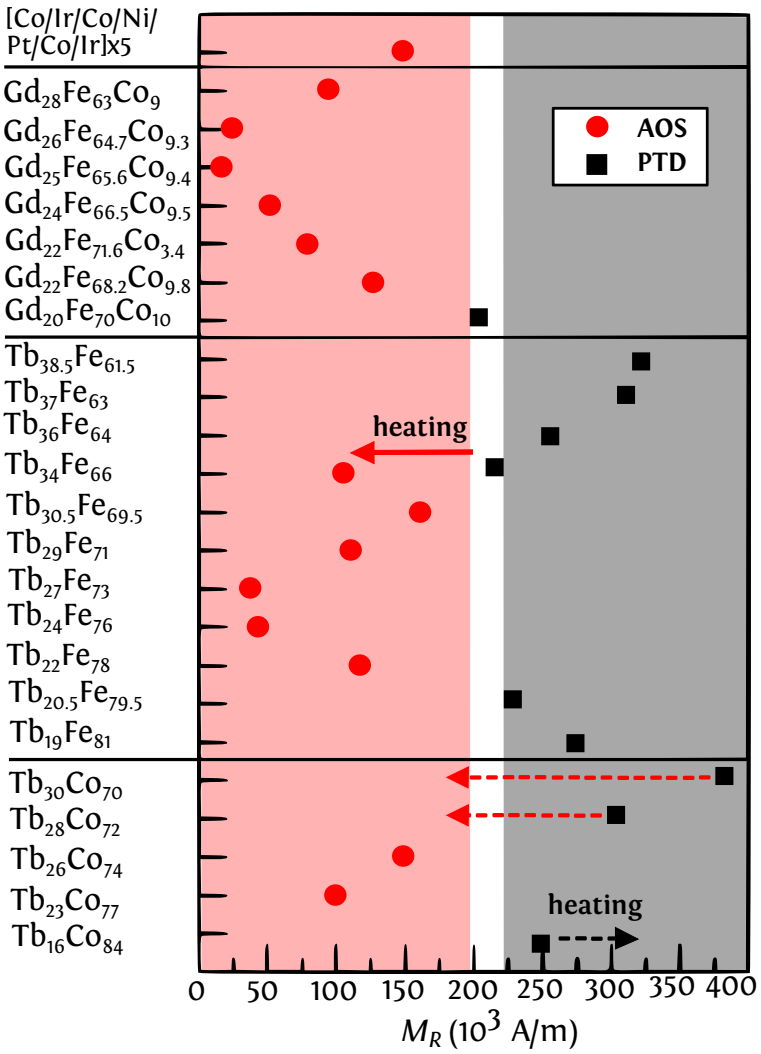

FIGURE 1.23: Overview of all-optical switching (AOS) in $Gd_xFe_{100-x-y}Co_y$, Tb_xFe_{100-x}, Tb_xCo_{100-x}, and $[Co/Ir/Co/Ni/Pt/Co/Ir]_5$. Red dots and light-red area indicate AOS. Black squares and light-gray area denote pure thermal demagnetization (PTD). Red (black) arrows represent the decrease (increase) of sample magnetization due to heating; the solid red arrow shows our result obtained in $Tb_{34}Fe_{66}$. The dashed red and black arrows visualize the trend in Tb_xCo_{100-x}. Figure adapted from [44].

1.6 Outlines of the thesis

The experimental investigations presented in this thesis address several key issues regarding the all-optical switching mechanism in ferri- and ferro-magnets. First, we will introduce in chapter 2 the experimental tools used in this thesis to fabricate and characterize the studied samples and to perform the all-optical switching experiments. Hereafter, chapter 3 focuses on the comprehensive investigation of the magnetic parameters ruling the observation of AO-HDS in ferrimagnetic alloys and ferromagnetic multilayers for a wide range of compositions and thicknesses. By taking into account the demagnetizing energy and the domain wall energy, the magnetic domain size is shown to be a relevant criterion for the observation of AO-HDS in both ferri- and ferro-magnets. Such criterion is confirmed by experimentally investigating the optical response of light-ion irradiated ferromagnets. In chapter 4, we introduce a novel approach combining both optics and spintronics, which consists in the investigation

of AO-HDS in Hall cross devices via the anomalous Hall effect. We distinguish between two types of all-optical switching mechanism, namely a single pulse switching for ferrimagnetic GdFeCo alloys as previously reported in chapter 1, and a two regimes switching process for both ferrimagnetic TbCo alloys and ferromagnetic Co/Pt multilayers. The newly demonstrated two regimes process consists of a helicity-independent multiple-domain formation, which is followed by a helicity-dependent remagnetization attributed to a helicity-dependent domain wall motion.

References

[1] H. Ohno, D. Chiba, F. Matsukura, T. Omiya, E. Abe, T. Dietl, Y. Ohno, and K. Ohtani, Electric-field control of ferromagnetism *Nature* **408**, 944-946 (2000).

[2] D. Chiba, M. Yamanouchi, F. Matsukura, and H. Ohno, Electrical manipulation of magnetization reversal in a ferromagnetic semiconductor *Science* **301**, 943-945 (2003).

[3] D. Chiba, M. Sawicki, Y. Nishitani, Y. Nakatani, F. Matsukura, and H. Ohno, Magnetization vector manipulation by electric fields, *Nature* **455**, 515-518 (2008).

[4] J. C. Slonczewski, Current-driven excitation of magnetic multilayers *J. Magn. Magn. Mater.* **159**, L1 (1996).

[5] L. Berger, Emission of spin waves by a magnetic multilayer traversed by a current *Phys. Rev. B* **54**, 9353 (1996).

[6] J. A. Katine, F. J. Albert, R. A. Buhrman, E. B. Myers, and D. C. Ralph, Current-driven magnetization reversal and spin-wave excitations in Co/Cu/Co pillars *Phys. Rev. Lett.* **84**, 3149 (2000).

[7] L. Liu, C.-F. Pai, Y. Li, H. W. Tseng, D. C. Ralph, R. A. Buhrman, Spin-torque switching with the giant spin Hall effect of Tantalum *Science* **336**, 555 (2012).

[8] L. Liu, O. J. Lee, T. J. Gudmundsen, D. C. Ralph, and R. A. Buhrman, Current-induced switching of perpendicularly magnetized magnetic layers using spin torque from the spin Hall effect *Phys. Rev. Lett.* **109**, 096602 (2012).

[9] M. Hatami, G. E. Bauer, Q. Zhang, and P. J. Kelly, Thermal spin-transfer torque in magnetoelectronic devices *Phys. Rev. Lett.* **99**, 066603 (2007).

[10] K. Uchida, S. Takahashi, K. Harii, J. Ieda, W. Koshibae, K. Ando, S. Maekawa, and E. Saitoh, Observation of the spin Seebeck effect *Nature* **455**, 778-781 (2008).

[11] H. Yu, S. Granville, D. P. Yu, and J.-Ph. Ansermet, Evidence for thermal spin-transfer torque *Phys. Rev. Lett.* **104**, 146601 (2010).

[12] C. D. Stanciu, F. Hansteen, A. V. Kimel, A. Kirilyuk, A. Tsukamoto, A. Itoh, and Th. Rasing, All-optical magnetic recording with circularly polarized light *Phys. Rev. Lett.* **99**, 047601 (2007).

[13] A. Vaterlaus, D. Guarisco, M. Lutz, M. Aeschlimann, M. Stampanoni, and F. Meier, Different spin and lattice temperatures observed by spin polarized photoemission with picosecond laser pulses *J. Appl. Phys.* **67**, 5661 (1990).

[14] A. Vaterlaus, T. Beutler, and F. Meier, Spin-lattice relaxation time of ferromagnetic gadolinium determined with time-resolved spin-polarized photoemission *Phys. Rev. Lett.* **67**, 3314 (1991).

[15] E. Beaurepaire, J. Merle, A. Daunois, and J. Bigot, Ultrafast spin dynamics in ferromagnetic Nickel *Phys. Rev. Lett.* **76**, 4250 (1996).

[16] M. Battiato, K. Carva, and P. M. Oppeneer, Superdiffusive spin transport as a mechanism of ultrafast demagnetization *Phys. Rev. Lett.* **105**, 027203 (2010).

[17] D. Rudolf, C. La-o-vorakiat, M. Battiato, R. Adam, J. Shaw, E. Turgut, P. Maldonado, S. Mathias, P. Grychtol, H. T. Nembach *et al.*, Ultrafast magnetization enhancement in metallic multilayers driven by superdiffusive spin current *Nat. Commun.* **3**, 1037 (2012).

[18] G. Malinowski, F. Dalla Longa, J. H. H. Rietjens, P. V. Paluskar, R. Huijink, H. J. M. Swagten, and B. Koopmans, Control of speed and efficiency of ultrafast demagnetization by direct transfer of spin angular momentum *Nat. Phys.* **4**, 855 (2008).

[19] E. Beaurepaire, G. M. Turner, S. M. Harrel, M. C. Beard, J.-Y. Bigot, and C. A. Schmuttenmaer, Coherent terahertz emission from ferromagnetic films excited by femtosecond laser pulses *Appl. Phys. Lett.* **84**, 3465 (2004).

[20] B. Koopmans, J. J. M. Ruigrok, F. Dalla Longa, and W. J. M. de Jonge, Unifying ultrafast magnetization dynamics *Phys. Rev. Lett.* **95**, 267207 (2005).

[21] U. Atxitia, O. Chubykalo-Fesenko, J. Walowski, A. Mann, and M. Munzenberg, Evidence for thermal mechanisms in laser-induced femtosecond spin dynamics *Phys. Rev. B* **81**, 174401 (2010).

[22] T. Roth, A. J. Schellekens, S. Alebrand, O. Schmitt, D. Steil, B. Koopmans, M. Cinchetti, and M. Aeschlimann, Temperature dependence of laser-induced demagnetization in Ni: A key for identifying the underlying mechanism *Phys. Rev. X* **2**, 021006 (2012).

[23] S. I. Anisimov, B. L. Kapeliovich, and T. L. Perelman, Electron emission from metal surfaces exposed to ultrashort laser pulses *Sov. Phys. JETP* **39**(2), 375 (1974).

[24] A. Kirilyuk, A. V. Kimel and Th. Rasing, Laser-induced magnetization dynamics and reversal in ferrimagnetic alloys *Rep. Prog. Phys.* **7** (2), 026501 (2013).

[25] W. S. Fann, R. Storz, H. W. K. Tom, and J. Bokor, Electron thermalization in gold *Phys. Rev. B* **46**, 13592 (1992).

[26] T. Gerrits, H. A. M. van den Berg, J. Hohlfeld, L. Bar and Th. Rasing, Ultrafast precessional magnetization reversal by picosecond magnetic field pulse shaping *Nature* **418**, 509-512 (2002).

[27] L. Landau and E. Lifschitz, On the theory of the dispersion of magnetic permeability in ferromagnetic bodies *Phys. Z. Sowjet.* **8**(153), 101-114 (1935).

[28] T. Gilbert, A phenomenological theory of damping in ferromagnetic materials *IEEE Trans. on Magn.* 40, 3443-3449 (2004).

[29] B. Skubic, J. Hellsvik, L. Nordstrom, and O. Eriksson, A method for atomistic spin dynamics simulations: implementation and examples *J. Phys.: Condens. Matter 20*, **315203** (2008).

[30] R. Kubo, The fluctuation-dissipation theorem *Rep. Prog. Phys.* **29**, 255 (1966).

[31] N. Kazantseva, U. Nowak, R. W. Chantrell, J. Hohlfeld, and A. Rebei, Slow recovery of the magnetisation after a sub-picosecond heat pulse *Europhys. Lett.* **81**, 27004 (2008).

[32] I. Radu, K. Vahaplar, C. Stamm, T. Kachel, N. Pontius, H. A. Durr, T. A. Ostler, J. Barker, R. F. Evans, R. W. Chantrell *et al.*, Transient ferromagnetic-like state mediating ultrafast reversal of antiferromagnetically coupled spins *Nature* **472**, 205-208 (2011).

[33] T. A. Ostler, J. Barker, R. F. L. Evans, R. W. Chantrell, U. Atxitia, O. Chubykalo-Fesenko, S. El Moussaoui, L. Le Guyader, E. Mengotti, L. J. Heyderman *et al.*, Ultrafast heating as a sufficient stimulus for magnetization reversal in a ferrimagnet *Nat. Commun.* **3**, 666 (2012).

[34] D. A. Garanin, Fokker-Planck and Landau-Lifshitz-Bloch equations for classical ferromagnets *Phys. Rev. B* **55**, 3050 (1997).

[35] R. W. Schoenlein, S. Chattopadhyay, H. H. W. Chong, T. E. Glover, P. A. Heimann, C. V. Shank, A. A. Zholents, and M. S. Zolotorev, Generation of femtosecond pulses of synchrotron radiation *Science* **287**, 2237 (2000).

[36] C. Stamm, T. Kachel, N. Pontius, R. Mitzner, T. Quast, K. Holldack, S. Khan, C. Lupulescu, E. F. Aziz, M. Wietstruk *et al.*, Femtosecond modification of electron localization and transfer of angular momentum in nickel *Nat. Mater.* **6**, 740 (2007).

[37] H.-P. D. Shieh and M. H. Kryder, Magneto optic recording materials with direct overwrite capability *Appl. Phys. Lett.* **49**, 473 (1986).

[38] N. Kazantseva, D. Hinzke, R. W. Chantrell and U. Nowak, Linear and elliptical magnetization reversal close to the Curie temperature *Europhys. Lett.* **86**, 27006 (2009).

[39] A. R. Khorsand, M. Savoini, A. Kirilyuk, A. V. Kimel, A. Tsukamoto, A. Itoh, and Th. Rasing, Role of magnetic circular dichroism in all-optical magnetic recording *Phys. Rev. Lett.* **108**, 127205 (2012).

[40] J. H. Mentink, J. Hellsvik, D. V. Afanasiev, B. A. Ivanov, A. Kirilyuk, A. V. Kimel, O. Eriksson, M. I. Katsnelson, and Th. Rasing, Ultrafast spin dynamics in multisublattice magnets *Phys. Rev. Lett.* **108**, 057202 (2012).

[41] S. Alebrand, M. Gottwald, M. Hehn, D. Steil, M. Cinchetti, D. Lacour, E. E. Fullerton, M. Aeschlimann, and S. Mangin, Light-induced magnetization reversal of high-anisotropy TbCo alloy films *Appl. Phys. Lett.* **101**, 162408 (2012).

[42] A. Hassdenteufel, B. Hebler, C. Schubert, A. Liebig, M. Teich, M. Helm, M. Aeschlimann, M. Albrecht, and R. Bratschitsch, Thermally assisted all-optical helicity dependent magnetic switching in amorphous $Fe_{100-x}Tb_x$ alloy films *Adv. Mat.* **25**, no. 22, 3122–3128 (2013).

[43] S. Mangin, M. Gottwald, C.-H. Lambert, D. Steil, V. Uhlir, L. Pang, M. Hehn, S. Alebrand, M. Cinchetti, G. Malinowski *et al.*, Engineered materials for all-optical helicity-dependent magnetic switching *Nat. Mater.* **13**, 286–292 (2014).

[44] A. Hassdenteufel, J. Schmidt, C. Schubert, B. Hebler, M. Helm, M. Albrecht, and R. Bratschitsch, Low remanence criterion for helicity-dependent all-optical magnetic switching in ferrimagnets and heterostructures *Phys. Rev. B* **91**, 104331 (2015).

[45] C. Schubert, A. Hassdenteufel, P. Matthes, J. Schmidt, M. Helm, R. Bratschitsch, and M. Albrecht, All-optical helicity dependent magnetic switching in an artificial zero moment magnet Appl. Phys. Lett. **104**, 082406 (2014).

[46] P. Hansen, C. Clausen, G. Much, M. Rosenkranz, and K. Witter, Magnetic and magneto-optical properties of rare-earth transition-metal alloys containing Gd, Tb, Fe, Co *J. Appl. Phys.* **66**, 756 (1989).

[47] P. Hansen, S. Klahn, C. Clausen, G. Much, and K. Witter, Magnetic and magneto-optical properties of rare-earth transition-metal alloys containing Dy, Ho, Fe, Co *J. Appl. Phys.* **69**, 3194 (1991).

[48] A. Khorsand, M. Savoini, A. Kirilyuk, A. Kimel, A. Tsukamoto, A. Itoh, and Th. Rasing, Element-specific probing of ultrafast spin dynamics in multisublattice magnets with visible light *Phys. Rev. Lett.* **110**, 107205 (2013).

[49] S. Mathias, C. La-O-Vorakiat, P. Grychtol, P. Granitzka, E. Turgut, J. Shaw, R. Adam, H. Nembach, M. Siemens, S. Eich *et al.*, Probing the timescale of the exchange interaction in a ferromagnetic alloy *Proc. of the Nat. Acad. of Sciences* **109**, no. 13, 4792–4797 (2012).

[50] D. Rudolf, L. Chan, M. Battiato, R. Adam, J. Shaw, E. Turgut, P. Maldonado, S. Mathias, P. Grychtol,H. Nembach et al., Ultrafast magnetization enhancement in metallic multilayers driven by superdiffusive spin current *Nat. Commun.* **3**, 1037 (2012).

[51] A. V. Kimel, All-optical switching: Three rules of design *Nat. Mater.* **13**, 225–226 (2014).

[52] A. Moser, K. Takano, D. Margulies, M. Albrecht, Y. Sonobe, Y. Ikeda, S. Sun, and E. E. Fullerton, Magnetic recording: advancing into the future *J. Phys. D: Appl. Phys.* **35**, 19 (2002).

[53] C. H. Lambert, S. Mangin, B. S. D. C. S. Varaprasad, Y. K. Takahashi, M. Hehn, M. Cinchetti, G. Malinowski, K. Hono, Y. Fainman, M. Aeschlimann *et al.*, All-optical control of ferromagnetic thin films and nanostructures *Science* **345**, 1337–1340 (2014).

[54] O. Hellwig, A. Berger, J.B. Kortright, and E.E. Fullerton, Domain structure and magnetization reversal of antiferromagnetically coupled perpendicular anisotropy films *J. Magn. Magn. Mater.* **319** (1-2), 13-55 (2007).

[55] L. Zhang, Y. K. Takahashi, K. Hono, B. C. Stipe, J. Y. Juang, and M. Grobis, $L1_0$-ordered FePtAg–C granular thin film for thermally assisted magnetic recording media *J. Appl. Phys.* **109**, 07B703 (2011).

[56] M. H. Kryder, E. C. Gage, T. W. McDaniel, W. A. Challener, R. E. Rottmayer, G. P. Ju, Y. T. Hsia, and M. F. Erden, Heat Assisted Magnetic Recording *Proc. IEEE* **96**, 1810–1835 (2008).

[57] J. Hohlfeld, C. D. Stanciu, and A. Rebei, Athermal all-optical femtosecond magnetization reversal in GdFeCo *Appl. Phys. Lett.* **94**, 152504 (2009).

[58] S. Alebrand, A. Hassdenteufel, D. Steil, M. Cinchetti, and M. Aeschlimann, Interplay of heating and helicity in all-optical magnetization switching *Phys. Rev. B* **85**, 092401 (2012).

[59] T. Y. Cheng, J. Wu, M. Willcox, T. Liu, J. W. Cai, R.W. Chantrell, and Y. B. Xu, Temperature dependence of all-optical ultrafast magnetization switching in TbFeCo *IEEE Trans. Magn.* **48**, 3387 (2012).

[60] K. Vahaplar, A. M. Kalashnikova, A. V. Kimel, S. Gerlach, D. Hinzke, U. Nowak, R. Chantrell, A. Tsukamoto, A. Itoh, A. Kirilyuk, and Th. Rasing, All-optical magnetization reversal by circularly polarized laser pulses: Experiment and multiscale modeling *Phys. Rev. B* **85**, 104402 (2012).

[61] J. P. van der Ziel, P. S. Pershan, and L. D. Malmstrom, Optically-induced magnetization resulting from the inverse Faraday effect *Phys. Rev. Lett.* **15**, 190 (1965).

[62] P. S. Pershan, J. P. van der Ziel, and L. D. Malmstrom, Theoretical discussion of the inverse Faraday effect, Raman scattering, and related phenomena *Phys. Rev.* **143**, 574 (1966).

[63] L. Pitaevskii, Electric forces in a transparent dispersive medium *Sov. Phys. JETP* **12**, 1008 (1961).

[64] A. V. Kimel, A. Kirilyuk, P. A. Usachev, R. V. Pisarev, A. M. Balbashov and Th. Rasing, Ultrafast non-thermal control of magnetization by instantaneous photomagnetic pulses *Nature* **435**, 655-657 (2005).

[65] T. D. Cornelissen, R. Cordoba, and B. Koopmans, Microscopic model for all optical switching in ferromagnets *Appl. Phys. Lett.* **108**, 142405 (2016).

[66] C. D. Stanciu, A. V. Kimel, F. Hansteen, A. Kirilyuk, A. Tsukamoto, A. Itoh, and Th. Rasing, Ultrafast spin dynamics across compensation points in ferrimagnetic GdFeCo: The role of angular momentum compensation *Phys. Rev. B* **73**, 220402 (2006).

[67] R. Beth, Mechanical detection and measurement of the angular momentum of light *Phys. Rev.* **50**, 115 (1936).

[68] B. Hebler, A. Hassdenteufel, P. Reinhardt, H. Karl, and M. Albrecht, Ferrimagnetic Tb–Fe alloy thin films: Composition and thickness dependence of magnetic properties and all-optical switching *Front. Mater.* **3**, 8 (2016).

Chapter 2

Experimental tools and samples

2.1 Introduction

In this second chapter, we introduce the main experimental techniques used in this thesis for the sample elaboration and the study of all-optical magnetization switching. First, we report in section 2.2 on the sputtering technique used to elaborate the studied ferri- and ferro-magnetic samples, and on the light-ion irradiation method enabling to tune the magnetic anisotropy. Second, we introduce in section 2.3 the femtosecond pulsed laser setup used to perform the optical excitation. We discuss in section 2.4 the physics behind magneto-optical Kerr effect (MOKE), and we finally give a brief description of the Faraday microscope used for the all-optical switching measurement.

2.2 Samples elaboration and characterization

2.2.1 DC sputtering technique

The sputtering technique was used in this thesis to elaborate samples. Sputtering is a physical vapor deposition (PVD) whereby atoms are ejected from a pure element called "target", and are subsequently deposited on the "substrate". The bombardment of the target requires the formation of gaseous plasma, which is typically made of inert gas ions such as Argon ions Ar^+. Indeed, Ar atoms are first introduced into a vacuum chamber at a pressure ranging from 1 to 10 mTorr. A DC voltage is then placed between the target and the substrate, enabling to ionize the Ar atoms and to create the plasma. These Ar^+ ions are accelerated to the cathode target, leading to the ejection of its atoms in the form of neutral particles into the vacuum space. These neutral particles can be either individual atoms, clusters of atoms or molecules. They can then ballistically travel from the target in straight lines until reaching the substrate. These ejected atoms start to bind to each other at the molecular level, thus forming a tightly bound atomic layer. Moreover, the electrons released during the ionization of Ar atoms are also accelerated to the anode substrate. These electrons collide subsequently with the additional Ar atoms, leading to more Ar ions and free electrons and thus continuing the cycle.

In order to enhance the sputtering process, sputtering systems often use magnetrons as for the Alliance system used in this thesis. Indeed, this so-called magnetron sputtering consists in using two permanent magnets of opposite polarity located below the target, as illustrated in figure 2.1.

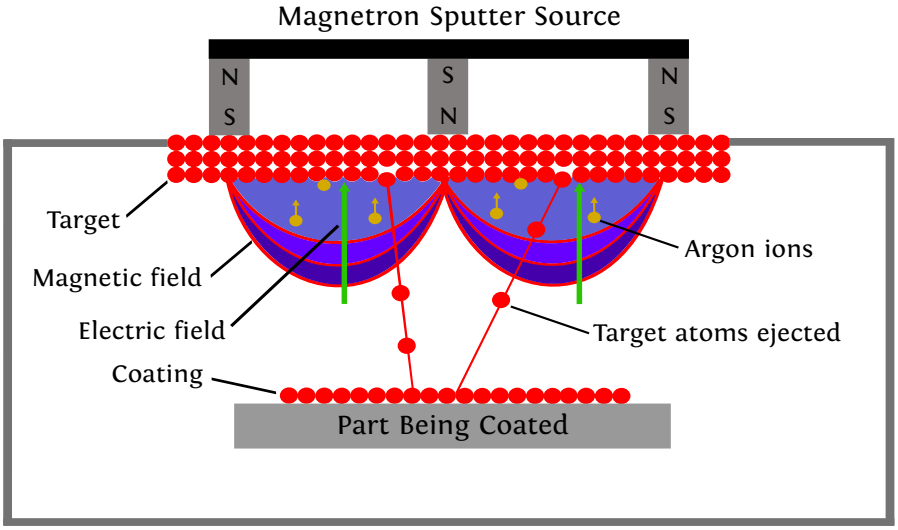

FIGURE 2.1: Scheme of a magnetron sputtering system.

These magnets create a strong magnetic field parallel to the target surface and orthogonal to the electric field used to ionize the Ar atoms. Moreover, these two fields create field lines that trap the electrons released during the ionization process. These electrons follow then helical paths around the magnetic field lines due to the Lorentz force, leading to more ionizing collisions with the gaseous neutral atoms near the target surface. Therefore, the magnetron generates stable plasma with high density of ions, which is confined to an area near the target. This technique increases the efficiency of the sputtering process and improves the quality of coatings.

2.2.2 Light-ion irradiation

The manipulation of magnetic anisotropy triggered a huge interest due to the strong contribution of the anisotropy in the recording stability in spintronic devices [1]. Therefore, Chappert *et al.* introduced in 1998 the light-ion irradiation as an innovative technique enabling to tailor the magnetic anisotropy in Co/Pt multilayers with PMA [2]. Indeed, this technique enables to modify both structural and magnetic properties in thin films; such modifications depend essentially on the energy density of the ion beam transferred to the atoms [3]. The ion irradiation differs from the ion implantation. Indeed, the latter enables to modify the physical properties of a material not by changing its structure, but via the direct effect of adding the atoms in the material.

In order to perform the ion irradiation, He^+ ions are mainly used Chappert98x,Devolder00x since they do not lead to extended collision cascades with energies going from 5 to 150 keV. The structural modifications are located in the vicinity of the ion path in the metal, and consist in recoils limited to one or two atomic distances [4]. The schematic representation of the He^+-irradiation setup is illustrated in figure 2.2. This device enables to ionize the Helium source by applying a high voltage, and thus creates He^+ ion beam with controlled energy and dose. As depicted in figure 2.2, the electrode allows extracting the He^+ ion beam from the source, which is then deflected by the magnet. The Faraday cage enables to set the voltage and the intensity, while the Einzel lens focuses the ion beam. Finally, the latter goes through a diaphragm before irradiating the sample. Our samples were irradiated with He^+ ions at irradiation doses ranging from $5\ 10^{14}$ to $5\ 10^{15}$ He^+/cm^2 and at a constant energy of 15 keV.

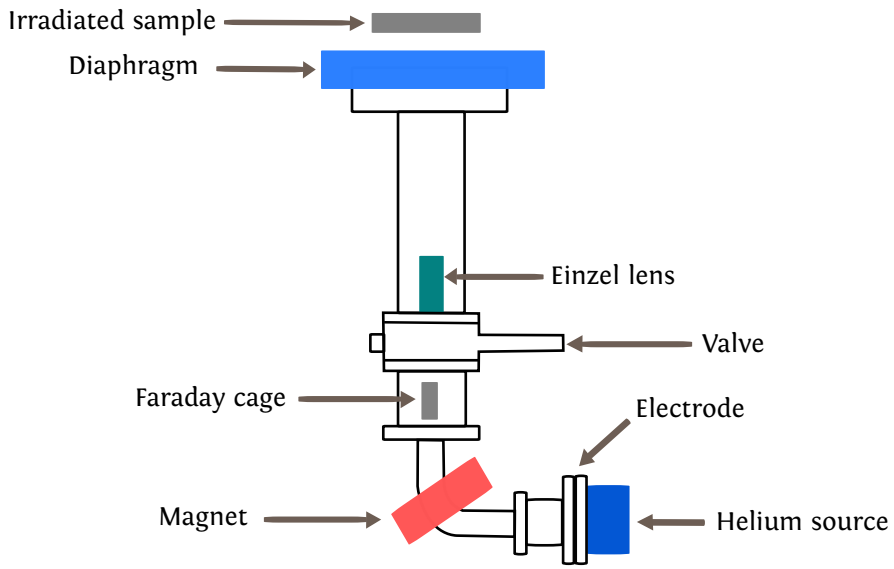

FIGURE 2.2: Schematic representation of He^+-irradiation setup.

2.2.3 Magnetic characterization

Vibrating sample magnetometer

The magnetic measurements of the studied ferri- and ferro-magnets have been performed in this thesis by using a vibrating sample magnetometer (VSM). This technique was originally developed by Foner and consists in vibrating a sample within a uniform magnetic field, thus inducing an electric voltage in placed sensing coils [5]. This induced electric voltage in the sensing coils is directly proportional to the magnetization of the sample. The magnetic field is generated either by using conventional electromagnets for field strengths up to 3 T or by using superconducting magnets for field strengths up to 16 T.

Two different equipments have been used in this thesis, namely a 3-T VSM system developed by DMS Society and 7-T VSM-SQUID equipment developed by Quantum Design Company. The VSM-DMS system is based on regular sensing coils and thus is limited by a noise floor of 10^{-6} emu, whereas the VSM-SQUID equipment uses a superconducting quantum interference device (SQuID) sensor enabling to measure the magnetic properties with a sensitivity of 10^{-8} emu. The theoretical sensitivity achieved with a SQUID-VSM is 10^{-12} emu, but it is practically limited to 10^{-8} emu because of the environmental noise. Moreover, the VSM gives an open loop measurement, since the sample and the field source do not present a closed flux line loop. Indeed, the internal field experienced by a sample differs from the applied field due to the demagnetizing field which depends on the sample geometry. Therefore, the measured parameters must be corrected for these demagnetizing effects in order to yield the true intrinsic magnetic parameters.

Ferrimagnetic alloy films

Two different ferrimagnetic alloy films studied in this thesis, namely GdFeCo and TbCo alloys. These materials are very interesting for their PMA, the possibility of tuning magnetic properties [6, 7] and their good magneto-optical properties. As illustrated in figure 2.3, these RE-TM alloys possess two different sublattices: TM = Fe-Co, Co and RE = Gd, Tb. Moreover, these two

sublattices are antiferromagnetically coupled and thus the net magnetization of the alloy is the sum of the magnetization of the RE and TM sublattices.

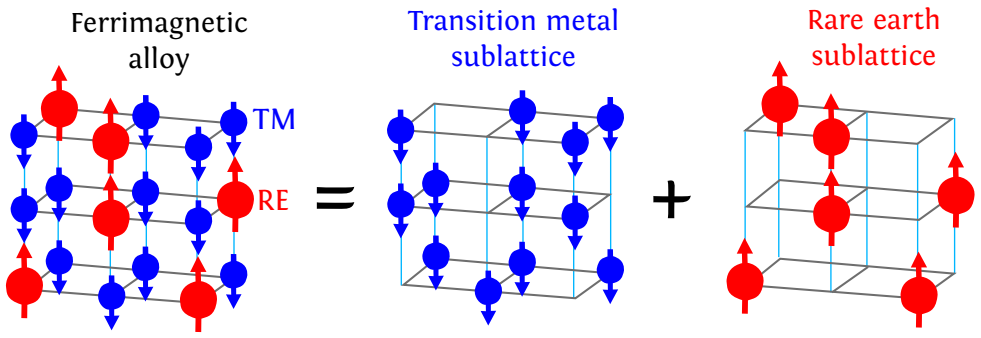

FIGURE 2.3: Schematic representation of the magnetic moment in ferrimagnetic alloys. The RE and TM sublattice magnetizations are antiferromagnetically coupled.

In general the first sublattice in these RE-TM alloys consists of a transition metal (TM) which is characterized by a high Curie temperature and a magnetism arising from the 3d shell, whereas the second is a rare earth (RE) which is an element among the lanthanide family. The latter is subdivided into two parts, namely the light RE and the heavy RE depending on the filling level of their 4f shell. Indeed, the light RE corresponds to a 4f shell which is less than half filled (e.g. Sm, Pr, Nd and Eu), leading to a ferromagnetic coupling with the TM sublattice. On the other hand, the heavy RE is above the half filling threshold (e.g. Gd, Tb, Dy, Ho and Tm), thus leading to an antiferromagnetic coupling with the TM sublattice [8]. The magnetic moment of RE has contribution from both 4f and 5d electrons. Nevertheless, magnetism of RE is mostly attributed to 4f electrons, since they approximately account for 90% of the absolute value of the RE atom. Moreover, the structure of RE elements can be in a raw approximation considered the same in alloys and pure elements as demonstrated by Uchiyama [9].

In RE-TM alloys, the microscopic coupling consists of three different contributions, namely the TM-TM coupling, TM-RE coupling and the RE-RE coupling. Indeed, the TM-TM coupling is a strong coupling and is due to the itinerant electrons from the 3d bands. Moreover, the TM-RE coupling arises mainly from the direct antiferromagnetic coupling between the 5d RE and 3d TM electrons, and is assisted by the indirect coupling between the 4f RE and 3d TM electrons [6, 7]. This intersublattice exchange coupling is weaker than TM-TM coupling, but larger the RE-RE coupling [10].

The magnetic properties in the RE-TM alloys are strongly related to the concentration of the RE elements. These properties range from the net magnetization, the damping parameter, the individual amplitude of the moments for the RE and TM to the Curie temperature. For instance, the magnetization for a given temperature can be equal to zero at a given RE concentration x_{comp}. Therefore, shown in figure 2.4 is the evolution of the saturation magnetization and the anisotropy field of Tb_xCo_{100-x} alloys as a function of the Tb concentration. These measurements were performed at RT using a VSM by Alebrand *et al.* [11]. Figure 2.4 shows that the net magnetization is zero for Tb concentration $x_{comp} = 20$. A transition from a Tb dominant to a Co dominant alloy occurs when x decreases below $x_{comp} = 20$. The measured anisotropy field ranges up to 6 T and corresponds to an anisotropy constant of $3\ 10^6$ ergs/cm^3, and thus is compatible with high thermal stability for high-density patterned recording media.

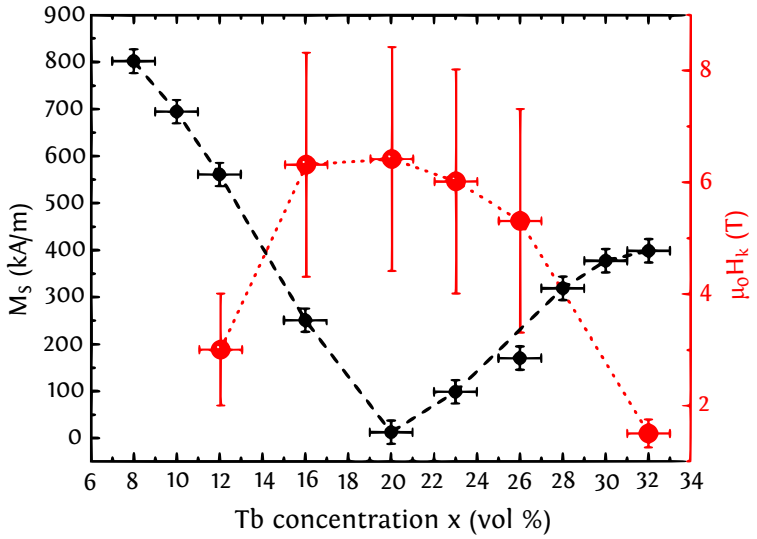

FIGURE 2.4: Magnetic properties of the Tb_xCo_{100-x} samples. Saturation magnetization M_s (black circles) and anisotropy field H_k (red circles) for the different Tb_xCo_{100-x} samples. The dashed and dotted lines are interpolations between the measured points. Large error bars are due to the uncertainty of magnetometry measurements for thin film samples with small magnetization. Figure adapted from [11].

The magnetization of both RE and TM sublattices evolve differently with temperature. Therefore, the net magnetization will also change with temperature. The RE-TM alloy at a given concentration presents thus a characteristic temperature, called compensation temperature T_{comp}, where the net magnetization of the alloy cancels out. As illustrated in figure 2.5, the individual RE and TM atoms at T_{comp} will be magnetized, but the global system will have a zero total magnetization due to the temperature dependence of the magnetization of the two sublattices. The RE (resp. TM) subsystem has usually a stronger magnitude than the TM (resp. RE) one for a temperature lower (resp. higher) than T_{comp}.

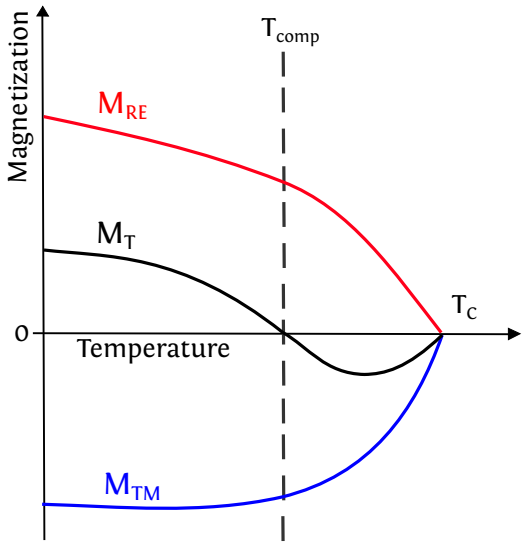

FIGURE 2.5: Temperature dependence of the net magnetization M_T and the sublattice magnetizations M_{RE} and M_{TM}. T_{comp} is the compensation temperature at which the two different sublattices compensate.

As mentioned previously, the net magnetization M_T of the RE-TM alloy is strongly related to the RE concentration. Hence, the temperature dependence of M_T is also related to the RE concentration, as depicted in figure 2.6 for GdCo alloys [6].

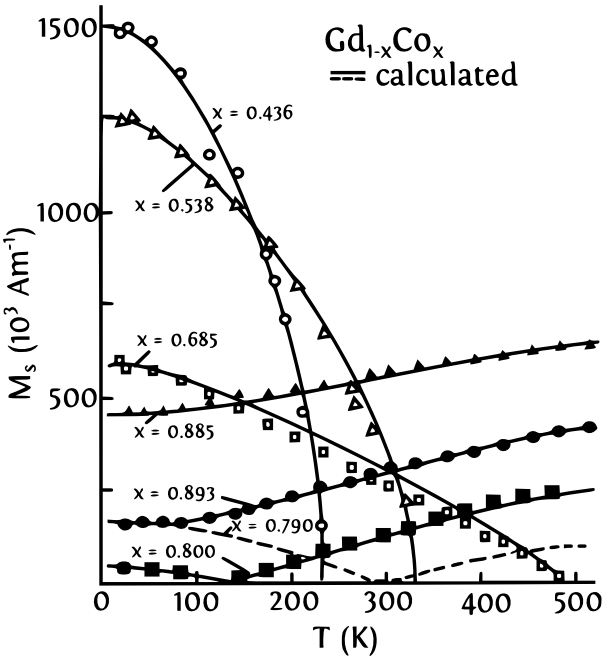

FIGURE 2.6: Temperature dependence of the saturation magnetization for GdCo alloys. The solid and dashed lines were calculated from the mean-field theory. Figure adapted from [6].

First, T_{comp} equals RT for the RE concentration x_{RE} = 21. Moreover, T_{comp} becomes higher than RT for 21 < x_{RE} < 31.5 and reaches 500 K for x = 31.5. For x_{RE} < 21, T_{comp} is lower than RT and the net magnetization M_T increases with temperature for RT < T < 500 K. While for TM-rich alloys with x_{RE} < 10, M_T only decreases with temperature.

Ferromagnetic multilayers

Two different ferromagnetic materials were studied in this thesis, namely Co/Pt and Co/Ni multilayers. Indeed, these materials are extremely interesting in terms of properties and applications such as the perpendicularly magnetized high density media. Both Co/Pt and Co/Ni multilayers show PMA and the Pt layer is magnetically polarized by Co [12, 13]. Therefore, the Kerr rotation of Co/Pt is very large due to the polarization of Pt. While performing AOS experiments on these ferromagnetic materials, the ultrashort laser pulses bring both angular momentum and heat. Thus, it is interesting to take into account the evolution of the magnetization as a function of temperature. Figure 2.7 shows that varying the Co thickness in Co/Pt multilayers modifies drastically the Curie temperature T_c. Indeed, decreasing the Co thickness leads to a reduction of T_c, which is attributed to the intermixing of Co and Pt that form a solid solution T_c. However, the Co/Pt multilayers studied for the AOS are much thinner than the one presented in figure 2.7. Therefore, their Curie temperature is expected to be much lower.

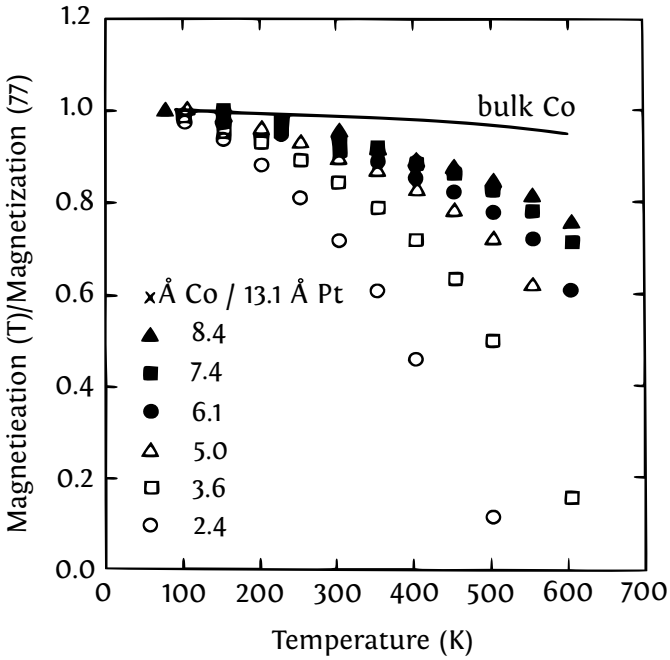

FIGURE 2.7: Temperature dependence of the magnetization of Co/Pt multilayers (60 bilayers) with varying Co thicknesses. The magnetizations are normalized to those at 77 K. Figure adapted from [14].

In Co/Ni multilayers, the magnetization arises from the interfacial coupling of Co and Ni elements. The structure seems similar to the (CoNi) alloys, but the ratio of the two atoms is very different as the Ni is the major ingredient in our case. However, Co/Ni multilayers have lower spin-orbit coupling and thus lower Kerr rotation than for Co/Pt multilayers. The magnetic properties of Co/Ni have been extensively investigated in the literature, thus a complete description could be find in these articles [15, 16, 17].

2.3 Femtosecond pulsed laser

The all-optical switching experiments were performed in this thesis using a Ti:sapphire laser developed by Coherent Inc. In general, a femtosecond laser source consists of an oscillator which produces ultrashort pulse trains, and an amplification stage enabling to increase the pulse energy by several order of magnitude (x 10^6). Hence, we will give in this section a brief description of the generation of femtosecond laser pulses, and basic information about the operating principle of Ti:sapphire oscillators and amplifiers.

2.3.1 Femtosecond laser pumping

In 1986, the first Ti:sapphire oscillator was developed by Moulton [18]. It enables producing ultrashort pulse trains, of the other of 5 fs for the most performing systems. Ti:sapphire can be tuned from 680 nm to 1130 nm, which is the widest tuning range of any crystal of its class. As depicted in figure 2.8, the Ti:sapphire oscillator emits preferentially around 800 nm, while its absorption band peaks near 490 nm. Therefore, Nd:YAG lasers are typically used to pump the Ti:sapphire crystal. Furthermore, the Kerr-lens modelocking (KLM) is used to achieve the femtosecond duration of the pulses. First, the continuous wave (CW) Gaussian beam propagates through the Kerr medium inside the laser cavity. Due to the optical Kerr effect, the refractive index experienced by the beam is greater in the center of the beam than at the edge.

Therefore, short bursts of light will then be focused differently from CW. Second, only short pulses will go through an aperture, since the latter is smaller than the CW beam diameter. Therefore, the Ti:sapphire oscillator will work in pulse mode.

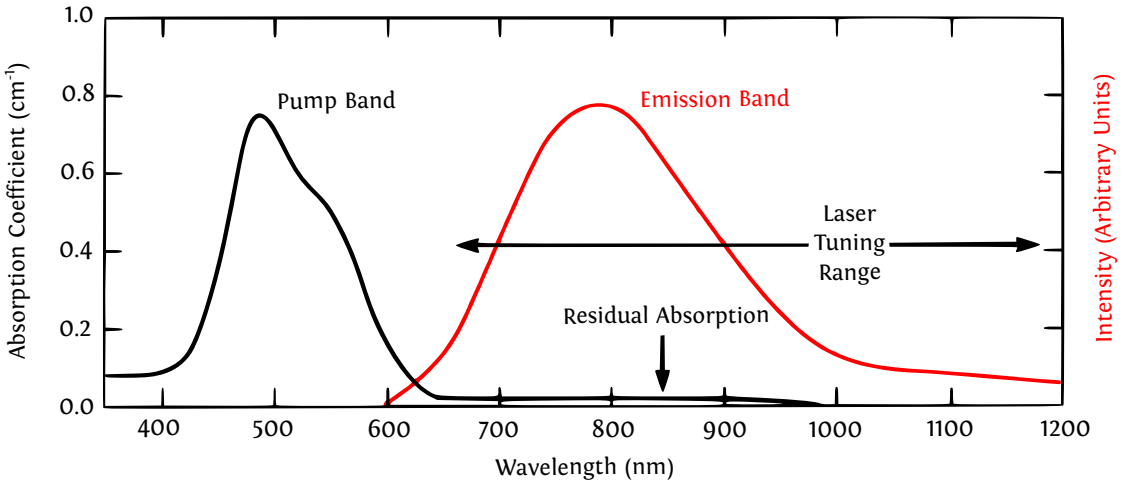

FIGURE 2.8: The emission and absorption bands of Ti:Al_2O_3. The absorption band, which peaks near 490 nm, occurs in the blue-green region of the spectrum and allows Ti:Al_2O_3 to be pumped by argon-ion lasers, frequency-doubled Nd:YAG lasers, copper-vapor lasers, or flash lamps. The emission band peaks near 790 nm. A weak absorption band that overlaps the emission band is known as the residual absorption. Figure adapted from [19].

Nevertheless, a group velocity dispersion (GVD) occurs due to the propagation of pulses through the dispersive components inside the cavity. The GVD causes a variation in the temporal profile of the laser pulses while the spectrum remains unchanged. In order to compensate this dispersion, a pair of prisms can be arranged to separate spectral components of the pulses and produce a negative dispersion, thus balancing the usually positive dispersion of the laser medium. Another alternative to prisms consists of using chirped mirrors. Indeed, these dielectric mirrors are coated so that different wavelengths have different penetration lengths, and thus different group delays.

2.3.2 Femtosecond laser amplification

To achieve a high peak power, the seed fs laser pulses generated by Ti:sapphire oscillators are amplified using the so-called chirped pulse amplification (CPA) introduced by Strickland *et al.* [20]. This amplification takes place also in a Ti:sapphire crystal, called gain medium, which is pumped by a Nd:YLF laser source. In order to avoid the damage of the gain medium by the high intensity of the seed pulses, their peak power is first decreased using a grating-based stretcher. The seed pulses can be safely amplified using a regenerative amplifier. Finally, the amplified pulses are then recompressed to the initial duration using a grating-based compressor.

Indeed, the seed pulses are first stretched out using a pair of gratings. These gratings expand the incident seed pulse spectrally and are arranged so that the low-frequency component of the laser pulse travels a shorter path than the high-frequency does, as depicted in figure 2.9. The stretcher introduces a negative dispersion. The pulse is thus stretched and has longer

pulse duration than the original by a factor of 10^3 to 10^5.

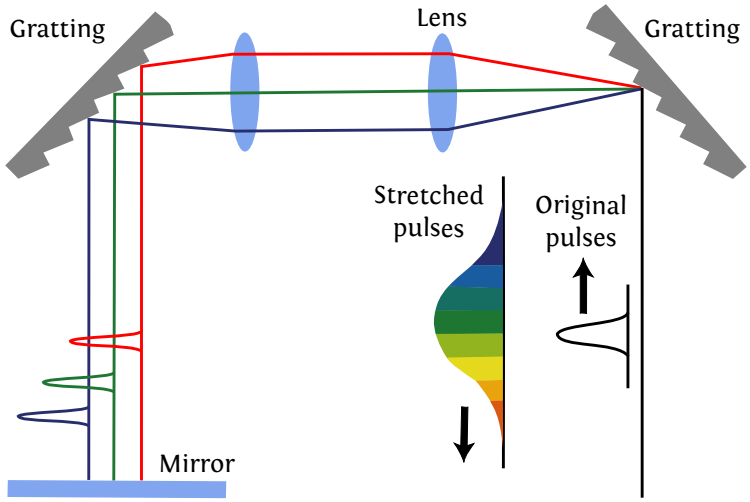

FIGURE 2.9: Schematic layout of a grating-based stretcher.

Therefore, the stretched pulses can be safely amplified by a factor 10^6 or more without damaging the gain medium. Two of the most widely used techniques for this amplification are the multipass and the regenerative amplification. In this thesis, we used the Legend Elite Duo amplification stage developed by Coherent Inc. This regenerative amplifier delivers up to 8 W with a 5-kHz repetition rate thanks to an additional Carrier-Envelope Phase (CEP) stabilization.

In the multipass amplification, different passes are geometrically separated and the number of passes is usually limited by the difficulties of focussing all the passes on a single spot of the gain medium. The bandwidth of the gain medium has to be broad enough to support the stretched pulse spectrum. Therefore, Ti:sapphire crystals with a wide tuning range are extensively used in the amplification process.

On the other hand, the regenerative amplification technique implies trapping of the pulse to be amplified in a laser cavity, as depicted in figure 2.10. The stretched pulse is kept in the resonator until all the energy stored in the Ti:sapphire crystal is extracted. The trapping and dumping of the pulse in and out of the resonator is performed using a Pockels cell and a broad-band thin film polarizer. Indeed, the Pockels cell is initially working as a quarter-wave plate. Once the stretched pulse is sent to the resonator, the voltage on the Pockels cell is applied (delay one) and the cell works then as a half-wave plate. Therefore, the pulse is kept in the cavity until reaching the saturation. Finally, a second voltage is applied (delay two) and the amplified pulse is then extracted from the resonator.

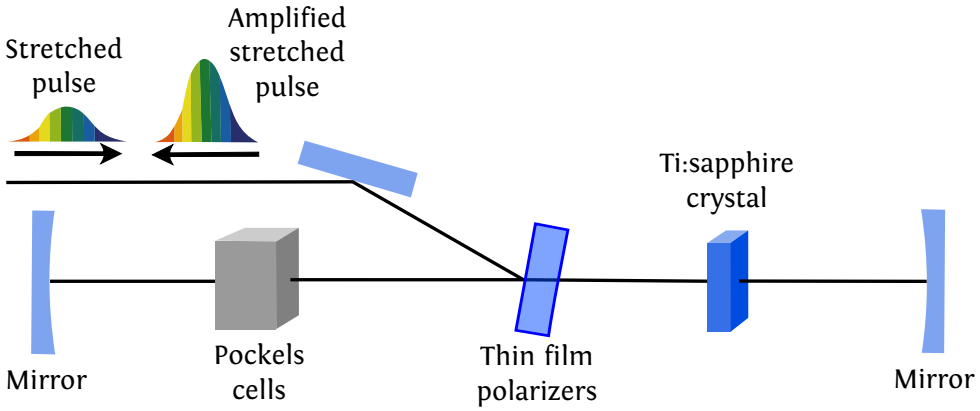

FIGURE 2.10: Schematic principle of a regenerative amplifier.

After the amplification process, the pulse is recompressed to its original duration through the reversal process of stretching, and using a grating-based compressor as illustrated in figure 2.11. Contrary to the stretcher, the compressor introduces a positive dispersion, as the high-frequency component of the amplified pulse travels a shorter path than the low-frequency does. In order to cancel the negative dispersion of the stretcher, the positive dispersion of the compressor is precisely tuned by changing the distance between gratings. Therefore, the compressed pulses with a 35-fs pulse duration achieve a peak power with orders of magnitude higher than the one generated by the laser system before the invention of CPA.

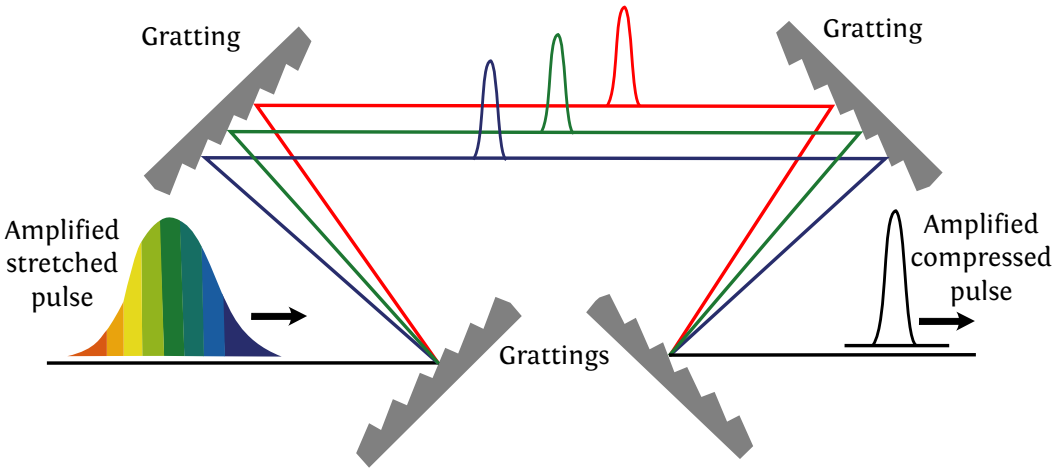

FIGURE 2.11: Schematic layout of a grating-based compressor.

The final pulse duration of 35 fs can be tuned up to 250 fs by adjusting the gratings. The wavelength can be also tuned using the TOPAS-prime developed by Coherent Inc. This optical parametric amplifier (OPA) includes a white light seeding for an increased input noise performance and gives access to wavelength ranging from 190 nm to 1200 nm. This OPA requires a 35-fs pulse input, and thus it is not compatible with the tuning of the pulse duration.

2.4 Magneto-optical Faraday microscope

In this section, we will first discuss the microscopic origin of the magneto-optical Kerr effect, and then give a brief description of the Faraday microscope used to probe the all-optical switching.

2.4.1 Magneto-optical Kerr effect

In 1845, Michael Faraday reported the first interaction between light and magnetism. Indeed, he demonstrated that linearly polarized light experiences a rotation when passing through a transparent magnetized medium, which is the Faraday effect. The rotation is called Faraday rotation and was shown to be linearly proportional to the component of the magnetic field in the direction of propagation. Thirty years later, John Kerr discovered that the same effect occurs when linearly polarized light reflects off a magnetic surface. This effect is called the magneto-optical Kerr effect (MOKE), and both effects have the same microscopic origin.

Indeed, the linearly polarized light is a linear combination of circularly polarized light with opposite helicities. Due to the magnetic circular birefringence (MCB), these two modes will transport differently in the magnetic material and will have a phase difference after reflection (or transmission), leading to a rotation of the polarization of the linearly polarized light. The schematic principle of MCB is depicted in figure 2.12.

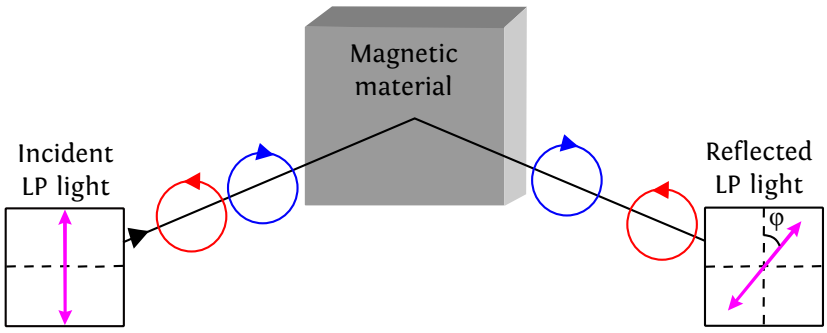

FIGURE 2.12: Schematic principle of magnetic circular birefringence (MCB). The magnetic material shows different refractive indices for left- and right-handed circular polarized light, leading to a rotation of the orientation of the linearly polarized reflected light.

On the other hand, the two components of the linearly polarized light will also have different amplitudes after reflection or transmission due to the magnetic circular dichroism (MCD), as depicted in figure 2.13(a). The incident linearly polarized light becomes then elliptical, and gives rise to the Kerr ellipticity. By taking into account both effects, the incident linearly polarized light becomes elliptically polarized and also undergoes a rotation after reflection or transmission through a magnetic material, as depicted in figure 2.13(b). Hence, information regarding the magnetization of the material can be obtained by measuring the rotation or ellipticity of the reflected or transmitted light.

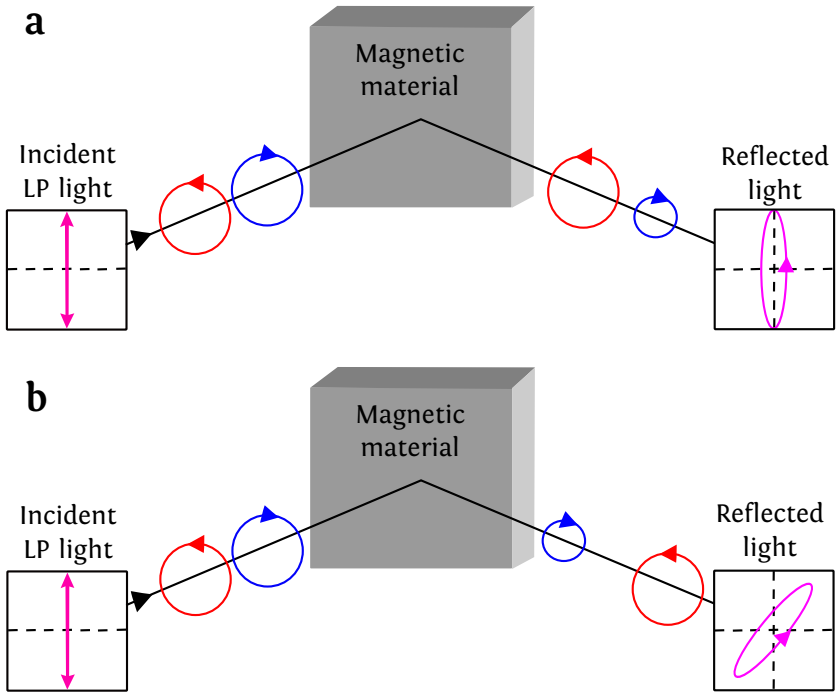

FIGURE 2.13: (a) Schematic principle of magnetic circular dichroism (MCD). The magnetic material shows different absorption rate for left- and right-handed circular polarized light, leading to an elliptically polarized reflected light. (b) Combination of both MCB and MCD. The linearly polarized light becomes elliptically polarized and experiences a rotation after reflection off a magnetic material.

From a phenomenological point of view, the optical response of an isotropic optical medium can be described using the dielectric tensor ϵ:

$$\epsilon = \begin{pmatrix} \epsilon_{xx} & 0 & 0 \\ 0 & \epsilon_{yy} & 0 \\ 0 & 0 & \epsilon_{zz} \end{pmatrix} \tag{2.1}$$

However, the medium becomes optically anisotropic in the presence of magnetization. The magnetization is described by the non-diagonal components of the dielectric tensor given by the Onsager formulation [21]:

$$\epsilon = \begin{pmatrix} \epsilon_{xx} & \epsilon_{xy} & \epsilon_{xz} \\ -\epsilon_{xy} & \epsilon_{yy} & \epsilon_{yz} \\ -\epsilon_{xz} & -\epsilon_{yz} & \epsilon_{zz} \end{pmatrix} \tag{2.2}$$

Now we consider that the medium is perpendicularly magnetized and that the incident linearly polarized light travels in the z direction. In this case, the z-components ϵ_{xz} and ϵ_{yz} become zero, and the eigenvalues $\epsilon = \epsilon_{xx} \pm i\epsilon_{xy}$ correspond to right-handed ($\sigma+$) and left-handed ($\sigma-$) circularly polarized light, respectively. Consequently, the complex refraction index of the material is different for $\sigma+$ and $\sigma-$, leading to the rotation of the polarization axis of the linearly polarized light. The complex Faraday rotation θ is given by [22]:

$$\theta = \varphi + i\delta = \frac{\epsilon_{xy}}{\sqrt{\epsilon_{xx}}(\epsilon_{xy} - 1)} \tag{2.3}$$

where φ is the Faraday rotation and δ is the Faraday ellipticity. The real and imaginary parts of the complex Faraday rotation are related by the Kramers-Kronig relations.

From a microscopic point of view, MOKE is due to the combination between the spin-orbit coupling and the exchange interaction, and also arises from the optical selection rules [23]. The optical transitions dictated by the selection rules have different absorption probabilities for $\sigma+$ and $\sigma-$ polarized beam. Indeed, the imaginary part of the non-diagonal components of the conductivity tensor σ_{xy} is responsible for the magneto-optical response. Moreover, $\mathrm{Im}(\sigma_{xy})$ changes sign when the magnetization M changes sign, thus providing the sensitivity of $\sigma+$ and $\sigma-$ to M [24]. In ferromagnetic materials, it was demonstrated that MOKE originates mainly from the spin-orbit coupling [25].

The relative orientation of the magnetization with respect to the sample normal and the light's plane of incidence can strongly influence the magneto-optical contrast. We can distinguish between three different configurations of MOKE. As illustrated in figure 2.14(a), the first configuration is the polar MOKE. In this configuration, the magnetization is perpendicular to the reflection surface and lies in the plane of incidence. Shown in figure 2.14(b) is the longitudinal MOKE configuration, where the magnetization lies in the plane of incidence and the reflection surface. Finally, the third configuration is the transversal MOKE, where the magnetization lies in the reflection surface but is perpendicular to the plane of incident (see figure 2.14(c)). Since our samples are all perpendicularly magnetized, the polar MOKE is used in this thesis to probe the magnetization change during the all-optical switching experiments.

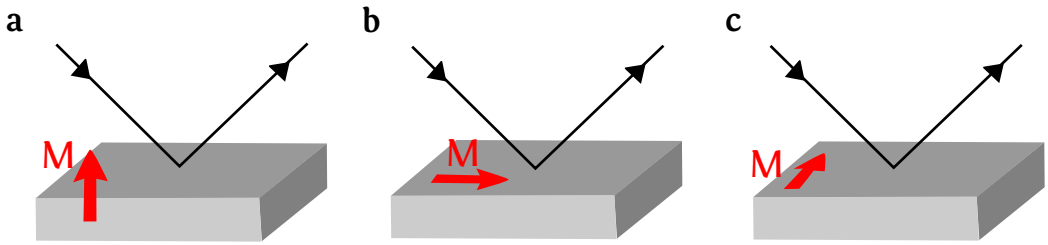

FIGURE 2.14: The three different configurations of MOKE. (a) Polar, (b) longitudinal, and (c) transversal MOKE.

2.4.2 Experimental setup

The study of all-optical switching in ferri- and ferro-magnetic continuous films is performed using the experimental setup depicted in figure 2.15. First, the 35-fs laser beam with a 5-kHz repetition rate and a 800-nm wavelength goes through a combination of a half-wave plate, a Glan-Taylor polarizer and a quarter-wave plate. The half-wave plate enables to tune the laser beam power, while the quarter-wave plate is used to transform the linearly polarized beam into right- and left-handed circularly polarized beam. The pulse-picker can also be used to select single pulses.

The response of magnetic films under the action of the laser beam is imaged using a Faraday imaging setup. The latter is a combination of a source of light, a pair of polarizer-analyzer, a converging lens and imaging device. Indeed, the light source is

a 680-nm monochromatic high intensity LED. Moreover, the polarizer-analyzer pair is responsible for the polarization of the incident light from LED and its extinction after passing through the sample. In order to obtain a high contrast, we used Glan-Taylor polarizers with high extinction coefficients. The magnetic domains are then imaged using a regular charge-coupled device (CCD) camera with a pixel size of 0.13 μm for a total surface of 2448 x 2048 pixels. This CCD camera is coupled to a 20x- magnetization microscope objective. A 50/50 beam-splitter is then used to overlap of the imaging source and the laser beam, allowing for a direct imaging of magnetization during laser excitation. The converging lens enables to reduce the laser spot down to 60 μm. Finally, an IR blocking filter is used to prevent damage to the CCD camera.

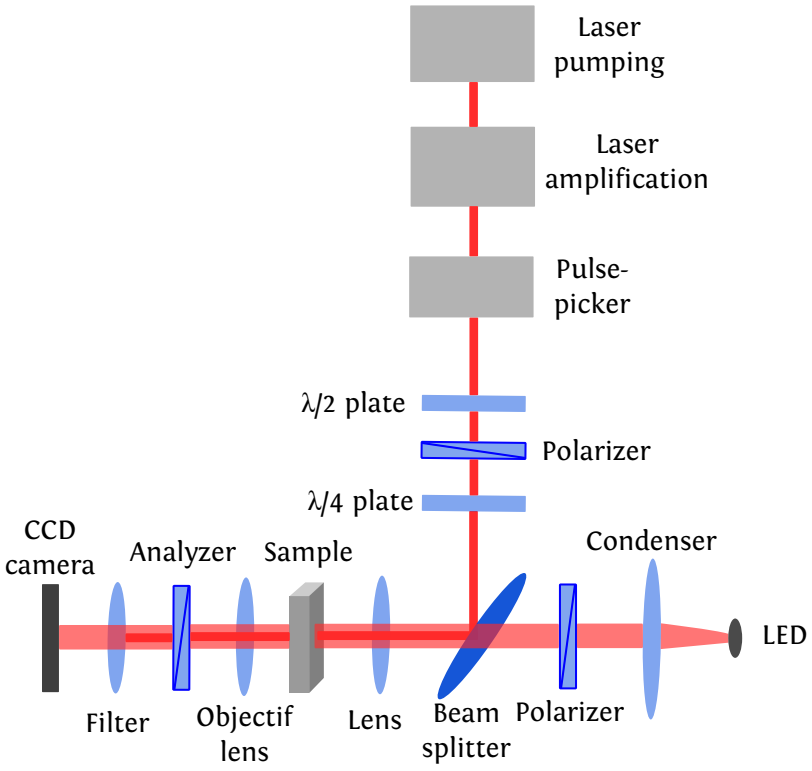

FIGURE 2.15: Experimental setup for femtosecond laser excitation and Faraday imaging.

References

[1] S. Mangin, D. Ravelosona , J. A. Katine, M. J. Carey, B. D. Terris and E. E. Fullerton, Current-induced magnetization reversal in nanopillars with perpendicular anisotropy *Nat. Mater.* **5**, 210 - 215 (2006).

[2] C. Chappert, H. Bernas, J. Ferré, V. Kottler, J. P. Jamet, Y. Chen, E. Cambril, T. Devolder, F. Rousseaux, V. Mathet, and H. Launois, Planar patterned magnetic media obtained by ion irradiation *Science* 280, 1919 (1998).

[3] J. Fassbender, D. Ravelosona and Y. Samson, Tailoring magnetism by light ion irradiation *J. Phys. D: Appl. Phys.* **37**, R179-R196 (2004).

[4] T. Devolder, Light ion irradiation of Co/Pt systems: Structural origin of the decrease in magnetic anisotropy *Phys. Rev. B* **62**, 9 (2000).

[5] S. Foner, Versatile and sensitive vibrating-sample magnetometer *Rev. Sci. Instrum.* **30**, 548–557 (1959).

[6] P. Hansen, C. Clausen, G. Much, M. Rosenkranz, and K. Witter, Magnetic and magneto-optical properties of rare-earth transition-metal alloys containing Gd, Tb, Fe, Co *J. Appl. Phys.* **66**, 756 (1989).

[7] P. Hansen, S. Klahn, C. Clausen, G. Much, and K. Witter, Magnetic and magneto-optical properties of rare-earth transition-metal alloys containing Dy, Ho, Fe, Co *J. Appl. Phys.* **69**, 3194 (1991).

[8] W. C. Koehler, Magnetic properties of rare-earth metals and alloys textitJ. Appl. Phys. **36**, 1078 (1965).

[9] S. Uchiyama, Magnetic properties of rare earth-cobalt amorphous films *Mater. Chem. and Phys.* **42**, 38 (1995).

[10] T. A. Ostler, R. F. L. Evans, R. W. Chantrell, U. Atxitia, O. Chubykalo-Fesenko, I. Radu, R. Abrudan, F. Radu, A. Tsukamoto, A. Itoh, A. Kirilyuk, Th. Rasing, and A. Kimel, Crystallographically amorphous ferrimagnetic alloys: Comparing a localized atomistic spin model with experiments *Phys. Rev. B* **84**, 024407 (2011).

[11] S. Alebrand, M. Gottwald, M. Hehn, D. Steil, M. Cinchetti, D. Lacour, E. E. Fullerton, M. Aeschlimann, and S. Mangin, Light-induced magnetization reversal of high-anisotropy TbCo alloy films *Appl. Phys. Lett.* **101**, 162408 (2012).

[12] G. Schutz, R. Wienke, W. Wilhelm, W. B. Zeper, H. Ebert, and K. Sporl, Spin dependent x ray absorption in Co/Pt multilayers and $Co_{50}Pt_{50}$ alloy *J. Appl. Phys.* **67**, 4456 (1990).

[13] J. W. Knepper and F. Y. Yang, Oscillatory interlayer coupling in Co Pt multilayers with perpendicular anisotropy *Phys. Rev. B* **71**, 224403 (2005).

[14] H. W. van Kesteren and W. B. Zeper, Controlling the Curie temperature of Co/Pt multilayer magneto-optical recording media *J. Magn. Magn. Mater.* **120**, 271–273 (1993).

[15] G. Daalderop, P. Kelly, and F. den Broeder, Prediction and confirmation of perpendicular magnetic anisotropy in Co/Ni multilayers *Phys. Rev. Lett.* **68**, 682 (1992).

[16] J. -M. L. Beaujour, W. Chen, K. Krycka, C. -C. Kao, J. Z. Sun, and A. D. Kent, Ferromagnetic resonance study of sputtered Co|Ni multilayers *Eur. Phys. J. B* **5**, 475–483 (2007).

[17] F. J. A. den Broeder, H. W. van Kesteren, W. Hoving, and W. B. Zeper, Co/Ni multilayers with perpendicular magnetic anisotropy: Kerr effect and thermomagnetic writing *Appl. Phys. Lett.* **61**, 1468 (1992).

[18] P. F. Moulton, Spectroscopic and laser characteristics of Ti:Al_2O_3 *J. Opt. Soc. Am. B*, vol. **3**, no. 1, 125–133 (1986).

[19] K. F. Wall and A. Sanchez, Titanium Sapphire Lasers *L. Lab. J.* **3**, 3 (1990).

[20] D. Strickland and G. Mourou, Compression of amplified chirped optical pulses *Opt. Commun.* **56**, 219 (1985).

[21] A. K. Zvezdin and V. A. Kotov, *Modern Magnetooptics and Magnetooptical Materials* (IOP, Bristol, 1997).

[22] M. Freiser, A survey of magnetooptic effects *IEEE Trans. on Magn.* **4**, 152 (1968).

[23] H. Ebert, Magneto-optical effects in transition metal systems *Rep. Prog. Phys.* **59**, 1665 (1996).

[24] P. Bruno, Y. Suzuki, and C. Chappert, Magneto-optical Kerr effect in a paramagnetic overlayer on a ferromagnetic substrate: A spin-polarized quantum size effect *Phys. Rev. B* **53**, 214 (1996).

[25] P. N. Argyres, Theory of the Faraday and Kerr effects in ferromagnetics *Phys. Rev.* **97**, 334 (1955).

Chapter 3

Domain size criterion for the observation of all-optical switching

3.1 Introduction

In the third chapter of this thesis, we present a comprehensive investigation of the magnetic parameters ruling the observation of all-optical helicity-dependent magnetization switching in ferrimagnetic alloys and ferromagnetic multilayers for a wide range of compositions and thicknesses. The aim of this investigation is to reconcile the contradictions between the previously reported low remanence criterion (M_R < 220 kA/m) for the observation of AO-HDS in ferrimagnetic materials [1, 2, 3], and the observation of AO-HDS in ferromagnetic materials with a high remanence (M_R > 1400 kA/m) and a magnetic thickness reduced to 2.4 nm [4]. First, we give in section 3.2 a short overview about the origin of magnetic interactions and domains, and discuss the magnetization reversal in magnetic thin films with PMA. Second, we report in section 3.3 the thickness-dependent investigation of AO-HDS in ferrimagnetic TbCo alloys and ferromagnetic Co/Pt and Co/Ni multilayers. This approach enables to prove that ferrimagnetic TbCo alloys with a high remanence (M_R = 830 kA/m) showing only thermal demagnetization (TD) for a high thickness exhibit AO-HDS if their thickness is strongly reduced. By taking into account the demagnetizing energy and the domain wall energy, we show in section 3.4 that the magnetic domain size is a relevant criterion for the observation of AO-HDS, which is common for both ferri- and ferro-magnets. Finally, we investigate in section 3.5 the optical response of light-ion irradiated ferromagnetic Co/Pt multilayers, confirming the large domain size criterion and highlighting the role of the domain wall energy in the AO-HDS process.

3.2 Magnetic interactions and domains

3.2.1 Magnetic interactions

In this section, we give a short overview about the origins of magnetic interactions.

Zeeman energy

The Zeeman interaction describes the action of an external magnetic field H_{app} on magnetic moments. The magnetization M of the material tends to minimize the so-called Zeeman energy E_z given by:

$$E_Z = -\mu_o \int \vec{M}.\vec{H}_{app} dV \tag{3.1}$$

where the integral is done over the volume of the magnetic material V. The Zeeman energy is minimized when the magnetization is parallel to the applied field. Hence, this interaction tends to align the magnetization along the direction of the magnetic field.

Exchange interaction

Magnetic order is due to the exchange interaction between spins. The exchange interaction originates from the Pauli exclusion principle and Coulomb interaction, which makes impossible the existence of two electrons in the same state. Thus, the energy between two interacting electrons is reduced or increased depending on the exchange constant J and the relative orientation of their spins. The exchange constant J is determined by the relative distance between the two spins. The exchange energy between two spins S_1 and S_2 is given by:

$$E_{ex} = -J\vec{S}_1.\vec{S}_2 \tag{3.2}$$

The sign of J influences the different magnetic configurations. Indeed, if $J > 0$ (resp. $J < 0$) the minimum energy is obtained for a parallel (resp. antiparallel) arrangement of the spins. The exchange interaction is a short-range interaction which is limited to first neighbor moments. It leads to magnetic order like ferromagnetic ($J > 0$) and antiferromagnetic ($J < 0$) order. Such order is lost at a certain critical temperature, called Curie temperature for ferromagnets and Néel temperature for antiferromagnets. If the temperature is higher than this critical value, the moments are randomly oriented because of the thermal fluctuations and then the material becomes paramagnetic.

Dipolar energy and shape anisotropy

The dipolar interaction is a long-range interaction which occurs between magnetic moments due to the dipolar magnetic field created by these moments. In a bulk material, this field points in the opposite direction of the global magnetization M, thus lowering the magnetization and creating a local distribution of magnetic moments. Therefore, this field is called the demagnetizing field H_d. This effect can be described considering magnetic charges left at the surfaces of the material which create H_d, as depicted in figure 3.1. The interaction of the magnetic moments with H_d leads to the demagnetizing energy given by:

$$E_d = -\frac{\mu_0}{2}\int \vec{M}.\vec{H}_d\,dV \tag{3.3}$$

H_d tends to orientate the magnetic moments to directions where E_d is minimum. The demagnetizing field H_d depends on the size and geometry of the sample and induces preferential orientations for the magnetization. This phenomenon is described as the shape anisotropy.

In general, the calculation of the demagnetizing field is difficult and can only be performed by numerical methods. In the case of uniform magnetizations, the relation between M and H_d is given by the so-called demagnetizing tensor [N] as follows:

$$\vec{H}_d = -[N].\vec{M} \tag{3.4}$$

The negative sign indicates that H_d and M are antiparallel. The demagnetizing tensor [N] depends on the shape of the sample. Simplifications are possible for certain particular geometries such as the ellipsoid with a uniform magnetization. In this particular case, the demagnetizing field is given by [5]:

$$H_d = -\begin{pmatrix} N_{xx} & 0 & 0 \\ 0 & N_{yy} & 0 \\ 0 & 0 & N_{zz} \end{pmatrix} M_s \tag{3.5}$$

The diagonal elements of N follow the relation: $N_{xx} + N_{yy} + N_{zz} = 1$. Hence, in the case of a sphere we get $N_{xx} = N_{yy} = N_{zz} = \frac{1}{3}$. While in the case of a thin film with a perpendicular magnetization, we get $N_{xx} = N_{yy} = 0$ and $N_{zz} = 1$ leading to a demagnetizing energy per unit volume:

$$E_d = -\frac{\mu_0}{2}\vec{M}_s.\vec{H}_d = \frac{\mu_0}{2}{M_s}^2 \tag{3.6}$$

where M_s is the projection of the magnetization along the preferential z axis.

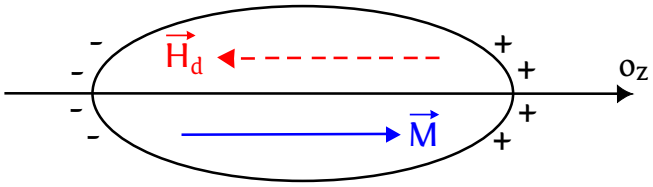

FIGURE 3.1: Ellipsoid uniformly magnetized along its z-axis. H_d is the demagnetizing field due to the existence of magnetic poles at the surface of the ellipsoid.

The magnetocrystalline anisotropy (MCA) refers to the dependence of the internal energy of a material on the orientation of its magnetization relative to specific axes of the material. This anisotropy originates from the interaction of the orbital magnetic moments with the crystal lattice, leading to preferential orientations for the magnetization. Axis along which the magnetization prefers to lie is called easy axis, whereas another axis that will be difficult to align the magnetization with is called hard axis.

In the case of crystals with a cubic symmetry, the energy per unit volume associated to the magnetocrystalline anisotropy is given by:

$$E_d = K_1(\alpha_2{}^2\alpha_3{}^2 + \alpha_3{}^2\alpha_1{}^2 + \alpha_1{}^2\alpha_1{}^2) + K_1\alpha_1{}^2\alpha_2{}^2\alpha_3{}^2 + ... \tag{3.7}$$

where α_1, α_2 and α_3 are the direction cosines with the crystallographic axes [100], [010] and [001], respectively. K_1 and K_2 are first and second anisotropy constants. Hence, figure 3.2 is the polar representation of the MCA in the simple case when $K_2 = 0$ and K_1 is positive or negative.

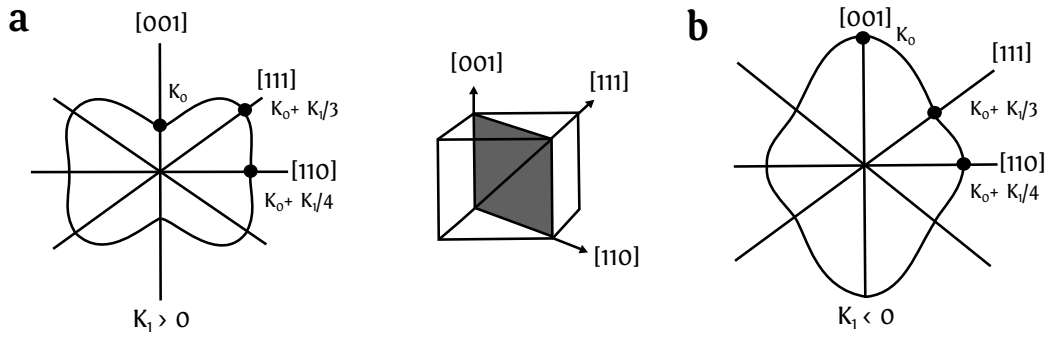

FIGURE 3.2: Polar representation of the energy associated to the magnetocrystalline anisotropy in the case of a cubic crystal. The energy is represented as a function of the magnetization direction in the plane (perpendicular to an axis with binary symmetry). This plane contains the three main symmetry axes. As the anisotropy is defined except to a constant term, K_0 is added to the anisotropy in order to facilitate the graphic presentation. Figure adapted from [6].

For $K_1 > 0$, the minimum of the MCA energy is obtained when moments are orientated in a ‹100› axis. The ‹100› axis thus corresponds to the easy axis. For $K_1 < 0$ this axis is a hard axis. In the case of crystals with uniaxial symmetry such as the hexagonal and the quadratic symmetries, the energy per unit volume associated to the MCA is given by:

$$E_{hex} = K_1 \sin^2\theta + K_2 \sin^4\theta + K_3 \sin^6\theta + K_4 \sin^6\theta \cos 6\varphi + \ldots \tag{3.8}$$

$$E_{qua} = K_1 \sin^2\theta + K_2 \sin^4\theta + K_3 \sin^4\theta \cos 4\varphi + \ldots \tag{3.9}$$

where K_i are the anisotropy constants. θ and φ are the angles between the magnetization and the crystallographic axis [001] and [100], as depicted in figure 3.3.

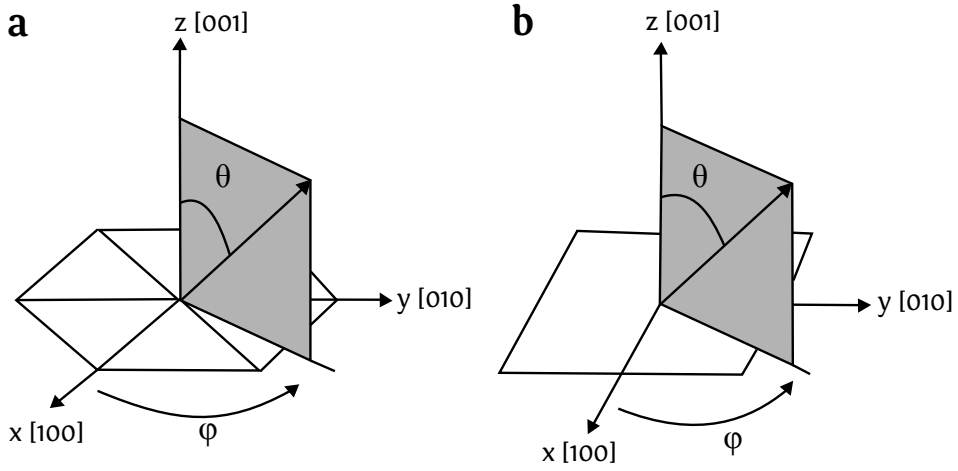

FIGURE 3.3: Definition of the angles θ and φ, for hexagonal (a) and quadratic (b) symmetry. Figure adapted from [6].

Magnetocrystalline anisotropy in RE and TM elements

In bulk transition metals (TM) such as Co, Fe and Ni, the atomic magnetic moment due to the 3d bands has two sources, namely the orbital and the spin moments. Both moments are coupled via the spin-orbit coupling (SOC). Moreover, the orbital moment is coupled to the crystalline lattice via the crystalline electrical field (CEF) leading to the MCA. Therefore, the total moment which consists of the spin and orbital contributions is coupled to the crystalline lattice.

The strong lattice-orbit coupling in TM leads to the quenching of the orbital contribution to the magnetic moment. Thus, the magnetization in 3d elements is shown to be mainly due to the spin contribution [7]. Moreover, the indirect coupling of the spins to the lattice via the SOC also vanishes, since the orbital moment vanishes. Therefore, the transition metals have in general small MCA, expect the hcp Co. For rare earth (RE) elements, the CEF is small compared to the one in TM. However, the SOC is in general strong. Consequently, for a temperature far below the Curie temperature, materials with RE elements like Tb with a large orbital moment have large MCA compared to TM.

Anisotropy in perpendicularly magnetized thins films

In magnetic thin films, the shape anisotropy tends to align the magnetic moments parallel to the plane and is given by:

$$K_{shape} = -\frac{\mu_0}{2} {M_s}^2 \tag{3.10}$$

where M_s is the saturation magnetization. The negative sign indicates that this anisotropy in the case of thin films favors an in-plane (IP) orientation of the magnetic moments. In order to obtain a perpendicular magnetic anisotropy (PMA), the shape anisotropy has to be overcome. Other sources of anisotropy favoring an out-of-plane (OOP) orientation of the magnetic moments exist, namely the magnetocrystalline volume anisotropy (K_u), and also the magnetocrystalline interface anisotropy (K_s) which was introduced by Néel in 1954 [8].

Indeed, the interface anisotropy is related to the atomic orbitals located at the interfaces or the surface. For thin films with thicknesses of the order of atomic monolayers, the magnetocrystalline symmetry leading to the quenching of the orbital contribution is broken by the interfaces due to the high surface to volume ratio. Therefore, Néel attributed the interface anisotropy to the increase of the orbital momentum at the interfaces. The symmetry breaking due to the interfaces distinguishes the direction perpendicular to the interface from all the other directions. For a thin magnetic layer, two interfaces (1) and (2) exist. The corresponding interface anisotropies are K_s^1 and K_s^2, and the interface contribution to the magnetocrystalline energy per unit volume is given by:

$$E_s = \frac{K_s^1 + K_s^2}{t} \sin^2 \theta \tag{3.11}$$

where t is the thickness of the magnetic layer. Since the orientation of the magnetization depends on the competition between the total MCA and the shape anisotropy,

we define the effective anisotropy K_{eff} as follows:

$$K_{eff} = K_u + \frac{K_s^1 + K_s^2}{t} - \frac{\mu_0}{2} M_s{}^2 \tag{3.12}$$

where K_u is the magnetocrystalline volume anisotropy constant. The film is perpendicularly magnetized for $K_{eff} > 0$ [9]. When the film thickness is scaled down, the interface contribution increases and the total MCA becomes larger than the shape anisotropy. Thus, the axis perpendicular to the film becomes an easy axis.

3.2.2 Magnetic domains and domain walls

Magnetic domains

A stable magnetic configuration corresponds to the minimization of the total magnetic energy. While the exchange interaction favors a uniformly magnetized sample, the dipolar interaction tends to orientate local magnetic moments in different directions in order to minimize the demagnetizing field. Therefore, the magnetic material can be divided into uniformly magnetized regions called magnetic domains. The region between two magnetic domains is called a domain wall (DW).

Indeed, a uniformly magnetized material as depicted in figure 3.4(a) exhibits magnetic charges at the surface, thus generating a strong demagnetizing field and leading to a large dipolar energy. This dipolar energy becomes low for a high length to width ratio. To reduce the dipolar energy, the magnetization could break into two domains as illustrated in figure 3.4(b). The dipolar energy is zero for the closure domain structure shown in figure 3.4(c), where the neighboring domains are not placed at an angle of 180° to each other. However, this is only possible for materials with a low uniaxial anisotropy.

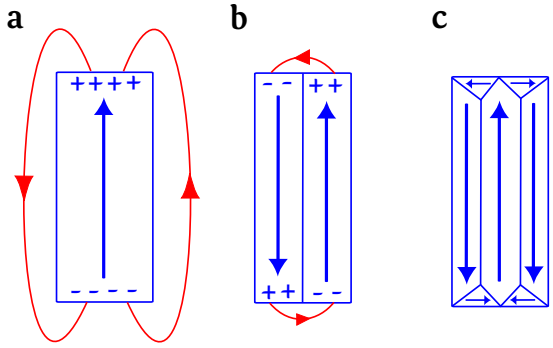

FIGURE 3.4: A variety of domain structures of a given particle. (+) and (-) represents the local magnetic charges: (a) uniformly magnetized (single domain), (b) two domains, and (c) more complex domain structures.

Domain walls

The division into magnetic domains takes place as long as the dipolar energy is still greater than the energy required to form the DW. The thickness and energy of the DW are determined by the competition between the exchange, the dipolar and the magnetocrystalline energies. Indeed, a strong magnetocrystalline anisotropy favors a narrow DW, whereas a strong exchange interaction favors a wider DW. In the case of a thin film with uniaxial perpendicular anisotropy K_u and an exchange constant A_{ex}, the balance between the MCA and the exchange interaction leads to the DW width δ and the DW energy per unit surface σ given by:

$$\delta = \sqrt{\frac{A_{ex}}{K_u}} \tag{3.13}$$

$$\sigma = 4\sqrt{A_{ex}K_u} \tag{3.14}$$

The DW thickness varies from a few atoms for materials with high anisotropy such as Fe/Pt multilayers [10] to the order of 100 nm for permalloy. Two types of DW can be distinguished, namely the Néel wall and the Bloch wall as depicted figure 3.5 [11, 12]. Other DWs types exist such as the transverse [13] or vortex walls in nanostrips [14].

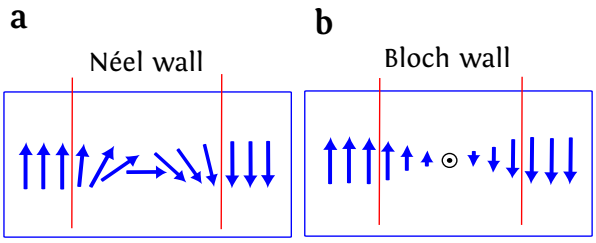

FIGURE 3.5: Schematic representation of two types of domains wall: (a) Néel wall and (b) Bloch wall.

In a Néel wall, the spins rotate in the plane perpendicular to the plane of the DW, whereas in the Bloch wall the spins rotate within the plane of the wall. In the case of in-plane magnetized thin films, the Bloch wall is preferable for large thicknesses, whereas the Néel wall becomes favorable when the film thickness becomes smaller than the DW thickness [15].

Domain size calculation

The remanent state of a non-saturated sample gives a good illustration of the competition between the long-range dipolar interaction and the short-range exchange interaction. As shown in figures 3.6(a) and 3.6(b), a stripe domain pattern nucleates and stabilizes in the remanent state in order to balance the dipolar and domain wall energies. A model proposed by Kooy *et al.* enables the estimation of the domain size in the case of periodic stripe domains with a strong uniaxial anisotropy in an infinite plate [16]. The DW thickness is supposed to be negligible compared to the domain size. The magnetization within the magnetic domains is perpendicular to the film plane. Therefore, the minimization of the total energy results in the magnetic domain size D given by:

$$D = t \exp\left[\frac{\pi D_0}{2t} + \ln \pi - 1 + \mu\left(\frac{1}{2} - \ln 2\right)\right] \tag{3.15}$$

where $D_0 = \frac{\sigma}{E_d}$ is the dipolar length and $\mu = 1 + \frac{E_d}{K_u}$ is the magnetic susceptibility. $E_d = \frac{\mu_0}{2} M_s{}^2$ is the demagnetizing energy per unit volume, $\sigma = 4\sqrt{A_{ex} K_u}$ is the DW energy per unit surface, and t is the magnetic thickness.

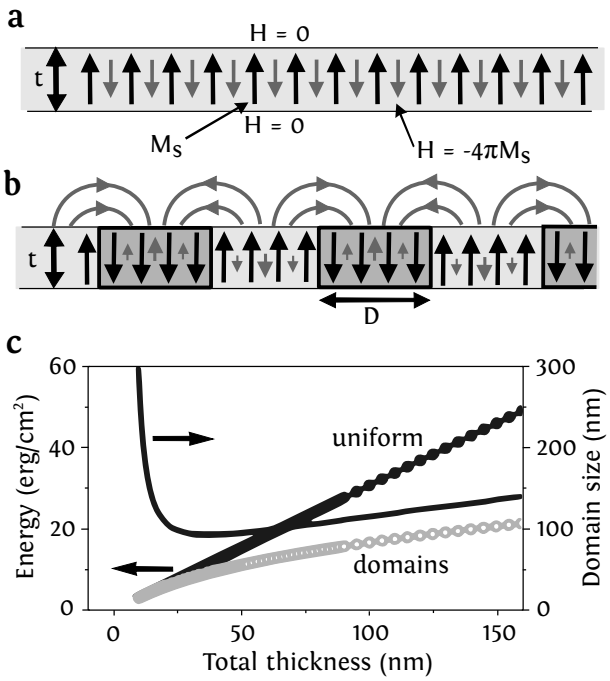

FIGURE 3.6: (a) Illustration of the magnetostatics for an infinitely extended, uniformly magnetized (magnetization M_s, big black arrows), perpendicular thin film of thickness t. (b) Similar film split up into stripe domains of characteristic width D. For both cases the grey arrows show the resulting dipolar fields. (c) Total magnetic energy per surface area (left axis) for both cases (a) and (b) and characteristic domain width D (right axis, solid line) for the domain state, all plotted versus magnetic film thickness t. Figure adapted from [17].

The typical evolution of the domain size D as a function of the thickness t is depicted in figure 3.6(c) in the case of Co/Pt multilayers. For thick films with $t \gg D_0$, the domain size scales as $2\sqrt{tD_0}$. For thin films with $t \ll D_0$, the magnetic energy gain becomes small and the domain size diverges as $t \exp\left(\frac{\pi D_0}{2t}\right)$.

3.2.3 Magnetization reversal in thin films

Nucleation-induced reversal

The most conventional way to reverse the magnetization of a thin magnetic film is by applying a magnetic field H_{app} opposite to the direction of the magnetization M. In the case of a thin film with PMA, the magnetization will homogeneously reverse to the direction of H_{app} when the Zeeman energy becomes larger than the total anisotropy energy. However, the anisotropy in real magnetic films is often not uniform, leading

to an inhomogeneous magnetization reversal. When applying H_{app} opposite to M, the first parts of the sample to switch are those with low anisotropy. These parts are either local defects or edges of the film. This process is called nucleation. The nucleation is a thermally activated and described as a Néel-Brown like process [18]. Hence, the nucleation rate increases at high temperatures. Moreover, a high magnetization M leads to a higher Zeeman energy, thus increasing the nucleation rate.

After the nucleation of the initial domains, two different modes of reversal are possible. In the first mode, the reversal can continue via the nucleation of small domains at fields H_{nuc} much lower than the fields H_{prop} necessary to move a DW. This so-called nucleation-induced reversal is illustrated in figure 3.7(a).

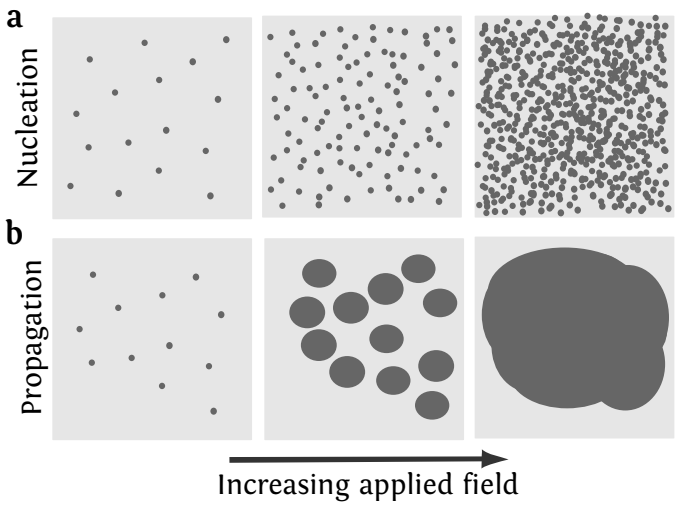

FIGURE 3.7: Schematic representation of magnetization reversal under the action of an external magnetic field for the nucleation-induced reversal (a) and the propagation-induced reversal (b).

Propagation induced-reversal

In the second mode, the reversal of the whole film can be achieved via the DW propagation at fields H_{prop} lower than the fields H_{nuc} necessary to nucleate reversed domains, as illustrated in figure 3.7(b). This mode is called propagation-induced reversal. For small applied fields, the DW propagation occurs by thermal activation and is strongly dependent on the structural defects of the sample. This regime is called DW creep regime [19]. While for large applied fields, the DW propagation deterministically flows through the film. This regime is the so-called flow regime. In real samples, the reversal behavior under the action of an external applied field is usually a mixture of the nucleation- and propagation induced reversal.

3.3 Thickness-dependence of all-optical switching in ferrimagnets and ferromagnets

In order to investigate the influence of the magnetic parameters and interactions discussed in section 3.2 on the observation of all-optical helicity-dependent switching, we study the optical response of ferri- and ferro-magnetic thin films of different compositions and thicknesses. All the studied films was grown by DC magnetron sputtering and show PMA leading to a magnetization perpendicular to film at zero applied field.

3.3.1 Studied ferri- and ferro-magnets

The investigated ferrimagnetic thin films are composed of Glass/Ta(3 nm)/Pt(5 nm)/ Tb_xCo_{100-x} (t)/Pt(5 nm). The top Pt layer prevents sample oxidation. Tb and Co magnetic moments are antiferromagnetically coupled, and their sum gives the net magnetization of the alloy. As mentioned in section 1.4, the magnetization for a given temperature can be equal to zero at a given Tb concentration x_{comp}. Hence, for larger (resp. lower) Tb concentration, the net magnetization will be pointing along the Tb (resp. Co) moment and the sample will be qualified as Tb dominant (resp. Co dominant). At RT and t = 20 nm, a transition from a Tb dominant to Co dominant ferrimagnet occurs if x is decreased below 20 [20].

Two nominal concentrations of Tb have been used, namely 16 at.% and 30 at.%. However, by strongly reducing the thickness of the TbCo alloy film, the nominal concentration x_{nom} varies from the effective concentration x defined by the deposition. The latter is deduced from the saturation magnetization M_s depicted in figures 3.8(a) and 3.8(b) and is compared with the one measured on thicker films (t = 20 nm) presented in [20]. Therefore, the Tb atomic concentration x in the studied TbCo alloy films is ranging from 8 at.% to 30 at.%, while the thickness t varies from 1.5 to 20 nm. As shown in figure 3.8(c), the composition x at which this crossover occurs depends on the magnetic thickness, which is agreement with previous studies [21, 22].

Several mechanisms have been reported in the literature to explain this behavior. Indeed, it was attributed in [21, 22] to the diffusion of rare earth atoms, causing a segregation process and a deviation of the Tb concentration in the studied films. Hence, this effect is particularly pronounced for low thicknesses due to the high surface to volume ratio. More recently, Hebler *et al.* demonstrated that the compensation point and the remanent magnetization of TbFe alloy films is related to a growth-induced modification of the microstructure of the amorphous films, thus affecting the short range order [3]. Therefore, the sperimagnetic cone angle of the Tb atoms changes, thus leading to a change of the saturation magnetization. Similar effects occur in our TbCo alloy thin films. In order to simplify the discussion, we report in the following the Tb concentration x which corresponds to the effective concentration in order to simplify the discussion.

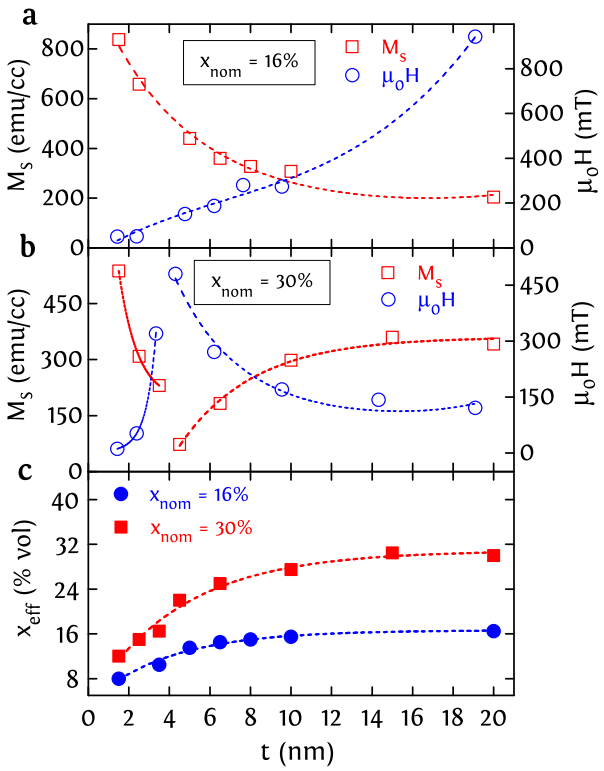

FIGURE 3.8: (a) (resp. (b)) Saturation magnetization and coercive field of TbCo alloy films for nominal Tb concentration x_{nom} of 16 at.% (resp. 30 at.%). (c) Effective concentration of Tb x_{eff} as a function of the thickness of TbCo alloy films with nominal Tb concentrations x_{nom} of 16 and 30. The dashed lines are guide to the eyes.

We also investigated two different ferromagnetic multilayer thin films, namely Glass/ Ta(3 nm)/Pt(3 nm)/[Pt(0.7 nm)/Co(0.6 nm)]$_N$/Pt(3.7 nm) multilayers and Glass/Ta(3 nm)/ Cu/[Co(0.2 nm)/Ni(0.6 nm)]$_N$/Cu/Pt(3 nm) multilayers. The top Pt layer prevents sample oxidation. The number of repeats N varies from 1 to 4 for Co/Pt multilayers and from 2 to 6 for Co/Ni multilayers. For [Co/Pt]$_N$ multilayers, the saturation magnetization M_s varies from 1483, 1609, 2194 to 2217 kA/m for N = 1, 2, 3 and 4, respectively. This increase of the saturation magnetization with the number of repeats is attributed to the spin polarization of Pt atoms by the adjacent Co layers [23]. Note that only the Co layer thickness is taken into account for the calculation of the saturation magnetization and the uniaxial anisotropy constant. For [Co/Ni]$_N$ multilayers, the saturation magnetization is M_s = 1100 kA/m and changes only weakly with the number of repeats.

3.3.2 Thickness-dependence of the all-optical switching in ferrimagnets

We investigated the AO-HDS ability in Tb_xCo_{100-x} (t) alloy films for a Tb concentration x ranging from 8 to 30 and a thickness t ranging from 1.5 nm to 20 nm. For AO-HDS experiments, we used a Ti:sapphire fs-laser with a 5-kHz repetition rate, a wavelength of 800 nm, and a pulse duration of 35 fs. The Gaussian beam is focused with a FWHM of approximately 50 µm. The response of the investigated magnetic films is probed using a Faraday microscope in order to image the magnetic domains in transmission.

The samples are excited through the glass substrate with laser powers ranging from 0.5 mW for films with lower thicknesses up to 3 mW for films with larger thicknesses. As demonstrated

in previous studies [24], the AO-HDS ability of Tb_xCo_{100-x} alloys is found to be maintained for a laser power ranging from the threshold below which the laser does not affect the magnetization to the damage threshold.

Prior to being optically excited, the studied films are saturated with an external magnetic field applied perpendicular to the film plane. During the optical excitation, no magnetic field is applied. The fs laser beam is swept from right to left for both right-(σ+) and left-(σ-) circular polarization with a sweeping speed of approximately 10 µm/s. The magneto-optical Faraday signal is mainly sensitive to the perpendicular component of the Co sublattice magnetization. After initial magnetization saturation up, the contrast corresponding to a reversal to down is dark (reps. white) for Co dominant (resp. Tb dominant) TbCo alloy films as shown in figures 3.9 and 3.10.

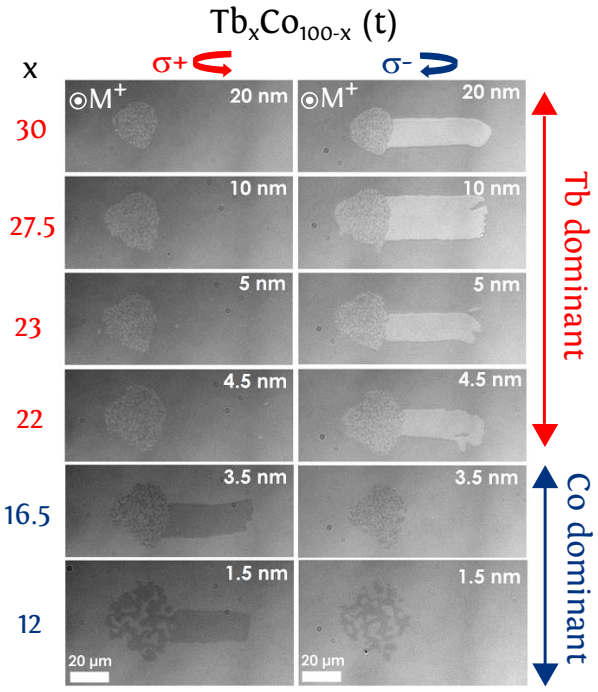

FIGURE 3.9: Optical response for Tb_xCo_{100-x} (t) alloy films for Tb concentration x ranging from 12 to 30 and alloy thickness varying from 1.5 nm to 20 nm. For each sample, right- and left-circularly polarized laser beam were swept over the sample from right to left. The initial magnetization saturation up is exemplarily shown. The white contrast for an alloy thickness varying from 20 nm to 4.5 nm, and the dark contrast for an alloy thickness 3.5 nm and 1.5 nm correspond to a reversal to down.

For a large thickness t = 20 nm, Figures 3.9 and 3.10 show that thermal demagnetization (TD) is observed for x = 16 (see figure 3.9) while AO-HDS is observed for x = 30, which is in agreement with previous studies [1, 20, 24]. These results were first attributed to the T_{comp} which is above (resp. below) RT for x = 30 (resp. x = 16) [20, 24]. Therefore, this T_{comp} can only be reached for x = 30 through laser-induced heating. On the other hand, these results were attributed by Hassdenteufel *et al.* to the low (resp. high) remanence at RT for x = 30 (resp. x = 16) [1]. As shown in figure 3.9, AO-HDS is obtained for x = 30 at first in the AOS rim at the edge of a demagnetized area. Then, AO-HDS is transferred to the scanned region leading to its total reversal. Furthermore, figure 3.9 shows that other Tb dominant alloys with x ranging from 22 to 27.5 and thickness down to 4.5 nm exhibit AO-HDS.

In regards to Co dominant alloys, figure 3.10 shows that the effect of the helicity starts to appear gradually by reducing the thickness. For t = 10 nm and x = 15.5, the helicity dependence is slightly observed at the level of the AOS rim, whereas the laser-induced multiple domains in the scanned region get larger. For t = 8 nm and x = 15, AO-HDS is almost obtained with a presence of a small stripe domain in the middle of the scanned region. However, a complete AO-HDS is achieved for $t \leqslant 6.5$ nm and x ranging from 8 to 16.5, as depicted in figures 3.9 and 3.10. This is the first demonstration of AO-HDS in Co dominant TbCo alloys, which is achieved by strongly reducing the magnetic thickness below 6.5 nm. For instance, the Co dominated Tb_8Co_{92} (1.5 nm) shows AO-HDS, even if such alloy does not present a compensation above RT and has a high saturation magnetization and remanence $M_S = M_R$ = 830 kA/m, thus contradicting the proposed low remanence criterion ($M_R \lesssim 220$ kA/m) for the observation of AO-HDS in ferrimagnets [1]. More importantly, these findings indicate that the magnetic film thickness plays an important role in the AO-HDS process.

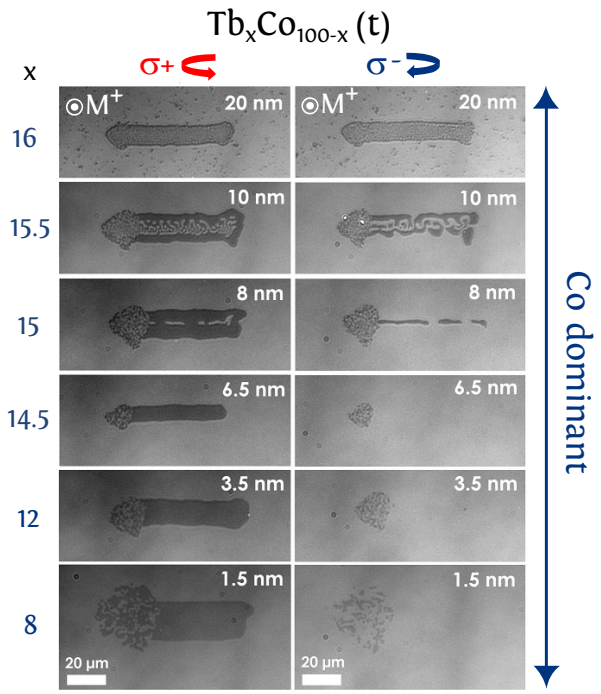

FIGURE 3.10: Optical response for Tb_xCo_{100-x} (t) alloy films for Tb concentration x ranging from 8 to 16 and alloy thickness varying from 1.5 nm to 20 nm. For each sample, right- and left-circularly polarized laser beam were swept over the sample from right to left. The initial magnetization saturation up is exemplarily shown. The dark contrast corresponds to a reversal to down. The laser power is ranging from 1.15 mW (for t ‹ 8nm) to 1.5 mW (for t › 8 nm).

Figures 3.9 and 3.10 show that after initial magnetization saturation up, right-(σ+) (resp. left-(σ-)) circular polarized beam switches the magnetization to down for Co dominant (resp. Tb dominant) TbCo alloy films. This finding is attributed to the fact that the helicity of switching depends on the orientation of the Co sublattice magnetization and not on the direction of the net magnetization of the TbCo alloy film [25]. These results are also a hint that a model based on the inverse Faraday effect (IFE) is less likely to explain the AO-HDS, since the reversal only depends on the absorption of the circular polarization by the Co sublattice and not on the direction of the net magnetization of the alloy.

Furthermore, multiple domains are obtained when the beam is turned off at the left of the scanned region. This is mainly related to the demagnetizing effect due to the cooling. One can clearly see that the size of magnetic domains in this demagnetized area increases for lower thicknesses, which is consistent with the model presented in section 3.2.2.

3.3.3 Thickness-dependence of the all-optical switching in ferromagnets

The recently discovery of AO-HDS in Co/Pt multilayers with a high saturation magnetization and no antiferromagnetic coupling between two sublattices [4] raises the question of what is the actual parameter ruling the observation of AO-HDS and if it is common to ferrimagnets and ferromagnets ? In this context, we have experimentally investigated the AO-HDS ability for both ferromagnetic Co/Ni and Co/Pt multilayers by performing the analog sweeping beam experiments to TbCo alloys.

In regards to $[Co/Ni]_N$ multilayers, figure 3.11 shows that the effect of the helicity starts to appear gradually by decreasing the number of repeats N and thus by decreasing the total magnetic thickness. Indeed, only TD is obtained for N ranging from 3 to 6, whereas AO-HDS is observed for $N = 2$. Moreover, the size of the multiple magnetic domains in the scanned area increases gradually by lowering N from 6 to 3, which is a hint that large domain size might also be an ingredient for the observation of AO-HDS.

We have also experimentally verified the AO-HDS ability in Co/Pt multilayers as previously demonstrated by Lambert *et al.* [4]. As depicted in figure 3.12, AO-HDS is observed for $N = 1$ and 2 whereas only thermal demagnetization is obtained for $N = 3$ and 4 with larger domain size in the scanned region for $N = 3$. Similarly to TbCo alloys, the switching ability for both Co/Pt and Co/Ni multilayers was maintained for a laser power ranging from the switching threshold to the damage threshold. To conclude, the AO-HDS is achieved in both Co/Pt and Co/Ni multilayers by strongly reducing the magnetic thickness. This behavior is similar to the one demonstrated in Co dominant TbCo alloy films in figure 3.10.

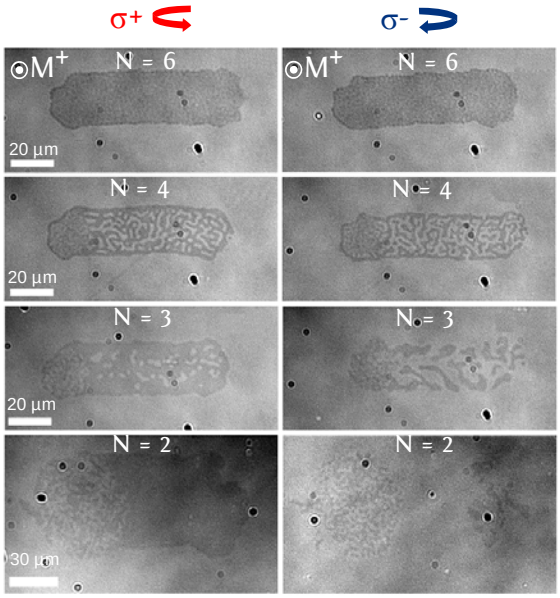

FIGURE 3.11: Optical response for $[Co(0.2\ nm)/Ni(0.6\ nm)]_N$ multilayers for number of repeats N ranging from 2 to 6. For each sample, right- and left-circularly polarized laser beam were swept over the sample from right to left. The initial magnetization saturation up is exemplarily shown. The dark contrast corresponds to a magnetization reversal to down.

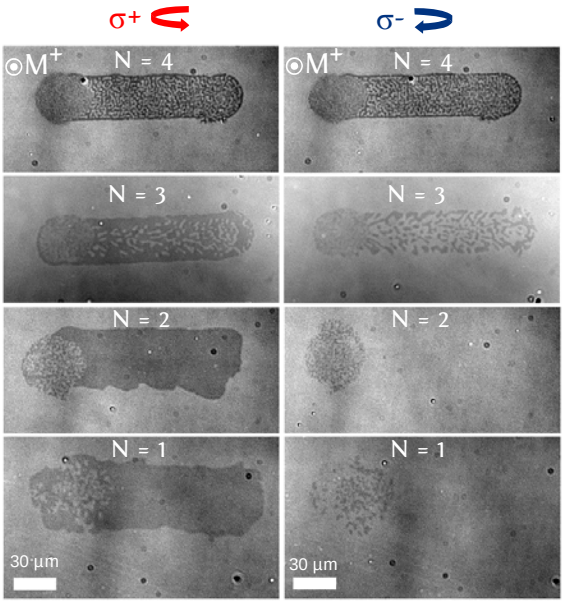

FIGURE 3.12: Optical response for $[Pt(0.7\ nm)/Co(0.6\ nm)]_N$ multilayers for number of repeats N ranging for 1 to 4. For each sample, right- and left-circularly polarized laser beam were swept over the sample from right to left. The initial magnetization saturation up is exemplarily shown. The dark contrast corresponds to a reversal to down.

3.4 Domain size criterion for the observation of all-optical switching

The thickness-dependent investigation in ferri- and ferro-magnets reveals that AO-HDS is observed when the magnetic film thickness is reduced. This behavior is common for both ferri- and ferro-magnets. Moreover, previous studies demonstrated that the magnetic domain size is strongly dependent on the magnetic thickness [16, 17]. As mentioned in section 3.2.2, this finding is associated to the competition between the dipolar energy that stabilizes small domains, and the domain wall energy that tends to stabilize big domains. Therefore, it is reasonable to infer that if the size of stable magnetic domains after the laser-induced heating is smaller than the size of the laser spot, TD will be observed as the magnetic system will break into small domains during cooling. Otherwise, AO-HDS will be observed if the magnetic domain size is larger than the size of the laser spot. Therefore, the magnetic domain size can be considered as a relevant predictive parameter for the observation of AO-HDS.

3.4.1 Magnetic parameters for studied materials

To estimate the magnetic domain size for the investigated ferro- and ferri-magnets, we use the model of periodic stripe domains with a strong uniaxial anisotropy in an infinite plate introduced in section 3.2.2 [16]. As can be seen from Eq. (3.15), the material parameters involved in the calculation of the domain size are the saturation magnetization M_s, the uniaxial anisotropy constant K_u and the exchange constant A_{ex}. An overview of the magnetic parameter values and the response to optical excitation for the studied films is presented in Table 1.

The M_s of all studied films and the K_u for Co/Pt and Co/Ni multilayers were measured with SQUID magnetometry. The values of K_u for TbCo alloys were deduced from the experimental data of Alebrand *et al.* [20]. The exchange constant A_{ex} for the investigated materials were estimated from literature data: $A_{ex}(Tb_{27}Co_{30})$ = 0.62 10^{-11} J/m [26], A_{ex}(Co/Pt) = 1.2 10^{-11} J/m [27] and A_{ex}(Co/Ni) = 0.88 10^{-11} J/m [28, 29]. In a first approximation, we suppose that A_{ex} is unchanged with Tb concentration and magnetic thickness t for Tb_xCo_{100-x} (t) alloy films, since its variation with t is negligible compared to the variation of the other magnetic parameters.

Ferri- and ferro-magnets		t (nm)	M_s (x 10^3 A/m)	K_u (x 10^3 J/m^3)	A_{ex} (x 10^{-11} J/m)	AOS vs TD
Tb_xCo_{100-x} (t)	x = 8	1.5	838	520	0.62	AOS
	x = 10.5	2.5	658	592	0.62	AOS
	x = 12	1.5	537	806	0.62	AOS
	x = 13.5	5	440	935	0.62	AOS
	x = 14.5	6.5	361	921	0.62	AOS
	x = 15	8	838	894	0.62	TD / AOS
	x = 15.5	10	308	893	0.62	TD
	x = 16	20	204	632	0.62	TD
	x = 16.5	3.5	230	725	0.62	AOS
	x = 25	6.5	183	503	0.62	AOS
	x = 27.5	10	298	641	0.62	AOS
	x = 30	20	341	678	0.62	AOS
	x = 30.5	15	360	432	0.62	AOS
$[Co(0.6)/Pt(0.7)]_N$	N = 1	0.6	1438	2650	1.2	AOS
	N = 2	1.2	1609	2472	1.2	AOS
	N = 3	1.8	2194	4162	1.2	TD / AOS
	N = 4	2.4	2217	4141	1.2	TD
$[Co(0.2)/Ni(0.6)]_N$	N = 2	1.6	1100	955	0.88	AOS
	N = 3	2.4	1100	955	0.88	TD / AOS
	N = 4	3.2	1100	955	0.88	TD
	N = 6	4.8	1100	955	0.88	TD

TABLE 3.1: Overview of the magnetic parameters and the response to optical excitation for studied ferrimagnetic alloys and ferromagnetic multilayers for different values of Tb concentration x and magnetic thickness t.

3.4.2 Domain size calculation for ferro- and ferrimagnets

Domain size at room temperature for ferromagnets

We first calculated the evolution of the magnetic domain size D as a function of the total magnetic thickness t at RT for the investigated Co/Pt and Co/Ni multilayers. As shown in figure 3.13(a), four different curves of the domain size D are shown for $[Co/Pt]_N$ multilayers with N ranging from 1 to 4. This is due to the different values of M_s and K_u for each value of N, attributed to the spin polarization of Pt atoms at the interfaces [23]. We define a domain size threshold D_{th} = 50 µm corresponding to the fs laser spot size (FWHM = 50 µm).

Figures 3.13(a) shows that for $[Pt(0.7)/Co(0.6)]_N$ multilayers with N = 1 (t = 0.6 nm) and N = 2 (t = 1.2 nm) which show AO-HDS, D is larger than D_{th}. While for $[Pt(0.7)/Co(0.6)]_N$ multilayers with N > 3 (t > 1.8 nm) which show TD, D is smaller than D_{th}. Moreover, for $[Co(0.2)/Ni(0.6)]_N$ multilayers D is larger than D_{th} only for t < 2.4 nm. Therefore, the observation of AO-HDS for

the investigated ferromagnets corresponds to a domain size at RT larger than the laser spot.

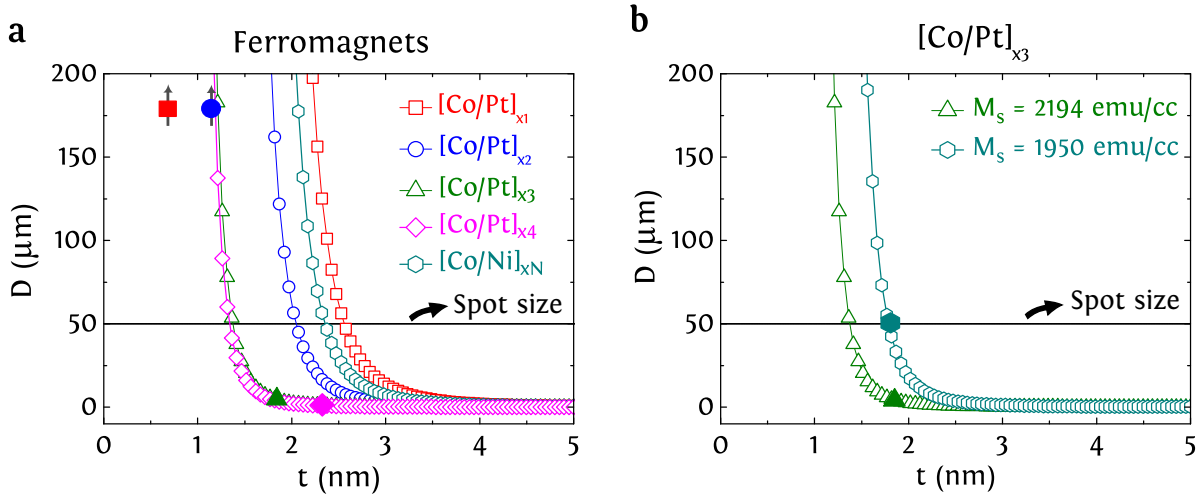

FIGURE 3.13: (a) Estimation of the magnetic domain size D as a function of the magnetic thickness t at RT for the studied ferromagnets, namely $[Pt(0.7\ nm)/\ Co(0.6\ nm)]_N$ and $[Co(0.2\ nm)/\ Ni(0.6\ nm)]_N$ multilayers. (b) Estimation of the domain size D as a function the magnetic thickness t for $[Pt(0.7\ nm)/Co(0.6\ nm)]_3$ multilayers for M_s = 2194 kA/m measured at RT and M_s = 1950 kA/m calculated at T = 400 K. For t = 1.8 nm with M_s = 1950 kA/m, the domain size coincides with laser spot size. The filled symbols indicate the magnetic thickness of the investigated $[Pt(0.7\ nm)/\ Co(0.6\ nm)]_N$ multilayers.

On the other hand, the sample temperature will increase during the AO-HDS process due to the laser-induced heating. Therefore, we should also take into account the evolution of the domain size during the cooling process. In the case of ferromagnets, fs laser beam heats the magnetic system leading to a strong decrease of M_s [30]. Moreover, as can be understood from Eq. (3.15), the effect of the variation of K_u and A_{ex} on the domain size during cooling is low compared to the one of M_s.

Due to the laser-induced decrease of M_s, the size of magnetic domains during cooling for $[Pt(0.7)/Co(0.6)]_1$ and $[Pt(0.7)/Co(0.6)]_2$ is always larger than D at RT, and therefore larger than the spot size D_{th}. For $[Pt(0.7)/Co(0.6)]_3$, let us consider that the sample has cooled down to a temperature of 400 K. We estimate the M_s at T = 400 K using the Curie-Weiss law with a Curie temperature T_c = 650 K, and find M_s = 1950 kA/m. Moreover, the estimated domain size for $[Pt(0.7)/Co(0.6)]_3$ with M_s = 1950 kA/m coincides with the spot size, as depicted in figure 3.13(b). Taking into account the decrease of K_u and A_{ex} at T = 400 K, it can be understood from Eq. (3.15) that the domains are always smaller than the spot size during cooling from 400 K to RT. Moreover, the domains are also smaller than D_{th} during cooling for $[Pt(0.7)/Co(0.6)]_4$. Consequently, we can conclude that a domain size constantly larger than the spot size during cooling is a criterion for the observation of a persistent switching for ferromagnets.

Domain size at room temperature for ferrimagnets

In order to demonstrate that this large domain size criterion is common for ferro- and ferrimagnets, we use the same approach to estimate the domain size during cooling for Tb_xCo_{100-x} (t) alloys for different ranges of Tb concentration x. It was demonstrated by Hansen *et al.* [31] for similar ferrimagnetic alloys that the saturation magnetization shows different behaviors with temperature depending on the Tb concentration. Therefore, three different ranges of x

can be distinguished, namely 8 ‹ x ‹ 13.5, 14.5 ‹ x ‹ 16.5 and 25 ‹ x ‹ 30.5. The evolution of the domain size D at RT is studied for these three concentration ranges as shown in figures 3.14(a), 3.15(a) and 3.14(b), respectively.

One can see from 3.14(a) that for Tb_xCo_{100-x} (t) films showing AO-HDS with x = 8, 10.5, 12, 13.5 and t = 1.5 nm, 2.5 nm, 3.5 nm, 5 nm, respectively, D is larger than D_{th} at RT. Moreover, for 8 ‹ x ‹ 13.5, M_s only decreases for T › RT as shown by Hansen *et al.* [31]. Hence, for this range of concentration, the domain size D during cooling for the samples showing AO-HDS is always larger than D at RT, and thus larger than the spot size. Therefore, the behavior of magnetic domains with temperature in this range of Tb composition is similar to the one of ferromagnets.

Concerning the range of Tb concentration 25 ‹ x ‹ 30.5, for $Tb_{25}Co_{75}$ (6.5 nm), $Tb_{27.5}Co_{72.5}$ (10 nm), $Tb_{30}Co_{70}$ (20 nm) and $Tb_{30.5}Co_{69.5}$ (15 nm) showing AO-HDS, D is larger than D_{th} at RT as shown in Figure 3.14(b). For this range of concentration, Tb_xCo_{100-x} alloys show a compensation temperature (T_{comp}) above RT. Hence, when the temperature decreases from T_c during cooling, M_s decreases with temperature and vanishes at T_{comp} [20, 31]. A further decrease of temperature from T_{comp} towards RT leads to an increase of M_s. However, since the nucleation is a thermally activated process and temperature is close to RT, the nucleation of new domains does not occur and AO-HDS is maintained. Consequently, the magnetic domains for these materials during cooling are larger than those at RT, and thus larger than the spot size.

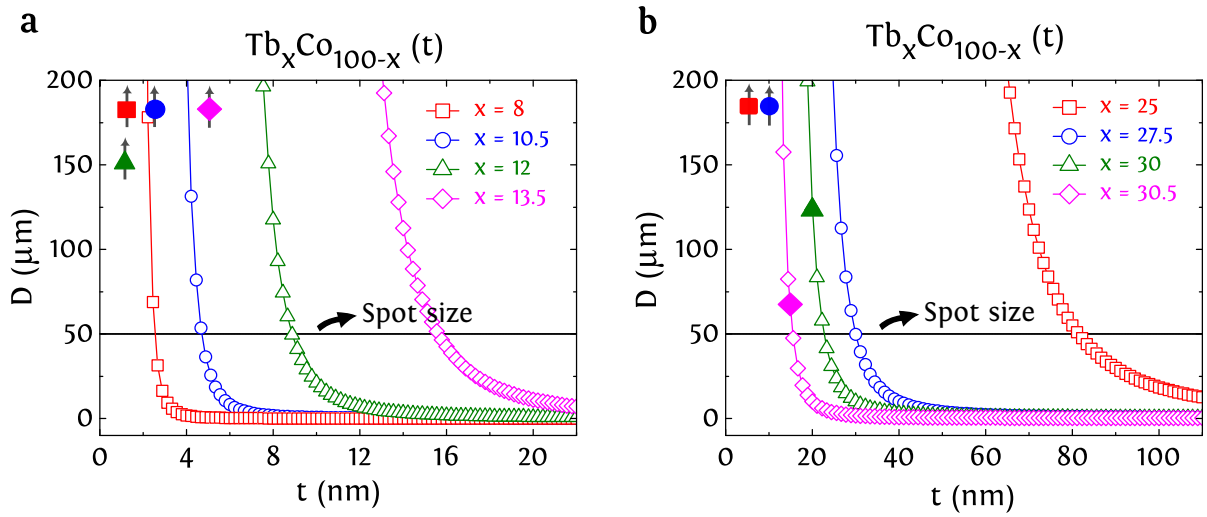

FIGURE 3.14: Estimation of the magnetic domain size D as a function of the magnetic thickness t at room temperature for the studied Tb_xCo_{100-x} alloys, (a) for x ranging from 8 to 13.5. (b) for x ranging from 25 to 30.5. The filled symbols indicate the magnetic thickness of the investigated Tb_xCo_{100-x} alloys.

A more tricky behavior is the one observed for the range of Tb concentration 14.5 ‹ x ‹ 16.5. Indeed, for $Tb_{14.5}Co_{85.5}$ (6.5 nm) and $Tb_{16.5}Co_{83.5}$(3.5 nm) AO-HDS is observed while for $Tb_{15}Co_{85}$ (8 nm), $Tb_{15.5}Co_{84.8}$ (10 nm) and $Tb_{16}Co_{84}$ (20 nm) only TD is obtained. However, figure 3.15(a) shows that the domain size for all these samples at RT is always larger than D_{th}. Nevertheless, M_s increases with temperature (RT ‹ T ‹ 500 K) for this range of concentration [31]. For instance, an increase in the M_s by 150 kA/m is estimated for $Tb_{16}Co_{84}$ at T = 500 K. As shown in figure 3.15(b), the domain size for $Tb_{16}Co_{84}$ (20 nm) with M_s = 380 kA/m is smaller than the spot size. Taking into account the decrease of K_u with temperature, the domains in $Tb_{16}Co_{84}$

(20 nm) are smaller than the spot size at T = 500 K. Hence, for $Tb_{16}Co_{84}$ (20 nm),$Tb_{15}Co_{85}$ (8 nm) and $Tb_{15.5}Co_{84.8}$ (10 nm) showing TD, the domains get smaller than the spot size during cooling thus canceling the initial effect of the helicity. Furthermore, for $Tb_{14.5}Co_{85.5}$ (6.5 nm) and $Tb_{16.5}Co_{83.5}$ (3.5 nm) showing AO-HDS, the domain size during cooling is smaller than the one at RT, but remains larger than the spot size despite an increase in M_S by 150 kA/m. Therefore, the criterion of a domain size larger than the spot size during cooling to achieve AO-HDS applies also for this range of Tb concentration.

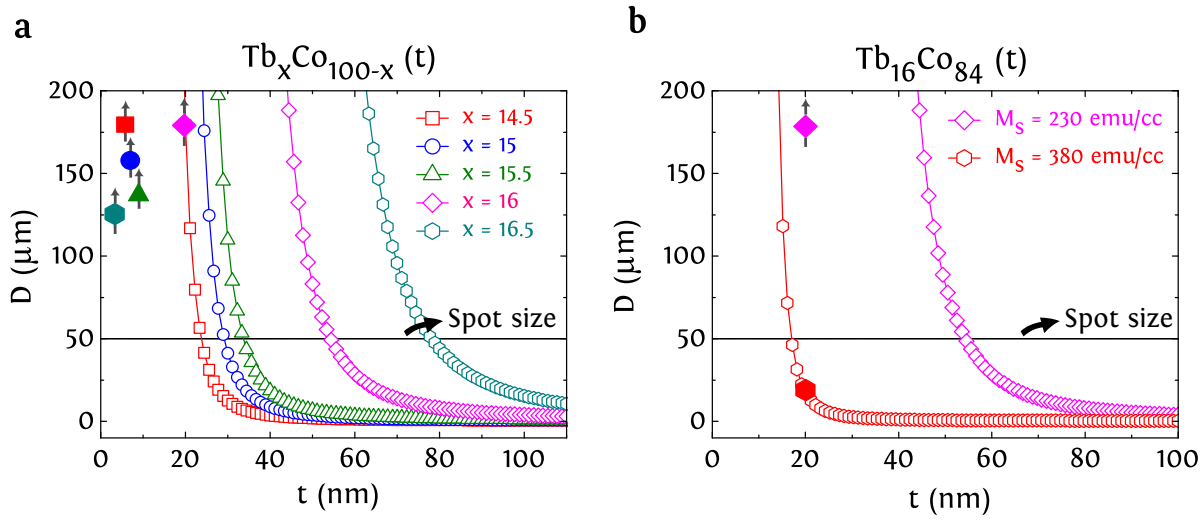

FIGURE 3.15: (a) Estimation of the magnetic domain size D as a function of the magnetic thickness t at RT for the studied Tb_xCo_{100-x} alloys for x ranging from 14.5 to 16.5 (b) Estimation of D as a function of t for $Tb_{16}Co_{84}$ (t) alloys for M_S = 230 kA/m measured at RT and M_S = 380 kA/m estimated at T = 500 K. For t = 20 nm with M_S = 380 kA/m, the domain size is smaller than the laser spot size. The filled symbols indicate the magnetic thickness of the investigated Tb_xCo_{100-x} alloys.

3.4.3 Conclusions

In this experimental investigation, we demonstrated that both ferro- and ferri-magnets with high saturation magnetization (M_S > 700 kA/m) show a persistent AO-HDS if the magnetic thickness is strongly reduced, thus contradicting the magnetic parameters previously proposed in literature to explain the observation of AO-HDS. The main conclusion of this investigation is that the large magnetic domain size is a relevant criterion for the observation of AO-HDS. Indeed, after the circularly polarized laser pulses heat the perpendicularly magnetized sample, the magnetization tends to break into domains during the cooling process. Hence, if the magnetic domain size during cooling is larger than the laser spot size then AO-HDS can be observed, otherwise TD is obtained. More importantly, such large domain size criterion is common for both ferri- and ferro-magnets.

From a phenomenological point of view, we anticipate that more magnetic materials are expected to show AO-HDS, however, the initial effect of the helicity of the optical pulse is hidden by the formation of small magnetic domains during the cooling process. From a technological point of view, this decisive role of magnetic domains allows identifying the optimal conditions for the observation of a persistent AO-HDS, whether by significantly reducing the magnetic thickness or by strongly decreasing the laser spot size in order to fulfill the criteria of a domain size constantly larger than the laser spot size during cooling.

3.5 Magnetic anisotropy dependence of the all-optical switching

As demonstrated in section 3.3, the observation of AO-HDS in ferri- and ferro-magnets depends not only on the saturation magnetization, but on the magnetic domain size which takes into account the competition between the dipolar energy and the domain wall energy. In order to confirm the role of the DW energy, we experimentally investigated the optical response of Co/Pt multilayers in which the magnetic anisotropy is decreased in a controlled way via He^+ ion irradiation.

3.5.1 Tailoring magnetic anisotropy by light-ion irradiation

Irradiation-induced evolution of structural and magnetic properties

In 1998 Chappert *et al.* demonstrated in their pioneering work that He^+ ion irradiation at 15 keV reduces the magnetic anisotropy and coercivity in perpendicularly magnetized Pt/Co/Pt sandwiches and [Pt/Co] multilayers [32]. As mentioned in section 2.1, the irradiation with He^+ ions at energies ranging from 5 to 150 keV does not lead to extended collision cascades, but the structural modifications are confined to the vicinity of the ion path in the metal [33, 34]. Indeed, all He^+ ions stop deep in the substrate and the irradiation involves recoils limited to one or two atomic distances, leading to substitution of atoms : Co -> Co, Pt -> Pt, Co -> Pt and Pt -> Co. Thus, the irradiation process induces intermixing at the interfaces, whereas the initial crystallographic structure and microstructure (grain size) are maintained [32, 34, 35]. In the case of Pt/Co/Pt structure, the irradiation induces two different motions. As shown in figure 3.16, the upper Co interface undergoes short-range mixing resulting in an increase of the roughness, whereas the lower Co interface mostly evolves by longer-range mixing leading to Co-Pt alloy formation [34]. Therefore, the chemical environment of Co atoms is homogenized due to of the neighboring atoms by Pt [36].

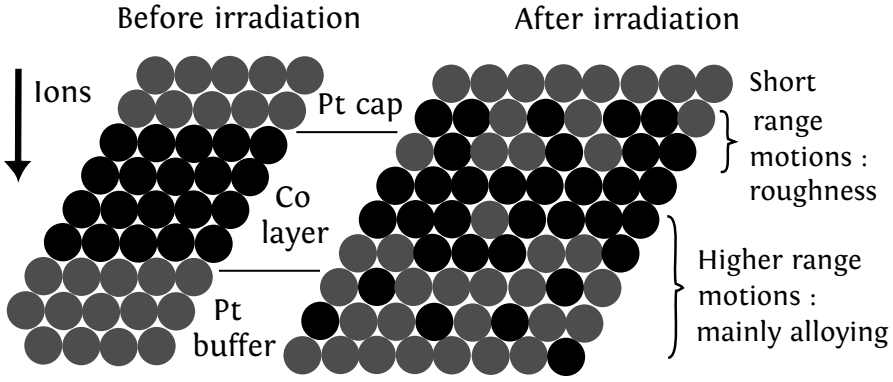

FIGURE 3.16: Qualitative schematic of a sandwich structure before and after irradiation. Co (Pt, respectively) atoms are in black (respectively, gray). Ions move towards the bottom of the figure. Co atoms moving in the ion direction travel more than one interatomic distance and become isolated (Co-Pt alloying), whereas Co atom moving in the opposite direction travel typically only one interatomic distance and contribute to roughness (local thickness fluctuations). Figure adapted from [34].

A model existing in the literature based on simple purely collisional mixing enables the estimation of the mixing rates, their range in Pt and Co, and the asymmetry between the upper and lower interfaces [34, 36, 37]. Indeed, figure 3.17 shows the asymmetric distribution of foreign atoms deduced from simulations for an irradiation dose ID = 8 10^{15} ions/cm^2 at 15 keV [34]. One

can clearly see that the Pt atoms penetrate deeper into the Co layer than the Co atoms do into Pt layers. Indeed, the path of a Co atom in a Pt layer is 0.3 nm, whereas the path of a Pt atom in a Co layer is 0.5 nm [33].

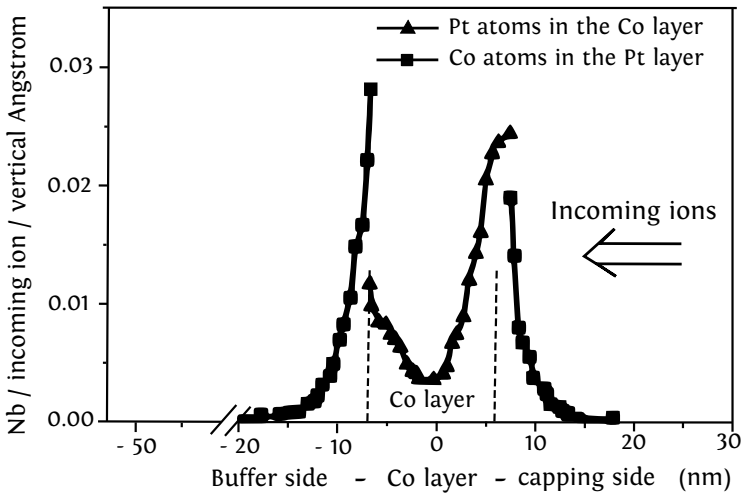

FIGURE 3.17: Distribution of foreign atoms in an irradiated Pt/Co(1.3 nm)/Pt structure, i.e., Co atoms (squares) in the buffer and capping layers and Pt atoms (triangles) in the nominal Co layer. TRIM simulation after 8 10^5 incoming ions. Figure adapted from [34].

The magnetic properties of light-ion irradiated Co/Pt multilayers with PMA have been reported in many experimental investigations [38]. The most important irradiation-induced change in the magnetic properties is the reduction of the magnetic anisotropy. Indeed, the irradiation of Co/Pt multilayers at sufficiently high fluences leads to a reduction of the PMA to the point where the shape anisotropy becomes dominant. Thus, the magnetic easy axis rotates into the film plane [32]. The irradiation also results in a reduction of the coercive field and the Curie temperature [38]. T_c remains very precisely defined, thus indicating that the effects of irradiation are homogeneous [38]. Nevertheless, the saturation magnetization remains constant [39].

To explain this reduction of PMA, the irradiation-induced evolution of the structure should be taken into account. First, since the saturation magnetization remains constant, the shape anisotropy is unchanged. Second, the irradiation leads to an intermixing at the interfaces. Therefore, the incorporation of Pt atoms into the hcp Co layer leads to a decrease of the volume contribution of the MCA from the hcp Co value K_u = 4.5 10^5 J/m^3, to a much lower value for a random fcc CoPt alloy [39]. The interface contribution of the MCA also decreases with the irradiation. Indeed, it is well known that the more abrupt the interfaces are, the higher the interface anisotropy K_s is [32]. Consequently, the irradiation-induced intermixing at the interfaces makes them less abrupt, and leads to a strong decrease of the interface anisotropy. Moreover, another consequence of the intermixing is the increase of the effective magnetic thickness of Co/Pt multilayers.

Studied light-ion irradiated Co/Pt multilayers

We investigated the ferromagnetic Glass/Ta(3 nm)/Pt(3 nm)/[Pt(0.7 nm)/Co(0.6 nm)]$_N$/Pt(3 nm) multilayers, where the number of repeats N = 2 or 4. The top Pt layer prevents sample oxidation. The films show PMA leading to a magnetization perpendicular to the film plane at zero fields. They were subsequently irradiated with He^+ ions at irradiation dose (ID) ranging

from 5 10^{14} He^+/cm^2 to 5 10^{15} He^+/cm^2. The irradiation was performed at RT and at a constant energy of 15 keV. The change in the magnetic properties as a function of the irradiation dose was measured using SQUID magnetometry.

For non-irradiated films, the saturation magnetization M_s = 1619 kA/m (resp. 1982 kA/m) and a first order anisotropy constant K_u = 2.41 10^6 J/m^3 (resp. 3.15 10^6 J/m^3) for N = 2 (resp. 4) were obtained. As mentioned in section 3.2.1, the increase of M_s with the number of repeats is attributed to the spin polarization of Pt atoms by the adjacent Co layers [23].

Concerning the irradiated $[Co/Pt]_2$ films, figure 3.18 shows that the anisotropy constant K_u decreases strongly for high ID down to K_u = 1.25 10^6 J/m^3 for ID = 5 10^{15} He^+/cm^2, in agreement with previous studies on Co/Pt multilayers [39, 40]. However, M_s slightly increases for ID = 8 10^{14} He^+/cm^2 up to 1741 kA/m, then decreases down to 1400 kA/m for higher ID. Moreover, the coercive field H_c at RT decreases from 4 mT measured for the non-irradiated films to H_c = 2 mT for ID = 5 10^{15} He^+/cm^2.

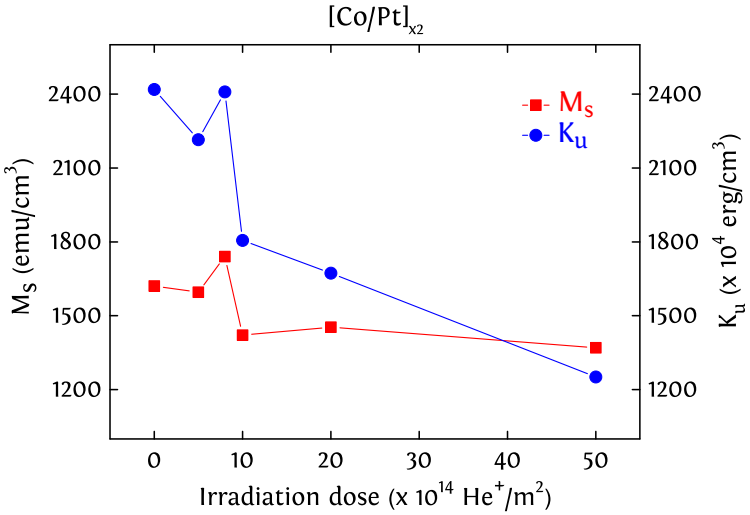

FIGURE 3.18: M_s and K_u dependence on the irradiation dose ID for $[Co(0.6\ nm)/Pt(0.7\ nm)]_2$ multilayers.

A similar trend is measured for irradiated $[Co/Pt]_4$ films. As depicted in figure 3.19, K_u strongly decreases down to 2.17 10^6 J/m^3 at ID = 10^{15} He^+/cm^2, while M_s slightly decreases down to 1710 kA/m. However, the measured coercive field is H_c = 7.6 mT and remains unchanged up to ID = 10^{15} He^+/cm^2. For $[Co/Pt]_4$ multilayers irradiated at ID > 10^{15} He^+/cm^2, the magnetization easy axis is rotated towards the in-plane orientation.

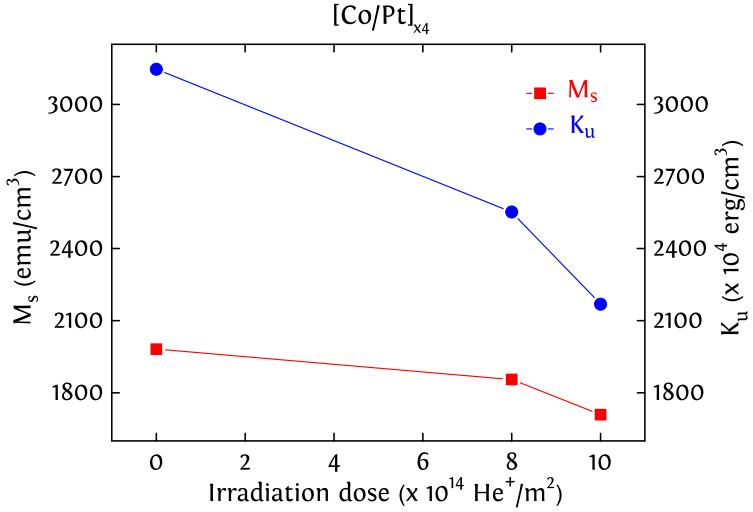

FIGURE 3.19: M_s and K_u dependence on the irradiation dose ID for [Co(0.6nm)/Pt(0.7nm)]$_4$ multilayers.

3.5.2 All-optical control of magnetization in irradiated Co/Pt multilayers

We now continue to measure the optical response to laser beam excitation of the irradiated Co/Pt multilayers using the analog sweeping beam experiments to ferri- and ferro-magnets introduced in section 3.2.2. Prior to being optically excited, the irradiated films are saturated with an external magnetic field. During the optical excitation, no magnetic field is applied and the 35-fs laser beam is swept from right to left for both circular polarizations with a low sweeping speed of approximately 10 µm/s.

[Co/Pt]$_2$ multilayers

First, we investigate the optical response of irradiated [Co/Pt]$_2$ multilayers at ID ranging from 5 10^{14} He^+/cm^2 to 5 10^{15} He^+/cm^2. Figure 3.20 shows that the non-irradiated (ID = 0) [Co/Pt]$_2$ multilayers exhibit AO-HDS, in agreement with the results presented in section 3.2.2. By increasing ID from 5 10^{14} He^+/cm^2 to 2 10^{15} He^+/cm^2, the effect of the helicity following the excitation in the irradiated [Co/Pt]$_2$ multilayers disappears gradually. Indeed, as shown in figure 3.20, multiple domains start appearing in the scanned region and are stretched towards to the center of the beam spot. This behavior is attributed to thermal-induced domain wall motion [41, 42]. For the maximum ID = 5 10^{15} He^+/cm^2, thermal demagnetization is obtained and the multiple domains in the scanned region get smaller.

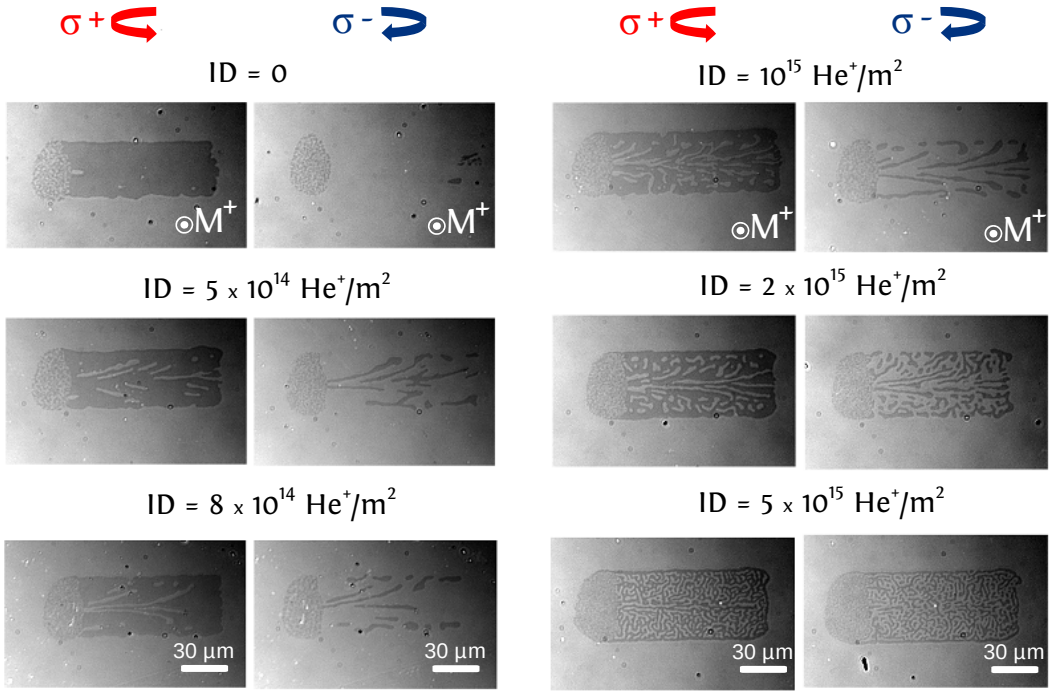

FIGURE 3.20: Optical response for [Co(0.6 nm)/Pt(0.7 nm)]$_2$ multilayers as a function of the irradiation dose ID. A gradual transition from AO-HDS to pure TD is obtained by increasing ID up to 5 10^{15} He^+/m^2. The measurements were performed using a constant laser power of 0.75 mW.

Since the increase of ID leads to strong decrease of K_u compared to the one of M_s, these findings indicates that the magnetic anisotropy and thus the DW formation energy plays undoubtedly an important role in the AO-HDS process. Moreover, the reduction of K_u leads to an increase of the magnetic size D, according to equation (3.15). In a first approximation, we suppose that the A_{ex} and M_s change only weakly with the irradiation dose, in agreement with previous studies on Co/Pt multilayers [34]. Therefore, we use the values of A_{ex} and M_s for non-irradiated samples in order to estimate the domain size. For instance, the measured K_u for $[Co/Pt]_2$ irradiation at ID = 5 10^{15} He^+/cm^2 is 1.25 10^6 J/m^3. As depicted in figure 3.21, the domain size D for $[Co/Pt]_2$ with K_u = 1.25 10^6 J/m^3 coincides with the laser spot for a magnetic thickness t = 1.33 nm. Moreover, the magnetic thickness of $[Co/Pt]_2$ at ID = 5 10^{15} He^+/cm^2 slightly increases due to the intermixing at the interfaces, since the recoils of Co atoms are limited to one or two atomic distances. Therefore, taking into account this irradiation-induced increase of t, the domain size of $[Co/Pt]_2$ at ID = 5 10^{15} He^+/cm^2 is smaller than the spot size.

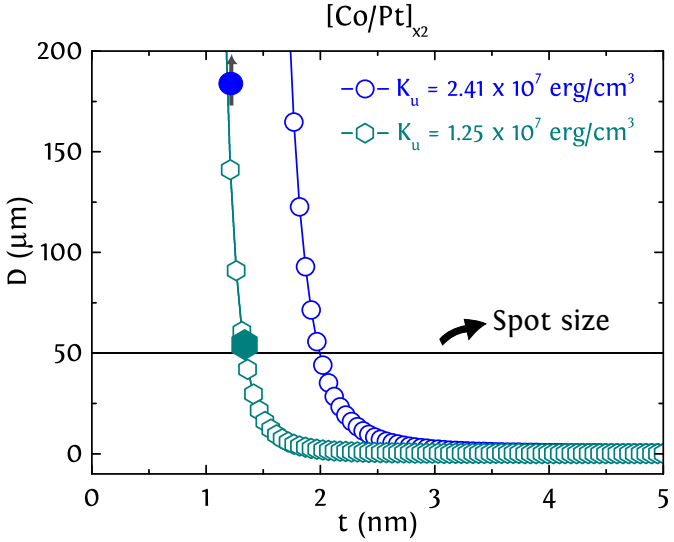

FIGURE 3.21: Estimation of D as a function of the Co layer thickness t for $[Co/Pt]_2$ multilayers for K_u = 2.41 10^6 J/m^3 measured for the non-irradiated sample and K_u = 1.25 10^6 J/m^3 measured for a sample irradiation with ID = 5 10^{15} He$^+$/cm^2. For t = 1.33 nm with K_u = 1.25 10^6 J/m^3, the domain size is smaller than the laser spot size. D is calculated with M_s = 1619 kA/m measured for the non-irradiated sample and A_{ex} = 1.2 10^{-11} J/m estimated from literature [27]. The filled symbols indicate the magnetic thickness of the investigated [Co(0.6 nm)/Pt(0.7 nm)]$_2$ multilayers.

To conclude, this experimental investigation on irradiated $[Co/Pt]_2$ shows that the AO-HDS ability is lost by gradually increasing the irradiation dose, corresponding to a gradual decrease of the magnetic anisotropy and thus the magnetic domain size. Hence, because of the strong decrease of K_u, a pure TD is obtained with the maximum ID leading to magnetic domains smaller than the spot size. These findings confirm the large domain size criterion for the observation of AO-HDS demonstrated in section 3.3, and highlight the crucial role of the DW energy in the AO-HDS process.

$[Co/Pt]_4$ multilayers

Finally, we verify the thermal demagnetization of irradiated $[Co/Pt]_4$ multilayers. Figure 3.22 shows that the non-irradiated $[Co/Pt]_4$ multilayers show TD, which is in agreement with the results presented in section 3.2.2. Similarly to $[Pt/Co]_2$, irradiating the $[Co/Pt]_4$ leads to a reduction of K_u and thus a decrease of the domain size. Since the domain size D for non-irradiated $[Co/Pt]_4$ is smaller than the spot size, D for the irradiated $[Co/Pt]_4$ is also smaller than the spot size. Therefore, only TD is expected for the irradiated $[Co/Pt]_4$ multilayers according to the domain size criterion. As expected, figure 3.22 shows that $[Co/Pt]_4$ multilayers irradiated at ID = 8 10^{14} and 10^{15} He$^+$/cm^2 exhibit pure TD, in agreement with the domain size criterion. Furthermore, the multiple domains in the scanned area of irradiated $[Co/Pt]_4$ become too small to be optically resolved, confirming the decrease of the domain size with the irradiation.

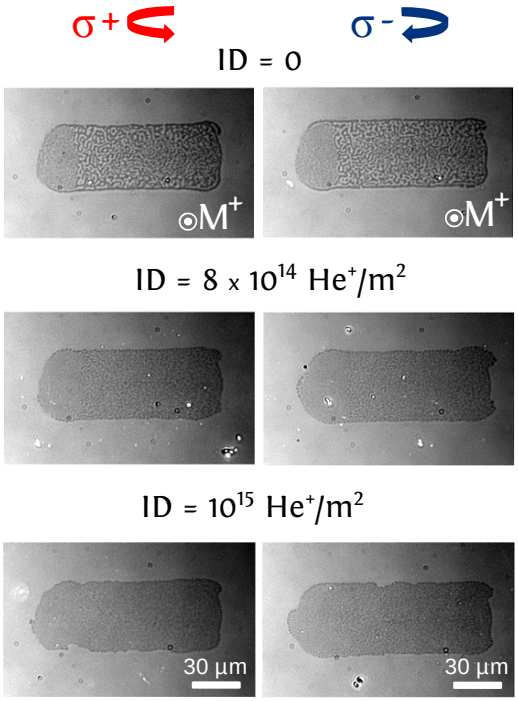

FIGURE 3.22: Optical response for [Co(0.6 nm)/Pt(0.7 nm)]$_4$ multilayers as a function of the irradiation dose ID. A pure TD is obtained and the domain size in the laser excited decreases by increasing ID up to 10^{15} He^+/m^2. The measurements were performed using a constant laser power of 2.5 mW.

3.6 Summary

In this third Chapter, we experimentally demonstrated that both ferro- and ferri-magnetic materials with high saturation magnetization show AO-HDS if the magnetic thickness is strongly reduced, thus contradicting the magnetic parameters previously proposed in literature to explain the observation of AO-HDS. By taking into account the demagnetizing energy and the domain wall energy, we are able to define a criterion to predict whether AO-HDS or thermal demagnetization will be observed. This criterion for the observation of AO-HDS is that the equilibrium size of magnetic domains forming during the cooling process should be constantly larger than the laser spot size. More importantly, this large domain size criterion is common for both ferri- and ferro-magnets.

From a phenomenological point of view, we anticipate that more magnetic materials are expected to show AO-HDS, however, the initial effect of the helicity of the optical pulses is hidden by the formation of small magnetic domains during the cooling process. From a technological point of view, the decisive role of magnetic domains allows identifying the optimal conditions for the observation of a persistent AO-HDS, whether by significantly reducing the magnetic thickness or by strongly decreasing the laser spot size in order to fulfill the large domain size criterion.

We have also verified the influence of the domain wall energy on the observation of AO-HDS by investigating the optical response of light-ion irradiated Co/Pt multilayers. Indeed, irradiating Co/Pt multilayers with He^+ ions leads to a strong decrease of the magnetic anisotropy, while the saturation magnetization changes only weakly. Thus, the domain energy decreases

strongly due to the irradiation, which leads to a decrease of the magnetic domain size. We demonstrated that the AO-HDS ability of Co/Pt multilayers is lost by gradually increasing the irradiation dose, which highlights the crucial role of the DW in the all-optical switching process. This investigation also confirms the large domain size criterion for the observation of AO-HDS.

References

[1] A. Hassdenteufel, J. Schmidt, C. Schubert, B. Hebler, M. Helm, M. Albrecht, and R. Bratschitsch, Low remanence criterion for helicity-dependent all-optical magnetic switching in ferrimagnets and heterostructures *Phys. Rev. B* **91**, 104431 (2015).

[2] C. Schubert, A. Hassdenteufel, P. Matthes, J. Schmidt, M. Helm, R. Bratschitsch, and M. Albrecht, All-optical helicity dependent magnetic switching in an artificial zero moment magnet *Appl. Phys. Lett.* **104**, 082406 (2014).

[3] B. Hebler, A. Hassdenteufel, P. Reinhardt, H. Karl, and M. Albrecht, Ferrimagnetic Tb–Fe alloy thin films: Composition and thickness dependence of magnetic properties and all-optical switching *Front. Mater.* **3**, 8 (2016).

[4] C. H. Lambert, S. Mangin, B. S. D. C. S. Varaprasad, Y. K. Takahashi, M. Hehn, M. Cinchetti, G. Malinowski, K. Hono, Y. Fainman, M. Aeschlimann, and E. E. Fullerton, All-optical control of ferromagnetic thin films and nanostructures *Science* **345**, 1337–1340 (2014).

[5] G. W. Crabtree, Demagnetizing fields in the de Haas-van Alphen effect *Phys. Rev. B* **16**, 1117 (1977).

[6] Etienne du Trémolet de Lacheisserie. Magnétisme, I - Fondements. EDP Sciences, 2000.

[7] C. T. Chen, Y. U. Idzerda, H.-J. Lin, N. V. Smith, G. Meigs, E. Chaban, G. H. Ho, E. Pellegrin, and F. Sette, Experimental confirmation of the X-ray magnetic circular dichroism sum rules for iron and cobalt *Phys. Rev. Lett.* **75**, 152 (1995).

[8] L. Néel, Anisotropie magnétique superficielle et surstructures d'orientation *J. Phys. Radium* **15**, 225–239 (1954).

[9] U. Gradmann, Magnetic surface anisotropies *J. Magn. Magn. Mater.* **54-57**, 733 (1986).

[10] K. Yakushiji, S. Yuasa, T. Nagahama, A. Fukushima, H. Kubota, T. Katayama, and K. Ando, Spin-transfer switching and thermal stability in an FePt/Au/FePt nanopillar prepared by alternate monatomic Layer deposition *Appl. Phys. Exp.* **1**, 041302 (2008).

[11] A. Holz, and A. Hubert, Wandstrukturen in dunnen magnetischen Schichten *Z. Angew. Phys.* **26**, 145 (1969).

[12] A. Hubert, and R. Schafer, Magnetic domains: the analysis of magnetic microstructure *Springer*, 1998.

[13] S. Goolaup, M. Ramu, C. Murapaka, and W. S. Lew, Transverse domain wall profile for spin logic applications *Sci. Rep.* **5**, 9603 (2015).

[14] V. D. Nguyen, O. Fruchart, S. Pizzini, J. Vogel, J.-C. Toussaint, and N. Rougemaille, Third type of domain wall in soft magnetic nanostrips *Sci. Rep.* **5**, 12417 (2015).

[15] S. Middelhoek, Domain walls in thin Ni–Fe films *J. Appl. Phys.* **34**, 1054 (1963).

[16] C. Kooy, and U. Enz, Experimental and theoretical study of the domain configuration in thin layers of $BaFe_{12}O_{19}$ *Philips Res. Rep.* **15**, 7 (1960).

[17] O. Hellwig, A. Berger, J.B. Kortright, and E. E. Fullerton, Domain structure and magnetization reversal of antiferromagnetically coupled perpendicular anisotropy films *J. Magn. Magn. Mater.* **319** (1-2), 13-55 (2007).

[18] A. Kirilyuk, J. Ferré, V. Grolier, J. P. Jamet, and D. Renard, Magnetization reversal in ultrathin ferromagnetic films with perpendicular anisotropy *J. Magn. Magn. Mater.* **171**, 45-63, (1997).

[19] P. J. Metaxas, J. P. Jamet, A. Mougin, M. Cormier, J. Ferré, V. Baltz, B. Rodmacq, B. Dieny, and R. L. Stamps, Creep and flow regimes of magnetic domain-wall motion in ultrathin Pt/Co/Pt films with perpendicular anisotropy *Phys. Rev. Lett.* **99**, 21708 (2007).

[20] S. Alebrand, M. Gottwald, M. Hehn, D. Steil, M. Cinchetti, D. Lacour, E. E. Fullerton, M. Aeschlimann, and S. Mangin, Light-induced magnetization reversal of high-anisotropy TbCo alloy films *Appl. Phys. Lett.* **101**, 162408 (2012).

[21] R. Malmhall, and T. Chen, Thickness dependence of magnetic hysteretic properties of rf sputtered amorphous Tb–Fe alloy thin films *J. Appl. Phys.* **53**, 7843 (1982).

[22] D. H. Shen, Y. Mizokawa, H. Iwasaki, D. F. Shen, T. Numata, and S. Nakamura, Comparative study of optical and magneto-optical properties of $GdFe_2$ and $GdCo_2$ *Jpn. J. Appl. Phys.* **20**, 757-760 (1982).

[23] J. W. Knepper, and F. Y. Yang, Oscillatory interlayer coupling in Co/Pt multilayers with perpendicular anisotropy *Phys. Rev. B* **71**, 224403 (2005).

[24] S. Mangin, M. Gottwald, C.-H. Lambert, D. Steil, V. Uhlir, L. Pang, M. Hehn, S. Alebrand, M. Cinchetti, G. Malinowski, Y. Fainman, M. Aeschlimann, and E. E. Fullerton, Engineered materials for all-optical helicity-dependent magnetic switching *Nat. Mater.* **13**, 286–292 (2014).

[25] A. Hassdenteufel, C. Schubert, J. Schmidt, P. Richter, D. R. T. Zahn, G. Salvan, M. Helm, R. Bratschitsch, and M. Albrecht, Dependence of all-optical magnetic switching on the sublattice magnetization orientation in Tb-Fe thin films *Appl. Phys. Lett.* **105**, 112403 (2014).

[26] M. Gottwald, Nouveaux systèmes mods à aimantation perpendiculaire pour l'étude des effets de transfert de spin, Ph.D. Thesis, Université Henri Poincaré (2011).

[27] C. Eyrich, W. Huttema, M. Arora, E. Montoya, F. Rashidi, C. Burrowes, B. Kardasz, E. Girt, B. Heinrich, O. N. Mryasov, M. From, and O. Karis, Exchange stiffness in thin film Co alloys *J. Appl. Phys.* **111**, 07C919 (2012).

[28] P. E. Tannenwald, Exchange integral in Cobalt from spin-wave resonance *Phys. Rev.* **121**, 715 (1961).

[29] D. H. Martin, Magnetism in Solids (Iliffe Books, London, 1967), p. 67.

[30] D. J. Dunlop, and O. Ozdemir, Rock Magnetism, Cambridge Studies in Magnetism (Cambridge University Press, Cambridge, UK, 1997), p. 52.

[31] P. Hansen, C. Clausen, G. Much, M. Rosenkranz, and K. Witter, Magnetic and magneto-optical properties of rare-earth transition-metal alloys containing Gd, Tb, Fe, Co *J. Appl. Phys.* **66**, 756 (1989).

[32] C. Chappert, H. Bernas, J. Ferré, V. Kottler, J. P. Jamet, Y. Chen, E. Cambril, T. Devolder, F. Rousseaux, V. Mathet, and H. Launois, The emergence of spin electronics in data storage *Science* **280**, 1919 (1998).

[33] J. Fassbender, D. Ravelosona, and Y. Samson, Tailor magnetism by ligh-ion irradiation *J. Phys. D: Appl. Phys.* **37**, 16 (2004).

[34] T. Devolder, Light ion irradiation of Co/Pt systems: Structural origin of the decrease in magnetic anisotropy *Phys. Rev. B* **62**, 9 (2000).

[35] G. S. Chang, Y. P. Lee, J. Y. Rhee, J. Lee, K. Jeong, and C. N. Whang, Realization of a large magnetic moment in the ferromagnetic CoPt bulk phase *Phys. Rev. Lett.* **87**, 067208 (2001).

[36] T. Devolder, S. Pizzini, J. Vogel, H. Bernas, C. Chappert, V. Mathet, and M. Borowski, X-ray absorption analysis of sputter-grown Co/Pt stackings before and after helium irradiation *Eur. Phys. J. B* **22**, 193-201 (2001).

[37] C. T. Rettner, S. Anders, J. E. E. Baglin, T. Thomson, and B. D. Terris, Characterization of the magnetic modification of Co/Pt multilayer films by He+, Ar+, and Ga+ ion irradiation *Appl. Phys. Lett.* **80**, 279 (2002).

[38] J. Ferré, C. Chappert, H. Bernas, J.-P. Jamet, P. Meyer, O. Kaitanov, S. Lemerle, V. Mathet, F. Rousseaux, and H. Launois, Irradiation induced effects on magnetic properties of Pt/Co/Pt ultrathin films *J. Magn. Magn. Mater.* **198–199**, 191 (1999).

[39] T. Devolder, C. Chappert, Y. Chen, E. Cambril, H. Launois, H. Bernas, J. Ferré, and J. P. Jamet, Patterning of planar magnetic nanostructures by ion irradiation *J. Vac. Sci. Technol. B* **17**, 3177 (1999).

[40] T Devolder, H Bernas, D Ravelosona, C Chappert, S Pizzini, J Vogel, J Ferré, J.-P Jamet, Y Chen, V Mathet, Beam-induced magnetic property modifications: basics, nanostructure fabrication and potential applications *Nucl. Instrum. Methods B*, **175**, 375-381 (2001).

[41] Y. Mimura, N. Imamura, and T. Kobayashi, Thermomagnetic Writing on Gd–Fe and Gd–Fe–Y Amorphous Films *Jpn. J. Appl. Phys.* **17**, 1365 (1978).

[42] A. Hassdenteufel, B. Hebler, C. Schubert, A. Liebig, M. Teich, M. Helm, M. Aeschlimann, M. Albrecht, and R. Bratschitsch, Thermally assisted all-optical helicity dependent magnetic switching in amorphous $Fe_{100-x}Tb_x$ alloy films *Adv. Mater.* **25**, 3122 (2013).

Chapter 4

Distinction between two types of all-optical switching mechanisms via magneto-transport measurements

4.1 Introduction

In the fourth chapter of this thesis, we present an experimental investigation of the all-optical switching in Hall cross devices via the anomalous Hall effect. This novel approach provides new insights in the underlying physics of the all-optical switching, and on the other hand helps paving the way for a new field combining optics and spintronics called opto-spintronics [1]. First, we report in section 4.2 an electrical characterization of all-optical helicity-dependent switching (AO-HDS) of ferromagnetic Pt/Co/Pt Hall crosses subject to multiple-pulse excitations. Hence, this all-electrical probing of magnetization enables a statistical quantification of the switching ratio for different laser parameters, such as the helicity, the laser power and the sweeping speed. Second, a first demonstration of the all-optical control of magnetization in ferromagnetic CoFeB Hall crosses is shown in section 4.3, whereas an electrical investigation of AO-HDS in ferrimagnetic $Tb_{27}Co_{73}$ Hall crosses is shown in section 4.4. Finally, we present in section 4.5 a time-dependent electrical investigation of the all-optical switching in ferrimagnetic and ferromagnetic Hall crosses, enabling to probe the switching on different timescales. Such an approach enables the distinction between two types of all-optical switching mechanisms; a "single pulse" switching for ferrimagnetic GdFeCo alloys as previously reported, and a "two regimes" switching process for both ferrimagnetic TbCo alloys and ferromagnetic Co/Pt multilayers which consists of a helicity-independent multiple-domain formation followed by a helicity-dependent remagnetization. The microscopic origin of such two regimes multiple-pulse helicity-dependent switching mechanism is then discussed.

4.2 Electrical characterization of AO-HDS in ferromagnetic Pt/Co/Pt Hall crosses

4.2.1 Introduction

The discovery of AO-HDS by Lambert *et al.* [2] in pure ferromagnetic materials, such as Co/Pt and Co/Ni multilayers as well as granular media, raised a number of questions about its underlying physics. Despite the fact that the microscopic origin of all-optical switching in ferromagnets is still under debate [2, 3], these experiments triggered great interest since all-optical switching has now a large potential for novel magnetic data storage. Moreover, the field of opto-spintronics makes use of the fact that both photons and electrons can carry a spin angular momentum, and thus is promising for both fundamental research such as the investigation of laser-induced magnetization dynamics [4, 5, 6] and applications [7, 8]. For instance,

AO-HDS could be implemented in spintronic devices such as spin-transfer torque (STT) based memories [9, 10] or heat-assisted magnetic recording (HAMR) [11, 12]. The main advantages of such integration are the speed and energy efficiency, since pulses are used instead of magnetic fields in today's technology.

In this context, we probe AO-HDS with pure magneto-transport read-out in ferromagnetic Pt/Co/Pt based Hall crosses. The helicity dependence plays a major role in this implementation, since it enables an all-optical writing and erasing of data without applying any external magnetic field. Furthermore, this novel method to probe the AO-HDS in Hall crosses via the anomalous Hall effect [13, 14] enables a statistical quantification of the switching ratio for different laser parameters, thus giving new insights into the rich physics underlying the all-optical switching. It also enables to investigate the switching on different timescales ranging from 1 µs to a few seconds, thus bridging the gap between the ultrafast [4] and the quasi-static optical methods [2, 15] used to probe magnetization. In sections 4.2, 4.3 and 4.4, the temporal resolution of the electrical measurements is 150 ms, whereas it equals 1 µs in section 4.5.

Anomalous Hall effect

The Hall resistivity in magnetic materials does not increase linearly with the applied field, and includes an additional contribution known as the anomalous Hall effect. Shown in figure 4.1 is a simple magnetic configuration with an applied magnetic field H and a magnetization M. We define B the magnetic flux through the sample due to M and H. The Hall resistivity can be expressed as follows:

$$\rho_{xy} = R_N \vec{B}.\hat{e}_z + R_{AHE} \vec{M}.\hat{e}_z \tag{4.1}$$

R_N is the normal Hall coefficient, whereas R_{AHE} is the anomalous Hall coefficient.

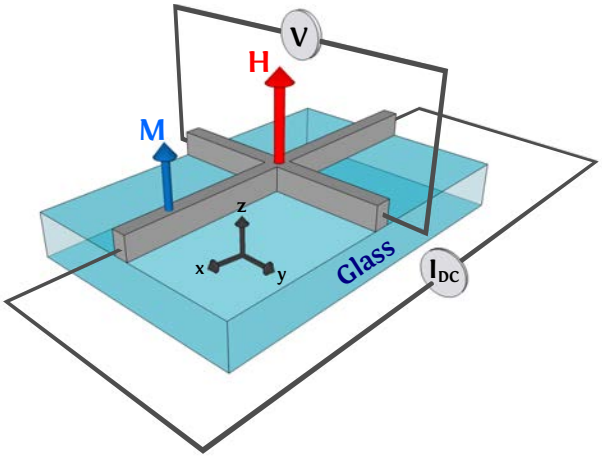

FIGURE 4.1: Geometric configuration of the Hall voltage measurement under an external applied field H. A DC current is injected along the x direction while the Hall voltage is measured along the y direction.

For the anomalous Hall coefficient, two contributions are discussed namely the skew scattering [13] and the side-jump mechanisms [14]. Hence, R_{AHE} can be expressed as a function of the resistivity ρ as follows:

$$R_{AHE} = A\rho + C\rho^2 \tag{4.2}$$

"*A*" is attributed to the skew scattering [13] whereas "*C*" is attributed to the side-jump mechanisms [14]. Since the anomalous Hall effect results from the spin-dependent scattering of conduction electrons and is enhanced with a large spin-orbit coupling [16], it is mostly much larger than the normal Hall effect.

Outline of the experiments

The investigated ferromagnetic sample is a thin film of Glass/Ta(3 nm)/Pt(3.7 nm)/Co(0.6 nm)/Pt(3.7 nm) grown by DC magnetron sputtering. The film has a saturation magnetization M_s = 1483 kA/m and with a first order anisotropy constant K_1 = 2.65 10^6 J/m^3, leading to a perpendicular magnetization in remanence with a RT coercive field H_c = 8 mT. The sample is patterned into a 5-µm-wide Hall cross using optical lithography, as shown in figure 4.2. A DC current is injected along the *x* axis, and the Hall voltage is measured along the *y* direction in order to measure the *z*-component of magnetization within the Hall cross. During the experiments, no external magnetic field is applied. Hence, the measured Hall voltage V_{AHE} can be expressed as follows:

$$V_{AHE} = \frac{\rho_{xy} I}{t} \tag{4.3}$$

with

$$\rho_{xy} = R_{AHE} \vec{M}.\hat{e}_z \tag{4.4}$$

R_{AHE} is the anomalous Hall coefficient, *t* the magnetic thickness and ρ_{xy} is the Hall resistivity. In our measurement, a current intensity *I* = 0.75 mA is applied and the typical value of the anomalous Hall voltage is V_{Hall} = 0.18 mV. Moreover, the corresponding current density is 30 MA/m^2. Such current density is negligible compared to the usual density (of the order of 0.3 TA/m^2) used to perform magnetization switching by current-induced spin-orbit torque (SOT) [17, 18]. Furthermore, the investigated Pt/Co/Pt structure is symmetric. Therefore, a direct current-induced switching is improbable.

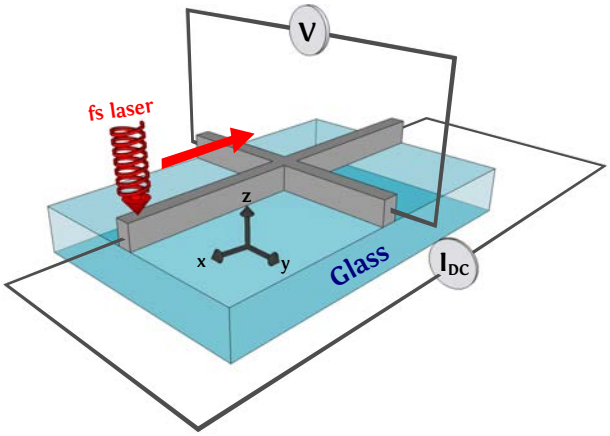

FIGURE 4.2: Sweeping beam measurement schematic: in a perpendicularly magnetized Hall cross (*z* axis), a DC current is injected along the *x* direction while the anomalous Hall voltage is measured along the *y* direction. The fs laser beam perpendicular to the film plane is swept along the *x* axis to perform the sweeping beam measurement, with sweeping speeds ranging from 40 µm/s to 2500 µm/s.

To investigate the magnetization switching within the Hall cross, we performed two different approaches using multiple-pulse excitation. In the first approach called "sweeping beam measurement", the fs laser beam is swept over the length of the magnetic wire along the *x* axis across the Hall cross as shown in figure 4.2. In the second approach called "static beam measurement", the laser spot is maintained at a fixed position on the Hall cross, and is whether "off-centered" as shown in figure 4.3, or "centered" as illustrated in figure 4.4. In the case of an off-centered laser spot, the center of the beam is about 40 µm from the center of the Hall cross to make the AOS rim overlap with the center of the Hall cross as shown in figure 4.3. In the case of a centered laser spot (see figure 4.4), the center of the beam overlaps with the center of the Hall cross.

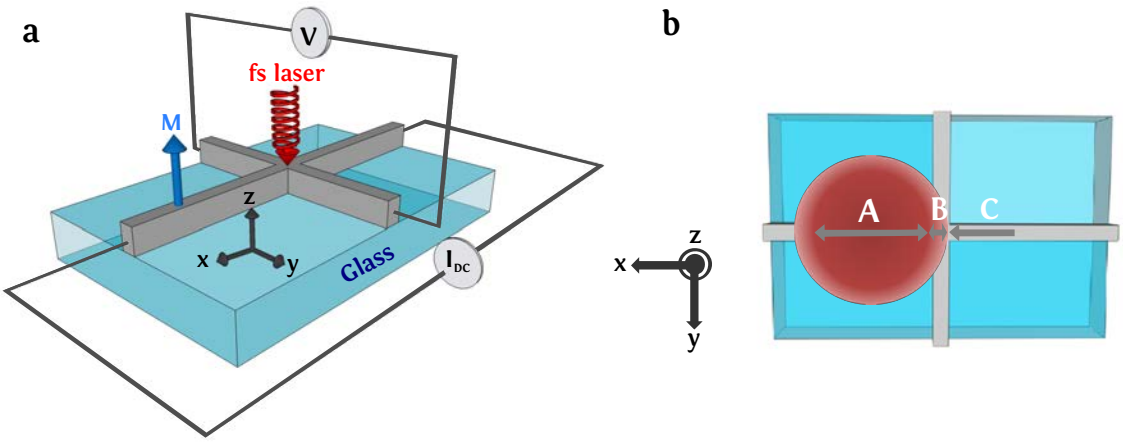

FIGURE 4.3: Experimental set-up schematic of the static beam measurement with an off-centered beam in a perpendicularly magnetized Hall cross (*z* axis). A DC current is injected along the *x* direction while the anomalous Hall voltage is measured along the *y* direction. The laser spot is shined on the *x* axis at a fixed position about 40 µm from the center of the Hall cross. (b) Schematic representation of the different areas of the laser spot. "*A*" where multiple domains are obtained, "*B*" is the AOS ring where AOS is obtained, and "*C*" is the area where no change of magnetization is induced. For the static beam measurement with an off-centered laser spot, the AOS rim overlaps with the center of the Hall cross.

For both approaches, the sample is saturated before illumination under an external magnetic field applied along the *z* axis in order to measure the Hall voltage for the two saturated magnetic states $\vec{M}_s.\hat{e}_z$ and $-\vec{M}_s.\hat{e}_z$. No magnetic is applied during illumination, therefore the continuously measured Hall voltage reflects the static magnetic state of the Hall cross. A decrease of the Hall voltage might also be due to a heat-induced change in the Hall resistivity via the temperature increase. Nevertheless, by adding an external magnetic field to saturate the magnetization within the laser-heated Hall cross, the anomalous Hall voltage does not change compared to the one of the unheated Hall cross. Hence, with the range of power used in these experiments, a significant change of the Hall resistivity is excluded.

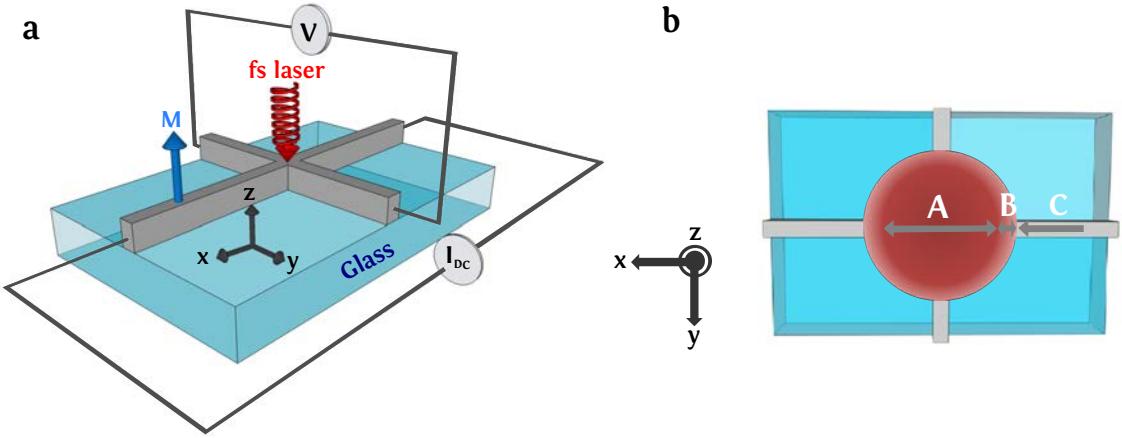

FIGURE 4.4: (a) Experimental set-up schematic of the static beam measurement with a centered beam in a perpendicularly magnetized Hall cross (z axis). The laser spot is shined on the *x* axis at a fixed position and in the center of the Hall cross. (b) Schematic representation of the different areas of the laser spot. For the static beam measurement with a centered laser spot, *"A"* where multiple domains are obtained overlaps with the center of the Hall cross.

4.2.2 Sweeping beam measurement

Circular polarization

We have firstly investigated the sweeping beam approach in Pt/Co/Pt based Hall cross for the four possible configurations of circular helicity and initial magnetization saturation. Hence, shown in figure 4.5 are the sweeping measurements for a sweeping speed of 40 µm/s and a power of 0.95 mW. The laser beam is swept from position -100 µm/s to 100 µm/s, while the zero position corresponds to the center of the Hall cross. Figure 4.5(a) shows that independently of the initial magnetization saturation, sweeping with left-circularly polarized beam over the Hall cross (x › 40 µm) switches magnetization to the up state ($\overline{V_{Hall}}$ = 1). Moreover, magnetization switching to down state ($\overline{V_{Hall}}$ = -1) is obtained by sweeping right-circularly polarized beam over the Hall cross as shown in figure 4.5(b), thus demonstrating the helicity-dependent switching of the investigated Hall cross.

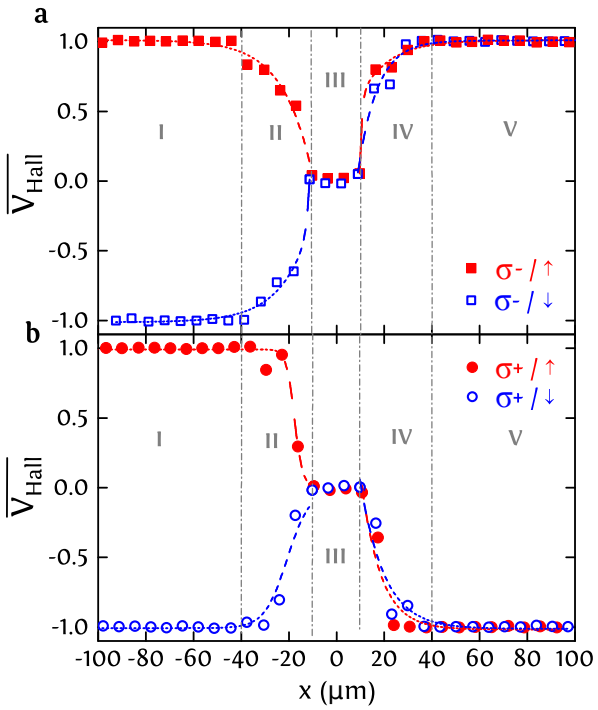

FIGURE 4.5: Normalized Hall voltage $\overline{V_{Hall}}$ as a function of the position of the beam *x* swept where (a)corresponds to left- handed circular polarization (σ-) and (b) to right-handed circular polarization (σ+). The values 1 and -1 of the $\overline{V_{Hall}}$ correspond to both saturated magnetic states. The laser beam is swept over the whole *x* axis of Hall cross from position -100 µm to 100 µm, with a sweeping speed of 40 µm/s and a power of 0.95 mW. The experiment is repeated for both positive and negative saturation of the magnetization. The dashed lines are guides to the eyes.

In order to understand the shapes of the curves in figure 4.5, we take into account the decomposition of the laser-induced area into regions intensities, as shown in previous studies in GdFeCo alloy films [15, 19] and Pt/Co/Pt multilayers [2] (see figure 1.5 in section 1.3.1). Indeed, the intensity in the central part of the laser spot is sufficiently high to demagnetize the Hall cross, whereas AO-HDS is obtained only at the level of a narrow rim with the optimum intensity called AOS rim. As shown in figure 4.5, the laser beam is far from the Hall cross in region *I* and does not effect of the magnetization. A drop of the absolute value of the Hall voltage is measured in region *II* since the first part of the inner circle of the laser beam enters the center of the Hall cross. This gradual drop of magnetization is probably due to a gradual presence of multiple domains. No switching is measured in the transition between regions *I* and *II*, which might be due to the small width of the AOS rim which is estimated using the Faraday microscope to 2-3 µm, and to the low temporal resolution of the measurement (150 ms). In region *III*, the laser beam is well centered on the Hall cross. The presence of multiple domains in it leads to a zero plateau of the Hall voltage. The helicity dependence starts to appear in region *IV* as the second part of the AOS rim goes through the center of the Hall cross. Independently of the initial magnetization saturation, σ- and σ+ switch gradually to up and down, respectively. In region *V*, the laser beam is far from the center of the Hall cross and the helicity-dependent switching is complete. This electrical measurement for the four configurations of initial saturation and circular polarization is a clear demonstration of the helicity-dependent switching in Pt/Co/Pt Hall crosses. It also enables the estimation of the size of the laser-induced area, corresponding to the diameter of the AOS rim. In our experimental set-up, this diameter equals 80 µm for a laser power of 0.95 mW.

A complete helicity-dependent switching is obtained with a sweeping speed of 40 µm/s and a power of 0.95 mW. We will now investigate the effect of decreasing the number of photons in interaction with the Hall cross on the switching process following two different approaches. The first approach consists of lowering the laser power, which enables to tune the maximum intensity of each pulse while the number and density of pulses is kept constant. The second approach consists of increasing the sweeping speed, leading to a decrease of the number of pulses per unit area. In this second approach, the sweeping speed is increased from 40 µm/s to 2500 µm/s. Hence, the distance between two consecutive pulses increases from 8 nm to 0.5 µm, which remains small compared to the laser-induced area that is about 80 µm and to the magnetic domain size. Figure 4.6 shows the temporal evolution of the anomalous Hall voltage for the sweeping beam measurement repeated four times with a sweeping speed of 1000 µm/s and a power of 0.95 mW. A reset of magnetization to its initial state is performed after laser beam with σ+ polarization is swept back and forth over the Hall cross. One can see that on average the switching is incomplete with a significant stochastic component. Note that due to the fast sweeping speed of 1000 µm/s and the low resolution of 150 ms, the laser-induced demagnetization similar to the one in regions II and *III* (figure 4.5) are not measured.

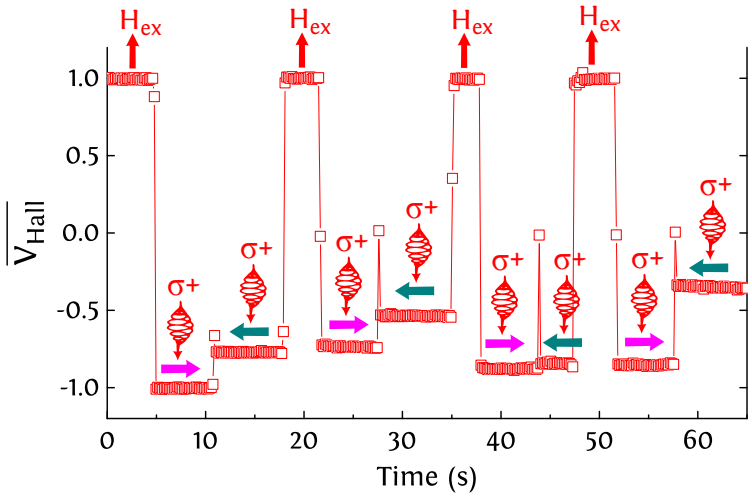

FIGURE 4.6: Time evolution of the normalized Hall voltage $\overline{V_{Hall}}$ for the sweeping beam measurement repeated four times, with σ+ sweeping and initial saturation up. The laser spot is swept back (dark cyan arrow) and forth (magneta arrow) over the whole *x* axis of the Hall cross, with a sweeping speed of 1000 µm/s and a power of 0.95 mW, leading on average to an incomplete switching and a significant stochastic component.

In order to take into account the stochastic component, all sweeping beam measurements with both approaches were performed 20 times with a reset of magnetization of its initial state after each sweep as shown in figure 4.7. For each measurement, we determine the switching ratio, corresponding to the relative change of the anomalous Hall voltage in comparison to the full switching. For instance, a value of $\tau = 100\%$ corresponds to complete and deterministic switching. The values of τ given in figure 4.7 are arithmetic means of the switching ratio measured for each individual measurement, whereas the value of the standard deviation is given by the length of the error bars. In figure 4.7(a), the switching ratio is presented as a function of the laser power for various sweeping speeds. The initial up magnetization saturation with σ+ sweeping is exemplarily shown. Independently of the sweeping speed ranging from 40 µm/s to 2500 µm/s, we clearly observe a threshold power below which the laser does not affect the magnetization, and above which AO-HDS is observed. Above

this threshold power, a complete and reproducible switching is only obtained for the lower sweeping speed of 40 µm/s, whereas the switching ratio saturates around 80% for higher sweeping speeds, and seems to be only weakly dependent on the laser power. Moreover, the standard deviation increases when the switching ratio decreases, meaning that the switching process is increasingly stochastic for sweeping speeds ranging from 200 µm/s to 2500 µm/s.

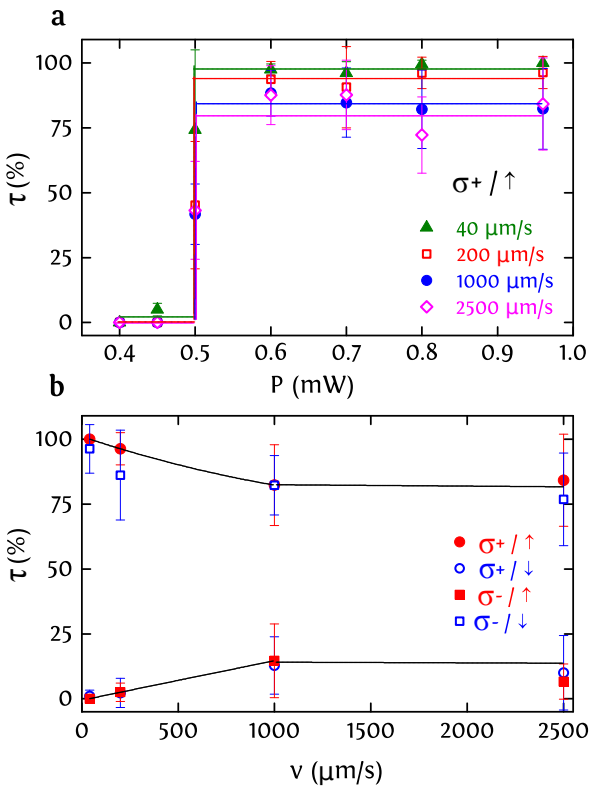

FIGURE 4.7: (a) Switching ratio τ as a function of the laser power *P* for different sweeping speeds. The initial up magnetization saturation with σ+ sweeping is exemplarily shown. (b) Switching ratio τ as a function of the swept beam's speed *v* with a power of 0.95 mW for the four different combinations of circular polarization and initial saturation. The dashed lines are guides to the eyes.

We now verify that the modification of the switching ratio by increasing the sweeping speed is symmetric and is also obtained with the other combinations of circular polarization and initial saturation, as shown in figure 4.7(b). These measurements were performed for a laser power of 0.95 mW, which is well above the threshold power. As depicted in figure 4.7(b), the excepted symmetric behavior is observed and the helicity dependence is conserved independently of the sweeping speed. For a sweeping speed of 200 µm/s, the difference in the switching ratio between the two circular polarizations for a given saturation is larger than 75%. For sweeping speeds higher than 200 µm/s, the switching ratio drops by 10% to 20% compared to the slowest speed of 40 µm/s and the standard deviation increases. This can be explained by the persistent formation of multiple magnetic domains within the Hall cross. Hence, these results give indirect evidence that AO-HDS is a cumulative process, since a complete and reproducible switching requires a certain number of pulses which becomes larger when the sweeping speed is decreased.

To confirm that the sweeping speed increase induces multiple domains formation, we performed similar sweeping beam experiments on Pt(3.7 nm)/Co(0.6 nm)/Pt(3.7 nm) continuous

films by varying the sweeping speed from 40 µm/s to 2500 µm/s. We also use another approach to investigate the effect of the number of pulses interacting with film on the switching achievement by tuning the repetition rate from the default value of 5 kHz to 5 Hz using a pulse picker. Figures 4.8(a), 4.8(b), 4.9(a) and 4.9 (b) show the magneto-optical response of the investigated Pt/Co/Pt films to $\sigma+$ sweeping with speeds of 40 µm/s, 200 µm/s, 1000 µm/s and 2500 µm/s, respectively.

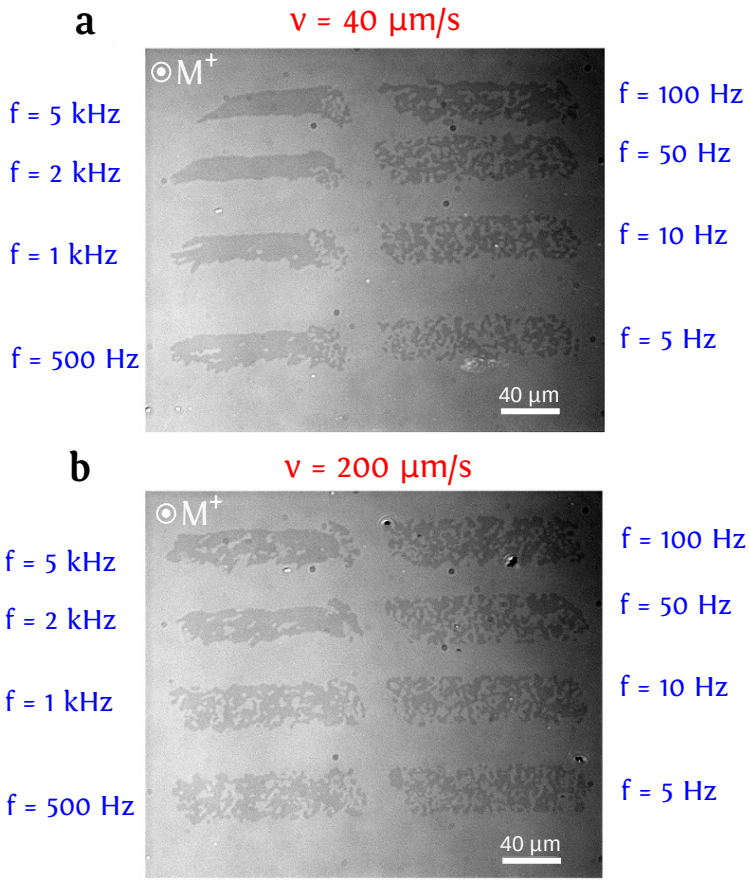

FIGURE 4.8: (a) and (b) Magneto-optical response of Pt(3.7 nm)/Co(0.6 nm)/Pt(3.7 nm) continuous film to right-circularly polarized laser beam swept from left to right a sweeping speeds of 40 µm/s and 200 µm/s, respectively. The laser power is 0.7 mW and the repetition rate is varied from 5 kHz to 5 Hz. The initial up magnetization saturation is exemplarily shown and the dark contrast corresponds to a reversal to down.

Starting with a sweeping speed of 40 µm/s as shown in figure 4.8(a), a full switching is obtained for a repetition rate f ranging from 5 kHz to 1 kHz. By further reducing the repetition rate, multiple magnetic domains start to appear gradually in the laser-scanned area. Knowing that lowering the repetition rate leads also to a decrease of the number of pulses interacting with the Hall cross, these findings show that the switching of Pt/Co/Pt films with a swept beam is a cumulative process, which is in agreement with the results obtained on the Pt/Co/Pt based Hall cross. Second, figure 4.8(b) shows that by increasing the sweeping speed up to 200 µm/s, the repetition rate limit below which multiple domains are observed increases. Furthermore, the same behavior is measured for sweeping speeds of 1000 µm/s and 2500 µm/s as depicted in figures 4.9(a) and 4.9(b), respectively. Indeed, for both sweeping speeds, a partial presence of multiple domains is obtained for the default repetition rate of 5 kHz. Figure 4.9 shows also that for a low repetition rate of 5 Hz, the distance between two consecutive pulses becomes

larger than the laser-induced area, which is around 30 µm for the used laser power. Hence, the effect of single pulses can be probed and corresponds to a thermal demagnetization, confirming the cumulative aspect of the AO-HDS with a swept beam.

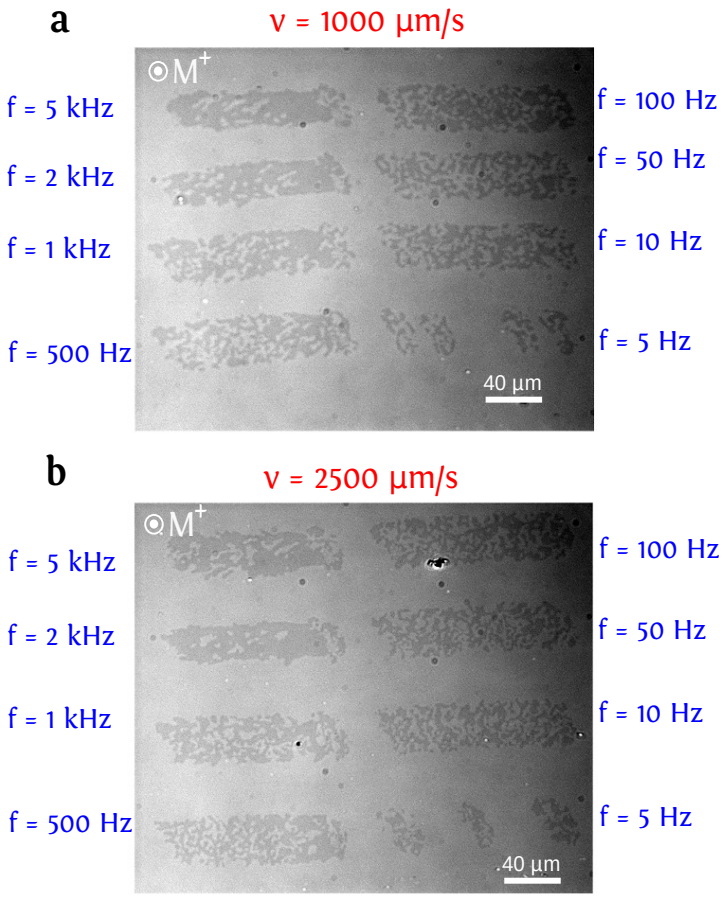

FIGURE 4.9: (a) and (b) Magneto-optical response of Pt(3.7 nm)/Co(0.6 nm)/Pt(3.7 nm) continuous film to right-circularly polarized laser beam swept from left to right a sweeping speeds of 1000 µm/s and 2500 µm/s, respectively. The used laser power is 0.7 mW and the repetition rate is varied from 5 kHz to 5 Hz. The initial up magnetization saturation is exemplarily shown and the dark contrast corresponds to a reversal to down.

Linear polarization

It was shown in previous studies that a swept linearly polarized beam (π) induces random magnetic domains up and down in ferrimagnets such as GdFeCo [15], TbCo films [20], and ferromagnets such as Co/Pt multilayers [2]. However, statistical quantification of the switching with linear polarization has not yet been performed. Here, we quantify the laser-induced multiple domain formation with linear polarization in Pt/Co/Pt based Hall cross following the sweeping beam approach, as shown in figures 4.10 and 4.11.

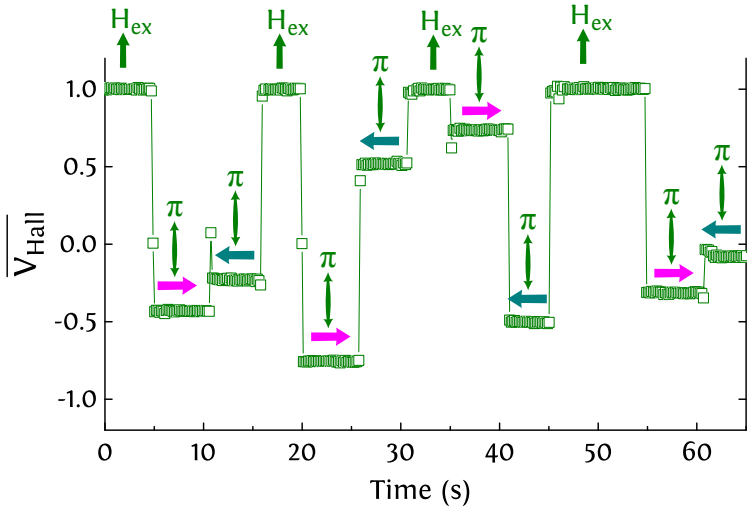

FIGURE 4.10: Time evolution of the normalized Hall voltage $\overline{V_{Hall}}$ for the sweeping beam measurement repeated four times, with linear polarization sweeping and initial saturation up. The laser spot is swept back (dark cyan arrow) and forth (magenta arrow) over the whole x axis of the Hall cross, with a sweeping speed of 1000 µm/s and a power of 0.95 mW, leading on average to a random switching ratio.

Figure 4.10 shows the temporal evolution of the anomalous Hall voltage for the sweeping beam measurement repeated four times with a sweeping speed of 1000 µm/s and a power of 0.95 mW. A reset of magnetization to its initial state is performed after laser beam with linear polarization is swept back and forth over the Hall cross. The switching is random on average with a large stochastic contribution. Furthermore, we perform this sweeping measurement 20 times with linear polarized beam swept and speeds ranging from 40 µm/s to 2500 µm/s. As depicted in figure 4.11, the switching ratio is measured for three different initial magnetic states, namely saturation up, saturation down and a demagnetized state.

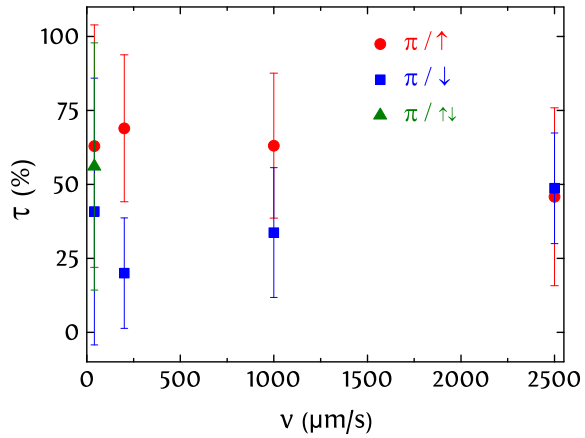

FIGURE 4.11: Switching ratio τ as a function of the swept beam's speed v with linear polarization and for three different initial magnetic states, namely saturation up (red), saturation down (red) and demagnetized state (green). The laser power is 0.95 mW.

One can see that the average value of the switching ratio with π sweeping for the investigated range of v varies from 50% to 70% with initial saturation up, from 20% to 50% with an initial

saturation down, and is around 50% with a sweeping speed of 40 µm/s and an initially demagnetized state. However, the standard deviation in all cases is extremely large, demonstrating the stochastic behavior with linear polarization. This can be explained by the fact that one of the domain orientations is predominant within the Hall cross. For a better understanding of such stochastic behavior, we perform sweeping experiment with linearly polarized beam on Pt/Co/Pt continuous film along a domain boundary. Figure 4.12(b) shows that sweeping with $\sigma+$ polarized beam switches magnetization to up, whereas sweeping with linearly polarized beam leads to thermally-induced domain wall (DW) motion. This so-called thermomagnetic writing is only achieved with linear polarization in Pt/Co/Pt films, and was already shown in other materials such as GdFe alloys [21] and TbFe alloys [22].

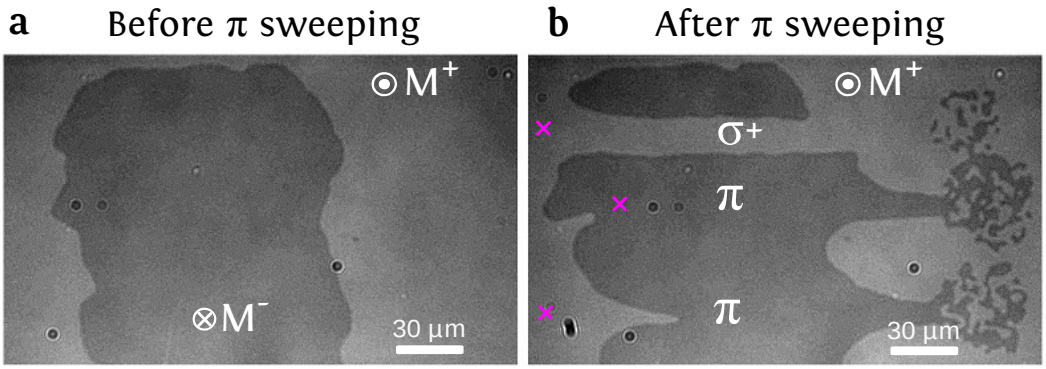

FIGURE 4.12: (a) Magneto-optical image of the initial magnetic state in a Pt(4.5 nm)/Co(0.6 nm)/Pt(4.5 nm) continuous film before laser exposure. (b) Magneto-optical response obtained with linearly and right-circularly polarized beam swept with a speed of 40 µm/s and a laser power of 0.7 mW. For each scan, the laser beam is swept from the area marked with magenta crosses to the demagnetized area. The latter is obtained when the laser is turned off.

Moreover, figure 4.12(b) shows that the stretched magnetic domains in the scanned area with linearly polarized beam are quite large. Taking into account such large domain size and the thermomagnetic writing in Pt/Co/Pt films, the switching of a 5 µm-wide Hall cross with π-sweeping is likely to be complete, partial or low. These findings are in agreement with the stochastic behavior demonstrated in figure 4.11.

Longitudinal resistance measurement

In order to correlate the switching occurrence following the sweeping beam approach with the temperature increase within the Hall cross, we quantify the change of the longitudinal resistance R while the laser beam is swept over the x axis of the Hall cross as depicted in figure 4.13. The temporal resolution of the experiment is 150 ms.

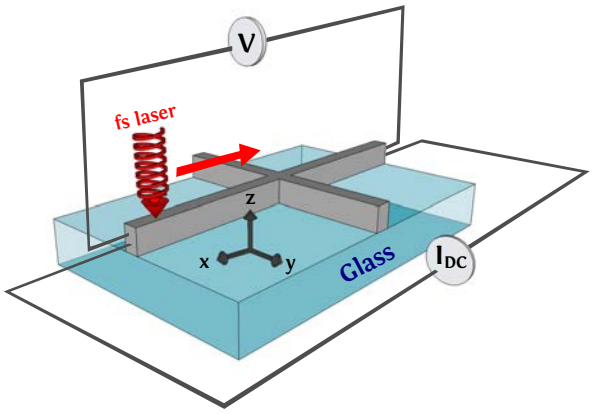

FIGURE 4.13: Schematic representation of the resistance measurement with a swept beam: a DC current is applied along *x* axis, while the voltage is continuously measured along the *x* direction. The fs laser beam perpendicular to the film plane is swept along the *x* axis.

Indeed, figure 4.14 shows typical time evolution of the longitudinal resistance *R* while performing the sweeping beam measurement with a sweeping speed of 40 µm/s, a laser power of 0.95 mW and an applied current of 0.75 mW. The initial up magnetization saturation and σ+ sweeping is exemplarily shown.

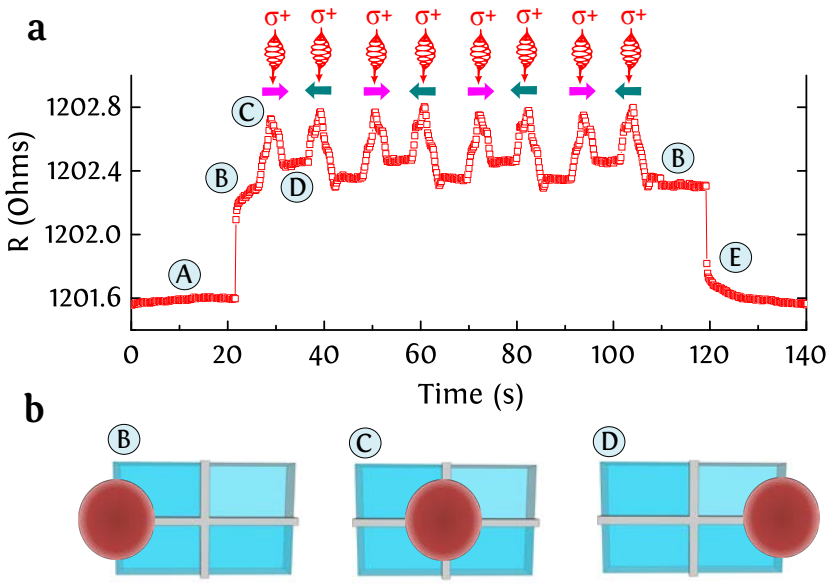

FIGURE 4.14: (a) Time evolution of the longitudinal resistance *R* while performing four consecutive sweeping beam measurements, with right-handed circular polarization and initial saturation up. The laser spot is swept back (dark cyan arrow) and forth (magenta arrow) over the whole *x* axis of the Hall cross, with a sweeping speed of 40 µm/s and a power of 0.95 mW. The applied current is 0.75 mA. The resistance at "*A*" corresponds to the default value before laser exposition, whereas resistance at "*E*" is obtained when the laser spot is switched off. (b) Schematic representation of the laser beam position on the *x* axis at "*B*, "*C*" and "*D*". "*B*" and "*D*" correspond to a laser spot on left and right edges of the Hall cross, respectively. The resistance at "*C*" is obtained when the laser spot is centered on the Hall cross.

First, the longitudinal resistance before laser exposition is measured R_A = 1201.6 Ohms. Second,

the laser beam is illuminated at the edge of the x at position - 100 µm, leading to a rise of the resistance to R_B = 1202.39 Ohms. The laser beam is then swept back and forth over the x axis from - 100 µm to 100 µm. As depicted in figure 4.14(b), the resistance increases to the maximum R_C = 1202.79 Ohms when the laser beam crosses the center of the Hall cross, before decreasing to R_D = 1202.43 Ohms when the laser beam reaches the edge of the x axis at position 100 µm. Such measurement is repeated four times and the resistance evolution is reproducible. The laser beam is finally turned off and the resistance decreases gradually to $R_E = R_A$ = 1201.6 Ohms. Moreover, the same evolution of the longitudinal resistance is measured by performing such experiment with left-circularly and linearly polarized beam with the same laser power and sweeping speed, thus indicating that the average and quasi-static laser-induced heating of the Hall cross is weakly dependent on the helicity.

We define the laser-induced longitudinal resistance shift is defined as follows:

$$\Delta R = \frac{R_C}{R_A} - 1 \tag{4.5}$$

which corresponds to the maximal resistance obtained when the laser spot is well centered on the Hall cross. Now we investigate the influence of the sweeping speed and the laser power on the resistance shift. Sweeping beam measurements are thus performed 20 times while varying the sweeping speed from 40 µm/s and 2500 µm/s and the laser power from 0.2 mW to 0.95 mW. The resistance shift values shown in figure 4.15 are arithmetic means of the resistance shift measured for each individual measurement. The initial up magnetization saturation with σ+ sweeping is exemplarily shown.

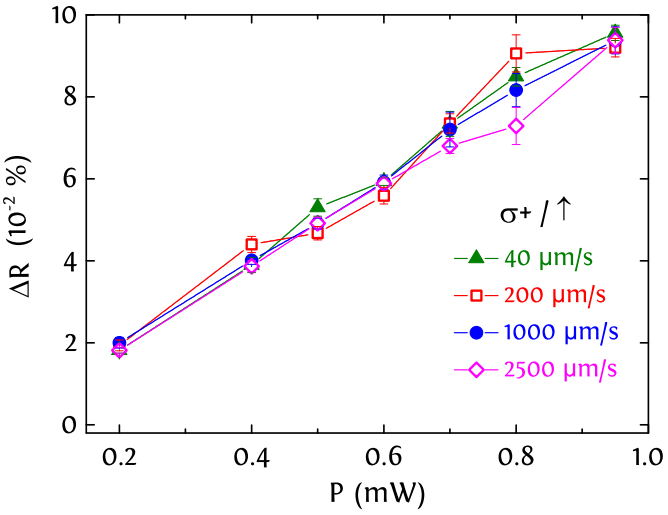

FIGURE 4.15: Resistance shift ΔR as a function of the laser power P for different sweeping speeds. The initial up magnetization saturation with σ+ sweeping is exemplarily shown.

One can see that the resistance rise scales linearly with laser power and seems to be only weakly dependent on the sweeping speed ranging from 40 µm/s to 2500 µm/s. This means that the average laser-induced heating is more related to the number of photons per pulse. Moreover, the laser-induced heating weakly change by varying the number of pulses interacting with the 5-µm-wide Hall cross from 625 to 10 pulses. Nevertheless, it was demonstrated earlier that, for a laser power above the switching power threshold, the achievement of a complete switching is strongly related to the number of pulses in interaction with the Hall cross

and is weakly dependent on the laser power (see figure 4.7). Hence, we can conclude that the cumulative helicity-dependent switching process in Pt/Co/Pt based Hall cross is weakly related to the average laser-induced heating, however, it is mainly dependent on the number of pulses.

Influence of current-induced heating

In Co/Pt based Hall crosses, the current density might affect the magnetization in various ways such as the DW propagation via the spin transfer torque (STT) [23] and the direct switching via the spin orbit torque (SOT) [17, 18]. The typical current density used to perform such experiments is of the order of 10 GA/m^2 and 0.23 TA/m^2, respectively. In the following we investigate the achievement of AO-HDS in the Pt/Co/Pt Hall cross via direct current-induced Joule heating, by varying the applied current intensity from 1 mA to 5 mA in a 7 µm-wide Pt/Co/Pt Hall cross. Hence, the current density varies from 28.5 MA/m^2 to 142 MA/m^2 and current-induced STT and SOT remain negligible. For each value of the applied current, we perform sweeping beam measurements with a sweeping speed of 40 µm/s and a laser power of 0.4 mW, corresponding to the switching power threshold (see figure 4.7). Figure 4.16 shows the evolution of the switching ratio and the resistivity as a function of the applied current intensity. We measured the resistivity change while no laser beam is applied, by assuming that the entire power is dissipated within the Hall cross and by taking into account the Ta buffer layer.

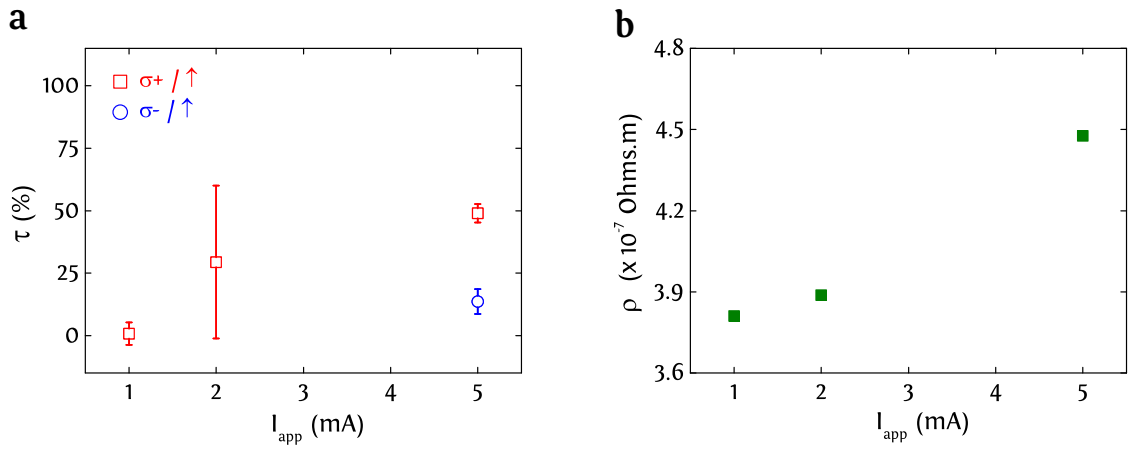

FIGURE 4.16: (a) Switching ratio as a function of the applied current intensity for sweeping beam measurements performed in a 7 µm-wide Pt/Co/Pt Hall cross with a speed of 40 µm/s and a laser power 0.4 mA. The initial up magnetization saturation is exemplarily shown. (b) Resistivity of Ta/Pt/Co/Pt as a function of the applied current intensity. No laser beam is applied during the resistivity measurement.

As depicted in figure 4.16(a), no switching occurs for the minimum applied current of 1 mA. Moreover, a partial switching is obtained with an average switching ratio of 25% by increasing the applied current to 2 mA. The large stochastic contribution is attributed to heat-induced magnetic domain fluctuations. For I_{app} = 5 mA, although a partial switching is obtained, the reversal is more reliable and a small helicity dependence starts to appear. The partial switching is probably due to the width of the laser-scanned area which is smaller than the width of the studied Hall cross. Such enhancement of AO-HDS via current-induced Joule heating indicates that the switching power threshold might be strongly dependent on sample temperature. A similar effect was demonstrated in the studies reported in section 1.5.1 on ferrimagnetic TbFeCo and TbCo alloys, where the switching power threshold is decreased (resp. increased) by heating (resp. cooling) the sample [24, 25, 26]. The resistivity increases with the applied

current as shown in figure 4.16(b), which is due to the current-induced Joule heating. For I_{app} = 5 mA, the resistivity is 4.47 10^{-7} Ohms.m.

We now quantify the average laser-induced temperature increase in the entire longitudinal axis of the studied Pt/Co/Pt Hall cross. In this context, we increase gradually the current intensity in a 100 µm-wide Pt/Co/Pt Hall cross and measure the resistivity change. For each value of applied current, we also estimate the current-induced temperature increase with an infrared camera. The evolution of the resistivity of the Pt/Co/Pt based Hall cross as a function of temperature is depicted in figure 4.17. As expected, the resistivity scales linearly with the temperature and the temperature coefficient per °C is 0.00727. By extrapolating the data, ρ = 4.47 10^{-7} Ohms.m is obtained when T = 122 °C. Therefore, the partial reestablishment of the helicity-dependent switching via Joule heating demonstrated in figure 4.16(a) is achieved at a temperature of 122 °C.

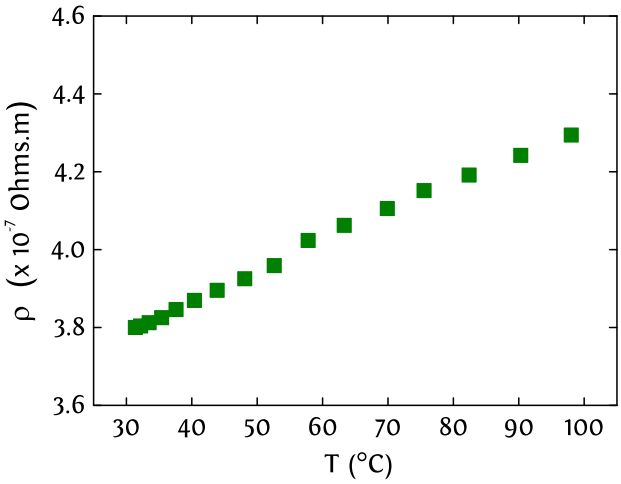

FIGURE 4.17: Evolution of the resistivity as a function of temperature measured in a 100 µm-wide Pt/Co/Pt Hall cross. The temperature is changed via current-induced Joule heating and is detected with an infrared camera.

4.2.3 Static beam measurement with an off-centered beam

We now investigate the AO-HDS mechanism in the Pt/Co/Pt based Hall cross using the second approach called static beam measurement, which provides insight into the switching process and a better integration of all-optical switching in spintronics devices. Achieving such investigation is hard using magneto-optical Faraday imaging, since the all-optical switching rim is too small to be optically resolved. To compare with the sweeping beam measurements, we measure in the following both the anomalous Hall voltage and the longitudinal resistance with an off-centered static beam.

Anomalous Hall voltage measurement

We start our investigation by performing the static beam measurement introduced in section 4.2.1 (see figure 4.3) for the four possible configurations of circular polarization and initial saturation. In order to avoid demagnetization effects due to cooling when the laser beam is turned off, the switching ratio for each configuration is measured as the beam is on. A reset of magnetization to its initial state is performed after each individual measurement. These

static beam measurements were performed 10 times and the values of τ given in figure 4.18 are arithmetic means of the switching ratio measured for each individual measurement. The helicity dependence has been verified and thus the initial saturation up with $\sigma+$ polarization is exemplarily shown.

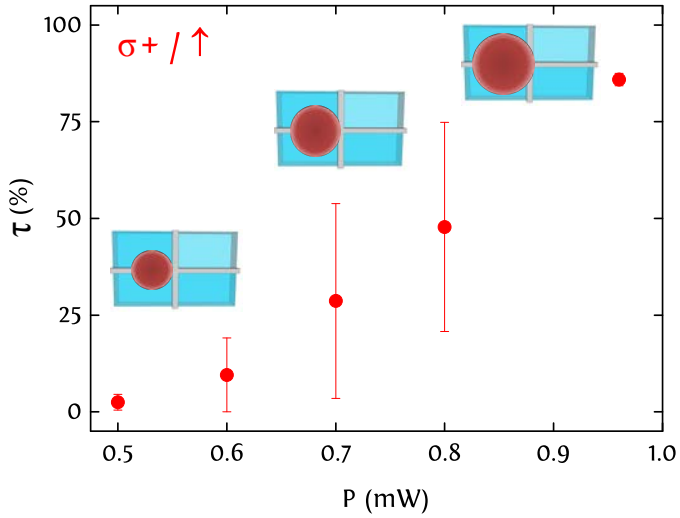

FIGURE 4.18: Switching ratio τ as a function of the laser power P for the static beam measurement. The center of the beam spot is kept fixed at a position approximately 40 µm from the Hall cross center. Shown in the inset is the schematic evolution of the diameter of the AOS rim.

As shown in figure 4.18, no switching occurs for the minimum power of 0.5 mW since the laser power is too low to influence the magnetic state. Note that the size of the laser-excited area increases by increasing the laser power, leading to the spatial shift of the AOS rim. This spatial shift is demonstrated on a Pt/Co/Pt continuous film as shown in figure 4.19. Hence, the switching ratio increases as the AOS rim gets gradually centered on the Hall cross by varying the power from 0.6 mW to 0.8 mW. Moreover, a significant stochastic component appears. We attribute this behavior to heat-induced magnetic domain fluctuations which might play an important role for this range of power. For a laser power of 0.95 mW, a switching of about 90% is achieved with a small standard deviation. The fact that such reliable switching is uncomplete could be due to the small width of the AOS rim which is not completely covering the probed area of the Hall cross. Finally, the spatial displacement of the AOS rim with the laser power shown in figure 4.19 is a hint that the switching at the level of the rim occurs always with a certain optimum power value. This optimum power and the width of the AOS rim should be material-dependent.

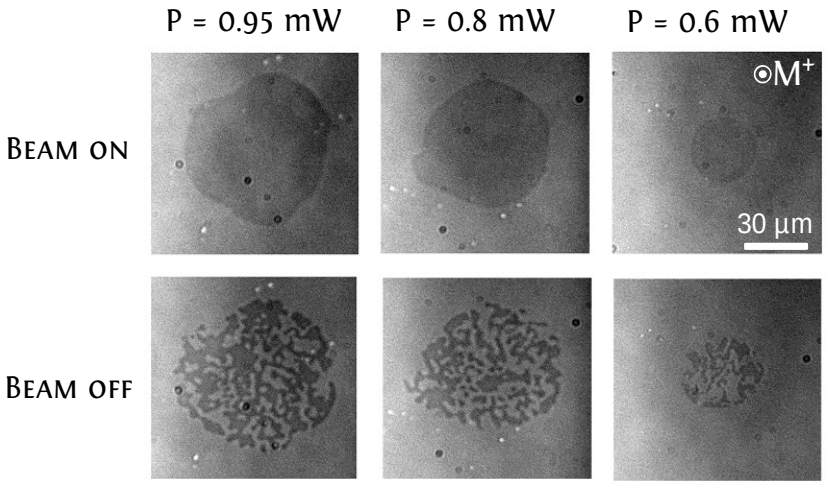

Figure 4.19: Magneto-optical response of Pt(3.7 nm)/Co(0.6 nm)/Pt(3.7 nm) continuous film to right-circularly polarized laser beam with a laser power ranging from 0.6 mW to 0.95 mW. The laser exposed area is demagnetized and the area where we see domains increases with laser power. The AOS ring is too small to be optically resolved when the beam is on. When the laser beam is turned off, multiple domains are obtained due to demagnetization effects. The initial saturation up is exemplarily shown and the dark contrast corresponds to a reversal to down. All pictures have the same dimensions.

Longitudinal resistance measurement

We now continue by measuring the laser-induced increase of the longitudinal resistance during the static beam measurement. As depicted in figure 4.20, the off-centered laser beam is shined on the x axis, while the longitudinal resistance is continuously measured with a temporal resolution of 150 ms.

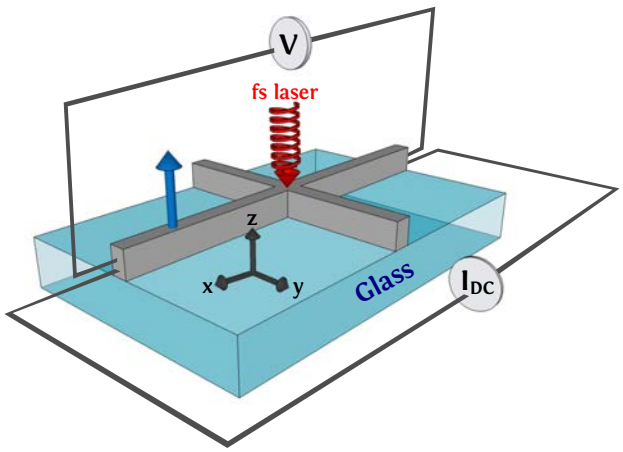

Figure 4.20: Schematic representation of the resistance measurement with an off-centered beam: a DC current is applied along the x axis, while the voltage is continuously measured along the x direction. The fs laser beam is shined on the x axis at a fixed position about 40 µm from the center of the Hall cross.

The typical time evolution of the longitudinal resistance while performing four consecutive static beam measurements with a laser power of 0.95 mW and an applied current of 0.75

mA is depicted in figure 4.21. The initial saturation down with σ- polarization is exemplarily shown. First, the resistance before laser exposition is measured R_A = 1201 Ohms. Once the laser beam is shine, the longitudinal resistance increases up to R_B = 1202 Ohms. When the laser beam is turned off, R decreases up to R_C = 1201.06 Ohms. By fitting the data with an exponential decay, the characteristic times for the laser-induced heating and cooling are determined. The characteristic time is determined for both laser-induced heating and cooling by fitting the data with an exponential decay, yielding t_B = 2.29 s and t_C = 1.41 s, respectively.

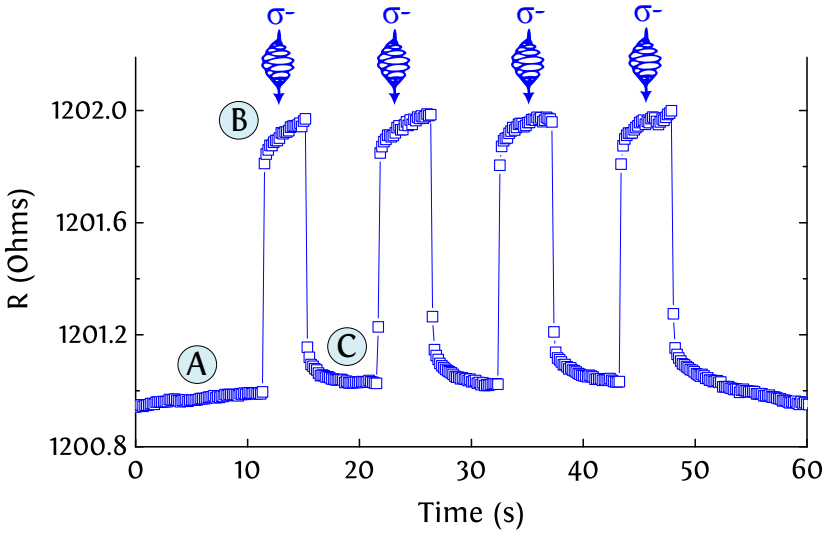

FIGURE 4.21: Time evolution of the longitudinal resistance R while performing the static beam measurement four times, with an applied current of 0.75 mA and a laser power 0.95 mW. The initial saturation down and left-handed circular polarization is exemplarily shown. The resistance at *"A"* corresponds to the default value before laser exposition. The resistance at *"B"* is obtained when the off-centered laser beam is shined, whereas the resistance at *"C"* is achieved when the laser beam is switched off.

We define the laser-induced resistance shift as:

$$\Delta R = \frac{R_B}{R_A} - 1 \tag{4.6}$$

R_B corresponds to the maximal resistance obtained when the laser beam is shined. The power dependence of the resistance shift is investigated by performing the static beam measurement 10 times. The resistance shift values shown in figure 4.22 are arithmetic means of the resistance shift measured for each individual measurement. The initial saturation down with σ- sweeping is exemplarily shown. Similarly to the longitudinal resistance measurement performed with a swept beam, figure 4.22 shows that resistance shift linearly with the laser power, meaning that laser-heating is strongly dependent on the number of photons per pulse absorbed by the Hall cross. Moreover, the same values of the longitudinal resistance are measured by performing such experiment with σ+ and linear polarizations, thus indicating that the average laser-induced heating with an off-centered beam is helicity-independent.

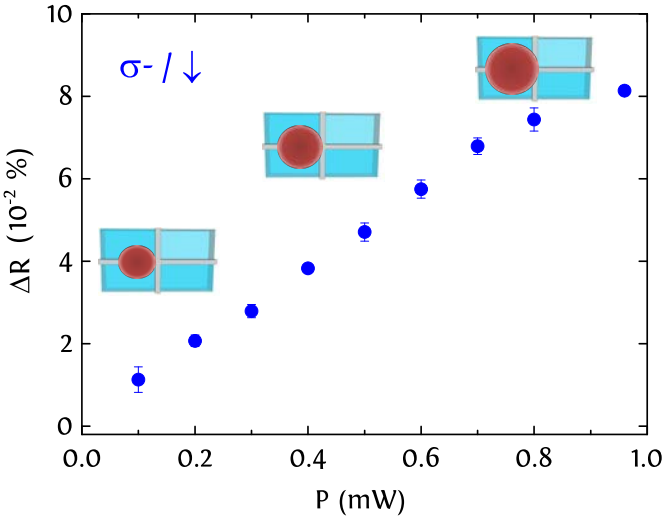

FIGURE 4.22: Resistance shift ΔR as a function of the laser power *P* for the static beam measurement with an off-centered beam. The center of the beam spot is kept fixed at a position approximately 40 μm from the Hall cross center. Shown in the inset is the schematic evolution of the diameter of the AOS rim. The initial saturation down with σ- polarization is exemplarily shown.

4.2.4 Static beam measurement with a centered beam

In this section we verify the demagnetization of the studied Pt/Co/Pt Hall cross with a beam kept well centered on the Hall cross. The experimental details were introduced previously in section 4.2.1 (see figure 4.4). Figure 4.23 shows the evolution of the switching ratio as a function of the laser power when the centered beam is on, and also when the latter is turned off. These measurements were repeated 10 times and the values of τ shown in figure 4.23 are arithmetic means of the switching ratio measured for each individual measurement. The initial saturation up with σ+ polarization is exemplarily shown.

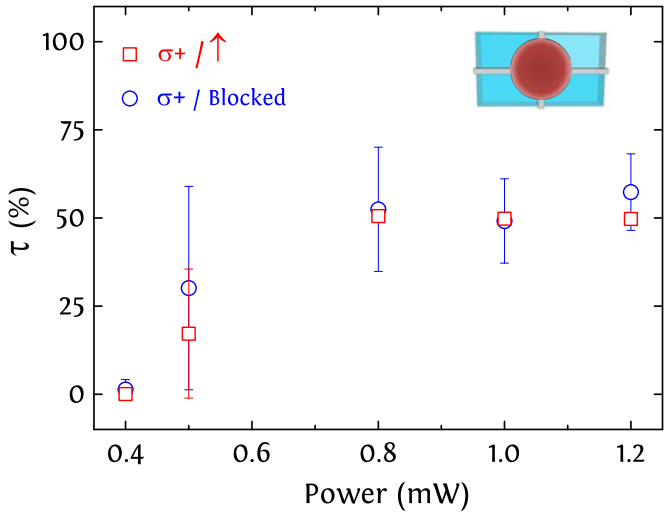

FIGURE 4.23: Switching ratio τ as a function of the laser power P for the static beam measurement with a centered beam as shown in the inset. The initial up magnetization saturation with σ+ polarization is exemplarily shown.

No magnetization change is measured for the minimum power of 0.4 mW since the laser power is too low to influence the magnetization. For a laser power of 0.5 mW, a partial demagnetization is obtained as the laser-induced area is still smaller than the Hall cross. However, multiple domains are obtained when the laser beam is turned off and are due to the demagnetizing effect, as depicted in figure 4.19. Hence, we attribute the large stochastic contribution when the laser beam is turned off to the large magnetic domain size in the Pt/Co/Pt multilayers, as shown in section 3.4.2. For a laser power ranging from 1 mW to 1.4 mW, the entire Hall cross is overheated, leading as expected to a full demagnetization (τ = 50%) with a negligible stochastic contribution.

4.2.5 Summary

In section 4.2, we investigated the underlying microscopic physics of the all-optical switching in ferromagnetic Co/Pt multilayers. Therefore, we probed AO-HDS in Pt/Co/Pt Hall crosses via the anomalous Hall effect. This novel approach combining both optics and spintronics enables a statistical quantification of the switching ratio for different laser parameters, thus giving new insight into the all-optical switching mechanism. Moreover, this approach enables to investigate the switching on different timescales ranging from 1 µs to a few seconds, thus bridging the gap between the ultrafast and the quasi-static methods used to probe magnetization.

We first demonstrated the AO-HDS in ferromagnetic Pt/Co/Pt films patterned into Hall crosses to allow electrical measurement of the magnetization via the anomalous Hall effect, using the sweeping beam and the static beam approaches. Both approaches indicate that a threshold power needs to be overcome in order to observe AO-HDS. We demonstrated that the switching becomes incomplete by increasing the sweeping speed, which is due to the persistent formation of multiple magnetic domains. These findings indicate that the AO-HDS in Pt/Co/Pt is a cumulative process, since a complete and reproducible switching requires a certain number of pulses.

In order to correlate the switching occurrence with the temperature increase within the Pt/Co/Pt Hall cross, we quantified the longitudinal resistance while sweeping with the laser beam over the Hall cross. We demonstrated that for a laser power above the switching power threshold, the AO-HDS process in Pt/Co/Pt is weakly related to the average laser-induced heating, however, it is mainly dependent on the number of pulses. Finally, we showed that the AO-HDS of Pt/Co/Pt Hall cross can be enhanced via current-induced Joule heating, indicating that the switching power threshold depends on sample temperature. In the next section, we will investigate for the first time the all-optical control of magnetization in ferromagnetic CoFeB/MgO based Hall crosses.

4.3 Electrical characterization of AOS in ferromagnetic CoFeB/MgO Hall crosses

Magnetic tunnel junctions (MTJs) with perpendicularly magnetized materials have triggered huge interest since they offer high thermal stability and low critical current for current-induced magnetic reversal [27]. Furthermore, CoFeB/MgO based MTJs with in-plane magnetization [28, 29] and especially with out-of-plane magnetization [30] were shown to be the most prominent candidate for the magnetic random access memory (MRAM), since they satisfy at the same time high thermal stability, high tunnel magnetoresistance and low current-induced magnetization switching. Ta/CoFeB/MgO heterostructures are also promising for domain wall

devices [31, 32], since they could exhibit PMA and reasonably low damping [30, 33]. In this context, we investigate the integration of the all-optical switching using fs laser pulses in Ta/CoFeB/MgO based spintronic devices.

Hence, the studied sample is a thin film of Glass/Ta(5 nm)/CoFeB(0.7 nm)/MgO(2.6 nm)/ Ta(5 nm)/Pt(2 nm) grown by DC sputtering. The film was annealed at a temperature of 250 °C for 1 h in order to get the PMA. The sample is patterned into 7-µm-wide Hall crosses using optical lithography. Note that the annealing temperature and duration influence the magnetic anisotropy of Ta/CoFeB/MgO heterostructures, since an overheating could rotate the magnetic easy axis from out-of-plane (OOP) to in-plane (IP) [34, 35]. This behavior is also expected by overheating the studied CoFeB/MgO Hall cross with laser beam. Moreover, a very low magnetic contrast is obtained in the studied CoFeB/MgO continuous films with our Faraday setup, thus the characterization of the all-optical control of magnetization in such material is only possible using patterned Hall crosses via the anomalous Hall effect. In order to explain this low magnetic contrast, we take into account the spin-orbit coupling. Indeed, the low damping in the studied CoFeB/MgO films scales with the spin-orbit coupling (SOC) [33]. Hence, SOC in CoFeB/MgO is low compared to the strong SOC in Co/Pt multilayers. On the other hand, it was shown that the Faraday rotation is strongly dependent on the spin-orbit coupling [36, 37]. Consequently, the Faraday rotation in Ta/CoFeB/MgO films is smaller than in Co/Pt films. In the following, we study the all-optical switching in the CoFeB/MgO based Hall crosses using both sweeping and static beam approaches introduction in section 4.2.1.

4.3.1 Sweeping beam measurement

We start our investigation by measuring the evolution of the anomalous Hall voltage while sweeping the laser beam back and forth over the entire longitudinal axis of the Hall cross as depicted in figure 4.24. A sweeping speed is 40 µm/s and a laser power of 1.35 mW are used in this experiment. For the applied current I = 0.75 mA, the typical value of the anomalous Hall voltage is V_{Hall} = 0.14 mV.

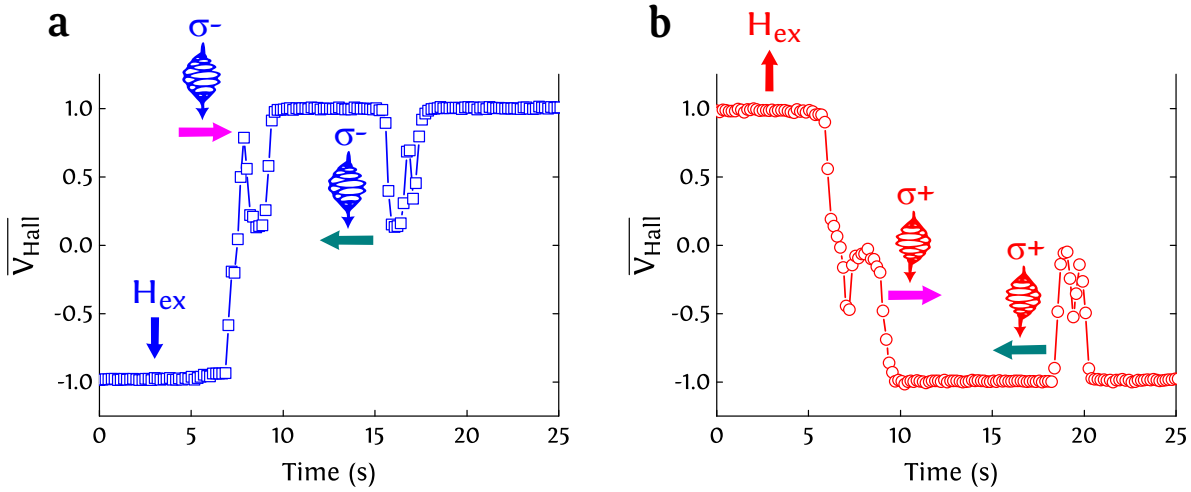

FIGURE 4.24: Time evolution of the normalized Hall voltage while performing sweeping beam measurement on the studied CoFeB/MgO based Hall cross. The initial down (resp. up) magnetization saturation with σ- (resp. σ+) sweeping is shown in (a) (resp. (b)). The laser beam is swept back and forth over the whole x axis of the Hall cross with a sweeping speed of 40 µm/s and a laser power of 1.35 mW.

Figure 4.24(a) shows that the magnetization with an initial saturation down switches gradually to up (70% of switching) when the first part of the inner circle of the laser beam with σ- polarization enters the Hall cross area. This behavior was not observed in Pt/Co/Pt based Hall crosses. Then, demagnetization takes place gradually when the center of the laser beam gets closer to the Hall cross. Finally, the magnetization switches completely to up when the laser beam moves away from the center of the Hall cross. Moreover, a demagnetization followed by a complete reversal to up is obtained by sweeping back with σ- polarization. The helicity dependence is conserved, as shown in figure 4.24(b). Independently of the initial magnetization saturation, σ- and σ+ switch magnetization up and down, respectively.

Nevertheless, we were not able to achieve a statistical quantification of the switching ratio of different laser parameters similar to the one performed in Pt/Co/Pt based Hall cross. Indeed, the measured Hall voltage decreases significantly when the laser is illuminating the CoFeB/MgO based Hall cross for a long time. At a certain point the Hall voltage vanishes indicating that the magnetic easy axis becomes in-plane. We attribute this behavior to a cumulative laser-induced annealing of the Hall cross leading to a gradual decrease of the magnetic anisotropy [34, 35]. Due to the laser-induced anisotropy reduction in the center of the Hall cross, a helicity-independent reversal could also be obtained. Indeed, a pure optical heating of the Hall cross center could result in a switching of magnetization in this region of the cross, whereas the outer closure would remain. We now continue to measure the change of the anomalous Hall voltage while sweeping the linearly polarized laser beam back and forth over the *x* axis of the CoFeB/MgO based Hall cross, as depicted in figure 4.25.

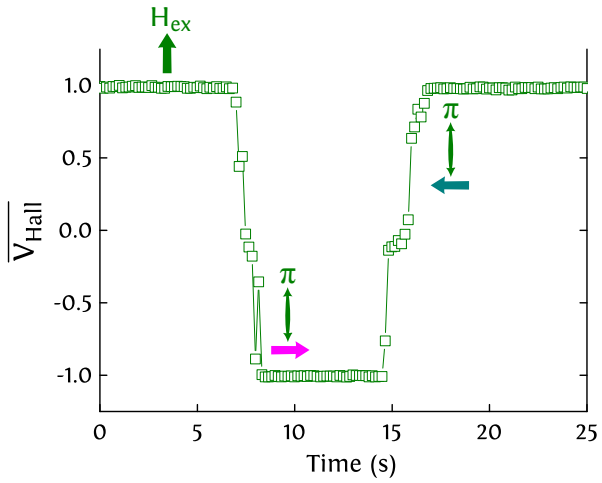

FIGURE 4.25: Time evolution of the normalized Hall voltage while performing sweeping beam measurement on the studied CoFeB/MgO based Hall cross. The initial up magnetization saturation with π sweeping is shown. The laser beam is swept back and forth over the whole *x* axis of the Hall cross with a sweeping speed of 40 µm/s and a laser power of 1.35 mW.

As shown in figure 4.25, demagnetization takes place gradually when the center of the linearly polarized laser beam gets closer to the initially saturated up Hall cross. Once the laser beam moves away from the Hall cross, magnetization switches completely to down. Furthermore, linearly polarized beam is swept back leading to a demagnetization followed by a complete reversal to up. Hence, sweeping with linearly polarized beam switches completely the magnetization independently of the initial magnetization saturation. This behavior is different from the stochastic behavior measured in Pt/Co/Pt Hall crosses. First, the possibility to switch

the CoFeB/MgO based Hall cross after each sweep with linear polarization is attributed to the thermomagnetic writing [21]. Second, the complete switching of the studied Hall cross can be attributed to the low thickness of the studied films (t_{CoFeB} = 0.7 nm) leading to a large magnetic domain size. Indeed, the magnetic domains left when the linearly polarized beam is swept over the CoFeB/MgO Hall cross might be larger than the probed area of the Hall cross (7x7 μm^2), leading to a complete switching of the Hall cross.

4.3.2 Static beam measurement with a centered beam

Next, we investigate the change of magnetization in the CoFeB based Hall cross with a beam kept centered on the Hall cross, as depicted in figure 4.4. In the following, the temporal evolution of the anomalous Hall voltage is measured when the centered beam is on, and also when the latter is turned off. Figure 4.26 and figure 4.27 show this evolution for both circular polarizations and linear polarization, respectively. The laser power used in this measurement is 1.35 mW.

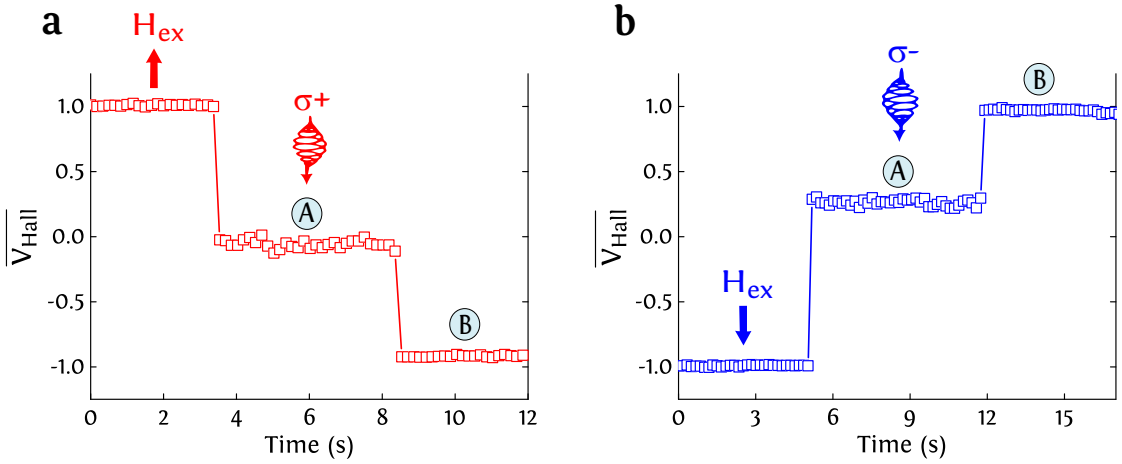

FIGURE 4.26: (a) (resp. (b)) Time evolution of the normalized Hall voltage while performing static beam measurement on the studied CoFeB/MgO based Hall cross with an initial saturation up (resp. down) and σ+ (resp. σ-) polarization. The laser beam is well centered and turned on in *"A"*, whereas it is turned off in *"B"*.

As expected, a plateau of the Hall voltage is measured when the centered laser beam is on and is slightly asymmetric around zero. This plateau corresponds to a multidomain state due to the laser-induced heating. This demagnetization is obtained independently of the initial magnetization saturation and the beam polarization. Second, a complete reversal is surprisingly achieved when the laser beam is turned off. We also attribute this complete reversal to the large size of the magnetic domains obtained when the laser is turned off, which might be larger than the probed area. It is once again different from the one measured in Pt/Co/Pt based Hall cross (see section 4.2.4), where multiple domains are obtained when the laser beam is turned off due to the demagnetizing effects.

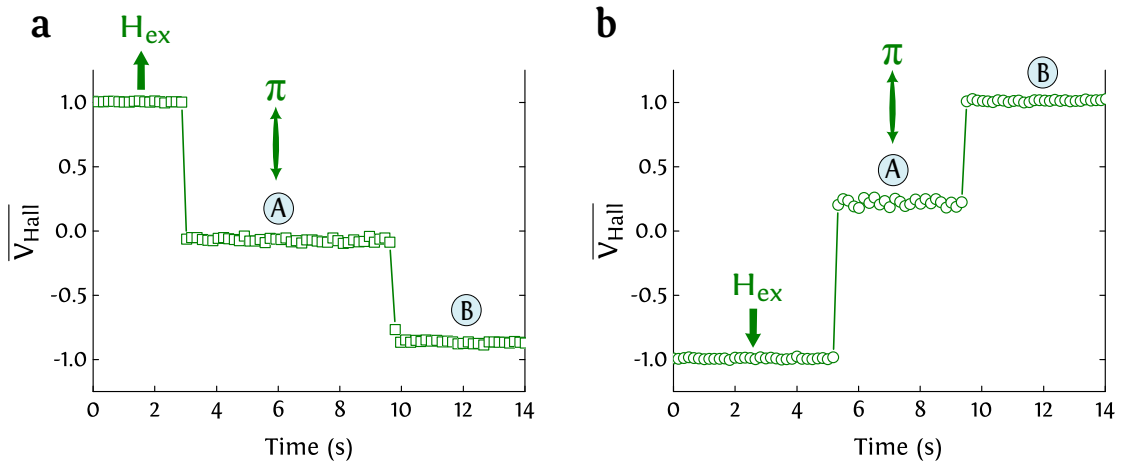

FIGURE 4.27: (a) and (b) Time evolution of the normalized Hall voltage while performing static beam measurement on the studied CoFeB/MgO based Hall cross with an initial saturation up and down, respectively. The linearly polarized laser beam is well centered and turned on in *"A"*, whereas the laser beam is turned off in *"B"*.

4.3.3 Summary

In section 4.3, we investigated the integration of the all-optical magnetization switching in CoFeB/MgO based Hall crosses. These ferromagnetic heterostructures triggered huge interest for their large potential for future spintronic devices. Hence we demonstrated the AO-HDS in CoFeB/MgO based Hall crosses with a swept laser beam. Nevertheless, we were not able to achieve a statistical quantification of the switching ratio of different laser parameters similar to one performed in Pt/Co/Pt based Hall cross, due to the laser-induced anisotropy reduction in the CoFeB/MgO based Hall cross. Moreover, we demonstrated that sweeping over the CoFeB/MgO Hall cross with a linearly polarized beam leads to a complete reversal of the Hall cross. This tricky behavior is attributed to the thermomagnetic writing and the large magnetic domains in CoFeB/MgO which might be larger than the probed area of the Hall cross.

4.4 Electrical characterization of AO-HDS in ferrimagnetic TbCo Hall crosses

It was already shown that ferrimagnetic 20 nm-thick Tb_xCo_{1-x} alloy films exhibit helicity-dependent magnetization switching in the case of Tb dominant alloys, for which T_{comp} is between RT and T_c [20, 38]. Moreover, we demonstrated in section 3.3.2 that AO-HDS is achieved even for Co dominant Tb_xCo_{1-x} films if the magnetic thickness is strongly reduced (t ‹ 5 nm). Now we study the implementation of all-optical switching in TbCo based Hall cross. The investigated ferrimagnetic sample is a thin film of Glass/Ta(5 nm)/$Tb_{27}Co_{73}$(20 nm)/Pt(3 nm) grown by DC magnetron sputtering. The film has a saturation magnetization M_s = 258 kA/m and an anisotropy constant K_1 = 0.58 10^6 J/m^3, leading to a perpendicular magnetization with a coercive field H_c = 360 mT. Furthermore, the studied $Tb_{27}Co_{73}$ alloy film is Tb dominant and present a compensation temperature above room temperature T_{comp} = 500 K. The sample is then patterned into 7-µm-wide and 10-µm-wide Hall crosses using optical lithography, and the all-optical switching ability is probed via the anomalous Hall effect, using both sweeping and static beam approaches depicted in section 4.2.1.

4.4.1 Sweeping beam measurement

We first investigate the sweeping beam measurements in the 7 µm-wide $Tb_{27}Co_{73}$ based Hall cross for the four combinations of circular helicity and initial magnetization saturation. The laser beam is swept over the whole x axis of the studied Hall cross from position -100 µm to 100 µm, with a sweeping speed of 40 µm/s and a power of 1.35 mW. Sweeping with left-circularly polarized beam is exemplarily shown in figure 4.28. The applied current is I = 0.5 mA and the typical value of the anomalous Hall voltage is V_{Hall} = 0.29 mV. The measured change of the anomalous Hall voltage in the Tb dominant $Tb_{27}Co_{73}$ based Hall cross corresponds to the Co sublattice magnetization "M_{Co}" change in agreement with previous studies [39, 40], since the conduction electrons come mainly from the Co sublattice. Therefore, the evolution of the anomalous Hall voltage is at the opposite of that of the net magnetization of the alloy "M_T".

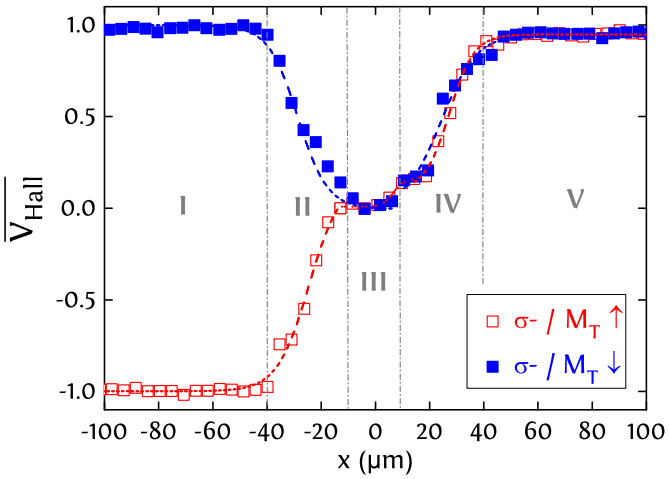

FIGURE 4.28: Normalized Hall voltage V_{Hall} as a function of the position of the beam x swept with left- handed circular polarization. The laser beam is swept with a sweeping speed of 40 µm/s and a power of 1.35 mW. The evolution of V_{Hall} corresponds to the Co sublattice magnetization change. The dashed lines are guides to the eyes.

The shapes of the curves in figure 4.28 are very similar to those demonstrated with a swept beam in Pt/Co/Pt based Hall crosses (see section 4.2.2). In region *I*, the laser beam is far from the center of the Hall cross and does not effect of the magnetization. In region *II*, the Hall voltage drops gradually to zero, which is probably due to a gradual presence of multiple domains. In region *III*, a zero plateau of the Hall voltage is obtained when the laser beam is well centered on the Hall cross, leading to the presence of multiple domains. In region *IV*, the helicity-dependent switching takes place since the second part of AOS rim goes through the Hall cross. Finally, in region *V* the laser beam is far from the center of the Hall cross, and left- (resp. right-) circularly polarized beam switches the Co sublattice magnetization M_{Co} to up (resp. down), and thus the net magnetization M_T to down (resp. up). In comparison with Pt/Co/Pt based Hall cross, figure 4.5 shows that right- (resp. left-) circularly polarized beam switches the net magnetization to down (resp. up). This finding is attributed to the fact that the helicity of switching depends on the orientation of the Co sublattice magnetization and not on the direction of the net magnetization of the Tb dominant $Tb_{27}Co_{73}$ alloy films [41].

4.4.2 Static beam measurement with an off-centered beam

Now we measure the helicity-dependent switching in a 10 µm-wide based Hall cross by performing the static beam measurement with an off-centered beam and both circular polarizations. As mentioned previously, the temporal resolution of the measurement is 150 ms. The applied current is I = 3 mA and the typical value of the anomalous Hall voltage is V_{Hall} = 2.05 mV. Figure 4.29 shows that σ- and σ+ switch M_{Co} to up and down, and thus M_T to down and up, respectively. A switching of about 90% is achieved and might be due to the small width of the AOS rim which is not completely covering the probed area of the Hall cross. This helicity-dependent switching is achieved independently of the initial magnetization saturation.

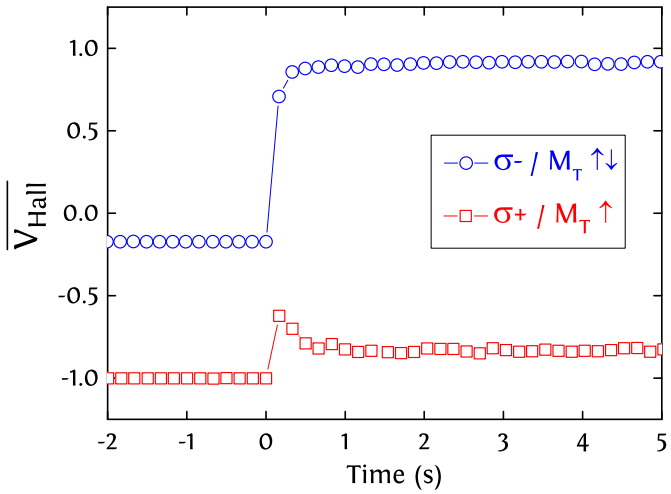

FIGURE 4.29: Time evolution of the normalized Hall voltage of the studied $Tb_{27}Co_{73}$ based Hall cross under the action of the off-centered laser beam with both circular polarizations. The evolution of V_{Hall} corresponds to the Co sublattice magnetization change.

We have additionally investigated the effect of adding a small external magnetic field H_{ex} of 20 mT while the off-centered beam is illuminating a 7 µm-wide $Tb_{27}Co_{73}$ based Hall cross. As shown in figure 4.30(a), the magnetization of the studied Hall cross is initially saturated up at "*A*" with H_{ex} = +20 mT. Since the studied alloy is Tb dominant and the measurement of V_{Hall} is mainly probing the Co sublattice, the sign of the Hall voltage while saturating with the positive H_{ex} is thus negative. Next, no magnetic field is applied at "*B*" and the off-centered beam with σ+ polarization is illuminating the probed Hall cross, leading to a switching of M_{Co} 80% to down. While at "C", the laser beam is still illuminating the Hall cross and a negative H_{ex} = - 20 mT is added. Surprisingly, M_{Co} follows the direction of the applied magnetic field and switches to down instead of up.

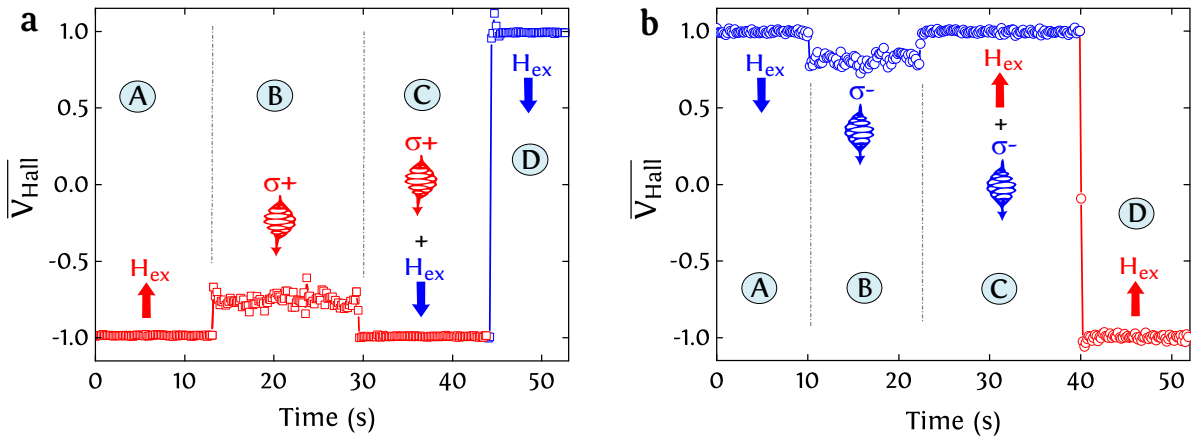

FIGURE 4.30: (a) and (b) Time evolution of the normalized Hall voltage while performing static beam measurement on the studied $Tb_{27}Co_{73}$ based Hall cross. The evolution of V_{Hall} corresponds to the Co sublattice magnetization change. In (a) (resp. (b), the Hall cross is initially saturated up (resp. down) in *"A"*. In *"B"*, the off-centered beam with σ+ (resp. σ-) polarization is illuminating the Hall cross. A negative (resp. positive) external magnetic field H_{ex} is added to the illuminated Hall cross in *"C"*. In *"D"*, the beam is turned off while H_{ex} is still applied.

In order to understand this behavior, we take into account the temperature dependence of Tb and Co sublattice magnetizations. The only way to explain this result is by assuming that the fs laser beam induces a temperature increase above T_{comp} = 500 K. Indeed, the $Tb_{27}Co_{73}$ alloy becomes Co dominant when T_{comp} is crossed due to laser heating [38, 42, 43]. Hence, despite that M_{Co} at *"B"* is pointing to down, M_T at *"B"* will also be pointing down. Therefore, the negative magnetic field at *"C"* will switch both M_T and M_{Co} to down. Finally, the σ+ polarized laser beam is turned off at *"D"* and negative magnetic field is still applied. The $Tb_{27}Co_{73}$ alloy becomes again Tb dominant since the temperature decreases to RT. Consequently, M_T (resp. M_{Co}) switches to down (resp. up) due to the negative magnetic field H_{ex} = - 20 mT.

This electrical measurement demonstrates that the fs laser beam with a power of 1.35 mW induces a local increase of the temperature of the probed area within the studied $Tb_{27}Co_{73}$ Hall cross above 500 K. This probed area is in the center of Hall cross and overlaps with the AOS rim. As depicted in figure 4.30(b), the same results are obtained by illuminating the Hall cross with σ- polarization and adding a positive external magnetic field.

4.4.3 Static beam measurement with a centered beam

We now continue by measuring the demagnetization of the 7-µm $Tb_{27}Co_{73}$ based Hall cross with a centered beam, thus the analog experiment to CoFeB/MgO based Hall cross depicted in figure 4.26. The time evolution of the anomalous Hall voltage is then measured when the circularly polarized centered beam with laser power of 1.35 mW is on and also when the latter is turned off, as depicted in figure 4.31.

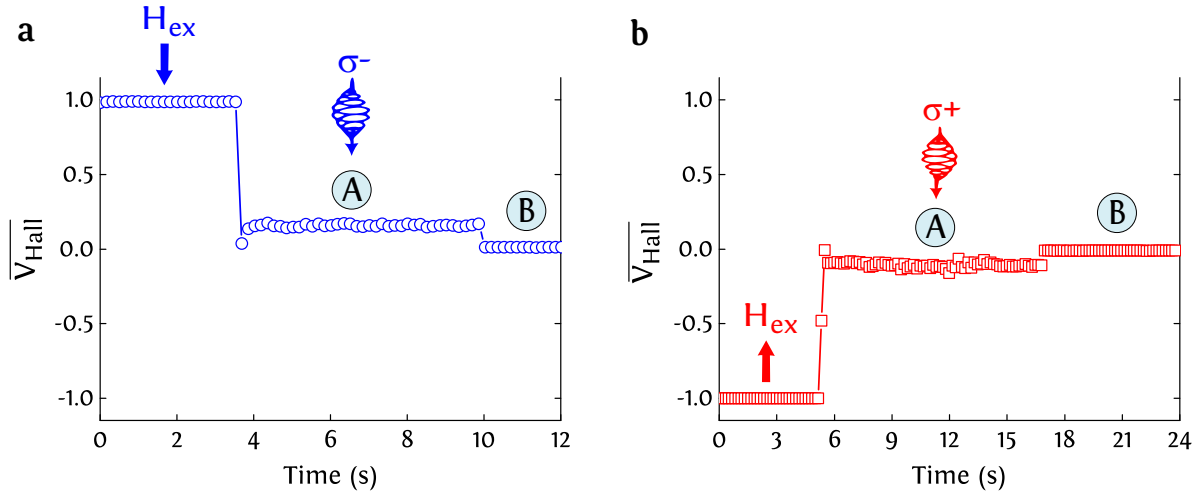

FIGURE 4.31: (a) (resp. (b)) Time evolution of the normalized Hall voltage while performing static beam measurement on the studied $Tb_{27}Co_{73}$ based Hall cross with an initial saturation down (resp. up) and σ- (resp. σ+) polarization. The laser beam is well centered and turned on in *"A"*, whereas it is turned off in *"B"*.

As shown in figure 4.31, the $Tb_{27}Co_{73}$ based Hall cross is overheated and thus demagnetized when the centered beam is on, leading to a plateau of the Hall voltage close to zero. A zero Hall voltage is also measured when the beam is turned off, since multiple domains are obtained due to the demagnetizing effects. This behavior is similar to the one measured in Pt/Co/Pt based Hall cross (see section 4.2.4). Moreover, it is different from the one measured in CoFeB/MgO based Hall crosses where a total reversal is achieved when the beam is turned off, as previously shown in section 4.3.2.

4.4.4 Summary

In section 4.4, we demonstrated the AO-HDS ability in $Tb_{27}Co_{73}$ based Hall crosses while the laser beam is swept or kept static and off-centered. The electrical measurements showed that the Tb dominant $Tb_{27}Co_{73}$ alloy becomes Co dominant due the laser-induced heating, indicating that the temperature of the probed area locally increase above T_{comp} = 500 K.

4.5 Two types of all-optical switching mechanism distinguished via the anomalous Hall effect

4.5.1 Introduction

The work presented in this part focuses on studying the microscopic mechanisms involved in the all-optical switching of different materials. By combining two different approaches, we experimentally investigated the all-optical switching in ferrimagnetic GdFeCo and TbCo alloys as well as ferromagnetic Co/Pt multilayers. In the first approach, the magnetic response to one or several fs laser pulses is imaged on a quasi-static time scale via magneto-optical Faraday imaging. In the second approach, the magnetization change under multiple-pulse exposure is probed by performing the static beam measurement with an off-centered beam on a much shorter time scale (see section 4.2.1). Hence, the main feature of using the magneto-transport measurement is to measure the magnetization change over a wide timescale ranging from 1 µs to a few seconds. In the following, we distinguish between two types of all-optical switching

mechanisms; a single-pulse helicity-independent switching in ferrimagnetic GdFeCo alloy films as previously shown [44, 45], and a two regimes helicity-dependent switching in ferrimagnetic TbCo alloys as well as ferromagnetic Co/Pt multilayers.

4.5.2 Single-pulse switching of GdFeCo based Hall crosses and continuous films

We have initially investigated the AO-HIS of ferrimagnetic 20 nm-thick Gd_{28} $Fe_{48}Co_{24}$ alloy capped, with 3 nm-thick Ta layer to prevent sample oxidation and grown on a Glass/Ta(3 nm) by DC magnetron sputtering. Due to the zero net orbital momentum of Gd, the spin-orbit coupling of Gd-based alloys is supposed to be small, leading to a low magneto-crystalline anisotropy. Hence, the studied $Gd_{28}Fe_{48}Co_{24}$ alloy film shows perpendicular magnetization in remanence. The RT coercive field is H_c = 20 mT. Moreover, $Gd_{28}Fe_{48}Co_{24}$ is Gd dominant and presents a T_{comp} above RT. The studied sample was also patterned into a 5 µm-wide Hall cross using optical lithography to perform the static beam measurement.

Helicity-independent single-pulse switching in continuous films

First of all, we verified the single-pulse AO-HIS in $Gd_{28}Fe_{48}$ Co_{24} continuous films. The studied continuous film is initially saturated up or down, prior to being excited with two consecutive pulses as depicted in figures 4.32(a) and 4.32(b), respectively. The single pulses are selected using a pulse picker and have a laser fluence of 19 mJ/cm^2.

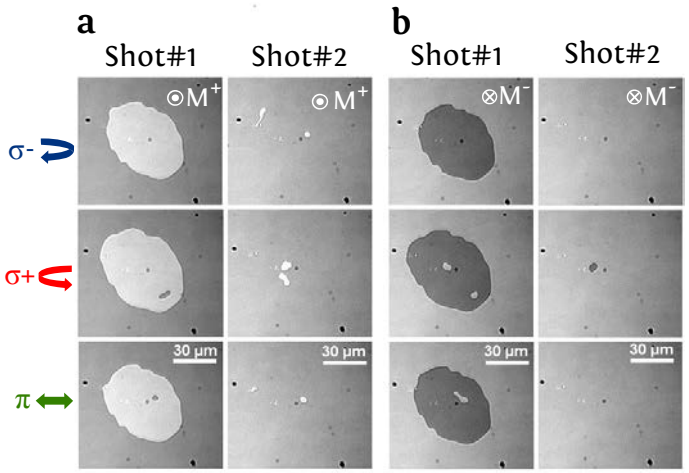

FIGURE 4.32: (a) and (b) Magneto-optical Faraday images of a $Gd_{28}Fe_{48}Co_{24}$ continuous film with initial magnetization saturation up and down, illuminated with two consecutive pulses with three different polarizations: from top to bottom, left circularly polarized pulse (σ-), right circularly polarized pulse (σ+) and linearly polarized pulse (π), and a laser fluence of 19 mJ/cm^2. Each of the two laser pulses illuminates the same region of the continuous film and induces a total magnetization reversal. The white (resp. dark) contrast in (a) (resp. (b)) corresponds to a reversal to down (resp. to up)

As shown in figure 4.32, a total reversal of magnetization occurs in the laser-excited area after the first pulse independently of its polarization and the initial magnetization saturation. The second pulse switches magnetization back to the saturated state, which is fully consistent with previous studies [45]. The laser-induced area gets larger by increasing the laser fluence. Its central area gets demagnetized with sufficiently high fluence due to overheating, whereas a large rim with helicity-independent switching is maintained. We now continue to measure the response of the studied $Gd_{28}Fe_{48}Co_{24}$ continuous film to the action of four consecutive

pulses. The sample is swept horizontally by 40 µm after each pulse, leading to an overlap between each two consecutive pulses. As shown in figure 4.33, each of the spacialy overlapped pulses switches completely the magnetization independently of the polarization and the initial magnetization saturation. Identical results were achieved on $Gd_{28}Fe_xCo_{72-x}$ alloy films for Fe concentration x = 57.6 and x = 60.

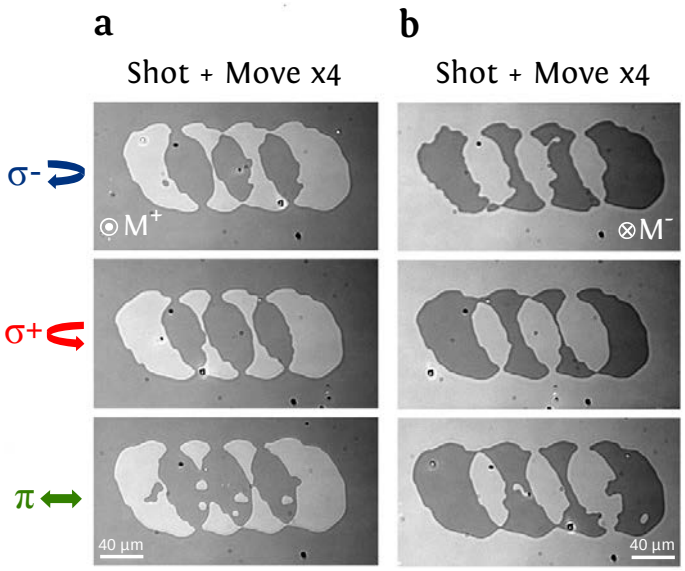

FIGURE 4.33: (a) and (b) Magneto-optical Faraday images of a $Gd_{28}Fe_{48}Co_{24}$ continuous film with initial magnetization saturation up and down, under the action of four 35-fs laser pulses with three different polarizations and a laser fluence of 19 mJ/cm^2. The sample is swept horizontally by 40 µm after each pulse, leading to an overlap between each two consecutive pulses. Each of the four laser pulses induces a total magnetization reversal of the illuminated area. The white (resp. dark) contrast in (a) (resp. (b)) corresponds to a magnetization pointing down (resp. up).

Helicity-independent single-pulse switching in Hall crosses

Next, we implement such single-pulse AO-HIS into $Gd_{28}Fe_{48}Co_{24}$ based Hall cross by performing the static beam measurement with an offcentered beam as introduced in section 4.2.1. First, the Hall cross is illuminated with a set of ten consecutive pulses, as depicted in figure 4.34. The measured change of the anomalous Hall voltage in the Gd dominant $Gd_{28}Fe_{48}Co_{24}$ based Hall cross corresponds to the FeCo sublattice magnetization "M_{FeCo}" change in agreement with previous studies [39, 40], since the conduction electrons come mainly from the 3d bands. Therefore, the evolution of the anomalous Hall voltage is at the opposite of that of the net magnetization of the alloy "M_T".

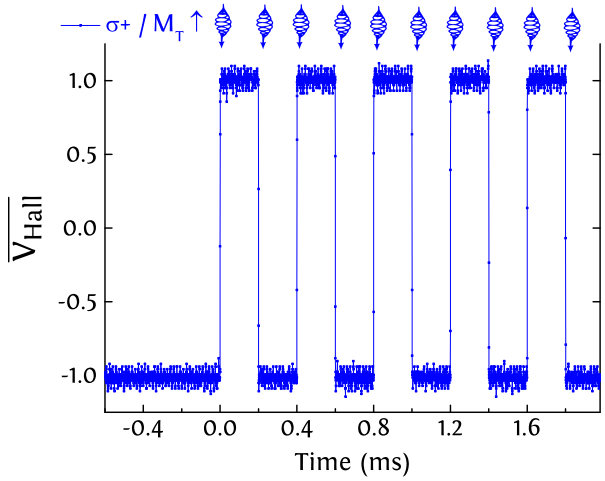

FIGURE 4.34: Time evolution of the normalized Hall voltage of a 5 µm-wide $Gd_{28}Fe_{48}Co_{24}$ based Hall cross under the action of ten consecutive pulses as marked with the blue pulses in the upper row, with initial magnetization saturation up with σ+ polarization and a repetition rate of 5 kHz. Each of the ten laser pulses illuminates the same region of the Hall cross and reverses the magnetization within it.

Each of the ten consecutive pulses with a repetition rate of 5 kHz switches completely the magnetization of the studied Hall cross. The same behavior has been measured for the six other combinations of pulse polarization and initial saturation. Moreover, identical results were obtained by illuminating the $Gd_{28}Fe_{48}Co_{24}$ Hall cross with a set of 1000 consecutive pulses. Moreover, the reversal time of the Hall voltage coincides with the temporal resolution of the measurement that equals 1 µs, as depicted in figure 4.35. This finding indicates that the reversal of magnetization takes a shorter time and is consistent with previous studies on GdFeCo continuous films [44].

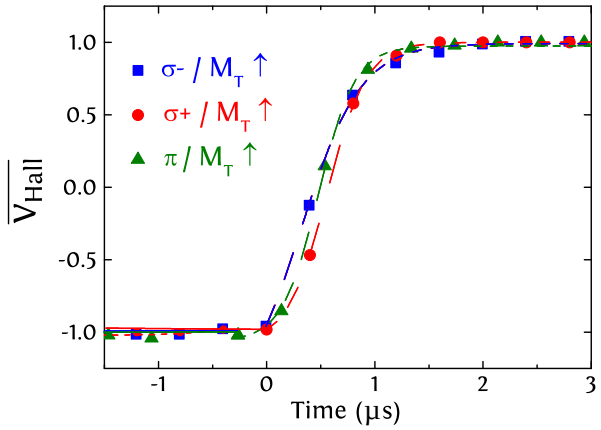

FIGURE 4.35: Reversal of the anomalous Hall voltage in the $Gd_{28}Fe_{48}Co_{24}$ based Hall cross under the action of a single laser pulse with three different polarizations and a fluence of 19 mJ/cm^2. Dashed lines are guides to the eyes.

4.5.3 Single-pulse induced demagnetization of $[Co/Pt]_N$ and TbCo continuous film

To give a novel insight into the all-optical switching mechanism in materials other than GdFeCo alloys, we now study the response of ferrimagnetic TbCo alloy films and ferromagnetic Co/Pt

multilayers to the action of two consecutive pulses. This experiment is thus the analog experiment to GdFeCo films shown in figure 4.32.

Co/Pt multilayers

The response to the action of single laser pulses in Co/Pt multilayers was investigated in two different samples; namely Pt/Co/Pt and $[Co/Pt]_3$ films as depicted in figures 4.36 and 4.39, respectively. As demonstrated previously in section 3.3.3, Pt/Co/Pt film presents AO-HDS with a swept beam, whereas $[Co/Pt]_3$ film shows only thermal demagnetization.

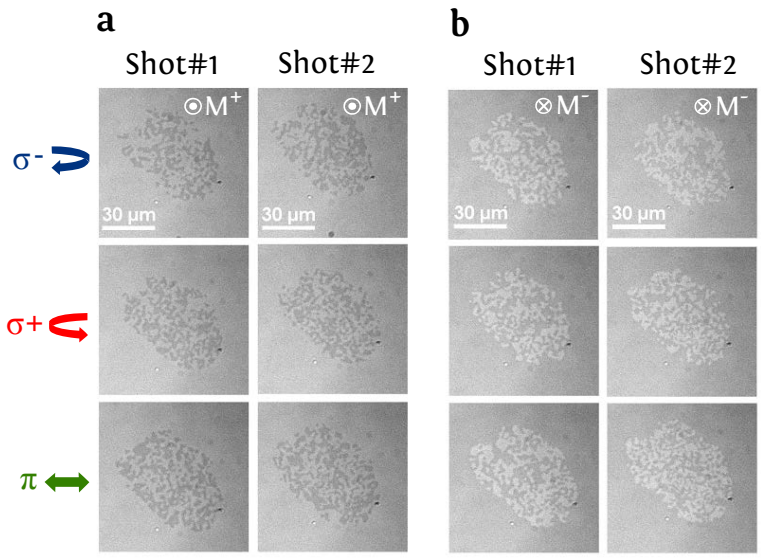

FIGURE 4.36: (a) and (b) Magneto-optical Faraday images of a Pt(4.5 nm)/Co(0.6 nm)/Pt(4.5 nm) continuous film with initial magnetization saturation up and down, illuminated with two consecutive pulses with three different polarizations and with an energy per pulse of 14 mJ/cm^2. Each of the two laser pulses induces thermal demagnetization of the irradiated area. The dark (resp. white) contrast in (a) (resp. (b)) corresponds to a reversal to down (resp. to up).

We first illuminate the Pt(4.5 nm)/Co(0.6 nm)/Pt(4.5 nm) film with two consecutive pulses with a laser fluence of 14 mJ/cm^2. Each of the two pulses induces a random thermal demagnetization independently of the initial magnetization saturation and pulse polarization, as depicted in figure 4.36. The domains distribution in the demagnetized area was quantified, leading to two close average values for magnetic domains up and down of approximately $50 \pm 2\%$. More importantly, one can see from figure 4.37 that the expected AOS rim does not emerge after two consecutive pulses for any of the six combinations of initial saturation and pulse polarization, confirming the cumulative aspect of the AO-HDS in Pt/Co/Pt films.

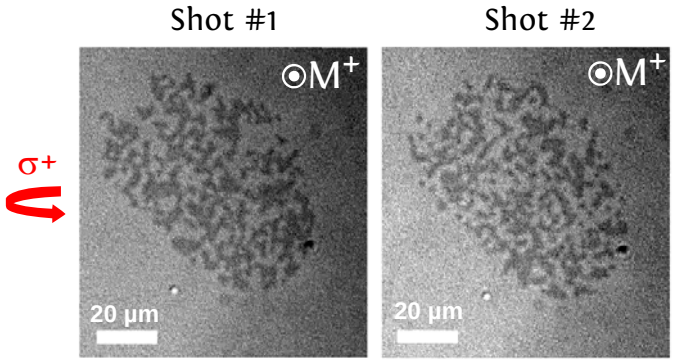

FIGURE 4.37: Magneto-optical Faraday images of a Pt(4.5 nm)/Co(0.6 nm)/Pt(4.5 nm) continuous film with initial magnetization saturation up, illuminated with two consecutive right-circularly polarized pulses with energy per pulse of 14 mJ/cm^2. The dark contrast corresponds to a reversal to down. Each of the two laser pulses induces thermal demagnetization of the irradiated area and the rim of helicity-dependent switching does not emerge.

Note that the fluence used in this experiment is high enough to induce a helicity-dependent switching with a laser beam swept over the sample, corresponding to an exposure time of the order of one second. Furthermore, only thermal demagnetization is obtained and the AOS rim does not completely emerge by varying the laser fluence from the demagnetization fluence threshold (F = 4.7 mJ/cm^2) to the damage fluence threshold (F = 70 mJ/cm^2), as shown in figure 4.38.

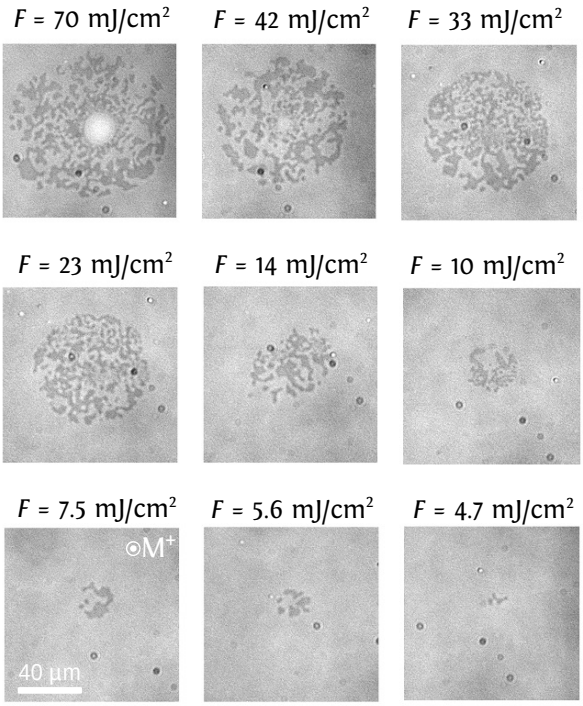

FIGURE 4.38: Magneto-optical Faraday images of a Pt(4.5 nm)/Co(0.6 nm)/Pt(4.5 nm) continuous film with initial magnetization saturation up, illuminated with a right-circularly polarized pulse with a fluence ranging from the switching fluence threshold (F = 4.7 mJ/cm^2) to the damage fluence threshold (F = 70 mJ/cm^2). The dark contrast corresponds to a reversal to down.

We now verify the laser-induced thermal demagnetization of $[Co(0.6\ nm)/Pt(0.7\ nm)]_3$ under the action of single laser pulse with a laser fluence of 14 mJ/cm^2. As shown in figure 4.39, small random magnetic domains are obtained independently of the initial magnetization saturation and pulse polarization. Moreover, it is hard to figure out the appearance of the AOS rim, since the magnetic domains are too small to be optically resolved. Nevertheless, the AOS rim is not expected to emerge taking into account the thermal demagnetization which is achieved in this material with a swept laser beam (see section 3.3).

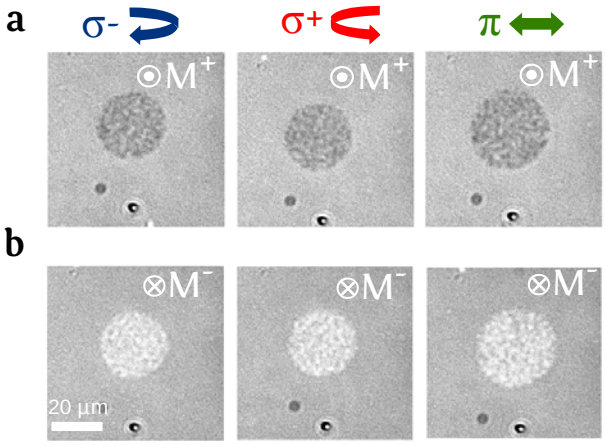

FIGURE 4.39: Magneto-optical Faraday images of a $[Co(0.6\ nm)/Pt(0.7\ nm)]_3$ continuous film illuminated with a 35-fs laser pulse with three different polarizations and a fluence of 14 mJ/cm^2. Each of the two laser pulses induces thermal demagnetization of the irradiated area. The dark (resp. white) contrast in (a) (resp. (b)) corresponds to a reversal to down (resp. to up). For each configuration, a thermal demagnetization of the irradiated area is obtained.

$Tb_{27}Co_{73}$ alloys

The helicity-dependent switching in 20 nm-thick $Tb_{27}Co_{73}$ alloy films was first obtained through multiple-pulse exposure with a swept laser beam [20, 38] or a static beam as demonstrated in section 4.4.2. This multiple-pulse switching is helicity-dependent and conserved for a laser fluence ranging from the switching fluence to the damage fluence threshold. Counterintuitively, this behavior is at the opposite of the one measured on ferrimagnetic GdFeCo alloy films for which the helicity-dependence was achieved only in a narrow range of fluence [46], and is similar to the one measured on ferromagnetic Co/Pt films. This begs the questions of what are the main differences between TbCo and GdFeCo alloys and is the switching mechanism the same for TbCo alloys and Co/Pt multilayers ?

Both studied GdFeCo and TbCo alloys have approximately the same RE concentration and are RE dominant at RT. They also have a similar T_{comp} around 500 K. Nevertheless, at the opposite of the zero orbital momentum of Gd, the orbital momentum in Tb is large, leading to a strong spin-orbit coupling and a large magneto-crystalline anisotropy. Moreover, it was shown that Gd- and Tb- based alloys show different ultrafast spin dynamics under the action of fs laser pulses [47], and also for pure elements [48]. Indeed, for both Gd- and Tb- based alloys, the transient ferromagnetic-like state is initiated. This transient state is followed by magnetization recovery in Tb-based alloy after the first 20 ps [47], whereas it is followed by magnetization reversal in Gd- based alloy [44]. These distinct magnetization dynamics were attributed to the large difference between SOC in Tb and Gd, and are a hint that the all-optical switching

mechanisms in Gd-based ferrimagnets and other ferrimagnets are distinct.

In the following we measure the response of $Tb_{27}Co_{73}$ continuous film to the action of two consecutive pulses with a fluence of 19 mJ/cm^2, thus the analog experiment to GdFeCo and Pt/Co/Pt films. As shown in figure 4.40, each of the two pulses induces thermal demagnetization of the laser-excited area independently of the pulse polarization and the initial magnetization saturation. As expected, these results are similar to the one measured on Pt/Co/Pt continuous films.

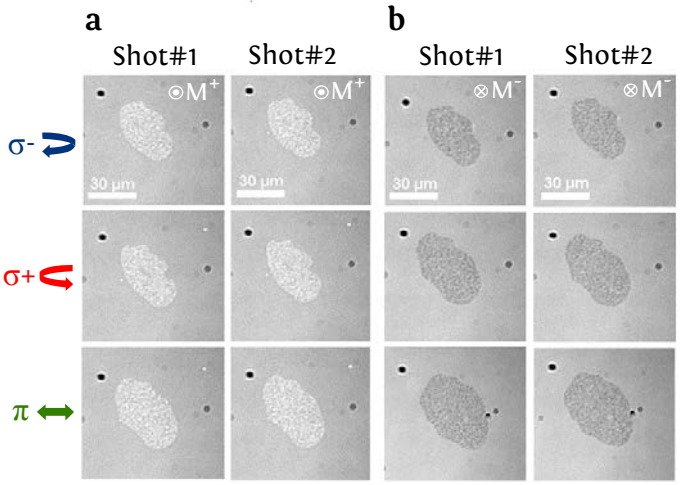

FIGURE 4.40: (a) and (b) Magneto-optical Faraday images of a TbCo alloy film, with initial magnetization saturation up and down, illuminated with two consecutive pulses with three different polarizations and with energy per pulse of 19 mJ/cm^2. Each of the two laser pulses induces thermal demagnetization of the irradiated area. The white (resp. dark) contrast in (a) (resp. (b)) corresponds to a reversal to down (resp. to up).

4.5.4 Multiple-shot switching of Co/Pt and TbCo based Hall crosses

Pt/Co/Pt based Hall cross

To elucidate the cumulative helicity-dependent switching process in Pt/Co/Pt films demonstrated with a swept beam in section 4.2.2, we now quantify the magnetization change in a 5 µm-wide Pt/Co/Pt based Hall cross under multiple-pulse exposure while performing the static beam measurement. Figure 4.41 shows the time-dependent evolution of the anomalous Hall voltage under the action of 600 consecutive pulses with a laser fluence of 10 mJ/cm^2, for different combinations of laser polarization and initial magnetization saturation. One can see from figure 4.44 that the reversal of the anomalous Hall voltage follows a two regimes process taking place at two different timescales. Indeed, a helicity-independent drop is induced by 6 pulses within the first 1 ms, which is followed by a helicity-dependent reversal of the Hall voltage on several tens of ms.

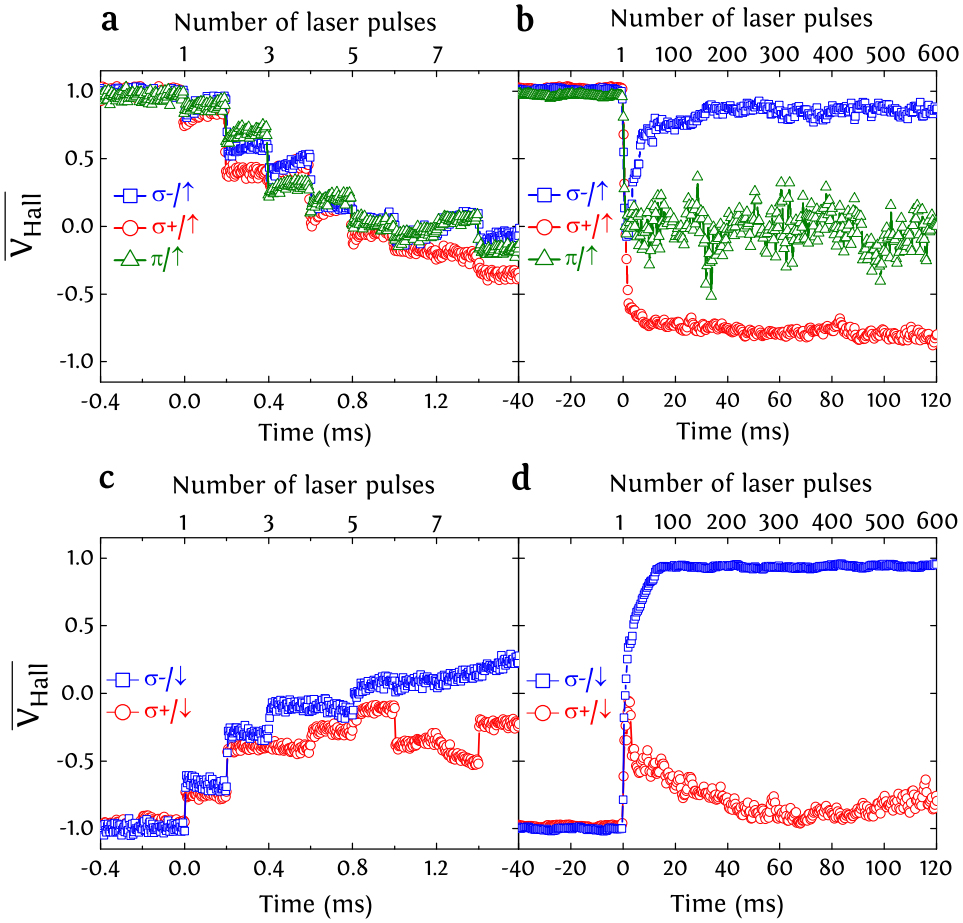

FIGURE 4.41: (a) and (b) Time evolution of the anomalous Hall voltage of a 5-µm-wide Pt(4.5 nm)/Co(0.6 nm)/Pt(4.5 nm) Hall cross initially saturated up, under the action of a 35-fs laser beam with a 5 kHz repetition rate and a fluence of 10 mJ/cm^2. The corresponding number of laser pulses is shown in the upper row. The helicity-dependent switching of the studied Hall cross is governed by a two-step process at two different timescales: (a) helicity-independent demagnetization within the first 1 ms. (b) helicity-dependent reversal measured on a 120 ms timescale. (c) and (d), the same behavior is measured as (a) and (b) with initial magnetization saturation down. The experimental temporal resolution of the experiment is 1 µs.

First, as shown in figures 4.41(a) and 4.41(c), the Hall voltage follows a step-like decrease within the first 1 ms due to the action of the 6 first pulses. Each jump is induced by a single pulse and coincides with the temporal resolution of 1 µs, indicating that each jump is occurring on a shorter time scale. These results are a hint that the studied Hall cross is subject to multiple-pulse demagnetization. Moreover, the helicity-independence highlights the important role of laser heating in this process. A slight increase of the Hall voltage toward its initial value after each pulse is measured. This behavior might be due to a slow magnetization relaxation toward its thermal equilibrium. This behavior might be due to a slow magnetization relaxation toward its thermal equilibrium induced by the cooling of the material.

To further investigate this step-like demagnetization, we added a small external magnetic field H_{ex} of 20 mT to the laser-illuminated Hall cross as shown in figure 4.42. No change of the anomalous Hall voltage is measured, thus excluding a significant change of the Hall resistivity and indicating that the measured demagnetization within the first 1 ms corresponds to a helicity-independent step-like multiple-domain formation. Indeed, the heating effect due to the first 6 pulses helps to bring the magnetic system in a demagnetized state, which reduces the demagnetizing energy. This demagnetized state consists of magnetic domains with random orientations up and down, whose size is smaller than the Hall cross area.

Second, figures 4.41(b) and 4.41(d) demonstrate that the effect of the helicity starts to appear only after crossing the zero Hall voltage, which corresponds to a fully demagnetized multi-domain state. Independently of the initial magnetization saturation, the anomalous Hall voltage and thus the magnetization of the Hall cross under the action of left- and right-circularly polarized pulses starts remagnetizing to up and down, respectively. Only 90% of the switching is achieved and might be due to the small width of the AOS rim, as previously mentioned in section 4.2.3. Furthermore, the reversal using circular polarized pulses with this used laser fluence is obtained only after an exposure time of approximately 30 ms, corresponding to 150 consecutive pulses. On the other hand, the Hall voltage under the excitation of linearly polarized pulses oscillates around the zero value up to 120 ms, as shown in figure 4.41(b). This finding indicates that multidomain configuration is permanently obtained with linear polarization.

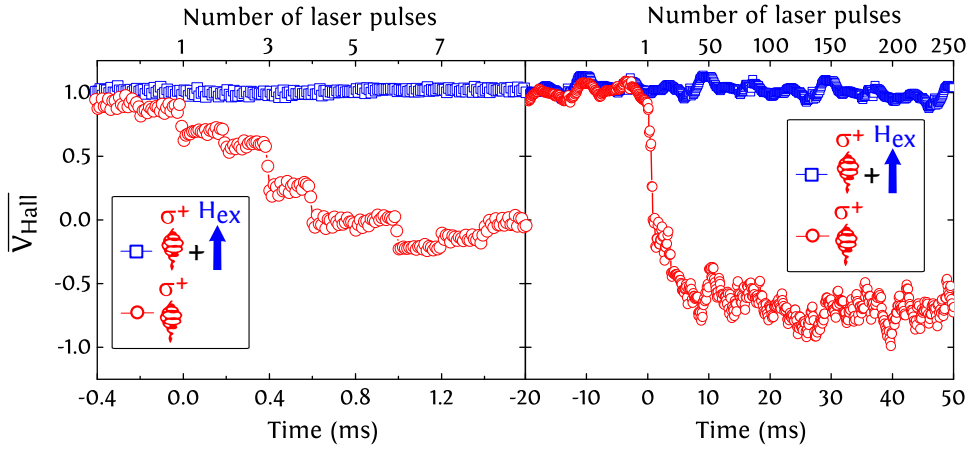

FIGURE 4.42: (a) and (b) Time evolution of the anomalous Hall voltage of a 5-µm-wide Pt(4.5 nm)/Co(0.6 nm)/Pt(4.5 nm) Hall cross initially saturated up, under the action of a 35-fs laser beam with a 5 kHz repetition rate and a laser fluence of 10 mJ/cm^2, with (blue curve) and without (red curve) adding a small external magnetic field H_{ex} of approximatively 20 mT.

Note that when the investigated Pt/Co/Pt Hall cross has an initial magnetization saturation up (resp. down), the remagnetization achieved with the right- (resp. left-) circularly polarized pulses and leading to a reversal to down (resp. up) takes place slightly before the opposite circular polarization. We attribute this behavior to the demagnetizing field which favors the magnetization reversal of the Hall cross in the opposite direction of the initial magnetization saturation. This demagnetizing field is mainly due to the outer parts of the Hall cross which remain unperturbed. To conclude, these experiments demonstrate that the all-optical switching of Pt/Co/Pt Hall crosses is helicity-dependent, cumulative and only achieved after a step-like multiple-domain formation. Therefore, this switching process is drastically different

from the GdFeCo switching mechanism.

We have additionally investigated the fluence dependence of the two regime reversal of the Pt/Co/Pt based Hall cross under multiple pulse illumination, as depicted in figure 4.43. The initial magnetization saturation up and σ+ polarization is exemplarily shown. As shown in figure 4.43(a), the step-like multiple-domain formation is maintained for a large range of fluence down to 20% of the switching fluence threshold. Nevertheless, figure 4.43(b) show that the helicity-dependent remagnetization vanishes for low fluences. This behavior is attributed to the spatial shift of the AOS rim, as previously demonstrated in section 4.2.3. Note that the small size of the AOS rim makes it difficult to overlap it with the center of the Hall cross after each decrease of the laser fluence. These findings indicate that the laser fluence does not play a primary role in the cumulative and two regimes switching of Pt/Co/Pt films.

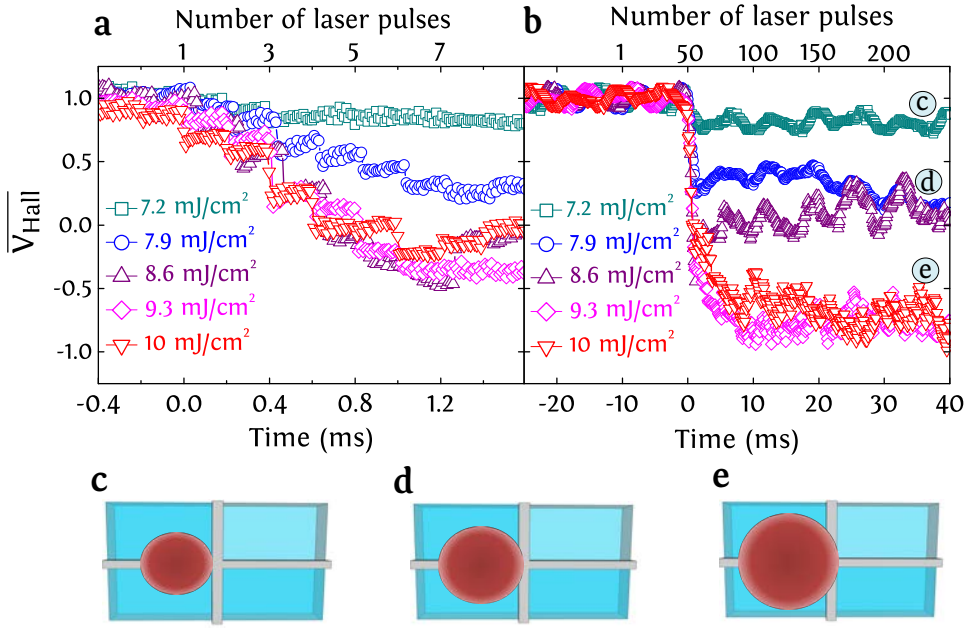

FIGURE 4.43: (a) and (b) Time evolution of the anomalous Hall voltage of a 5-µm-wide Pt(4.5 nm)/Co(0.6 nm)/Pt(4.5 nm) Hall cross initially saturated up, under the action of a 35-fs right circularly polarized laser beam with a 5 kHz repetition rate and a laser fluence ranging from 7.2 mJ/cm^2 to 10 mJ/cm^2. (c), (d) and (e), schematic evolution of the diameter of the laser-induced area for laser fluences of 7.2 mJ/cm^2, 7.9-8.6 mJ/cm^2 and 9.3-10 mJ/cm^2, respectively.

We continue by measuring the demagnetization of a 20-µm wide Pt/Co/Pt Hall using the same laser fluence F = 10 mJ/cm^2, as shown in figure 4.44. The demagnetized state is reached only after an exposure time of 6 ms, corresponding to 30 consecutive pulses. This finding indicates that the number of pulses required to achieve the helicity-independent multiple-domain formation is related to the Hall cross size. The remagnetization does not take place in the 20-µm wide Hall cross since the AOS rim only overlaps with a small area of the cross.

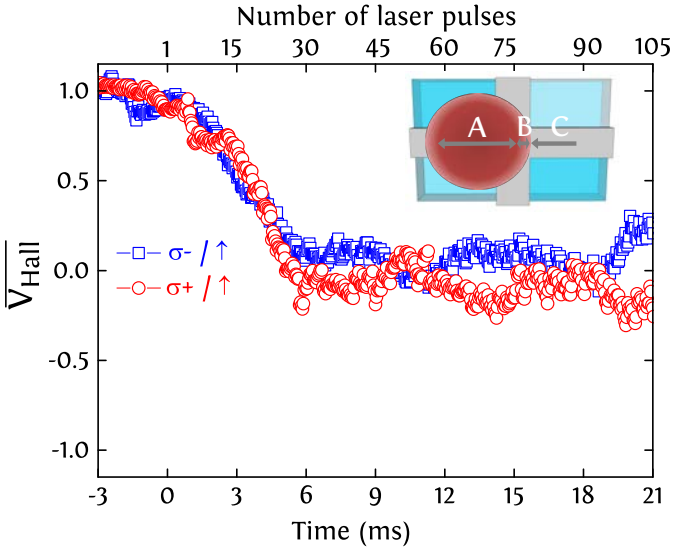

FIGURE 4.44: Time evolution of the anomalous Hall voltage of a 20-µm-wide Pt(4.5 nm)/Co(0.6 nm)/Pt(4.5 nm) Hall cross initially saturated up, under the action of a 35-fs laser beam with a 5 kHz repetition rate and a laser fluence of 10 mJ/cm^2. A helicity-independent demagnetization occurs within the first 6 ms (30 pulses) followed by an oscillation of the Hall voltage around the zero value. The inset shows the schematic representation of the different areas of the fs laser beam: *"A"* where multiple magnetic domains are obtained, *"B"* is the AOS rim; and *"C"* where no change of magnetization is induced. The remagnetization does not take place since the helicity-dependent switching rim (2-4 µm size) only overlaps with a small area of the 20-µm-wide Hall cross.

Next, we measure the magnetization reversal in the studied 5-µm-wide Pt/Co/Pt based Hall cross under the action of 600 consecutive pulses and with σ+ polarization and an initial partially demagnetized state ($\overline{V_{Hall}} = \pm 0.25$) . As shown in figure 4.45, a pure demagnetized state is achieved with the two first pulses. Then, the gradual reversal to down takes place and a reliable switching is obtained only after an exposure time of approximately 30 ms, corresponding to 150 consecutive pulses.

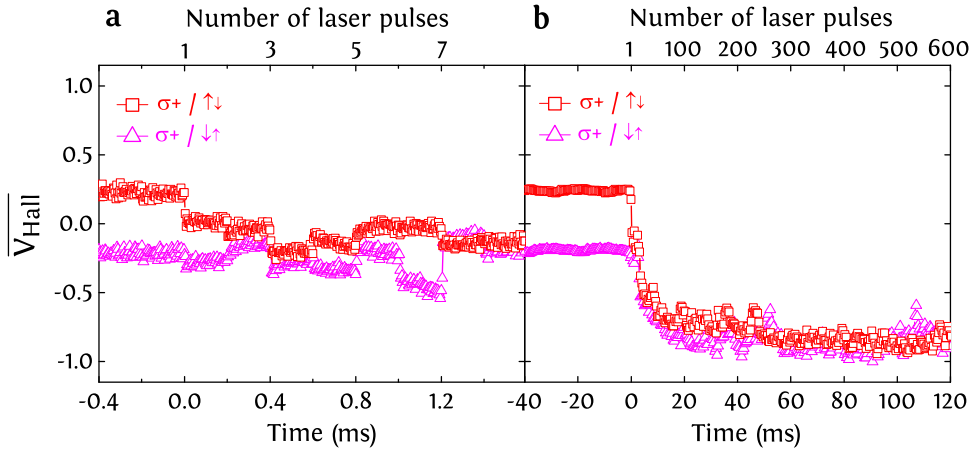

FIGURE 4.45: (a) and (b) Time evolution of the anomalous Hall voltage of a 5-µm-wide Pt(4.5 nm)/Co(0.6 nm)/Pt(4.5 nm) Hall cross which is initially partially demagnetized ($\overline{V_{Hall}} = \pm 0.25$), under the action of right-circularly polarized beam with a 5 kHz repetition rate and a laser fluence of 10 mJ/cm^2.

$[Co/Pt]_3$ based Hall cross

We now investigate the time evolution of the anomalous Hall voltage in $[Co/Pt]_3$ based Hall cross under the action of 600 consecutive pulses with a laser fluence of 14 mJ/cm^2 and three different polarizations. As previously demonstrated in section 3.3.3, only thermal demagnetization was obtained in a $[Co/Pt]_3$ continuous film with a swept beam. One can see from figure 4.46(a) that a step-like multiple-domain formation is first induced in the studied $[Co/Pt]_3$ Hall cross with the first 6 pulses, similarly to Pt/Co/Pt based Hall crosses. As expected, a zero plateau of the Hall voltage is then measured after the first 6 pulses as shown figure 4.46(b). This indicates that a multidomain configuration is permanently obtained with the laser beam independently of its polarization, and is attributed to the small size of magnetic domains in $[Co/Pt]_3$ films (see section 3.4.2).

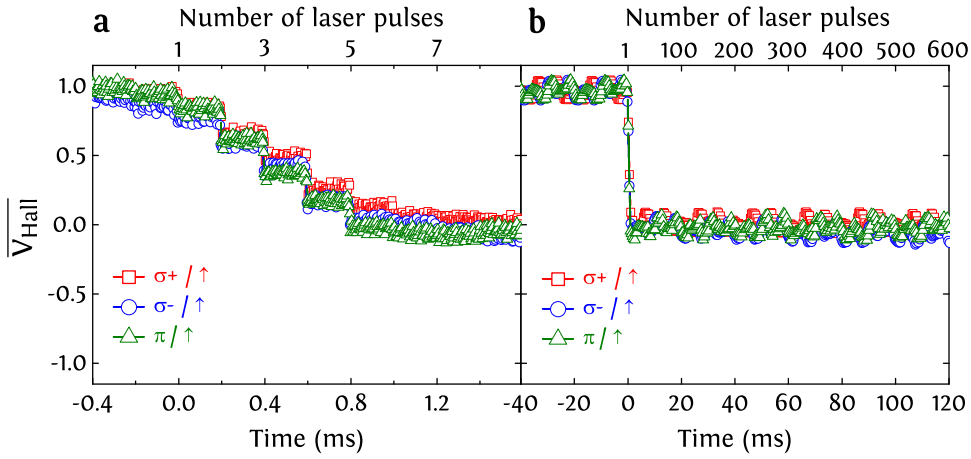

FIGURE 4.46: (a) and (b) Time evolution of the anomalous Hall voltage of a 5-µm-wide [Pt(0.7 nm)/Co(0.6 nm)]$_3$ Hall cross initially saturated up, under the action of a 35-fs laser beam with a 5 kHz repetition rate and a fluence of 19 mJ/cm^2.

$Tb_{27}Co_{73}$ based Hall cross

We now turn our attention to the switching process in ferrimagnetic $Tb_{27}Co_{73}$ alloys via the same time-dependent measurements performed on GdFeCo and Co/Pt based Hall crosses. Indeed, we probed the magnetization change of a $Tb_{27}Co_{73}$ based Hall cross under the action of 600 consecutive pulses for the four combinations of circular polarization and initial saturation. As depicted in figures 4.47(a) and 4.47(b), the response of the anomalous Hall voltage to laser pulses is very similar to the one measured on Pt/Co/Pt Hall crosses, since it is also governed by a two regimes process. First, a step-like helicity-independent multiple-domain formation within the first 1 ms. Second, a gradual helicity-dependent remagnetization takes place within a 100 ms timescale, indicating that 500 pulses are needed to obtain a reliable switching. To conclude, these experiments undoubtedly demonstrate that two types all-optical switching mechanism can be distinguished; namely the single-pulse helicity-independent switching in ferrimagnetic GdFeCo alloy films, and a cumulative two regimes switching in ferrimagnetic TbCo alloys and ferromagnetic Pt/Co/Pt multilayers. More importantly, we show that for the latter, the helicity-dependent remagnetization takes place only after a step-like helicity-independent domain formation. In the following, we will discuss the microscopic origin of the demonstrated two regimes switching process.

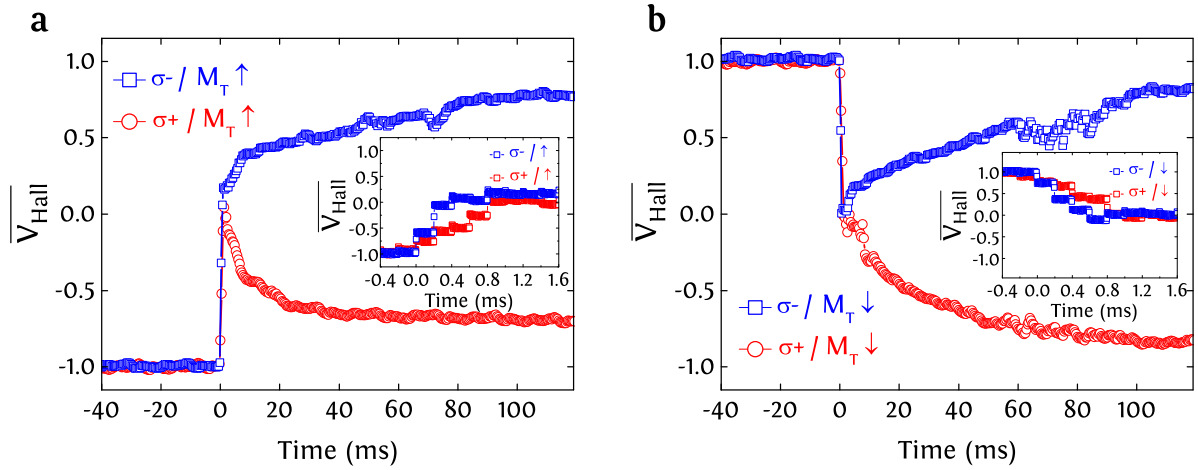

FIGURE 4.47: (a) and (b) Helicity-dependent reversal of the anomalous Hall voltage of a $Tb_{27}Co_{73}$ based Hall cross initially saturated up and down within a 120 ms timescale. The experiment is performed using a 35-fs laser beam with a 5 kHz repetition rate and a fluence of 19 mJ/cm^2. The corresponding number of laser pulses is shown in the upper row. The inset in (a) (resp. (b)) shows the helicity-independent demagnetization of the Hall cross with an initial saturation magnetization up (resp. down) occurring within the first 1 ms.

4.5.5 Discussion: Microscopic origin of multiple-pulse helicity- dependent switching

The main conclusion of these time-dependent measurements is that there are two different all-optical switching mechanisms. The most intriguing part of the observed reversal mechanism in Pt/Co/Pt and TbCo films is the helicity-dependent remagnetization that takes place only after the helicity-independent multiple domain formation. A potential scenario of such remagnetization would be a helicity-dependent domain wall (DW) motion.

Indeed, once the heat-only multiple domain state is achieved, a space-dependent symmetry breaking might arise from a difference in absorption of the two circular polarizations in the different materials. This particular point is in agreement with previous studies on GdFeCo films demonstrating the role of magnetic circular dichroism (MCD) in the helicity-dependent switching obtained with multiple- or single-pulse exposure [46]. Therefore, the domain-dependent and thus space-dependent absorption would create a non-uniform heat distribution in the multiple domain state, thus stimulating spin currents via the spin Seebeck effect (SSE) [49, 50]. Following this, these stimulated spin currents passing through a domain wall might induce a spin transfer torque (STT) leading to a helicity-dependent shift of DWs and thus to the gradual helicity-dependent remagnetization [51, 52, 53]. Moreover, the motion of magnetic DWs might be purely thermal due to the time-dependent thermal gradient, as demonstrated by Torrejon *et al.* [54]. Furthermore, superdiffusive spin currents might also play a major role in the helicity-dependent remagnetization, as it has already been shown on GdFeCo alloys [55]. On the other hand, recent studies have shown that the all-optical switching of Co/Pt multilayers could also be explained by the inverse Faraday effect (IFE) [3]. However, the reversal in these models is obtained with a single laser pulse, which is not consistent with the measured cumulative reversal in Co/Pt multilayers. Hence, IFE is less likely to explain the helicity-dependent remagnetization.

One last issue we discuss here is the reason why the two regimes process does not take place again after the magnetization reaches the steady state, especially when the helicity which is

used does not lead to a reversal. Indeed, only the central area of the cross is probed with the anomalous Hall effect. Hence, a changed domain configuration in the surroundings of the probed area cannot be measured and might be the underlying difference with the initial state. As already mentioned, the all-optical switching in such materials occurs only in the AOS rim with an optimal intensity at the edge of demagnetized area [2]. Therefore, the main difference between the initial and steady state is the multiple domains obtained in the surroundings of the Hall cross center at the steady state. Such explanation is consistent with the role of magnetic domains as well as DW motion in the cumulative switching process in Pt/Co/Pt multilayers and TbCo alloys.

4.5.6 Summary

In section section 4.5, we investigated the underlying microscopic physics of the all-optical switching in ferro- and ferri-magnetic materials, namely ferromagnetic Pt/Co multilayers, as well as ferrimagnetic TbCo and GdFeCo alloys. Hence, we combined two different approaches to investigate the all-optical switching in ferrimagnetic GdFeCo and TbCo alloys and ferromagnetic Co/Pt multilayers. In the first approach, the magnetic response to one or two 35-fs laser pulses is imaged on a quasi-static time scale via magneto-optical Faraday imaging. While in the second approach, the magnetization change under multiple-pulse exposure is probed by performing the static beam measurement in Hall crosses with an off-centered beam and a temporal resolution of 1 μs.

We demonstrated that two different types of all-optical switching processes can be distinguished. The first type is the single-pulse helicity-independent switching in ferrimagnetic GdFeCo alloy films as shown in previous studies, while the second type is a two regimes helicity-dependent switching in both ferrimagnetic TbCo alloys and ferromagnetic Co/Pt multilayers. More importantly, we showed that the latter takes place at two different timescales, and consists in a step-like helicity-independent multiple-domain formation within the first 1 ms followed by a helicity-dependent remagnetization on several tens of ms. We attributed this remagnetization to a helicity-dependent domain wall motion. Indeed, once the heat-only multiple domain state is achieved, a space-dependent symmetry breaking might arise from a difference in absorption of the two circular polarizations, stimulating spin currents via the spin Seebeck effect and leading to the shift of domain walls and thus to the gradual helicity-dependent remagnetization. On the other hand, the inverse Faraday effect could also explain the helicity-dependent remagnetization as demonstrated in recent theoretical investigations. However, the reversal in these models is obtained with a single laser pulse, which is not consistent with the measured cumulative reversal in Co/Pt multilayers.

References

[1] C. Caspers, D. Yoon, M. Soundararajan and J. - P. Ansermet, Opto-spintronics in InP using ferromagnetic tunnel spin filters *New J. Phys.* **17**, 022004 (2015).

[2] C.-H. Lambert, S. Mangin, B. S. D. C. S. Varaprasad, Y. K. Takahashi, M. Hehn, M. Cinchetti, G. Malinowski, K. Hono, Y. Fainman, M. Aeschlimann *et al.*, All-optical control of ferromagnetic thin films and nanostructures *Science* **345**, 1337–1340 (2014).

[3] T. D. Cornelissen, R. Cordoba, and B. Koopmans, Microscopic model for all optical switching in ferromagnets *Appl. Phys. Lett.* **108**, 142405 (2016).

[4] E. Beaurepaire, J. Merle, A. Daunois, and J. Bigot, Ultrafast spin dynamics in ferromagnetic nickel *Phys. Rev. Lett.* **76**, 4250 (1996).

[5] J.-Y. Bigot, M. Vomir, and E. Beaurepaire, Coherent ultrafast magnetism induced by femtosecond laser pulses *Nat. Phys.* **5**, 515–520 (2009).

[6] G. Malinowski, F. Dalla Longa, J. H. H. Rietjens, P. V. Paluskar, R. Huijink, H. J. M. Swagten, and B. Koopmans, Control of speed and efficiency of ultrafast demagnetization by direct transfer of spin angular momentum *Nat. Phys.* **4**, 855–858 (2008).

[7] C. Chappert, A. Fert, and F. Nguyen Van Dau, The emergence of spin electronics in data storage *Nat. Mater.* **6**, 813–823 (2007).

[8] S. A. Wolf, D. D. Awschalom, R. A. Buhrman, J. M. Daughton, S. von Molnar, M. L. Roukes, A. Y. Chtchelkanova, and D. M. Treger, Spintronics: a spin-based electronics vision for the future *Science* **294**, 1488–1495 (2001).

[9] A. D. Kent and D. C. Worledge, A new spin on magnetic memories *Nat. Nanotechnol.* **10**, 187–191 (2015).

[10] S. Parkin and S.-H. Yang, Memory on the racetrack *Nat. Nanotechnol.* **10**, 195–198 (2015).

[11] M. H. Kryder, E. C. Gage, T. W. McDaniel, W. A. Challener, R. E. Rottmayer, G. P. Ju, Y. T. Hsia, and M. F. Erden, Heat assisted magnetic recording *Proc. IEEE* **96**, 1810–1835 (2008).

[12] B. C. Stipe, T. C. Strand, C. C. Poon, H. Balamane, T. D. Boone, J. A. Katine, J. L. Li, V. Rawat, H. Nemoto, A. Hirotsune *et al.*, Magnetic recording at 1.5 Pb m^{-2} using an integrated plasmonic antenna *Nat. Photonics* **4**, 484–488 (2010).

[13] J. M. Luttinger, Theory of the Hall effect in ferromagnetic substances *Phys. Rev.* **112**, 739 (1958).

[14] L. Berger, Side-jump mechanism for the Hall effect of ferromagnets *Phys. Rev. B* **2**, 4559 (1970).

[15] C. D. Stanciu, F. Hansteen, A. V. Kimel, A. Kirilyuk, A. Tsukamoto, A. Itoh, and T. Rasing, All-optical magnetic recording with circularly polarized light *Phys. Rev. Lett.* **99**, 047601 (2007).

[16] J. Moritz, B. Rodmacq, S. Auffret, and B. Dieny, Extraordinary Hall effect in thin magnetic films and its potential for sensors, memories and magnetic logic applications *J. Phys. D: Appl. Phys.* **41**, 135001 (2008).

[17] L. Liu, O. J. Lee, T. J. Gudmundsen, D. C. Ralph, and R. A. Buhrman, Current-induced switching of perpendicularly magnetized magnetic layers using spin torque from the spin Hall effect *Phys. Rev. Lett.* **109**, 096602 (2012).

[18] J.-C. Rojas-Sanchez, P. Laczkowski, J. Sampaio, S. Collin, K. Bouzehouane, N. Reyren, H. Jaffres, A. Mougin, and J.-M. George, Perpendicular magnetization reversal in Pt/$[Co/Ni]_3$/Al multilayers via the spin Hall effect of Pt *Appl. Phys. Lett.* **108**, 082406 (2016).

[19] A. Kirilyuk, A. V. Kimel, and T. Rasing, Laser-induced magnetization dynamics and reversal in ferrimagnetic *Rep. Prog. Phys.* **7** (2), 026501 (2013).

[20] S. Mangin, M. Gottwald, C.-H. Lambert, D. Steil, V. Uhlir, L. Pang, M. Hehn, S. Alebrand, M. Cinchetti, G. Malinowski *et al.*, Engineered materials for all-optical helicity-dependent magnetic switching *Nat. Mater.* **13**, 286–292 (2014).

[21] Y. Mimura, N. Imamura, T. Kobayashi, Thermomagnetic writing on Gd–Fe and Gd–Fe–Y amorphous films *Jpn. J. Appl. Phys.* **17**, 1365 (1978).

[22] A. Hassdenteufel, B. Hebler, C. Schubert, A. Liebig, M. Teich, M. Helm, M. Aeschlimann, M. Albrecht, and R. Bratschitsch, Thermally assisted all-optical helicity dependent magnetic switching in amorphous $Fe_{100-x}Tb_x$ alloy films *Adv. Mater.* **25**, 3122 (2013).

[23] J. Heinen, O. Boulle, K. Rousseau, G. Malinowski, M. Klaui, H. J. M. Swagten, B. Koopmans, C. Ulysse and G. Faini, Current-induced domain wall motion in Co/Pt nanowires: Separating spin torque and Oersted-field effects *Appl. Phys. Lett.* **96**, 202510 (2010).

[24] T. Y. Cheng, J. Wu, M. Willcox, T. Liu, J. W. Cai, R.W. Chantrell, and Y. B. Xu, Temperature dependence of all-optical ultrafast magnetization switching in TbFeCo *IEEE Trans. Magn.* **48**, 3387 (2012).

[25] S. Alebrand, A. Hassdenteufel, D. Steil, M. Cinchetti, and M. Aeschlimann, Interplay of heating and helicity in all-optical magnetization switching *Phys. Rev. B* **85**, 092401 (2012).

[26] A. Hassdenteufel, J. Schmidt, C. Schubert, B. Hebler, M. Helm, M. Albrecht, and R. Bratschitsch, Low remanence criterion for helicity-dependent all-optical magnetic switching in ferrimagnets and heterostructures *Phys. Rev. B* **91**, 104331 (2015).

[27] S. Mangin, D. Ravelosona , J. A. Katine, M. J. Carey, B. D. Terris and E. E. Fullerton, Current-induced magnetization reversal in nanopillars with perpendicular anisotropy *Nat. Mater.* **5**, 210 - 215 (2006).

[28] S. S. P. Parkin, C. Kaiser, A. Panchula, P. M. Rice, B. Hughes, M. Samant and S.-H. Yang, Giant tunnelling magnetoresistance at room temperature with MgO (100) tunnel barriers *Nat. Mater.* **3**, 862–867 (2004).

[29] S. Yuasa, T. Nagahama, A. Fukushima, Y. Suzuki and K. Ando, Giant room-temperature magnetoresistance in single-crystal Fe/MgO/Fe magnetic tunnel junctions *Nat. Mater.* **3**, 868–871 (2004).

[30] S. Ikeda, K. Miura, H. Yamamoto, K. Mizunuma, H. D. Gan, M. Endo, S. Kanai, J. Hayakawa, F. Matsukura and H. Ohno, A perpendicular-anisotropy CoFeB–MgO magnetic tunnel junction *Nat. Mater.* **9**, 721–724 (2010).

[31] S. Fukami, T. Suzuki, Y. Nakatani, N. Ishiwata, M. Yamanouchi, S. Ikeda, N. Kasai and H. Ohno, Current-induced domain wall motion in perpendicularly magnetized CoFeB nanowire *Appl. Phys. Lett.* **98**, 082504 (2011).

[32] T. Suzuki, S. Fukami, N. Ishiwata, M. Yamanouchi, S. Ikeda, N. Kasai and H. Ohno, Current-induced effective field in perpendicularly magnetized Ta/CoFeB/MgO wire *Appl. Phys. Lett.* **98**, 142505 (2011).

[33] T. Devolder, P.-H. Ducrot, J.-P. Adam, I. Barisic, N. Vernier, Joo-Von Kim, B. Ockert and D. Ravelosona, Damping of $Co_xFe_{80-x}B_{20}$ ultrathin films with perpendicular magnetic anisotropy *Appl. Phys. Lett.* **102**, 022407 (2013).

[34] H. Meng, W. H. Lum, R. Sbiaa, S. Y. H. Lua, and H. K. Tan, Annealing effects on CoFeB-MgO magnetic tunnel junctions with perpendicular anisotropy *J. Appl. Phys.* **110**, 033904 (2011).

[35] H. Meng, R. Sbiaa, C. C. Wang, S. Y. H. Lua, and M. A. K. Akhtar, Annealing temperature window for tunneling magnetoresistance and spin torque switching in CoFeB/MgO/CoFeB perpendicular magnetic tunnel junctions *J. Appl. Phys.* **110**, 103915 (2011).

[36] A. M. Clogston, Optical Faraday rotation in ferrimagnetic garnet *J. Phys. Radium* **20**, 151-154 (1959).

[37] A. K. Zvezdin and V. A. Kotov, Modern Magnetooptics and Magnetooptical Materials (IOP, Bristol, 1997).

[38] S. Alebrand, M. Gottwald, M. Hehn, D. Steil, M. Cinchetti, D. Lacour, E.E. Fullerton, M. Aeschlimann, and S. Mangin, Light-induced magnetization reversal of high-anisotropy TbCo alloy films *Appl. Phys. Lett.* **101**, 162408 (2012).

[39] R. Malmhall, Extraordinary Hall resistivity in amorphous terbium–iron thin films and its temperature dependence *J. Appl. Phys.* **54**, 5128 (1983).

[40] Y. Mimura, N. Imamura, and Y. Kushiro, Hall effect in rare-earth-transition-metal amorphous alloy films *J. Appl. Phys.* **47**, 3371 (1976).

[41] A. Hassdenteufel, C. Schubert, J. Schmidt, P. Richter, D. R. T. Zahn, G. Salvan, M. Helm, R. Bratschitsch and M. Albrecht, Dependence of all-optical magnetic switching on the sublattice magnetization orientation in Tb-Fe thin films *Appl. Phys. Lett.* **105**, 112403 (2014).

[42] P. Hansen, C. Clausen, G. Much, M. Rosenkranz, and K. Witter, Magnetic and magneto-optical properties of rare-earth transition-metal alloys containing Gd, Tb, Fe, Co *J. Appl. Phys.* **66**, 756 (1989).

[43] B. Hebler, A. Hassdenteufel, P. Reinhardt, H. Karl, and M. Albrecht, Ferrimagnetic Tb–Fe alloy thin films: Composition and thickness dependence of magnetic properties and all-optical switching *Front. Mater.* **3**, 8 (2016).

[44] I. Radu, K. Vahaplar, C. Stamm, T. Kachel, N. Pontius, H. A. Durr, T. A. Ostler, J. Barker, R. F. Evans, R. W. Chantrell *et al.*, Transient ferromagnetic-like state mediating ultrafast reversal of antiferromagnetically coupled spins *Nature* **472**, 205–208 (2011).

[45] T. A. Ostler, J. Barker, R. F. L. Evans, R. W. Chantrell, U. Atxitia, O. Chubykalo-Fesenko, S. El Moussaoui, L. Le Guyader, E. Mengotti, L. J. Heyderman *et al.*, Ultrafast heating as a sufficient stimulus for magnetization reversal in a ferrimagnet *Nat. Commun.* **3**, 666 (2012).

[46] A. R. Khorsand, M. Savoini, A. Kirilyuk, A. V. Kimel, A. Tsukamoto, A. Itoh, and Th. Rasing, Role of magnetic circular dichroism in all-optical magnetic recording *Phys. Rev. Lett.* **108**, 127205 (2012).

[47] A. Khorsand M. Savoini, A. Kirilyuk, A. Kimel, A. Tsukamoto, A. Itoh, and Th. Rasing, Element-specific probing of ultrafast spin dynamics in multisublattice magnets with visible light *Phys. Rev. Lett.* **110**, 107205 (2013).

[48] M. Wietstruk, A. Melnikov, C. Stamm, T. Kachel, N. Pontius, M. Sultan, C. Gahl, M. Weinelt, H. A. Durr, and U. Bovensiepen, Hot-electron-driven enhancement of spin-lattice coupling in Gd and Tb 4*f* ferromagnets observed by femtosecond X-ray magnetic circular dichroism *Phys. Rev. Lett.* **106**, 127401 (2011).

[49] K. Uchida, S. Takahashi, K. Harii, J. Ieda, W. Koshibae, K. Ando, S. Maekawa, and E. Saitoh, Observation of the spin Seebeck effect *Nature* **455**, 778-781 (2008).

[50] H. Adachi, K. Uchida, E. Saitoh, and S. Maekawa, Theory of the spin Seebeck effect *Rep. Prog. Phys.* **76**, 036501 (2013).

[51] G. Tatara, and H. Kohno, Theory of current-driven domain wall motion: spin transfer versus momentum transfer *Phys. Rev. Lett.* **92**, 086601 (2004).

[52] D. Hinzke, and U. Nowak, Domain wall motion by the magnonic spin Seebeck effect *Phys. Rev. Lett.* **107**, 027205 (2011).

[53] K.-S. Ryu, L. Thomas, S.-H. Yang, S. Parkin, Chiral spin torque at magnetic domain walls *Nat. Nanotechnol.* **8**, 527-533 (2013).

[54] J. Torrejon, G. Malinowski, M. Pelloux, R. Weil, A. Thiaville, J. Curiale, D. Lacour, F. Montaigne, and M. Hehn, Unidirectional thermal effects in current-induced domain wall motion *Phys. Rev. Lett.* **109**, 106601 (2012).

[55] C. E. Graves, A. H. Reid, T. Wang, B. Wu, S. de Jong, K. Vahaplar, I. Radu, D. P. Bernstein, M. Messerschmidt, L. Muller *et al.*, Nanoscale spin reversal by non-local angular momentum transfer following ultrafast laser excitation in ferrimagnetic GdFeCo *Nat. Mater.* **12**, 293-298 (2013).

Chapter 5

General conclusions and perspectives

In this thesis, we have experimentally investigated the optical response of ferrimagnetic alloys and ferromagnetic multilayers under the action of 35-fs laser pulses and addressed mainly two key issues regarding the rich physics underlying the all-optical switching. The first issue we addressed in this thesis is the magnetic parameter governing the observation of the AO-HDS in both ferrimagnetic TbCo alloys and ferromagnetic Co/Ni and Co/Pt multilayers. The second key issue we addressed is the uniqueness of the all-optical switching mechanism in both ferri- and ferro-magnets. In the following, we will now present a summary of the results in this thesis.

The first part of this thesis aims to elucidate the magnetic parameters governing the observation of the all-optical switching. Indeed, several limitations have been proposed in the literature to explain the observation of AO-HDS in ferrimagnets. Experimental investigations on ferrimagnets proposed the perpendicular magnetic anisotropy and the antiferromagnetic coupling between non-equivalent sublattices as rules for the observation of AO-HDS. Later, the low remanence (M_R < 220 kA/m) was demonstrated as a criterion for the observation of AO-HDS in ferrimagnets. Nevertheless, the recent discovery of AO-HDS in ferromagnetic multilayers with a high saturation magnetization and no antiferromagnetic coupling between two sublattices casts doubt upon the models explaining the AO-HDS for ferrimagnets, and thus questions the uniqueness of the limitating parameter for both ferri- and ferro-magnets.

In this context, we performed a comprehensive investigation of the AO-HDS ability in ferromagnetic Co/Ni and Co/Pt multilayers as well as ferrimagnetic TbCo alloys for a wide range of composition and thickness. The optical response of the studied films under the action of 35-fs laser beam was probed using a magneto-optical Faraday microscope in order to image the magnetic domains in transmission. Therefore, we demonstrated that Co dominant TbCo alloys with a high saturation magnetization and remanence (M_R = 830 kA/m) and showing only thermal demagnetization for a high thickness (t = 20 nm) exhibit AO-HDS if their thickness is strongly reduced down to few nm. This finding contradicts the proposed low remanence criterion for the observation of AO-HDS in ferrimagnets.

It was shown in previous studies that the magnetic domain size is strongly dependent on the magnetic thickness, which is associated to the competition between the dipolar energy and the domain wall energy stabilizing small and large domains, respectively. Hence, we inferred that if the size of domain after laser-induced heating is smaller than the laser spot size, thermal demagnetization will be observed since the magnetic system will break into small domains during the cooling. While if the domain size is larger than the laser spot size, AO-HDS will be observed. Therefore, we estimated the domain size for the investigated films using the model of periodic stripe domains with a strong uniaxial anisotropy in an infinite plate. The magnetic parameters involved in the calculation of the domain size are the saturation magnetization,

the uniaxial anisotropy constant and the exchange constant.

The calculations demonstrate that the occurrence of AO-HDS corresponds to a domain size constantly larger than the spot size during cooling, a criterion that is common for both investigated ferri- and ferro-magnets. These findings are a hint that much more materials are expected to exhibit AO-HDS, and the initial effect of the helicity is nevertheless canceled by the formation of small magnetic domains during the cooling process. From a technological point of view, such large domain criterion allows identifying the optimal conditions for the observation of a persistent AO-HDS, whether by significantly reducing the magnetic thickness or by strongly decreasing the laser spot size. These results have been published in *Physical Review B* [1].

Finally, we verified the influence of the DW energy on AO-HDS by investigating the optical response of light-ion irradiated Co/Pt multilayers. Indeed, irradiating Co/Pt multilayers with He^+ ions leads to a strong decrease of the magnetic anisotropy, while the saturation magnetization changes only weakly. Thus, the domain energy decreases strongly due to the irradiation, leading to a decrease of the magnetic domain size. We measured the optical response of the irradiated films using magneto-optical Faraday microscopy. We demonstrated that the AO-HDS ability of Co/Pt multilayers is lost by gradually increasing the irradiation dose, which highlights the crucial role of the DW in the all-optical switching process. Moreover, we estimated the domain size of the irradiated films. We found that the magnetic domains in the irradiated films showing TD are smaller than the laser spot size, thus confirming the large domain size criterion for the observation of AO-HDS (to be submitted).

The recent discovery of AO-HDS for a much larger variety of ferri- and ferro-magnetic films and granular nanostructures, where the theoretical models explaining the switching in GdFeCo does not appear to apply, questions the uniqueness of the all-optical switching mechanism. Hence, the second part of this thesis aims to investigate the underlying microscopic physics of the all-optical switching in ferro- and ferri-magnetic materials, namely ferromagnetic Co/Pt multilayers and CoFeB/MgO heterostructures, as well as ferrimagnetic TbCo alloys. Therefore, we probed AO-HDS in ferro- and ferri-magnetic Hall crosses via the anomalous Hall effect. This novel approach combining both optics and spintronics enables a statistical quantification of the switching ratio for different laser parameters, thus giving new insights into the all-optical switching mechanism. Moreover, this approach enables to investigate the switching on different timescales ranging from 1 µs to a few seconds, thus bridging the gap between the ultrafast and the quasi-static methods used to probe magnetization. From a technological point of view, these investigations showed a first integration of AO-HDS into spintronic devices, by storing the circular polarization of the light in the remanence state of the magnetization.

We first demonstrated the AO-HDS in ferromagnetic Pt/Co/Pt films patterned into Hall crosses to allow electrical measurement of the magnetization via the anomalous Hall effect. Two methods were used: either the fs laser beam was swept over the Hall cross, or kept static and off-centered to make the AOS rim overlap with the center of Hall cross. Both approaches indicate that a power threshold needs to be overcome in order to observe AO-HDS. Moreover, we showed that the switching becomes incomplete by increasing the sweeping speed, which is due to the persistent formation of multiple magnetic domains. Therefore, these findings indicate that the AO-HDS in Pt/Co/Pt is a cumulative process, since a complete and reproducible switching requires a certain number of pulses. These results have already been published in *Applied Physics Letters* [2]. Furthermore, a stochastic behavior is measured by sweeping over the Pt/Co/Pt Hall cross with a linearly polarized beam, and is attributed to the large domain

size and the thermomagnetic writing in Pt/Co/Pt films.

In order to correlate the switching occurrence with the temperature increase within the Pt/Co/Pt Hall cross, we quantified the longitudinal resistance while sweeping with the laser beam over the Hall cross. We demonstrated that for a laser power above the switching power threshold, the AO-HDS process in Pt/Co/Pt is weakly related to the average laser-induced heating, however, it is mainly dependent on the number of pulses. Finally, we showed that the AO-HDS of Pt/Co/Pt Hall cross can be enhanced via current-induced Joule heating, indicating that the switching power threshold is dependent on sample temperature.

We also investigated the integration of the all-optical magnetization switching in CoFeB/MgO based Hall crosses. These ferromagnetic heterostructures triggered huge interest from the scientific community for their large potential for future spintronic devices. We first demonstrated the AO-HDS in CoFeB/MgO based Hall crosses with a swept laser beam. Nevertheless, we were not able to achieve a statistical quantification of the switching ratio of different laser parameters similar to the one performed in Pt/Co/Pt based Hall cross, due to the laser-induced anisotropy reduction in the CoFeB/MgO based Hall cross. Moreover, we demonstrated that sweeping over the CoFeB/MgO Hall cross with a linearly polarized beam leads to a complete reversal of the Hall cross. This tricky behavior is attributed to the thermomagnetic writing and the large magnetic domains in CoFeB/MgO which might be larger than the probed area of the Hall cross (to be submitted).

The AO-HDS ability was also demonstrated in $Tb_{27}Co_{73}$ based Hall crosses while the laser beam is swept or kept static and off-centered. Moreover, these electrical measurements showed that the Tb dominant $Tb_{27}Co_{73}$ alloy becomes Co dominant due the laser-induced heating, indicating that the temperature of the probed area locally increase above T_{comp} = 500 K.

Finally, the most important investigations in the second part of the thesis concern the microscopic mechanisms involved in the all-optical switching of both ferri- and ferro-magnets. Hence, we combined two different approaches to investigate the all-optical switching in ferrimagnetic GdFeCo and TbCo alloys and ferromagnetic Co/Pt multilayers. In the first approach, the magnetic response to one or two 35-fs laser pulses is imaged on a quasi-static time scale via magneto-optical Faraday imaging. In the second approach, the magnetization change under multiple-pulse exposure is probed by performing the static beam measurement in Hall crosses with an off-centered beam and a temporal resolution of 1 µs.

Therefore, we showed that two different types of all-optical switching processes can be distinguished. Indeed, the first type is the single-pulse helicity-independent switching in ferrimagnetic GdFeCo alloy films as shown in previous studies. The second type is a two regimes helicity-dependent switching in both ferrimagnetic TbCo alloys and ferromagnetic Co/Pt multilayers. We demonstrated that the latter takes place at two different timescales, and consists in a step-like helicity-independent multiple-domain formation within the first 1 ms followed by a helicity-dependent remagnetization on several tens of ms. We attributed this remagnetization to a helicity-dependent domain wall motion. Indeed, once the heat-only multiple domain state is achieved, a space-dependent symmetry breaking might arise from a difference in absorption of the two circular polarizations, stimulating spin currents via the spin Seebeck effect and leading to the shift of domain walls and thus to the gradual helicity-dependent remagnetization. On the other hand, the inverse Faraday effect could also explain the helicity-dependent remagnetization as demonstrated in recent theoretical investigations. However, the reversal in these models is obtained with a single laser pulse, which is not consistent with the measured cumulative reversal in Co/Pt multilayers. These results have been published in

Physical Review B [3].

The investigations presented in this thesis have significantly contributed to a deeper understanding of the all-optical switching mechanism in different ferri- and ferro-magnetic materials. Nevertheless, several important features remain to be confirmed or clarified, and thus further theoretical and experimental work would be definitely required.

First, the large domain size criterion for the observation of AO-HDS could be confirmed by investigating the response of materials which exhibit only TD under the action of fs laser beam with a size strongly decreased to few μm. Second, the newly demonstrated two regimes reversal process might be measured using a time-resolved magneto-optical imaging technique. However, performing a time-resolved imaging of the domain structures within the 2 μm-wide AOS rim requires both high temporal and spatial resolutions, which is difficult to fulfill. Hence, the use of a magnetic force microscope might be an alternative to probe the domain structures within the AOS rim after each laser pulse.

Another key issue which remains to be addressed is the origin of the symmetry breaking behind the helicity-dependent remagnetization measured in Co/Pt multilayers and TbCo alloys. Indeed, the two major origins debated in the literature are the inverse Faraday effect and the magnetic circular dichroism. Furthermore, it was experimentally shown that the microscopic origin of the helicity-dependent reversal in GdFeCo films is is more likely to be explained by the MCD, and not the IFE. Therefore, we believe that the MCD is more likely to explain the helicity-dependent remagnetization measured in Co/Pt multilayers and TbCo alloys. Nevertheless, additional studies are needed to experimentally determine the symmetry breaking origin.

Résumé

La manipulation de l'aimantation sans application de champ magnétique est un domaine de recherche émergent qui permet d'explorer de nouveaux phénomènes physiques et de développer des applications technologiques telles que les disques dures magnétiques. En 2007, une nouvelle possibilité pour retourner l'aimantation en utilisant des impulsions laser femtoseconde (fs) a été découverte par Stanciu *et al.* [4] et a suscité un grand intérêt au sein de la communauté scientifique. Ce retournement tout-optique de l'aimantation a été démontré initialement dans un film fait d'alliage ferrimagnétique de GdFeCo et s'est avéré dépendant de l'hélicité, le sens de l'aimantation étant donné par la polarisation circulaire droite ou gauche de la lumière [4]. Il s'agit du retournement tout-optique dépendant de l'hélicité, en anglais "all-optical helicity-dependent switching" (AO-HDS).

En 2011, Ostler *et al.* ont démontré dans le même matériau que le retournement tout-optique est indépendant de l'hélicité et obtenu avec une impulsion fs unique polarisée linéairement [5]. Alors que le retournement indépendant de l'hélicité a été attribué aux dynamiques distinctes des deux sous-réseaux de Gd et FeCo [6], l'origine microscopique du comportement dépendant de l'hélicité est fortement débattue, mais fut principalement attribuée au dichroïsme magnétique circulaire par Khorsand *et al.* [7]. Plus récemment, le retournement tout-optique a été également démontré pour une variété de matériaux ferrimagnétiques, sous formes d'alliages, de multicouches ainsi que dans des hétérostructures ferrimagnétiques synthétiques sans terres rares [8, 9, 10]. Récemment, ce phénomène a été également observé pour des films minces uniques de matériaux ferromagnétiques, ce qui ouvre la voie à l'intégration du retournement tout-optique dans l'industrie des mémoires magnétiques [11]. Contrairement aux alliages de GdFeCo, le retournement tout-optique dans ces matériaux ferri- et ferro-magnétiques est toujours dépendant de l'hélicité indépendamment de la puissance du faisceau laser.

Ces découvertes ont suscité un débat intensif à propos de plusieurs aspects du mécanisme du retournement tout-optique dans les matériaux ferri- et ferro-magnétiques. En effet, plusieurs études ont élucidé les paramètres magnétiques gouvernant l'observation du retournement tout-optique, le rôle du chauffage dans le processus du retournement, ainsi que l'origine de la brisure de symétrie. Pendant ce travail de thèse, nous avons étudié la réponse aux impulsions laser fs d'alliages ferrimagnétiques et de multicouches ferromagnétiques, dans l'objectif d'élucider divers aspects du mécanisme du retournement tout-optique. Ainsi, notre étude s'est articulée en deux grands axes : le premier vise à déterminer le paramètre magnétique gouvernant l'observation du retournement tout-optique dans les alliages ferrimagnétiques et les multicouches ferromagnétiques, tandis que le deuxième vise à élucider le mécanisme du retournement dépendant de l'hélicité dans ces deux types de matériaux. Nous allons à présent réaliser un bilan des résultats obtenus sur ces deux axes au cours de cette thèse.

Dans la première partie, nous avons étudié l'influence de plusieurs paramètres magnétiques sur l'observation du retournement tout-optique. Plusieurs modèles ont été reportés dans la littérature pour expliquer les conditions nécessaires pour observer le retournement tout-optique dans les matériaux ferrimagnétiques. En effet, Kimel a proposé l'anisotropie magnétique perpendiculaire et le couplage antiferromagnétique entre deux sous-réseaux non-équivalents comme conditions pour l'observation de l'AO-HDS [12]. En outre, la faible rémanence (M_R <

220 kA/m) a été proposée ultérieurement comme critère pour l'observation de l'AO-HDS dans les matériaux ferrimagnétiques [13]. Cependant, la récente découverte de l'AO-HDS dans des multicouches ferromagnétiques [11] avec une aimantation à saturation élevée et sans couplage antiferromagnétique remet en question les modèles proposés dans la littérature. Ainsi, nous avons effectué une investigation approfondie de l'aptitude de l'AO-HDS dans des multicouches ferromagnétiques de Co/Ni et Co/Pt, ainsi que dans des alliages ferrimagnétiques de TbCo pour une large gamme de compositions et d'épaisseurs. La réponse des films étudiés au faisceau laser avec une durée d'impulsion de 35 fs a été mesurée en utilisant la microscopie magnéto-optique Faraday afin d'imager les domaines magnétiques en transmission. Les alliages ferrimagnétiques de TbCo qui sont Co dominant avec une aimantation à saturation et une rémanence élevées (M_R = 830 kA/m) montrent une désaimantation thermique pour une large épaisseur (t = 20 nm). Néanmoins, nous avons démontré que ces films peuvent montrer l'AO-HDS si leur épaisseur est fortement réduite à quelques nm, comme illustré en figure 3.10 (voir section 3.3). Ce résultat contredit le critère de faible rémanence pour l'observation de l'AO-HDS dans les matériaux ferrimagnétiques.

Il a été montré que la taille des domaines magnétiques est fortement dépendante de l'épaisseur magnétique, ce qui est dû à la compétition entre l'énergie dipolaire stabilisant des domaines petits, et l'énergie de paroi favorisant des domaines grands [14]. Ainsi, il est raisonnable de supposer que si après le chauffage induit par les impulsions laser la taille des domaines est inférieure à la taille du faisceau laser, la désaimantation thermique (TD) aura lieu. Ceci sera dû à la brisure du système magnétique en petits domaines lors du processus de refroidissement. Par contre, l'AO-HDS sera observé si la taille des domaines est supérieure à la taille du faisceau laser. Afin de vérifier ce critère, nous avons calculé la taille des domaines dans les films étudiés en utilisant le modèle proposé par Kooy et Enz [15] permettant d'estimer la taille des domaines magnétiques rectilignes parallèles à forte anisotropie uniaxiale. Dans ce modèle, les paramètres magnétiques impliqués dans le calcul de la taille des domaines sont l'aimantation à saturation, la constante d'anisotropie uniaxiale et la constante d'échange.

Les calculs montrent que l'AO-HDS a lieu dans des matériaux magnétiques ayant des domaines magnétiques constamment plus larges que la taille du faisceau laser pendant le processus de refroidissement. En outre, ce critère pour l'observation de l'AO-HDS est commun pour les matériaux ferri- et ferro-magnétiques. Ces résultats indiquent qu'un grand nombre de matériaux devraient présenter l'AO-HDS, mais l'effet de l'hélicité est annulé par la formation de petits domaines magnétiques au cours du refroidissement. D'un point de vue technologique, ce critère de large taille de domaines permet d'identifier les conditions optimales pour l'observation de l'AO-HDS, que ce soit par une réduction significative de l'épaisseur magnétique, ou par une diminution forte de la taille du faisceau laser.

Finalement, nous avons vérifié l'influence de l'énergie de paroi sur l'AO-HDS en étudiant la réponse aux impulsions laser fs des multicouches de Co/Pt irradiés avec des ions légers. En effet, l'irradiation des multicouches de Co/Pt avec des ions He^+ entraîne une forte diminution de l'anisotropie magnétique, tandis que l'aimantation à saturation ne change que faiblement [16]. Par conséquent, l'énergie de paroi décroît fortement pour des fluences d'irradiation élevées, entraînant ainsi une diminution de la taille des domaines. La réponse optique des films irradiés a été mesurée par microscopie Faraday, comme illustré en figure 3.20 (voir section 3.5). Nous avons démontré que la capacité de l'AO-HDS dans les multicouches de Co/Pt tend à disparaître progressivement en augmentant la fluence d'irradiation, mettant ainsi en évidence le rôle des parois de domaines dans le processus du retournement tout-optique. De surcroît, l'estimation de la taille de domaines des films irradiés montre que les films montrant de la désaimantation thermique ont une taille de domaines inférieure à la taille du faisceau laser. Ces résultats

confirment le critère de larges domaines pour l'observation de l'AO-HDS.

La récente découverte de l'AO-HDS dans une large variété de films ferri- et ferro-magnétiques et nanostructures granulaires, où les modèles théoriques expliquant le retournement tout-optique dans le GdFeCo ne semblent pas s'appliquer, remet en question l'unicité du mécanisme du retournement tout-optique. Ainsi, nous avons étudié dans la deuxième partie de cette thèse l'origine microscopique du retournement tout-optique dans des matériaux ferri- et ferro-magnétiques, à savoir les multicouches de Co/Pt, les hétérostructures de CoFeB/MgO et les alliages de CoTb. Nous avons ainsi caractérisé l'AO-HDS dans des croix de Hall ferri- et ferro-magnétiques via l'effet Hall extraordinaire [17, 18]. Cette approche innovante combinant à la fois l'optique et la spintronique permet d'effectuer une quantification statistique du taux de renversement pour des paramètres laser différents, permettant ainsi une compréhension plus approfondie du mécanisme du retournement tout-optique. En outre, cette approche permet de mesurer le renversement sur des échelles temporelles allant de 1 µs à quelques secondes, comblant ainsi l'écart entre les méthodes ultra-rapides et quasi-statiques souvent utilisées pour sonder l'aimantation. D'un point de vue technologique, ces investigations montrent une première intégration de l'AO-HDS dans des dispositifs de spintronique, en mémorisant la polarisation circulaire de la lumière dans l'état rémanent de l'aimantation.

Nous avons tout d'abord démontré l'AO-HDS dans des films ferromagnétiques de Pt/Co/Pt microstructurés en croix de Hall en utilisant deux approches différentes. La première approche consiste à balayer le faisceau laser fs sur la croix de Hall, comme illustré en figure 4.5 (voir section 4.2) avec une vitesse de balayage de 40 µm/s. La deuxième approche consiste à garder le faisceau sur une position statique et décalée afin de permettre un recouvrement de l'anneau du retournement avec le centre de la croix de Hall. Les deux approches indiquent qu'un seuil de puissance doit être dépassé pour observer l'AO-HDS.

De surcroît, nous avons montré que le renversement devient incomplet en augmentant la vitesse de balayage, ce qui est dû à la formation de multidomaines magnétiques. Par conséquent, ces résultats indiquent que l'AO-HDS dans les films de Pt/Co/Pt est un processus cumulatif, car un renversement complet et reproductible nécessite un certain nombre d'impulsions. En outre, un comportement stochastique a été mesuré en balayant la croix de Hall de Pt/Co/Pt avec un faisceau polarisé linéairement, ce qui est attribué à la grande taille des domaines et à l'écriture thermomagnétique dans les films de Pt/Co/Pt [19].

Afin de corréler l'observation du retournement avec l'élévation de la température dans les croix de Hall de Pt/Co/Pt, nous avons quantifié l'évolution de la résistance longitudinale pendant le balayage de la croix par le faisceau laser. Nous avons ainsi montré que pour une puissance laser au-dessus de la puissance seuil, le processus de l'AO-HDS dans les croix de Hall de Pt/Co/Pt est faiblement lié au chauffage induit par les impulsions laser, mais fortement dépendant du nombre d'impulsions. Enfin, nous avons montré que la puissance seuil de l'AO-HDS dans les croix de Hall de Pt/Co/Pt peut être diminuée via le chauffage par effet Joule induit par courant, indiquant ainsi que la puissance seuil dépend de la température de l'échantillon.

Nous avons également élucidé pour la première fois l'intégration du retournement tout-optique dans les croix de Hall à base de CoFeB/MgO. Ces hétérostructures ferromagnétiques ont suscité un grand intérêt au sein de la communauté scientifique pour leur potentiel dans les futures applications en spintronique. Nous avons tout d'abord démontré l'AO-HDS avec un faisceau laser balayé. Néanmoins, nous n'avons pas été capables d'effectuer une étude statistique similaire à celle effectuée dans les croix de Hall de Co/Pt, en raison de la réduction d'anisotropie induite par le faisceau laser dans les croix de Hall de CoFeB/MgO. En outre,

nous avons montré que le balayage de la croix de Hall de CoFeB/MgO avec une polarisation linéaire entraîne un retournement complet de l'aimantation de la croix de Hall. Ce comportement est attribué à l'écriture thermomagnétique et aux larges domaines magnétiques dans les CoFeB/MgO qui peuvent être plus grands que la zone sondée de la croix de Hall.

Nous avons également démontré l'AO-HDS dans les croix de Hall de $Tb_{27}Co_{73}$ avec un faisceau balayé ou gardé sur une position statique et décalée. Ces mesures ont également démontré que l'alliage de $Tb_{27}Co_{73}$ étant Tb dominant devient Co dominant sous l'effet du chauffage induit par les impulsions laser fs, indiquant que la température de la zone sondé de la croix de Hall dépasse localement la température de compensation T_{comp} = 500 K.

Les investigations les plus importantes de cette seconde partie de thèse concernent les mécanismes impliqués dans le retournement tout-optique pour les matériaux ferri- et ferromagnétiques. Nous avons ainsi combiné deux différentes approches pour étudier le retournement tout-optique dans les alliages ferrimagnétiques de GdFeCo et TbCo, ainsi que dans les multicouches ferromagnétiques de Co/Pt. Dans la première approche, la réponse magnétique à une ou deux impulsions est visualisée par imagerie Faraday sur une échelle temporelle quasi-statique. Dans la deuxième approche, l'évolution de l'aimantation sous l'action d'impulsions laser multiples est quantifiée en effectuant les mesures électriques sur les croix de Hall avec une résolution temporelle de 1 µs. Ainsi, nous avons fait la distinction entre deux types de processus de retournement tout-optique. En effet, le premier type est le retournement indépendant de l'hélicité obtenu avec une impulsion unique dans les alliages ferrimagnétiques de GdFeCo comme il a été démontré dans des études précédentes [5]. Le second type est un retournement dépendant de l'hélicité suivant deux régimes différents dans les alliages ferrimagnétiques de TbCo et les multicouches ferromagnétiques de Co/Pt. Nous avons démontré que ce deuxième type de retournement a lieu sur deux échelles temporelles différentes, comme illustré en figure 4.41 (voir section 4.5). En effet, il consiste en une formation indépendante de l'hélicité de multidomaines magnétiques pendant la première 1 ms suivie d'une ré-aimantation dépendante de l'hélicité sur plusieurs dizaines de millisecondes.

Nous avons attribué la ré-aimantation à une propagation de parois de domaines dépendante de l'hélicité. En effet, une fois que la formation de multidomaines s'est produite pendant la première 1 ms, une brisure de symétrie dépendant de l'espace peut provenir d'une différence d'absorption des deux polarisations circulaires. Ceci peut stimuler des courants de spins via l'effet Seebeck de spin [20, 21], entraînant le déplacement de parois de domaines et la ré-aimantation graduelle. D'autre part, l'effet Faraday inverse (IFE) peut aussi expliquer la ré-aimantation dépendante de l'hélicité comme il a été démontré dans des études théoriques récentes [22]. Cependant, le retournement tout-optique dans ces modèles a été obtenu avec une impulsion unique, ce qui n'est pas cohérent avec le retournement cumulatif mesuré sur les multicouches de Co/Pt.

Les résultats obtenus dans cette étude ont contribué significativement à la compréhension du mécanisme du retournement tout-optique de l'aimantation dans différents matériaux ferri- et ferro-magnétiques. Néanmoins, plusieurs pistes peuvent être considérées pour développer ce travail de thèse, et des travaux théoriques et expérimentaux complémentaires seraient certainement nécessaires. Tout d'abord, le critère de large taille de domaines pour l'observation de l'AO-HDS peut être confirmé en étudiant la réponse de films magnétiques montrant de la désaimantation thermique sous l'action d'un faisceau laser dont la taille est fortement réduite à quelques nm. En outre, le processus de retournement à deux régimes peut être également mesuré avec une technique d'imagerie magnéto-optique résolue dans le temps. Cependant, ceci nécessite d'une part une bonne résolution temporelle pour suivre le taux de répétition du

laser, et d'autre part une bonne résolution spatiale pour imager les structures en domaines au sein de l'anneau du retournement faisant quelques µm, ce qui est difficile à réaliser. Ainsi, l'utilisation du microscope à force magnétique peut être une alternative pour imager les structures en domaines au sein de l'anneau du retournement.

Une question fondamentale qui reste encore à résoudre est l'origine de la brisure de symétrie permettant la ré-aimantation dépendante de l'hélicité mesurée dans les multicouches de Co/Pt et les alliages de TbCo. En effet, deux origines majeures sont débattues dans la littérature, à savoir l'effet Faraday inverse (IFE) et le dichroïsme magnétique circulaire (MCD). Par ailleurs, il a été démontré expérimentalement que l'origine microscopique de l'AO-HDS dans les alliages de GdFeCo est expliquée par le MCD, et non pas par l'IFE [7]. Ainsi, nous estimons que le MCD est plus susceptible d'expliquer la ré-aimantation dépendante de l'hélicité mesurée dans les multicouches de Co/Pt et les alliages de TbCo. Néanmoins, des études complémentaires sont nécessaires pour déterminer l'origine de la brisure de symétrie dans ces matériaux.

References

[1] M. S. El Hadri, M. Hehn, P. Pirro, C.-H. Lambert, G. Malinowski, E. E. Fullerton, and S. Mangin, Domain size criterion for the observation of all-optical helicity-dependent switching in magnetic thin films *Phys. Rev. B* **94**, 064419 (2016).

[2] M. S. El Hadri, P. Pirro, C.-H. Lambert, N. Bergeard, S. Petit-Watelot, M. Hehn, G. Malinowski, F. Montaigne, Y. Quessab, R. Medapalli *et al.*, Electrical characterization of all-optical helicity-dependent switching in ferrimagnetic Hall crosses *Appl. Phys. Lett.* **108**, 092405 (2016).

[3] M. S. El Hadri, P. Pirro, C.-H. Lambert, S. Petit-Watelot, Y. Quessab, M. Hehn, F. Montaigne, G. Malinowski, and S. Mangin, Two types of all-optical magnetization switching mechanisms using femtosecond laser pulses *Phys. Rev. B* **94**, 064412 (2016).

[4] C. D. Stanciu, F. Hansteen, A. V. Kimel, A. Kirilyuk, A. Tsukamoto, A. Itoh, and T. Rasing, All-optical magnetic recording with circularly polarized light *Phys. Rev. Lett.* **99**, 047601 (2007).

[5] T. A. Ostler, J. Barker, R. F. L. Evans, R. W. Chantrell, U. Atxitia, O. Chubykalo-Fesenko, S. El Moussaoui, L. Le Guyader, E. Mengotti, L. J. Heyderman *et al.*, Ultrafast heating as a sufficient stimulus for magnetization reversal in a ferrimagnet *Nat. Commun.* **3**, 666 (2012).

[6] I. Radu, K. Vahaplar, C. Stamm, T. Kachel, N. Pontius, H. A. Durr, T. A. Ostler, J. Barker, R. F. Evans, R. W. Chantrell *et al.*, Transient ferromagnetic-like state mediating ultrafast reversal of antiferromagnetically coupled spins *Nature* **472**, 205–208 (2011).

[7] A. R. Khorsand, M. Savoini, A. Kirilyuk, A. V. Kimel, A. Tsukamoto, A. Itoh, and Th. Rasing, Role of magnetic circular dichroism in all-optical magnetic recording *Phys. Rev. Lett.* **108**, 127205 (2012).

[8] S. Alebrand, M. Gottwald, M. Hehn, D. Steil, M. Cinchetti, D. Lacour, E.E. Fullerton, M. Aeschlimann, and S. Mangin, Light-induced magnetization reversal of high-anisotropy TbCo alloy films *Appl. Phys. Lett.* **101**, 162408 (2012).

[9] A. Hassdenteufel, B. Hebler, C. Schubert, A. Liebig, M. Teich, M. Helm, M. Aeschlimann, M. Albrecht, and R. Bratschitsch, Thermally assisted all-optical helicity dependent magnetic switching in amorphous $Fe_{100-x}Tb_x$ alloy films *Adv. Mater.* **25**, 3122 (2013).

[10] S. Mangin, M. Gottwald, C.-H. Lambert, D. Steil, V. Uhlir, L. Pang, M. Hehn, S. Alebrand, M. Cinchetti, G. Malinowski *et al.*, Engineered materials for all-optical helicity-dependent magnetic switching *Nat. Mater.* **13**, 286–292 (2014).

[11] C.-H. Lambert, S. Mangin, B. S. D. C. S. Varaprasad, Y. K. Takahashi, M. Hehn, M. Cinchetti, G. Malinowski, K. Hono, Y. Fainman, M. Aeschlimann *et al.*, All-optical control of ferromagnetic thin films and nanostructures *Science* **345**, 1337–1340 (2014).

[12] A. V. Kimel, All-optical switching: Three rules of design *Nat. Mater.* **13**, 225–226 (2014).

[13] A. Hassdenteufel, J. Schmidt, C. Schubert, B. Hebler, M. Helm, M. Albrecht, and R. Bratschitsch, Low remanence criterion for helicity-dependent all-optical magnetic switching in ferrimagnets and heterostructures *Phys. Rev. B* **91**, 104331 (2015).

[14] O. Hellwig, A. Berger, J.B. Kortright, and E. E. Fullerton, Domain structure and magnetization reversal of antiferromagnetically coupled perpendicular anisotropy films *J. Magn. Magn. Mater.* **319** (1-2), 13-55 (2007).

[15] C. Kooy, and U. Enz, Experimental and theoretical study of the domain configuration in thin layers of $BaFe_{12}O_{19}$ *Philips Res. Rep.* **15**, 7 (1960).

[16] T. Devolder, Light ion irradiation of Co/Pt systems: Structural origin of the decrease in magnetic anisotropy *Phys. Rev. B* **62**, 9 (2000).

[17] J. M. Luttinger, Theory of the Hall effect in ferromagnetic substances *Phys. Rev.* **112**, 739 (1958).

[18] L. Berger, Side-jump mechanism for the Hall effect of ferromagnets *Phys. Rev. B* **2**, 4559 (1970).

[19] Y. Mimura, N. Imamura, T. Kobayashi, Thermomagnetic writing on Gd–Fe and Gd–Fe–Y amorphous films *Jpn. J. Appl. Phys.* **17**, 1365 (1978).

[20] K. Uchida, S. Takahashi, K. Harii, J. Ieda, W. Koshibae, K. Ando, S. Maekawa, and E. Saitoh, Observation of the spin Seebeck effect *Nature* **455**, 778-781 (2008).

[21] H. Adachi, K. Uchida, E. Saitoh, and S. Maekawa, Theory of the spin Seebeck effect *Rep. Prog. Phys.* **76**, 036501 (2013).

[22] T. D. Cornelissen, R. Cordoba, and B. Koopmans, Microscopic model for all optical switching in ferromagnets *Appl. Phys. Lett.* **108**, 142405 (2016).

Mécanisme de retournement d'aimantation entraînant le retournement tout-optique dépendant de l'hélicité

Le contrôle de l'aimantation sans application de champ magnétique externe est un domaine de recherche en plein essor, étant prometteur pour les applications technologiques d'enregistrement magnétique et de spintronique. En 2007, Stanciu *et al.* ont découvert la possibilité de retourner l'aimantation dans un film fait d'alliage ferrimagnétique de GdFeCo en utilisant des impulsions laser femtoseconde. Longtemps cantonné aux alliages de GdFeCo, ce retournement tout-optique s'avère un phénomène plus général, puisqu'il a été mesuré plus récemment dans une large variété de matériaux ferrimagnétiques et ferromagnétiques. Cette découverte a ainsi ouvert la voie à l'intégration de l'écriture tout-optique dans l'industrie des mémoires magnétiques. Néanmoins, l'ensemble des modèles théoriques expliquant le retournement tout-optique dans le GdFeCo ne semblent pas s'appliquer aux autres matériaux magnétiques, mettant ainsi en question l'unicité de l'origine microscopique de ce phénomène.

Au cours de cette thèse, nous avons étudié la réponse aux impulsions laser femtoseconde des alliages ferrimagnétiques et des multicouches ferromagnétiques, dans l'objectif d'élucider divers aspects du mécanisme du retournement optique. Nous avons élucidé expérimentalement les paramètres magnétiques gouvernant le retournement tout-optique. Nous avons montré que l'observation du retournement tout-optique nécessite des domaines magnétiques plus grands que la taille du faisceau laser pendant le processus de refroidissement, un critère qui est commun à la fois aux matériaux ferrimagnétiques et ferromagnétiques. En outre, nous nous sommes intéressés à l'intégration du retournement tout-optique dans des dispositifs de spintronique. Grâce à une caractérisation temporelle de l'aimantation dans des croix de Hall via l'effet Hall extraordinaire, nous avons distingué entre deux types de mécanismes du retournement optique. Le premier type est un retournement purement thermique obtenu avec une impulsion unique dans les alliages ferrimagnétiques de GdFeCo, tandis que le deuxième type est un retournement cumulative et à deux régimes dans les alliages ferrimagnétiques de TbCo et les multicouches ferromagnétiques de Co/Pt. Ce dernier consiste en une formation indépendante de l'hélicité de multidomaines magnétiques suivie d'une ré-aimantation dépendante de l'hélicité sur plusieurs dizaines de millisecondes.

Mots clés : magnétisme, spintronique, retournement tout-optique, renversement de l'aimantation.

Magnetization reversal mechanism leading to all-optical helicity-dependent switching

The control of magnetization without external magnetic fields is an emergent field of research due to the prospect of impacting many technological applications such as magnetic recording and spintronics. In 2007, Stanciu *et al.* discovered an intriguing new possibility to switch magnetization in a ferrimagnetic GdFeCo alloy film using femtosecond laser pulses. This all-optical switching of magnetization had long been restricted to GdFeCo alloys, though it turned out to be a more general phenomenon for a variety of ferromagnetic and ferromagnetic materials. This discovery paved the way for an integration of the all-optical writing in storage industries. Nevertheless, the theoretical models explaining the switching in GdFeCo alloys films do not appear to apply in the other materials, thus questioning the uniqueness of the microscopic origin of all-optical switching.

In this thesis, we have investigated the response of femtosecond laser pulses in ferrimagnetic alloys and ferromagnetic multilayers to the action of femtosecond laser pulses, in order to elucidate several aspects of the all-optical switching mechanism. We have experimentally studied the magnetic parameters governing the all-optical switching. We showed that the observation of all-optical switching requires magnetic domains larger than the laser spot size during the cooling process; such a criterion is common for both ferrimagnets and ferromagnets. Furthermore, we have investigated the integration of all-optical switching in spintronic devices via the anomalous Hall effect. Through a time-dependent electrical investigation of the magnetization in Hall crosses, we distinguished between two types of all-optical switching mechanisms. The first type is the single-pulse helicity-independent switching in ferrimagnetic GdFeCo alloy films as shown in previous studies, whereas the second is a two regimes helicity-dependent switching in both ferrimagnetic TbCo alloys and ferromagnetic Co/Pt multilayers. The latter consists in a step-like helicity-independent multiple-domain formation followed by a helicity-dependent remagnetization on several tens of milliseconds.

Keywords: magnetism, spintronics, all-optical switching, magnetization reversal.